Molecular Beam Epitaxial Growth Optimization for Next Generation Optoelectronic Devices Based on III-V Semiconductors

by

Man Chun Alan Tam

A thesis
presented to the University of Waterloo
in fulfillment of the
thesis requirement for the degree of
Doctor of Philosophy
in
Electrical and Computer Engineering - Nanotechnology

Waterloo, Ontario, Canada, 2020

© Man Chun Alan Tam 2020

Examining Committee Membership

The following served on the Examining Committee for this thesis. The decision of the Examining Committee is by majority vote.

External Examiner:	Jan Dubowski Professor, Electrical and Computer Engineering, Universite de Sherbrooke
Supervisor:	Zbigniew Wasilewski Professor, Electrical and Computer Engineering, University of Waterloo
Internal Member:	Dayan Ban Professor, Electrical and Computer Engineering, University of Waterloo
Internal Member:	Guoxing Miao Professor, Electrical and Computer Engineering, University of Waterloo
Internal-External Member:	Jan Kycia Professor, Physics and Astronomy, University of Waterloo

Author's Declaration

I hereby declare that I am the sole author of this thesis. This is a true copy of the thesis, including any required final revisions, as accepted by my examiners.

I understand that my thesis may be made electronically available to the public.

Abstract

Molecular beam epitaxy (MBE) has been serving as the best tool for group III-V compound growths due to its capability of depositing epilayers with high single-crystalline quality, high purity and Angstrom-scale thickness precision. In spite of decades of work, further optimizations of MBE growth conditions are required in order to meet the increasing demands of next-generation and novel devices. For instance, low temperature (LT) deposition far away from thermal equilibrium growth conditions brings several benefits such as suppressed undesirable interface inter-diffusion, dopant diffusion and segregation. More importantly, it has been proven to be a very useful method in forming non-stoichiometric III-V compounds. Although this creates defects like group V antisites and interstitials, they can be utilized in making terahertz (THz) photoconductive antennas (PCAs). Since the development of THz technology in the late 20^{th} century, THz PCAs have been drawing tremendous research interest due to their low-cost and portability. The amount of embedded excess As which alters the LT grown III-V material properties is sensitive to the V/III flux ratio, and more importantly, the growth temperature at the range of ∼200–300°C. It is crucial to determine a critical substrate temperature that simultaneously maximizes the excess As incorporation without losing single crystallinity, as both features are essential for high-performance broadband THz PCAs applications. However, substrate temperature monitoring becomes difficult when the growth is switched to the LT regime. Conventional substrate temperature measurement techniques such as pyrometry have limited precision at LT due to the exponential decrease of the substrate thermal radiation intensity with the temperature, hence an alternative means for precise temperature monitoring is required. InAlGaAs has been an emerging candidate for 1319 nm laser-pumped, high-efficiency photonic power converters (PPCs). To acquire smooth surface morphology and minimize crystalline defects, such quaternary material is preferred to be lattice-matched on InP(001) substrates. A clear correlation between group III compositions, lattice constant and bandgap of InAlGaAs, as well as a reproducible approach to grow lattice-matched InAlGaAs structures need to be established to optimize the PPC performance.

This thesis conducts a comprehensive study of optimizing MBE growth conditions of several III-V materials, including LT GaAs, mid-temperature (MT) and LT InGaAs-InAlAs superlattice (SL), and InAlGaAs, with parameters such as substrate temperature, As overpressure and doping concentration being repetitively tuned. In particular, an integrated spectral pyrometry (ISP) technique is proposed, which is particularly well suited to monitor the growth temperature of InAs and InSb. Potentially, ISP can also be applied to other LT growths with semiconductors of smaller bandgaps when pyrometer does not work. In-growth and post-growth surface morphologies were investigated with the

aid of reflection high energy electron diffraction (RHEED) and Nomarski microscopy. LT GaAs and InGaAs-InAlAs SL based THz PCAs were characterized with 780 and 1550 nm pumped time-domain spectroscopy (TDS) measurements and the correlation between THz signal amplitude, pulse width and bandwidth with growth and annealing temperatures are discussed. The material properties of InAlGaAs structures were investigated with an emphasis on discussing challenges of lattice mismatch and in-growth flux drift studied by high-resolution x-ray diffraction (HRXRD) fitting. The performance of InAlGaAs p-n junctions was optimized by MBE. State-of-the-art 1319 nm pumped single-junction (SJ) and two-junction (TJ) PPC devices are presented. The effects of growth temperature on current-voltage characteristics and unintentionally strained InAlGaAs epilayers on quantum efficiency are discussed.

Acknowledgements

I would like to express my sincere gratitude to my supervisor, Prof. Zbigniew Wasilewski, for his patient guidance and continuous support in the last six and a half years. His valuable advice and keeping of a positive attitude during difficult times have inspired me a lot not only in research but also in life perspective.

My special thanks to Prof. Dayan Ban, Prof. Guoxing Miao and Prof. Jan Kycia for being the members of my thesis examination committee, with Prof. Jan Dubowski from Université de Sherbrooke as my external examiner. Thanks all of you for reviewing my thesis and attending my defense within such a tight schedule during the unfortunate epidemic that happened this year.

Another special thanks to Prof. Bo Cui's Nanofabrication group and all staff from TeTechS Inc., especially Dr. Daryoosh Saeedkia for providing optical instrument support even when the resource is limited. Super big thanks to Dr. Navid Jahed for processing my antenna samples and conducting the terahertz measurements which none of those is an easy job.

Yet another special thanks to SUNLAB in the University of Ottawa, especially Prof. Karin Hinzer and Ms. Meghan Beattie for building and testing those impressive p-n junction devices, which eventually help me add a meaningful part to my thesis.

I would also like to thank my family, friends and colleagues for their continuous support and encouragement during the past years. I couldn't have made it this far without any of you.

Dedication

To those who shaped my childhood.

Table of Contents

List of Figures

List of Tables

List of Abbreviations

$(NH_4)_2C_4H_4O_6$ Ammonium tartrate. 29

3D Three-dimensional. 13, 35, 84, 96, 102, 105, 106, 114, 139

4pp Four-point-probe. 6, 7, 13, 96, 102–106, 139

a.u. Arbitrary unit. 30, 53

AC Alternative current. 28

As_{Ga} As antisite. 39, 42

BEP Beam equivalent pressure. 12, 14, 15, 22, 24, 27

BET Band edge thermometry. 2, 6, 12, 17, 32–34, 43, 48, 49, 54, 56, 58, 85, 87, 102, 109, 119, 138, 139

BFM Beam flux monitor. 6, 11, 12, 14–20, 22, 27, 59, 62, 63, 89–91, 119–122, 127, 129, 141

BS Beam-splitter. 36, 37

BSF Back surface field. 113–116, 118

BW Bandwidth. 40, 43, 80, 82, 109, 111, 139

CCD Charge-coupled device. 102

CT Cluster tool module. 10

CW Continuous wave. 37

DC Direct current. 37

DICM Differential interference contrast microscopy. 35

DR Differential reflection. 36

DT Differential transmission. 36

ECV Electrochemical capacitance-voltage. 6, 7, 13, 28, 29, 31, 103, 107, 140

EDTA Ethylenediaminetetraacetic acid. 29

EM Electromagnetic. 3–5

EQE External quantum efficiency. 133, 137

FEL Free-electron laser. 3

FFT Fast Fourier transform. 44

FSF Front surface field. 113–116, 118

FWHM Full-width-half-maximum. 79, 80, 82, 109

GM Growth module. 9–13, 21, 22, 48, 59, 70, 84, 103, 104, 119, 122

HBT Heterojunction bipolar transistors. 1

HRXRD High-resolution x-ray diffraction. v, 6, 7, 13, 17, 24–27, 59, 65, 70–73, 88, 96–101, 104, 127–131, 139, 140

inf Infinite. 130, 131

ISP Integrated spectral pyrometry. iv, 6, 43, 48–54, 56, 57, 87, 102, 138, 139, 141

LED Light-emitting diode. 5, 58

LL Load-lock module. 10

LN_2 Liquid nitrogen. 9, 11

LT Low temperature. iv, v, 1, 2, 4–6, 28, 39, 40, 42, 43, 52, 58–65, 70, 73–76, 79, 81–88, 96–99, 102, 103, 107, 109–111, 138–141

MBE Molecular beam epitaxy. iv, v, 1, 2, 4–12, 15, 20, 21, 25, 27, 32, 33, 39, 43, 45, 48, 58–60, 65, 70, 84, 88, 102, 104, 109, 138, 139, 141

MJ Multi-junction. 5, 45, 46, 112, 133

ML Monolayer. 24, 27, 127

MLHS Multilayer heterostructure. 43, 44

MOVPE Metalorganic vapor phase epitaxy. 103

MT Middle temperature. iv, 84–88, 96, 97, 100, 107, 110, 119, 139

NaOH Sodium hydroxide. 29

NIR Near-infrared. 2, 11, 12, 33, 48, 51–54, 102, 119

Op Overpressure. 6, 17, 22, 50, 58, 65, 84, 112, 119, 139

PBN Pyrolytic boron nitride. 9

PCA Photoconductive antenna. iv, v, 4, 6, 7, 36–40, 42, 43, 58, 76, 77, 82, 96, 102, 106–108, 139–141

PID Proportional-integral-derivative. 10

PM Preparation module. 10

PPC Photonic power converter. iv, v, 5–7, 45, 47, 112, 113, 115, 127–129, 132–135, 137, 138, 140

Q2” Quarter-2-inch. 48–50

Q3” Quarter-3-inch. 58, 59, 65, 76, 84, 96, 102–104, 119

QCL Quantum cascade laser. 4, 15

QE Quantum efficiency. 5, 7, 129, 132–135, 137, 140

RADS Rocking-Curve Analysis by Dynamical Simulation. 25, 127

RGA Residual gas analyzer. 11, 12

RHEED Reflection high energy electron diffraction. v, 6, 11, 12, 21, 23, 27, 58, 59, 64, 139

RIE Reactive ion etching. 76, 82, 107

RTA Rapid thermal annealer. 59–61, 70, 104

Rx Receiver. 76–83, 107–110, 139, 140

SEM Scanning electron microscopy. 76, 77, 107, 108

SI Semi-insulating. 26, 32–34, 48, 54, 59, 85, 86, 96, 104, 113, 115, 119, 138–140

SJ Single-junction. v, 5, 7, 45, 46, 113–116, 128, 130–135, 137, 140

SL superlattice. iv, v, 4–6, 25, 28, 39, 42–44, 84–91, 96–104, 106, 107, 109–111, 119, 127, 128, 134, 138–140

SNR Signal to noise ratio. 139

SRS Stanford Research Systems. 12, 17, 19, 22, 91, 119, 121

TA Triple-axis. 25, 65, 70–72, 97–100, 127, 131

TD Tunnel diode. 45, 115, 117, 118, 133, 134, 136

TDS Time-domain spectroscopy. v, 4, 6, 7, 36, 37, 42, 43, 58, 76, 79–83, 107, 109, 111, 138–140

TEM Transmission electron microscopy. 39, 40

THz Terahertz. iv, v, 3, 4, 6, 7, 36–40, 42–44, 58, 76–83, 85, 96, 102, 107–109, 111, 138–141

TJ Two-junction. v, 7, 115, 118, 119, 134, 137, 140

Tx Transmitter. 76, 78–83, 85, 107, 109, 110, 139, 140

UHV Ultra-high vacuum. 1, 8–10, 12

V_{Ga} Ga vacancy. 39

List of Symbols

A Cell coefficient [Torr K]. 15, 20

$\mathcal{A}$ Area [m^2]. 13, 14, 29

$A_{\mathbf{cap}}$ InGaAs cap absorbance. 137

a_f Lattice constant of unstrained layer [Å]. 17

$a_{\parallel}$ Lattice constant parallel to the wafer surface [Å]. 17, 20

$a_{\perp}$ Lattice constant along the growth direction [Å]. 17, 20, 24

a_s Lattice constant of the substrate [Å]. 17

B Cell coefficient [K]. 15, 20, 129

b Bowing factor [Å]. 24

$\mathcal{B}_{\mathbf{cell}}$ Spectral intensity coefficient of cell [a.u.]. 53

$\mathcal{B}_{\mathbf{sub}}$ Spectral intensity coefficient of substrate [a.u.]. 53

c Speed of light in vacuum, $3 \times 10^8 ms^{-1}$. 30

C Cell coefficient [$cm^{-2}s^{-1}Torr^{-1}K^{-1/2}$]. 14, 15, 20, 21, 129

C_1 ISP calibration coefficient [a.u.]. 49

C_2 ISP calibration coefficient [K]. 49

$\mathcal{C}$ Capacitance [F]. 29

d Target epilayer thickness [Å]. 26, 127, 130, 131

d_1 Target epilayer thickness [Å]. 115

d_2 Target epilayer thickness [Å]. 115

d' Fitted epilayer thickness [Å]. 26, 127, 130, 131

$d'_{\mathbf{AlAs}}$ Fitted AlAs epilayer thickness [Å]. 75

$d'_{\mathbf{LT\text{-}GaAs}}$ Fitted LT-GaAs epilayer thickness [Å]. 75

$\mathcal{E}$ Emissivity. 30, 32

ε_0 Free space permittivity, $8.85 \times 10^{-12}\mathrm{Fm}^{-1}$. 29

ε_r Dielectric constant. 29

ϵ_x Strain parallel to the wafer surface. 17

ϵ_y Strain parallel to the wafer surface. 17

ϵ_z Strain along the growth direction. 17

$f(v)$ Probability distribution function [$\mathrm{m}^{-1}\mathrm{s}^{1}$]. 13

ϕ Molecular beam flux [$\mathrm{cm}^{-2}\mathrm{s}^{-1}$]. 13, 15, 24

ϕ_d Dopant flux [$\mathrm{cm}^{-2}\mathrm{s}^{-1}$]. 29, 30

G Growth rate [Å/s]. 17, 24

$G_{\mathbf{AlAs}}$ AlAs growth rate [Å/s]. 75

$G_{\mathbf{LT\text{-}GaAs}}$ LT-GaAs growth rate [Å/s]. 75

$G_{\mathbf{ref}}$ Reference growth rate used in group V cell calibration [Å/s]. 22

$G_{\mathbf{target}}$ Target growth rate [Å/s]. 22

$\mathcal{G}$ Geometric factor [a.u.]. 30, 32

h Planck constant, $6.63 \times 10^{-34}\mathrm{Js}$. 30

I Spectral intensity [a.u.]. 30

$I_{\mathbf{all}}$ ISP intensity from all sources [a.u.]. 50–52

$I_{\mathbf{InAs}}$ ISP intensity from InAs substrate [a.u.]. 48–50

I_j ISP intensity from extra source other than wafer [a.u.]. 49

$I_{\mathbf{Si}}$ ISP intensity from Si cell [a.u.]. 51

$I^*_{\mathbf{Si}}$ ISP intensity from Si cell [a.u.]. 51

$\mathcal{I}$ Beam equivalent pressure [Torr]. 14, 15, 17, 20

$\mathcal{I}_{\mathbf{ref}}$ Reference beam equivalent pressure acquired in group V cell calibration [Torr]. 22

$\mathcal{I}_c$ Carbon Cell Current [A]. 87

J Current density [Am^{-2}]. 5, 7, 45, 47, 129, 132–134, 136, 137, 140

$\mathcal{J}$ Spectral radiance [Wm^{-3}]. 30

k Extinction coefficient of epilayer. 28, 132

k_s Extinction coefficient of virtual substrate. 28

k_B Boltzmann's constant, $1.38 \times 10^{-23}\mathrm{JK}^{-1}$. 13

L Ion gauge length [m]. 14

l Lattice constant of compressed/extended epilayer [Å]. 17

l_0 Lattice constant of unstrained epilayer [Å]. 17

$\mathcal{L}$ Diffraction order no. 25

$\mathcal{L}_i$ Diffraction order no. 25

$\mathcal{L}_j$ Diffraction order no. 25

Λ SL period thickness [Å]. 25, 101

λ Wavelength [nm] or [Å]. 25, 28, 30, 32

λ_c Band edge wavelength [nm]. 33

M Growth rate [ML/s]. 24

m Mass of molecules in the vapor phase [kg]. 13

$\mathcal{M}_{\mathbf{mol}}$ Molar mass of etched epilayer [gmol^{-1}]. 29

$N_{\mathbf{A}}$ Avogadro number, 6.02×10^{23}mol^{-1}. 29

N No. of atoms/molecules/particles. 14

$\mathcal{N}$ No. of atoms enter the ion gauge per second [s^{-1}]. 14

$\mathfrak{n}$ No. of atoms per unit volume / doping concentration [cm^{-3}]. 13, 29

$\mathfrak{n}_{\mathbf{As}}$ As_{Ga} defect density [cm^{-3}]. 40

n Refractive index of epilayer. 28

n_s Refractive index of virtual substrate. 28

ν Poisson ratio. 17

ω Angle between x-ray beam and wafer surface [°]. 25

ω_B Bragg angle [°]. 25

ω_i Bragg angle correspond to the $\mathcal{L}_i$ diffraction order [°]. 25

ω_j Bragg angle correspond to the $\mathcal{L}_j$ diffraction order [°]. 25

$\omega_{\mathbf{LT\text{-}GaAs}}$ Bragg angle of the LT GaAs peak ["]. 73

$\omega_{\mathbf{SL0,as\text{-}grown}}$ Bragg angle of the as-grown 0$^{\text{th}}$ order SL peak ["]. 101

$\omega_{\mathbf{SL0,annealed}}$ Bragg angle of the annealed 0$^{\text{th}}$ order SL peak ["]. 101

$\langle \Delta\omega \rangle$ Average separation between adjacent SL peaks ["]. 101

P Pressure [Torr]. 14

$P_{\mathbf{target}}$ Target overpressure. 22

$\mathcal{P}$ Ionization probability of an atom. 14

p_0 Band edge calibration coefficient [°C]. 33

p_1 Band edge calibration coefficient [°Cnm^{-1}]. 33

p_2 Band edge calibration coefficient [°Cnm^{-2}]. 33

p_3 Band edge calibration coefficient [°Cnm^{-3}]. 33

Q Total measured charge [C]. 29

q Elementary charge, 1.6×10^{-19}C. 29

$\mathcal{R}$ Reflectance. 30, 32, 133, 137

$r_{\mathbf{Al}}$ Al flux deviation [%]. 127, 128, 130, 131

$r_{\mathbf{Ga}}$ Ga flux deviation [%]. 127, 128, 130, 131

$r_{\mathbf{In}}$ In flux deviation [%]. 127, 130, 131

$R_{\mathbf{sheet}}$ Sheet resistance [Ω/sq]. 96, 102, 104–106

ϱ Mass density of etched epilayer [kgm^{-3}]. 29

s Radial displacement from wafer centre [mm]. 96

σ Carrier capture cross section [m^2]. 40

T Cell temperature [°C]. 13–15, 17, 20

T_c Substrate heater thermocouple temperature [°C]. 17–19, 48–52, 54, 56, 59, 62, 63, 85, 89–91, 104, 119–122

$T_{\mathbf{BET}}$ Band edge thermometer temperature [°C]. 17, 18, 33, 48–50, 54, 56, 59, 62, 63, 85, 87, 89–91, 119–122

$T_{\mathbf{ISP}}$ ISP temperature [°C]. 19, 49, 51, 52, 54, 56, 87–89, 119, 121

$T_{\mathbf{pyro}}$ Pyrometer temperature [°C]. 17–19, 51, 52, 87–89, 119–122

T_g Growth temperature [°C]. 30, 60, 61, 73, 86, 87, 117

T_a Annealing temperature [°C]. 60, 61, 73, 86, 87

τ_c Carrier lifetime [ps]. 40

t Time [s]. 13, 14, 17, 87

Δt Time-delay between pump and probe pulse [ps]. 36, 37, 79, 109

$\mathcal{T}$ Transmittance. 30

$\mathcal{T}_0$ Transmittance without the pump pulse. 36

$\Delta\mathcal{T}$ Change in transmittance. 36

θ Angle between detector arm and wafer [°]. 25

ϑ Angle [°]. 13, 96, 104

u Target Ga composition. 112–114, 127, 130, 131

u' Fitted Ga composition. 127, 130, 131

V Voltage [V]. 5, 7, 29, 45, 47, 129, 132–134, 136, 137, 140

$V_{\mathbf{fb}}$ Flat-band potential [V]. 29

$V_{\mathbf{OC}}$ Open circuit voltage [V]. 133, 136

v Target Al composition. 112–114, 127, 130, 131

v' Fitted Al composition. 127, 130, 131

$\mathfrak{v}$ No. of valency electrons per unit molecule. 29

$\mathbf{V}$ Volume [m^3]. 14

$\mathcal{V}$ Total volume in the three dimensional velocity space [m^3s^{-3}]. 13

$v_{\mathbf{th}}$ Mean thermal carrier velocity [ms^{-1}]. 40

v Speed of atom [ms^{-1}]. 13

w Target In composition. 112–114, 127, 130, 131

$w_{\mathbf{InAlAs}}$ Target In composition in InAlAs. 86, 87

$w_{\mathbf{InGaAs}}$ Target In composition in InGaAs. 86, 87

w' Fitted In composition. 127, 130, 131

$\mathbf{x_{depletion}}$ Depletion width [μm]. 29

$\mathbf{x_{etch}}$ Etch depth [μm]. 29

x Composition. 22

X Perpendicular displacement from wafer centre [mm]. 102

Y Perpendicular displacement from wafer centre [mm]. 102

Chapter 1

Introduction

1.1 MBE Growth Conditions and Group III-V Material Properties

In the past few decades, molecular beam epitaxy (MBE) has been playing a key role in the evolution of high-speed internet, telecommunication and semiconductor technology. Through precise control of Angstrom scale epilayer thickness and composition of different elements under an ultra-high vacuum (UHV) growth environment that minimizes impurity [1], an increasing variety of group III-V compound based, high-speed optoelectronic devices have been fabricated by MBE. The III-V material attributes are intrinsic to the MBE growth conditions, e.g. growth temperature, V/III flux ratio and growth rate, which influences all aspects of the epitaxial crystal quality: lattice defects, interface roughness, surface morphology, dopant energy levels, impurity incorporation and redistribution [2]. These eventually alter the optical and electrical properties of semiconductor devices. For instance, dopant diffusion is strongly sensitive to various growth conditions. Just to name a few related studies, a combination of high V/III flux ratio and low temperature growth helps alleviate Be diffusion during epitaxy or post-growth process annealing, which were reported for GaAs [3], InGaAs [4], AlGaAs-GaAs:Be and [5] InGaAs-InAlAs heterojunction bipolar transistors (HBTs) [6]. Inter-diffusion in III-V heterostructures is dependent on quantum well thickness [7], while growth temperature and growth rate can also affect surface diffusion length [8], III-V composition dependence [9] and segregation [10]. Even though MBE was invented back almost half a century ago, the understandings and techniques for optimizing the performance of some modern optoelectronic devices are still far from being established. Low temperature (LT) growth is perhaps one of the best represen-

tative examples of why more research in epitaxial technology needs to be done. Apart from the aforementioned effect on dopant diffusion and segregation, LT growth is also capable of creating non-stoichiometric III-V material. By growing III-V materials in ∼200–300°C, much lower than the conventional temperature at ∼500–600°C, up to 2% excess As can be embedded into the epilayer [11, 12]. Since the growth conditions, especially grow temperature strongly alters the amount of As incorporation, accurate growth temperature monitoring becomes uttermost important for producing the desired material properties. However, with the current technology available, it is unfortunately not very easy to conduct reliable temperature measurement in LT regime, especially for growth that involves substrate or epilayer materials with smaller bandgaps.

1.2 Temperature Monitoring of Small Bandgap Semiconductors

Narrow bandgap materials, especially antimonides are gaining a lot of interest because of their applications in ultra-low power high-speed electronics, wide-range infrared emitters and sensors as well as applications in spintronics and quantum information processing. As an example, in recent years there were studies about using InSb nanowire to create majorana fermions, which are potential candidates for topological quantum computers [13, 14, 15]. The key parameters that determine their optical, electrical and heterostructure interfacial properties include growth rates, V/III flux ratios and last but not least, growth temperature. Therefore precise monitoring and control of the substrate temperature are requisites for high-quality semiconductor growths. The accurate measurement of the substrate temperature of small band gap semiconductors such as InAs and GaSb has been a challenging issue for researchers for years. Typical MBE growths involve two substrate temperature measurement techniques: optical pyrometry [16, 17, 18] and band edge thermometry (BET) [19, 20, 21]. Pyrometry allows monitoring of substrate temperature down to ∼400°C, but its reliability is often limited by the following factors: emissivity of the substrate, coating on the viewport, rotation manipulator induced substrate wobbling, stray lights from effusion cells and viewport heaters inside the growth chamber [22]. On the other hand, BET is insensitive to substrate wobbling, viewports coating and extra scattered radiations from other hot sources. However, BET has limited accuracy for measuring the temperature of doped substrates because its band edge shape is strongly related to the doping concentration. In addition, BET cannot measure the temperature of materials with smaller bandgaps such as InAs, InSb and GaSb, since their band edges locate outside the spectral range of near-infrared band edge thermometers (NIR BET). Therefore a novel

method for temperature monitoring of narrow bandgap materials is required.

1.3 THz Generation and Detection with LT GaAs and InGaAs

Terahertz (THz) is a term referring to electromagnetic (EM) waves with frequencies lying between microwave and infra-red spectrum, which approximately ranges between 0.1–10 THz, equivalent to wavelengths between 3000–30 μm and photon energies between 0.4–40 meV. This frequency range has been catching researchers' attention thanks to its non-invasive penetration nature for many organic materials, which brings tremendous potential in numerous applications such as material spectroscopy, bio-tissue sensing, imaging, quality control in medical industry, security measures and high-speed telecommunications [23, 24, 25, 26]. THz radiation is abundant in our daily life, from blackbody radiation to cosmic background radiation. However, it remains the least explored region in the EM spectrum. Historically, such frequency range was also known as the "THz gap" [24, 25, 26], due to the fact that there was a lack of a workable physical mechanism for THz generation. In classical electric circuits, the charge carriers are not fast enough to generate oscillations above 1 THz; on the other hand, the distinction between any two quantum states with energy difference in the order of meV can be easily obscured by thermal excitation and relaxation, which makes THz radiation hard to be utilized. Simply speaking, any generation and detection technologies used for other radiation cannot be directly applied in the THz regime. Thanks to the advancement of semiconductor technology in the last few decades, numerous new principles and new methods have been invented to generate THz radiation. Those include but not limited to: manipulating free electron movement in vacuum, relativistic electron accelerator techniques such as synchrotron [27, 28] and large-orbit gyrotron [29, 30, 31], as well as emission by undulated periodic electron beam such as backward-wave oscillator [32, 33] and free-electron laser (FEL) [34, 35]; frequency up-conversion by Schottky diode frequency multipliers [36, 37, 38, 39]; frequency down conversion via nonlinear-optical means such as optical rectification [40, 41, 42] and difference-frequency generation [43, 44]. In parallel, a variety of THz detection devices have also been developed, with some of them being just the reciprocal process of the aforementioned THz techniques, such as electro-optical modulation as a reverse of optical rectification [40]. The Schottky diode can also be used as a heterodyne receiver to down-convert THz radiation to lower frequency output by frequency mixing [36, 45]. Nonetheless, many of the aforementioned techniques are outdated with various drawbacks. For instance, due to the massive size of electron accelerators and FELs, it becomes very difficult to implement such

THz equipment for industrial or medical applications. In addition, most of them are also impractically expensive.

Therefore in recent years, more emphasis has been put on developing semiconductor-based THz emitters and detectors for cost reduction and portability, such as transient photoconductive switching and photomixing by photoconductive antennas (PCAs) [46, 47], electrically or optically pumped p-type germanium laser [48] and quantum cascade laser (QCL) [49, 50]. In particular, PCA is one of the most well-established and frequently-used optoelectronic device for THz technology. The advantage of PCA is it can serve for both THz generation and detection by either transient photoconductive switching or photomixing. A PCA is an electrical switch where it undergoes an ultrafast change of conductivity upon optical excitation. Incident photons with an energy matching the material bandgap generate electron-hole pairs. The generation of THz wave is well described by Maxwell's equations, in which the antenna pair can be essentially considered as a radiating electric dipole. In order to emit or detect THz radiation, such switching of photoconductivity must occur in the sub-picosecond scale. The ultrashort transient current occurring in the antennas results in an ultrashort pulse of EM radiation in the form of a bundle of frequency range. The shorter the pulse, the broader the THz spectrum. Therefore, a high-quality PCA material should have effective absorption, ultrashort photocarrier lifetime, high carrier mobility and high dark resistivity [51, 52]. The availability of precise and reliable semiconductor growth techniques is the key to create such special PCA materials to meet THz application requirements. Arguably, the most promising technique to meet such requirements is MBE. Two kinds of group III-V based compounds are widely used to fabricate THz PCAs nowadays: GaAs and InGaAs. Since the 1990s, low temperature (LT) grown GaAs has been the most popular ultrafast material that demonstrates excellent optoelectronic properties. With proper MBE growth and annealing conditions applied, LT GaAs exhibits sub-picosecond photo-carrier lifetime, high mobility and high dark resistivity. Beryllium (Be) doped, LT grown InGaAs-InAlAs superlattice (SL) structure was first proposed by Takahashi et al. in 1994 as a possible material for ultrafast optical devices [53]. Early studies on this material focused on its optical nonlinearity and non-radiative excitonic features [53, 54, 55]. In 2008, a research group from Fraunhofer Institute for Telecommunication developed the first LT InGaAs-InAlAs SL based, 1550 nm operated THz time-domain spectrometer [51]. In this PCA material, InGaAs serves as the photoconductive region while InAlAs increases the resistivity of the structure by trapping the excited photocarriers. The same group later performed more studies on the optoelectronic properties of LT InGaAs-InAlAs SL and optimizations of THz PCAs [56, 57, 58, 59, 60, 61]. Up to date, the best performance of 1550 nm excited, InGaAs-InAlAs SL based THz time-domain spectroscopy (TDS) system has a dynamic range of 90 dB and bandwidth of more

than 6 THz. The MBE optimizations for PCA materials to achieve THz TDS performance comparable to Fraunhofer's benchmark remains a very challenging task.

1.4 Ternary and Quaternary Compound Based Photonic Power Converter

Since its advent in the late 20$^{\text{th}}$ century, high-efficiency, low attenuation, low noise photovoltaic power-over-fiber system have been becoming crucial for modern telecommunications. Unlike copper cables that are sensitive to EM or thermal interference and vulnerable to electric break down, by converting electricity into light with lasers or light-emitting diodes (LEDs), photonic power transmission via optical fiber is immune to EM noise and more suitable for operation under extreme environments [62]. A photonic power converter (PPC) is a photovoltaic device that converts the transmitted light back to electricity, similar to a solar cell. Monocrystalline III-V compounds are favorable PPC materials due to their tunable band gaps in the range of 1.3–1.4 eV which is needed for maximum efficiency in a single-junction (SJ). They have significantly longer diffusion length compared to absorption length and because they can be grown lattice-matched with various group III compositions, it allows energy barriers within a device to contain generated carriers [63]. Conventional high-efficiency PPCs are GaAs based and operate under 830 nm excitation with efficiency up to ∼58–65% [64, 65, 66, 67]. Nevertheless, 830 nm light through a silica fiber suffers from attenuation of 37% over 1 km. On the other hand, light with wavelength within the telecommunication regime is more suitable for long-distance transmission. For instance, the light at 1310 nm has a smaller attenuation of only a 6.7% loss over 1 km [62]. Therefore the ternary and quaternary III-V compounds such as InGaAs and InAlGaAs become more favorable material choices for high-efficiency PPC operating in the telecommunication regime. Over the past few decades, InGaAs and InAlGaAs based, single or multi-junction (MJ) PPCs have been studied with pumping wavelengths of 1070 nm [68] and 1300–1500 nm [69]. Since the current vs voltage (J-V) characteristics and quantum efficiency (QE) of PPCs are strongly dependent on the bandgap of InAlGaAs that is intrinsic to its group III compositions, the MBE technique to grow InAlGaAs p-n junctions with desired PPC properties has become increasingly demanding.

1.5 Thesis Outline

The objective of this thesis is to optimize the MBE technique for the fabrication of LT GaAs on GaAs(001) substrate, as well as InGaAs-InAlAs SL and InAlGaAs of varying bandgaps on InP(001) substrate. These are for applications including 780 and 1550 nm pumped THz TDS, as well as 1310 nm pumped PPC.

Chapter 2 provides an introduction of the MBE equipment used for this work and growth techniques, with a focus on the beam flux monitor (BFM) ion gauge, growth rate, flux and overpressure (Op) calibration of group III, dopant and group V cells. In addition, *in situ* growth monitoring techniques such as reflection high energy electron diffraction (RHEED), pyrometry, BET and growth rate determination via optical reflectance from the substrate are described, as well as *ex situ* characterization tools such as high-resolution x-ray diffraction (HRXRD) and electrochemical capacitance-voltage (ECV) profiling are also introduced. In addition, the general backgrounds of optoelectronic materials and devices fabricated from the epitaxial growths involved in this work, such as LT III-V materials, THz TDS and PPC are also covered.

Chapter 3 proposes a novel technique, integrated spectral pyrometry (ISP), that improves the accuracy of temperature measurement of InAs and GaSb substrates by performing a prior growth calibration with the use of a special GaAs-InAs combined substrate and an InGaAs spectrometer in the 900–1700 nm range. To demonstrate the usage of ISP, an InAs:Si growth on InAs(001) substrate, as well as a metamorphic multi-layer growth, where several binary and ternary antimonide compounds were grown on a GaAs substrate, were also performed. The experimental results have been published in [70].

Chapters 4 and 5 are about the comprehensive studies of LT GaAs and InGaAs-InAlAs SL for THz PCA fabrications with varying growth and annealing conditions. The *in situ* MBE growth conditions such as substrate temperature, As Op and substrate reflectance, are presented in detail. In addition, Nomarski microscopy, black box imaging and HRXRD as well as the photocurrent scan in the temporal and spectral domain of 780 and 1550 nm pumped THz TDS tests, are presented. In particular, the effect of processed antenna type, growth and annealing temperature on THz TDS performance are discussed, especially the comparison between InGaAs and LT GaAs as 1550 nm pumped THz receivers with the later one operated via mid-gap state mediated two-step excitation [71, 72, 73, 74, 75]. In addition, a section of four-point-probe (4pp) measurements is included to discuss the importance of understanding the effect of dopant type and concentration on the sheet resistance of InGaAs-InAlAs SL. Two dopants were used in this study: Beryllium and carbon. Beryllium is a widely used, well-working p-dopant for III-V materials, but the

drawback is it can easily diffuse into other epilayers [3, 4, 5, 6]. On the other hand, carbon does not have such a diffusion problem and it is proved to work very well as a p-dopant for GaAs [76, 77, 78]. However, it is unknown whether carbon behaves as a p-dopant when being embedded into InGaAs and this study attempted to examine it. This is a collaborative project with the Nanofabrication Group in University of Waterloo and TeTechS Inc.

Chapter 6 involves the growth and characterization, with particular emphasis on HRXRD fitting, of InAlGaAs based ellipsometry calibrations and PPC structures. The challenges of growing lattice-matched InAlGaAs of various group III compositions, flux stability as well as the lattice relaxation induced by strongly strained $In_{0.3}Al_{0.7}As$ layer are discussed. Applications in ellipsometry, illuminated J-V characteristics, QE vs wavelength on SJ and two-junction (TJ) devices are described and discussed. This is a collaborative project with SUNLAB of the University of Ottawa. The ellipsometry and PPC characterization results have been published in [62, 79, 80].

For the works presented in this thesis, I was mainly in charge of the MBE growths, annealing of grown wafers and several types of *ex situ* characterizations, including Nomarski microscopy, black box imaging, HRXRD, ECV profiling and 4pp measurements. The samples presented in Chapters 4–6 were labeled in chronological order, with a sample grown at a later date having a larger growth number. The processing of all PCA devices was done by the Nanofabrication Group at the University of Waterloo. The THz TDS tests were done by the collaborative company, TeTechS Inc., while I partially assisted in the 780 nm pumped THz TDS measurements. The ellipsometry of InAlGaAs calibration growths, processing of PPC devices with characterizations, including illuminated current density vs voltage (J-V) characteristics and QE measurements were done by the SUNLAB of the University of Ottawa.

Chapter 2

Background and Methods

2.1 Molecular Beam Epitaxy of Group III-V Compounds

2.1.1 Growth Module, Group III-V and Dopant Sources

MBE is a film growth technique where atoms or molecules are thermally evaporated and deposited on a heated crystalline substrate which is placed under a UHV environment [1, 11]. MBE is well known to be maturely developed for group III and V compound semiconductor growths which are closely related to semiconductor science and industrial applications. Typical group III elements include gallium (Ga), aluminum (Al) and indium (In), while for group V, arsenic (As) and antimony (Sb) are commonly used. In principle, any element from the periodic table can be used as a source for the epitaxial material in an MBE system; however, depending on the element, different mechanisms are needed for producing the molecular beam. For example, thermal evaporation cells are common sources for group III and dopant elements; valved cracker cells are mostly used for group V molecules; while for deposition of refractory metals such as Molybdenum (Mo) or Niobium (Nb), e-beam evaporators are used [1, 2]. In a typical III-V MBE growth, As atoms emerge from effusion furnace around 300–400°C mostly exist as tetramers (As_4), while with the use of a cracking zone around 900°C, As_4 can be decomposed as dimers (As_2). However, in practical situations, As_4 is usually produced at a higher temperature (650°C) to prevent clogging the cracking zone and to minimize the cracking of As_4 at the same time. In order to alter electrical conductivity or other material properties, dopant elements are

often embedded inside the MBE structure, where silicon (Si) is used as an n-type dopant; beryllium (Be) and carbon (C) are used as p-type dopants for III-V compounds.

Fig. 2.1 shows the conceptual sketch of the growth module (GM) of the Veeco GEN10 MBE system used for all the wafer growths in this project. The GM consists of a cryogenic pump and an ion pump to create a UHV environment with pressure down to $\sim 10^{-11}$ Torr at idling condition, which is a requisite for high purity MBE growths. A mini ion pump is also installed at the bottom of the GM to further improve the UHV cleanliness via differential pumping. The substrate is mounted on a ring-shape Mo holder, with additional Mo inserts to fix its position in case if the substrate is cleaved, and rotated by a manipulator during the growth. The radiative substrate heater generally consists of a Mo block and a thermocouple positioned behind it which is close to but not touching the wafer. Generally, the substrate heater temperature measured by the thermocouple is higher than the actual substrate temperature, with the difference varies with the substrate material, e.g. ∼100°C for GaAs, ∼40–50°C for InAs and InP. The exact temperature difference also varies with the substrate size, geometry, mounting and the substrate temperature itself. The ten ports are loaded with various sources, including two Ga, one Al and two In cells as group III, labeled as "Ga1", "Ga2", "Al1", "In1" and "In2"; As and Sb with one for each as group V, labeled as "As1" and "Sb1"; Si, Be, GaTe and C with one for each as dopants, labeled as "Si1" and "Be1", "GaTe1" and "C1" respectively. The liquid nitrogen (LN_2) cryopanel serves as a thermal insulator among different cells [1], which have largely different temperatures between 200 and 1500°C and are located very close to each other. Each group III cell is a dual-filament source, which consists of a pyrolytic boron nitride (PBN) SUMO crucible and two independent heater filaments: a base heater for the crucible body and a tip heater for the crucible orifice. The atomic flux is dominated by the base temperature, which would also be referred to as the "cell temperature" in the rest of this dissertation. The tip heater is generally set hotter than the base in order to alleviate the radiative heat loss in the orifice, with the tip-base gradient adjusted at ∼100–200°C depending on the element type and base temperature. On the other hand, each group V source consists of three parts: body, valve and cracking head. For As, molecules are sublimated in the crucible of the out-of-vacuum body part, also referred to as the "bulk zone", at 350–400°C, then they are regulated by the valve located near the crucible orifice with its opening controlled by an automated valve positioner, and pass through the in-vacuum cracking head, surrounded with a resistively heated filament, where either remain as tetramers or decomposed into dimers depending on the cracker zone temperature. For the Sb cell, besides the parts aforementioned, it also includes a conductance tube, also surrounded with a resistively heated filament, between the crucible and the valve, with the conductance zone temperature usually set to the same temperature as the cracker zone at

idling. The Si, Be and GaTe dopant cells operate in a way similar to that of group III cells except Si and Be are single-filament sources with the base heater only. Unlike other effusion cells, the SUKO-D carbon source operates by sublimating carbon from a high purity pyrolytic graphite filament with its flux controlled by the filament current. Except for GaTe, all the other ten cells had been used for this work and the aforementioned cell labels will be used for later chapters. Each flux is collimated by a beam collimation shield sitting on the cryopanel for the wafer growth, as illustrated by the As cell in Fig. 2.2. In the case of material depletion in those sources, long-period system maintenance needs to be performed, which includes removal of source material coatings and flakes over the chamber, refilling the sources and baking the system to restore UHV conditions [1].

2.1.2 Pre-Growth Outgassings

Before conducting any MBE growth, there are three outgassing procedures that need to be done. Apart from GM, the Veeco GEN 10 system also consists of other chambers: a load-lock module (LL) where the wafer is loaded from the outer atmospheric environment into the UHV system; a preparation module (PM), maintained at $\sim 10^{-9}$ Torr by a turbopump, where the wafer is outgassed, and a cluster tool module (CT), kept at $\sim 10^{-10}$ Torr by an ion pump, for wafer storage and transfer among the other three modules with the use of an automated robot arm. Once the wafer is loaded into the LL, the module is ramped up to 200°C for outgassing for 4 hours with the pressure pumped down to $\sim 10^{-8}$ Torr by a turbopump. This is done to ensure the cleanliness of LL before contact with other UHV parts. Afterwards, the wafer is transferred into PM for another outgassing with a temperature of 300–400°C depending on the material type of wafer and duration of typically ∼2 hours. This minimizes the contaminants on the wafer before any deposition. The substrate manipulator and cells also require outgassing, typically for ∼3 hours, with the manipulator ramped to 800°C and the cells ramped to temperatures corresponding to target fluxes, in order to evaporate any coatings or impurities on these components before the wafer is moved into GM for MBE growth.

2.1.3 Growth Monitor, Characterization and Processing Tools

The cell and substrate heater temperatures can be ramped either under proportional-integral–derivative (PID) or constant power mode. Molly 2000 software is used to execute MBE deposition procedures by controlling the values and duration of cell temperatures, substrate heater temperature, shutter status and substrate rotation azimuth with a programmed growth recipe. It is also used to monitor the aforementioned parameters, as

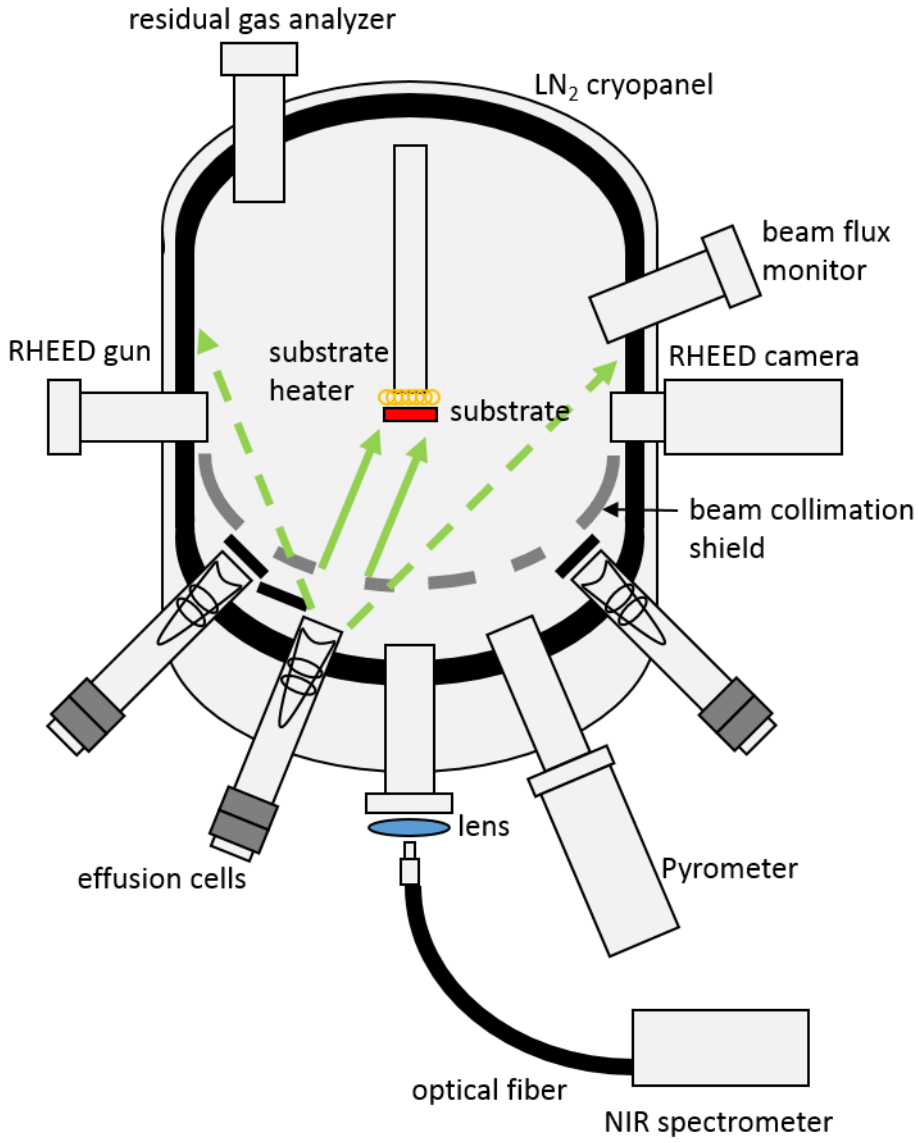

Figure 2.1: Conceptual sketch of the Veeco GEN10 MBE GM, which shows the substrate heater with the substrate, effusion cells, LN_2 cryopanel, beam collimation shield, BFM, RGA, RHEED gun and camera, pyrometer, NIR spectrometer with the fiber optic parts. Another RGA, ion and cyrogenic pumps are not shown.

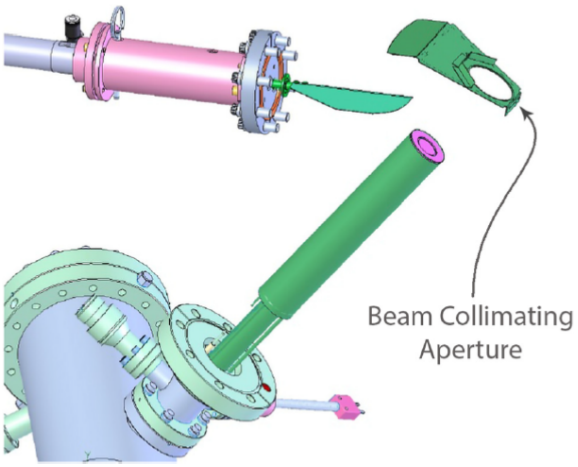

Figure 2.2: Schematic of a Veeco GEN10 MBE system with beam collimation shield, which sits on the As cryopanel bay and blocks most of the As flux, resulted in a collimated beam needed for the wafer growth. Figure adopted and reprinted from Ref. [81].

well as pressures measured by ion gauges. In the work presented in this thesis, two ion gauges were used to monitor the pressure of the growth module, with one of them logged by Molly 2000 and another one logged by a Stanford Research System SRS IGC100 ion gauge controller. These ion gauges have their positions interchangeable to each another to fit the needs for different growth configurations, and the values recorded are labeled as "GM" and "SRS" pressure respectively which will be used in later chapters and sections. The BFM is an extendable ion gauge in the GM, which can be inserted under the substrate to measure the beam equivalent pressure (BEP) of the beam(s) from one or more cells with open shutter(s). Alternatively, such ion gauge can also be retracted to the sidewall position of the GM to monitor group V overpressure which will be explained in a later section. Besides BFM, the "GM" and "SRS" can also be used to monitor group V overpressure. Two residual gas analyzers (RGAs), one from Stanford Research System (SRS200) and another from Inficon (FabGuard), are installed on the top and at the bottom of the GM respectively to monitor the UHV environment by sensing each element as the atoms or molecules pass through the quadrupole and are analyzed by mass spectrometry.

In addition to the aforementioned components, the Veeco GEN 10 GM is also installed with other apparatuses for *in situ* growth monitoring. Those include: an SVT AccuTempTM pyrometer for pyrometric temperature measurement and growth rate monitoring; a Control Development InGaAs NIR spectrometer, operated at spectral range of 900–1700 nm, for BET temperature measurement; a kSA 400 Staib Instruments RHEED

electron gun and camera for monitoring surface reconstruction, smoothness and growth kinetics. For *ex situ* characterization and processing, a Nikon Optiphot-66 Nomarski microscope is used to examine surface topography of grown or processed wafers; a Nikon D90 digital camera is used for black-box imaging; a Jordan Valley QC3 HRXRD diffractometer is used to analyze epitaxial layer thickness and composition; a WEP CVP 21 ECV profiler is used to measure doping profiles in grown wafers; an AccuThermo AW610 rapid thermal processing system is used for *ex situ* wafer annealing and a Creative Design Engineering ResMap 4pp system is used for sheet resistance measurement.

2.2 MBE Growths and Characterizations

2.2.1 Molecular Beam Flux

Assume in the GM, $\mathfrak{n}$ is the number of atoms ejected from a group III cell per unit volume. The atom movement in the GM follows the Maxwell-Boltzmann distribution:

$$f(\upsilon) = 4\pi \left(\frac{m}{2\pi k_B T} \right)^{3/2} \upsilon^2 e^{-\frac{m\upsilon^2}{2k_B T}} \tag{2.1}$$

Here $f(\upsilon)$ is the probability distribution function of the atoms with velocity magnitude υ in the three-dimensional (3D) velocity space $\mathcal{V}$; T is the temperature of the effusion cell which the atoms eject from, m is the mass of molecules in the vapor phase and k_B is the Boltzmann's constant. $f(\upsilon)$ is normalized in a way such that by integrating it over all possible velocities, $\int_0^\infty f(\upsilon)d\upsilon = 1$. To determine the molecular beam flux, we may consider the number of atoms dN passing through an area $\mathcal{A}$ with speed υ at angle ϑ from the normal within time interval t, which can be expressed as

$$dN = \mathfrak{n} f(\upsilon) d\upsilon \times \upsilon \cos\vartheta \mathcal{A} t \tag{2.2}$$

By integrating dN over all possible velocities,

$$\int_{\mathcal{V}} dN = \mathfrak{n}\mathcal{A}t\sqrt{\frac{k_B T}{2\pi m}} \tag{2.3}$$

Therefore the molecular beam flux, ϕ, which is the number of atoms per unit area per unit time, usually written in the unit of $\mathrm{cm}^{-2}\mathrm{s}^{-1}$, can be expressed as

$$\phi = \mathfrak{n}\sqrt{\frac{k_B T}{2\pi m}} \tag{2.4}$$

From ideal gas law, for a system with equilibrium pressure P, volume $\mathbf{V}$ and number of particles N, $P\mathbf{V} = Nk_BT \Rightarrow P = Nk_BT/\mathbf{V} = \mathfrak{n}k_BT$, the flux can be expressed in terms of P and T:

$$\phi = \frac{P}{\sqrt{2\pi m k_B T}} \tag{2.5}$$

2.2.2 Beam Flux Monitor

The atomic or molecular flux can be calculated if we know its correlation with the BEP, $\mathcal{I}$, measured by the BFM. Suppose the ion gauge has an area $\mathcal{A}$ and length L where atoms enter and pass through. The flux is

$$\phi = \mathcal{N}/\mathcal{A} \tag{2.6}$$

where $\mathcal{N}$ is the number of atoms enter per second, which is indicated by the ion gauge current. However, not all atoms entering the gauge can be detected and here we need to take a certain probability into account. Suppose $\mathcal{P}$ is the probability of an atom to be ionized and detected. Assume that $\mathcal{P}$ is proportional to the duration of an atom staying inside the ion gauge, i.e. $\mathcal{P} \propto t$. Therefore BEP is directly proportional to be the product of $\mathcal{N}$ and t, i.e.

$$\mathcal{I} = \zeta \mathcal{N} t \tag{2.7}$$

for some constant ζ. Since $t = L/v$, therefore the flux can be expressed as a function of BEP and velocity of atoms:

$$\phi = \frac{\mathcal{I}v}{\zeta \mathcal{A} L} \tag{2.8}$$

From fundamental thermodynamics, we know that the velocity of gas molecules is proportional to the square root of temperature, i.e. $v \propto \sqrt{T}$. Hence the flux can be further expressed as a function of $\mathcal{I}$ and T:

$$\phi = C\mathcal{I}\sqrt{T} \tag{2.9}$$

where C is a coefficient correlated with the ion gauge geometry and ionization probability. Now if we combine Eq. 2.5 with Eq. 2.9,

$$\mathcal{I} = \frac{P}{CT\sqrt{2\pi m k_B}} \tag{2.10}$$

Suppose this P follows an Arrhenius exponential vs T, i.e. $P \propto e^{-B/T}$. The BEP can now be expressed as a function of cell temperature:

$$\mathcal{I} = \frac{A}{T} e^{-\frac{B}{T}} \tag{2.11}$$

where A is correlated with both C and the equilibrium pressure; B is correlated with the activation energy of the element inside the cell crucible. T can be expressed in terms of $\mathcal{I}$ by using the Lambert W function $y = ze^z \Leftrightarrow z = W(y)$, i.e.

$$T = -\frac{B}{W_{-1}\left(-\frac{BI}{A}\right)} \tag{2.12}$$

where W_{-1} represents the lower branch of the function. Similarly, since

$$\phi = \frac{AC}{\sqrt{T}} e^{-\frac{B}{T}} \tag{2.13}$$

T can also be expressed in terms of ϕ:

$$T = -\frac{2B}{W_{-1}\left(-\frac{2B\phi^2}{A^2C^2}\right)} \tag{2.14}$$

2.2.3 Calibration of Group III Cell Coefficients

In order to grow epilayers that require thickness precision in the order of Å such as QCL, it is of utmost crucial to know the exact values of the cell coefficients A, B, C for every group III cell. Usually A and B are determined by a BFM calibration measurement that occurs at the beginning of a growth campaign where all cells have been reloaded and the MBE system has just been baked and ready for epitaxy. Fig. 2.3 illustrates part of a BFM measurement recipe involving group III cells Ga1, Ga2, Al1 and In1 with six different base temperature setpoints. For the shutter status graph, "high" and "low" represent "closed" and "open" respectively. At each setpoint, every cell has its BEP measured one after another, with its shutter opened for 150 s twice before being ramped to the next setpoint. To improve accuracy, the measurement process of these six setpoints is repeated three to four times. Afterwards, A and B are obtained by fitting the data points in a linear regression plot of $\log(\mathcal{I}T)$ vs T. On the other hand, the determination of C requires a calibration growth where binary compounds are grown on a wafer. Fig. 2.4 illustrates a calibration growth for Ga and Al cells, where GaAs and AlAs, with target thicknesses of 3,000Å and 6,000Å respectively, were grown on a GaAs(001) substrate. In the beginning, the substrate was oxide desorbed for 12,000–12,500 s at 630°C, followed by a GaAs buffer of 2,000Å target thickness grown with an increasing temperature of 580–620°C at 13,100–14,100 s. The 470 and 950 nm reflectance oscillations at 14,700–17,700 s and 21,900–24,900 s represent the GaAs and AlAs deposition at 580–590°C. All the aforementioned substrate

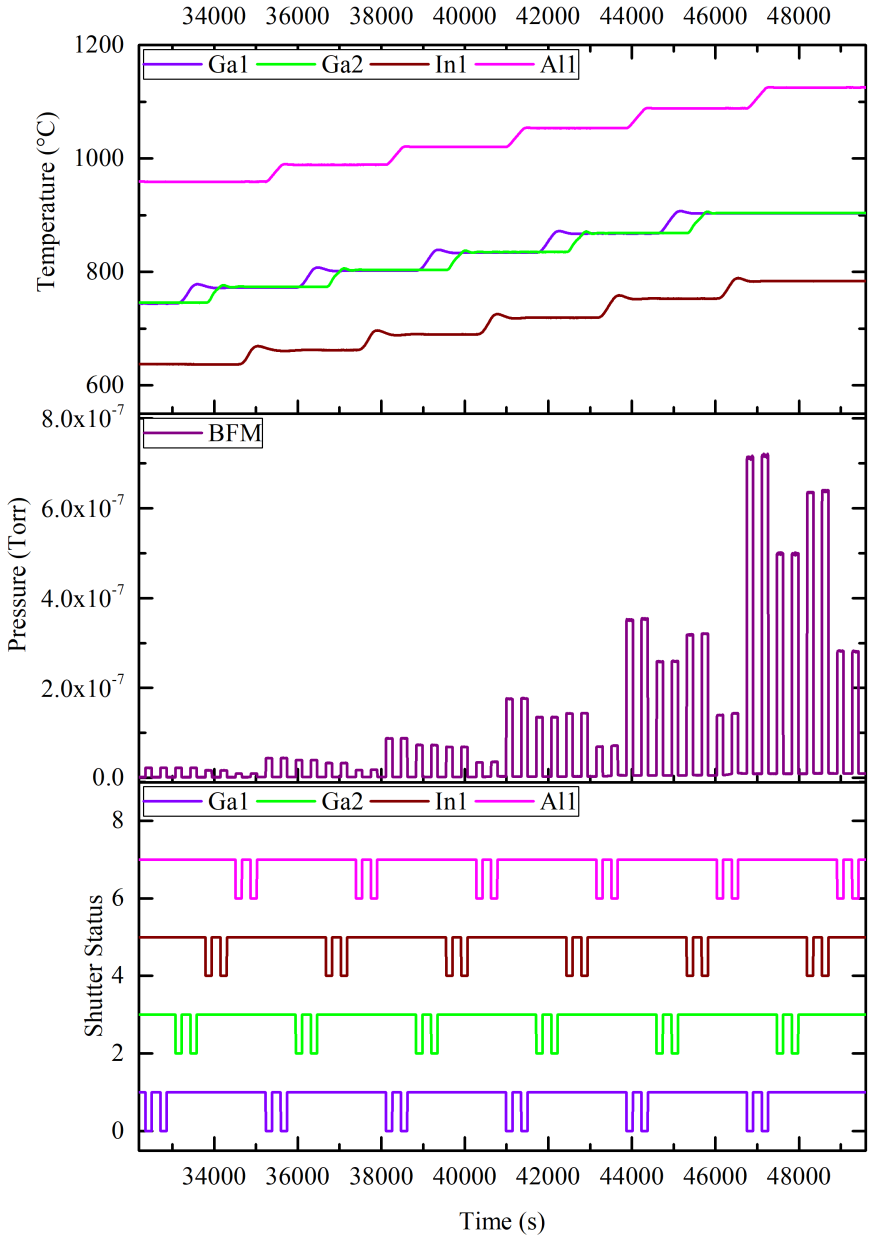

Figure 2.3: *In situ* parameters of a BFM calibration recipe. From top to bottom: base temperature of Ga1 (violet), Ga2 (green), In1 (brown) and Al1 (pink); BFM pressure (purple); shutter status of Ga1 (violet), Ga2 (green), In1 (brown) and Al1 (pink).

temperatures are indicated by the pyrometer (T_{pyro}) and BET (T_{BET}) readings. Typically, for GaAs(001) substrate, the substrate heater, indicated by the thermocouple temperature (T_c), is hotter than the substrate by ∼100°C. Between the two epilayers, at 17,700–19,400 s, an As Op calibration was also done where the BFM was measured with varying As valve openings. The deposition was evaporated afterwards by ramping the substrate to 700°C. Fig. 2.5 illustrates another In cell calibration growth where AlSb and InAs, with target thicknesses of 200Å and 3000Å respectively, were grown on an InAs(001) substrate at ∼500°C. For convenience, the status of each shutter was also shown. The substrate was oxide desorbed at ∼525°C, followed by an InAs buffer of 2000Å target thickness grown at ∼500°C. Since the retracted BFM and SRS ion gauges are less sensitive to Sb compared to As, during AlSb deposition, those two readings also dropped quickly and recovered when the deposition was switched to InAs, which is indicated by the optical reflectance oscillation afterwards. After growth, the wafer was taken out for HRXRD to determine the actual thickness $d = Gt$, where G is the growth rate in Å/s and t is the deposition duration. G is correlated to the flux by

$$G = \frac{a_\perp a_\parallel^2}{4}\phi \tag{2.15}$$

where $a_\perp$ and $a_\parallel$ are the lattice constants along the growth direction and parallel to the wafer surface respectively, with $a_\perp a_\parallel^2$ being the volume of a strained unit cell assuming there is no relaxation. The division by a factor of 4 is taken into account, based on the fact that for group III-V zincblende compounds, there are 4 group III atoms in every unit cell. For lattice-matched or strained growth without lattice relaxation, $a_\parallel$ is equal to the lattice constant of the substrate, a_s, while $a_\perp$ is given by

$$a_\perp = a_f\frac{1+\nu}{1-\nu} - a_s\frac{2\nu}{1-\nu} \tag{2.16}$$

where a_f is the lattice constant of an unstrained layer and ν is the Poisson ratio. The strain along a particular direction is defined by $\epsilon = (l - l_0)/l$, where l and l_0 are the lattice constants of compressed/extended and unstrained layers respectively. ν can be expressed in terms of strains:

$$\frac{\nu}{1-\nu} = -\frac{\epsilon_z}{\epsilon_x + \epsilon_y} \tag{2.17}$$

where ϵ_z is the strain along the growth direction, ϵ_x and ϵ_y are the strains parallel to the wafer surface. With $\mathcal{I}$ and T being known, the coefficient can, therefore, be calculated by

$$C = \frac{4G}{a_\perp a_\parallel^2 \mathcal{I}\sqrt{T}} \tag{2.18}$$

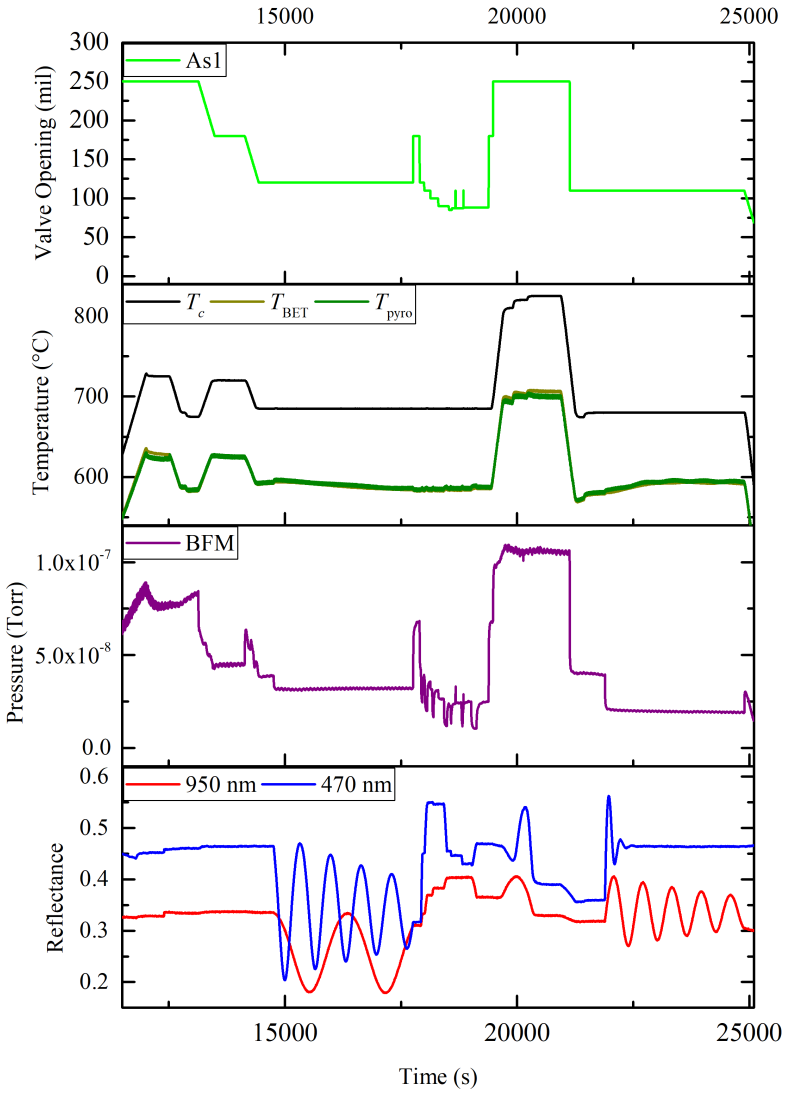

Figure 2.4: *In situ* growth parameters of a calibration growth for Ga and Al cells. From top to bottom: As valve opening (green); T_c (black), T_{BET} (dark yellow) and T_{pyro} (dark green); BFM pressure (purple); 950 nm (red) and 470 nm (blue) reflectance.

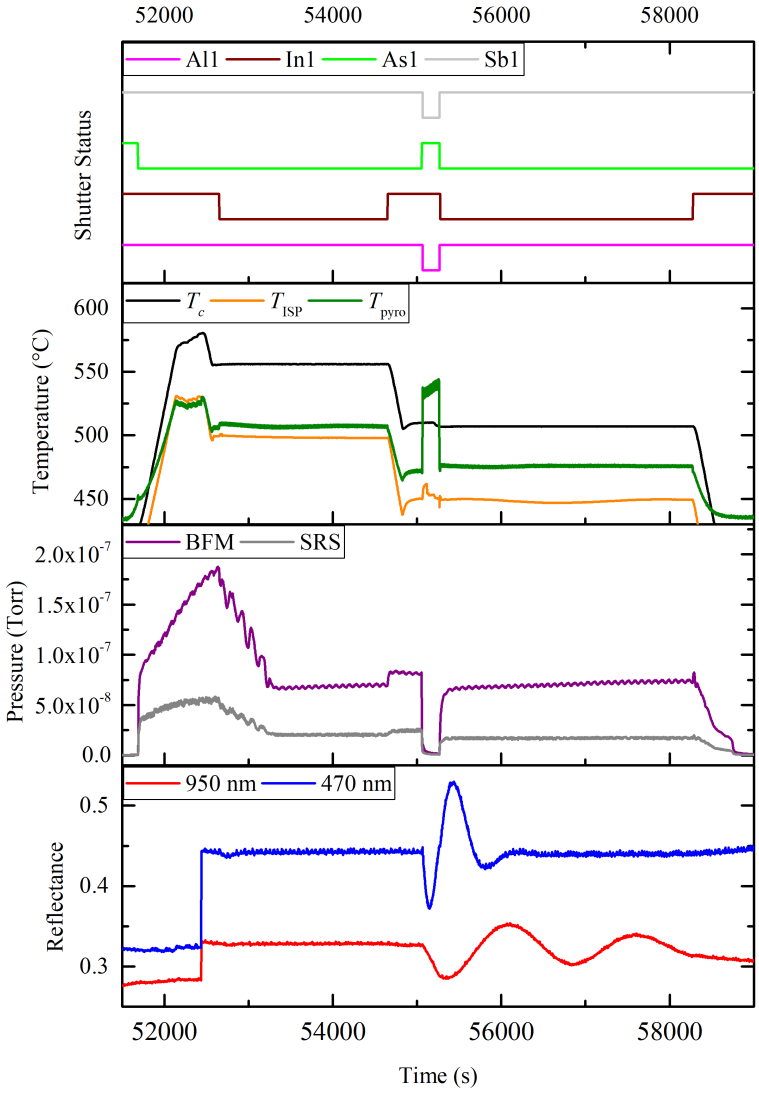

Figure 2.5: *In situ* growth parameters of a calibration growth for In cell. From top to bottom: shutter status of Al1 (pink), In1 (brown), As1 (green) and Sb1 (light gray); T_c (black), T_{ISP} (orange) and T_{pyro} (dark green); BFM (purple) and SRS (gray) pressure; 950 nm (red) and 470 nm (blue) reflectance.

After A, B, C for all group III cells have been determined, the MBE system is ready for growing other structures for various applications. The growth rate can be expressed as a function of T. Conversely, similar to Eqs. 2.12 and 2.14, the cell temperature can be expressed as a function of the target growth rate:

$$G = \frac{a_{\perp} a_{\parallel}^2 AC}{4\sqrt{T}} e^{-\frac{B}{T}} \tag{2.19}$$

$$T = -\frac{2B}{W_{-1}\left(-\frac{32BG^2}{a_{\perp}^2 a_{\parallel}^4 A^2 C^2}\right)} \tag{2.20}$$

Once a group III cell has been calibrated, Eqs. 2.19 and 2.20 can be used for all binary compounds which involve the corresponding group III element. For example, once the coefficients of Ga cell are all known, the growth rate of both GaAs and GaSb can be calculated as functions of cell temperature using Eq. 2.19, with $a_{\perp}$ and $a_{\parallel}$ depending on the type of binary compound and substrate. It is worth noting that those coefficients change over time though when the load inside a crucible becomes lower and the BFM ion gauge sensitivity changes as the coating on it piles up. The re-determinations of B and C require additional BFM calibration measurements and cell calibration growths, but A can be corrected every time by measuring $\mathcal{I}$, T and use Eq. 2.11 inversely, i.e.

$$A = \mathcal{I} T e^{\frac{B}{T}} \tag{2.21}$$

A, B and C change noticeably when the load inside the crucible is close to depletion, which implies a significant flux and growth rate drop indicated by a sudden decrease of BFM reading, RHEED pattern turning spotty or optical reflectance decline during a growth. The mass of the load consumed in each cell can be estimated by an approach as described below. Every time when the cell is heated to a particular epitaxy-ready temperature, the flux and duration are recorded. Such flux can be acquired by measuring the cell temperature and BFM with the use of Eq. 2.9, or just the cell temperature with the use of Eq. 2.13, where A, B and C are logged on a regular basis. The flux is integrated as a function of time and the sum of those time-integrated fluxes since the beginning of a growth campaign, with all cells fully loaded back then, can be obtained. For the Veeco GEN 10 system used in this work, $\sim$4% of the flux provided by each cell would end up depositing on a full 3" wafer. In other words, the total number of atoms consumed in each cell can be calculated by multiplying the aforementioned sum of time-integrated fluxes by an area which is $\sim$25 times of a full 3" wafer. Finally, with the atomic and mass densities of all III-V elements being known, the load consumption in each cell can be calculated by converting the number of atoms into the mass.

2.2.4 RHEED and Calibration of Group V Overpressure

RHEED is a powerful *in situ* growth diagnostic technique. By monitoring the diffraction pattern of high energy electrons ejected from the epilayer surface, details about surface kinetics, roughness, growth rate and reconstruction processes can be acquired [1]. For the growths presented in this work, RHEED images were taken with the electron gun operated at an electron energy of 9.9 keV, filament current of 1.4–1.5 A and angle between the beam and the diffracting surface of $\sim 2^{\circ}$. When the wafer was set up for rotation during growth, RHEED images were captured at several azimuths corresponding to specific crystallographic directions. Besides the aforementioned capabilities, one of the most remarkable usages of RHEED for MBE is the determination of group V overpressure. Eqs. 2.19 and 2.20 are valid based on two assumptions. First, the sticking coefficient of the flux equals unity, which is true for group III atoms under general circumstances; second, the group V flux overwhelms that of group III during epitaxy such that every group III atom hitting the wafer would surely have a group V atom to pair with. The first assumption is invalid for group V atoms, which have poor sticking coefficients regardless of whether the GM is filled with group III atoms or not. Therefore the aforementioned coefficients and equations do not apply for group V cells and they need to be calibrated with an entirely different approach. The working mechanism for a group V cell is fundamentally different from that of any group III cell. For instance, although the As flux can be altered by adjusting its bulk temperature, from a practical perspective, it is much more convenient to control the flux by the re-sizable valve. Similar to group III cell calibration for coefficient C, to calibrate a group V cell, a calibration growth is required where a binary compound is deposited on the substrate with a target growth rate. The main difference, however, is the group III shutter is repetitively opened and closed with the group V valve opening is adjusted back and forth, as illustrated in Fig. 2.4 where the As calibration took place between the 3,000Å AlAs and 6,000Å GaAs depositions. RHEED plays the most crucial role here. The reconstruction pattern, which is indicated by the separation between adjacent peaks and drastically dependent on the substrate temperature and group V flux, is monitored when changing the valve opening. Illustrated by Fig. 2.6, for instance, when calibrating the As cell, GaAs is deposited on GaAs(001) with target growth rate of 2Å/s. According to Ref. [82], for an As rich regime where the As flux overwhelms the Ga flux, the RHEED shows 2×4 reconstruction; when the As flux decreases, the pattern would turn into an As stable regime with 3×1 reconstruction; further decrease of As flux would eventually result in a Ga stable regime that Ga flux is larger than that of As which has 4×2 reconstruction. The purpose of this calibration growth is to adjust the As valve to a critical point that the growth barely remains As stable without switching to Ga stable and this is where the group V to III flux ratio equals 1. This is also known as the minimal

As Op of 1, i.e. $P_{\text{min}} = 1$. The ion gauge reading $\mathcal{I}_{\text{ref}}$, either BEP, SRS or GM pressure, corresponds to such marginal value that would be measured and used as a reference of Op for other epitaxial growths. For the example above, $P_{\text{min}} = 1$ corresponds to a growth rate of 2Å/s. By assuming the actual As flux is proportional to the BEP reading, when growing other structures with different target growth rate or Op, we just need to adjust the As valve so that the ion gauge reads a target BEP such that

$$\mathcal{I}_{\text{target}} \approx \mathcal{I}_{\text{ref}} \times P_{\text{target}} \times \frac{G_{\text{target}}}{G_{\text{ref}}} \tag{2.22}$$

where $\mathcal{I}_{\text{ref}}$ and G_{ref} are the reference BEP and growth rate acquired from the group V cell calibration respectively, G_{target} is the target growth rate and P_{target} is the desired Op. In general situations, group V cells do not need very precise calibrations as group III cells do, since the actual growth rate of any structure is still mainly dependent of group III fluxes provided that GM is pre-filled with group V molecules, which is the case for group V rich or stable growths. For BEP measurement, Sb behaves similarly as group III fluxes with steady reading over time and hence it is easy to adjust the Op for Sb, but As has a tendency of having an increasing BEP reading over time that affects the reliability of the Op determination. More examples are given in later chapters. This originates from the configuration of the Veeco GEN10 GM that the BFM is located roughly above the As cell. Because As molecules have poor sticking coefficients, during growth, many of those which do not deposit on the substrate are reflected and strike directly towards the retracted BFM ion gauge. The BEP reading increases over time and this effect becomes more severe as the substrate gets hotter. To resolve this issue, for later growths, the As Op was calibrated with the SRS and GM ion gauge readings were used as references instead, which have more steady pressure readings over time.

2.2.5 Growth Rate of Ternary and Quaternary Compounds

When growing a ternary or quaternary III-V compound, it is important to know its lattice constant in order to get the correct thickness and composition. Consider a ternary compound, e.g. AlGaSb, which may be treated as a mixture of two binary materials "1" and "2", e.g. GaSb and AlSb, with compositions x and $1-x$ respectively. By Vegard's law, the unstrained lattice constant and the Poisson ratio of the ternary compound can be expressed as a linear sum of those two binary compounds weighted by their compositions:

$$a_c = xa_1 + (1-x)a_2 \tag{2.23}$$

$$\nu_c = x\nu_1 + (1-x)\nu_2 \tag{2.24}$$

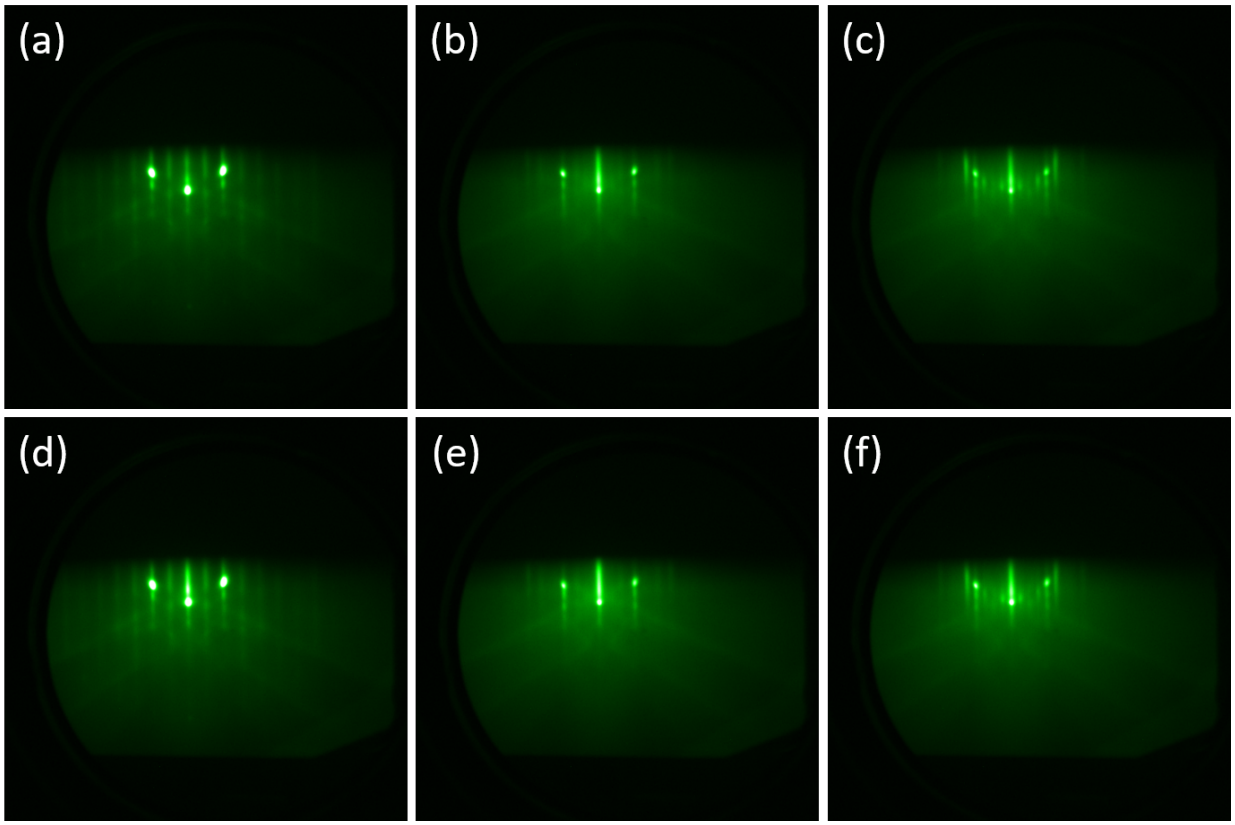

Figure 2.6: RHEED images of GaAs surface reconstruction in [110] direction for As_2 in (a) As rich 2×4, (b) As stable 3×1, (c) Ga stable 4×2 regime, and that for As_4 in (d) As rich 2×4, (e) As stable 3×1, (f) Ga stable 4×2 regime.

However, Vegard's law is invalid for certain ternary materials, e.g. AlGaAs [83]. A quadratic correction term is often added to Eq. 2.23 to compensate such error, i.e.

$$a_c = xa_1 + (1-x)a_2 + bx(1-x) \tag{2.25}$$

where b is known as the bowing factor. The growth rate in monolayer per second (ML/s), M, is related to ϕ and G by

$$M = \frac{a_{\parallel}^2}{2}\phi \tag{2.26}$$

$$M = \frac{2G}{a_{\perp}} \tag{2.27}$$

For group III-V zincblende structures, 1 ML corresponds to half of the lattice constant. The growth of a ternary compound involves the use of two group III cells and the total flux is just simply the sum of them:

$$\phi_{\text{total}} = \phi_1 + \phi_2 \tag{2.28}$$

Similarly, the total growth rate in ML/s can also be written as the sum of the growth rate of the two binary compounds:

$$M_{\text{total}} = M_1 + M_2 \tag{2.29}$$

provided that there is no lattice relaxation, i.e. $a_{\parallel} = a_s$. By expressing Eq. 2.29 in terms of growth rate in Å/s,

$$\frac{G_{\perp,\text{total}}}{a_{\perp,\text{total}}} = \frac{G_1}{a_{\perp,1}} + \frac{G_2}{a_{\perp,2}} \tag{2.30}$$

For each ternary compound, the unstrained lattice constant can be calculated by using Eq. 2.23 or 2.25, while the strained $a_{\perp}$ can be calculated by using Eq. 2.16. The expressions for lattice constant and growth rate of quaternary compound are similar to that of ternary compound, with the corresponding term for a 3$^{\text{rd}}$ material added to Eqs. 2.23–2.25 and 2.28–2.30. For convenience, in this project, a MATLAB standalone application was developed to calculate the BEP, flux, growth rate in both Å/s and ML/s of each binary compound, as well as the composition and total growth rate of ternary or quaternary compounds when the cell temperatures are given. Reversely, such a calculator can also calculate the required cell temperature with a given target flux or growth rate.

2.2.6 High-Resolution X-Ray Diffraction

HRXRD is one of the most precise techniques for determining a variety of lattice parameters, which includes but not limited to thickness, composition, mosaicity, strain and

relaxation. In a HRXRD scan, the Bragg angle ω_B of a particular epilayer peak is given by the Bragg formula:

$$2D \sin \omega_B = \mathcal{L}\lambda \tag{2.31}$$

where $D = a_\perp / \sqrt{\mathtt{h}^2 + \mathtt{k}^2 + \mathtt{l}^2}$ is the spacing between adjacent lattice planes with Miller indices (hkl), λ is the x-ray wavelength and $\mathcal{L}$ is a positive integer which gives the diffraction order. In this project, a Jordan Valley QC3 high-resolution diffractometer was used for HRXRD with Cu K-α_1 wavelength of $\lambda = 1.54056$Å. Triple-axis (TA) coupled ω–2θ scans were applied to all grown wafers at diffraction plane (004), where ω is the angle between the x-ray beam and the wafer plane, θ is the angle between the detector arm and the wafer plane. A Jordan Valley Rocking-Curve Analysis by Dynamical Simulation (RADS) software was used for all HRXRD fittings. For a strained lattice growth without relaxation, the actual group III compositions of individual ternary epilayer can be determined by using Eq. 2.31 with Eqs. 2.16 and 2.23–2.25. For single or multi-layer growths, the actual thickness of individual epilayer can be acquired by fitting the Pendellösung fringes with a RADS model. Fig. 2.7 illustrates how the HRXRD TA scans are used for group III cell calibrations with the Bragg peaks of the substrates set at 0". The growth rates of GaAs and AlAs on GaAs(001) substrate and InAs and AlSb on InAs(001) substrate were fitted by RADS with the results summarized in Table 2.1. The homogeneous buffer epilayers do not show up in the HRXRD scans and cannot be fitted. The fitting of Fig. 2.7(b) is more tricky due to possible alloy mixing at the InAs and AlSb interfaces, hence "unintended" AlAs and InAsSb epilayers have to be included on both sides of AlSb to get a proper fitting. For the calibration growths illustrated above, the fitted GaAs thickness is very close to its target, while it is quite off for the case of InAs. Generally, those calibrations were done at the beginning of a new growth campaign, but the cell temperatures used to give the target growth rates and thicknesses were determined from the cell coefficients in the previous growth campaign. However, during MBE system maintenance between two campaigns, the configuration of a cell can be altered drastically such as re-positioning the crucible within, moving the cell to another port or even replacing the cell with a new one, which would significantly change the cell coefficients. In this example, the most reasonable explanation is the In cell was substantially reconfigured while not much modification was done for the Ga cell, which resulted in the difference in those calibration growths. For SL structures, the thickness can be acquired by measuring the separation between SL satellites peaks which is inversely proportional to the thickness of every period Λ [84]:

$$\frac{2}{\lambda}(\sin \omega_i - \sin \omega_j) = \frac{\mathcal{L}_i - \mathcal{L}_j}{\Lambda} \tag{2.32}$$

where λ is the x-ray wavelength, ω_i and ω_j are the Bragg angles correspond to the ${\mathcal{L}_i}^{\text{th}}$ and ${\mathcal{L}_j}^{\text{th}}$ diffraction order respectively.

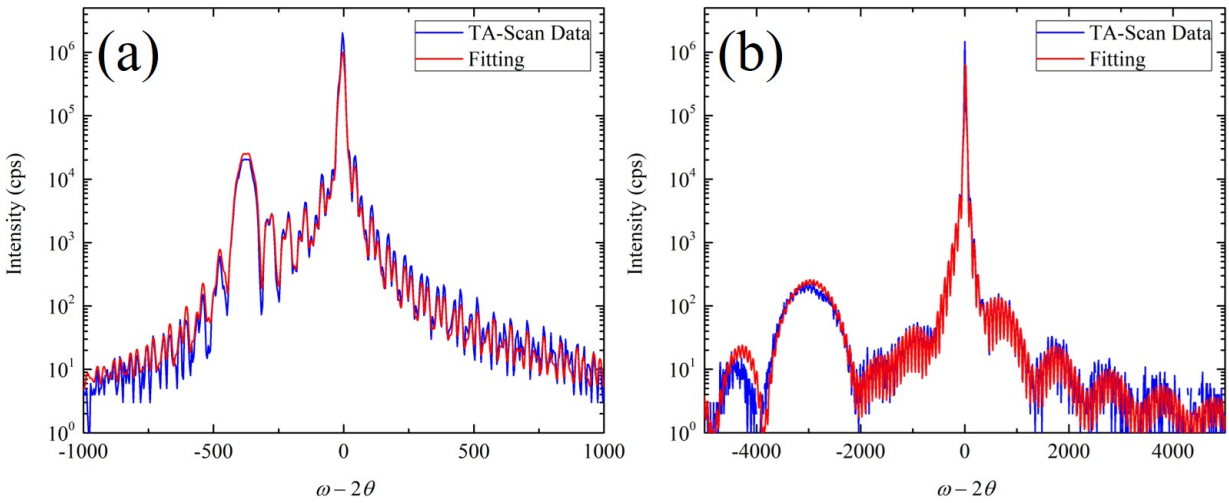

Figure 2.7: HRXRD scan (blue) and fitting (red) for (a) GaAs and AlAs grown on GaAs(001) substrate; (b) InAs and AlSb grown on InAs(001) substrate.

Name	Material	d (Å)	d' (Å)
Substrate	SI GaAs(001)		
Buffer Layer	GaAs	2000	
Al Calibration Layer	AlAs	3000	2882.31
Ga Calibration Layer	GaAs	6000	6016.00

Name	Material	d (Å)	d' (Å)
Substrate	n^+(S) InAs(001)		
Buffer Layer	InAs	2000	
Unintended	$InAs_{0.642}Sb_{0.358}$		12.80
Unintended	AlAs		0.10
Hetero Layer	AlSb	200	170.79
Unintended	AlAs		4.56
In Calibration Layer	InAs	3000	2503.53

Table 2.1: Summary of target epilayer thicknesses (d) and actual thicknesses(d') fitted by HRXRD of a calibration growth for Ga and Al cells (top); In cell (bottom).

2.2.7 Growth Rate Monitoring and Reflectance Fitting

Pre-growth and post-growth BFM measurements provide the flux drift of each group III cell at the end of the growth compared to its initial value, thus giving a rough idea of the epitaxial quality as well as an estimation of epilayer thickness. However, since the BFM ion gauge has to be inserted under the substrate to carry out a measurement, it is difficult to monitor the actual flux drift throughout the entire growth. Flux stability over time might be deduced by examining the traces of tip or base temperature and power output of each group III cell during growth, but this is an indirect approach and there are a lot of uncertainties. More BEP data can be acquired by interrupting the growth and inserting BFM between deposition steps for several times, but such an approach is usually unfavorable as it would lengthen the entire epitaxy duration and sometimes can worsen the epitaxial quality. With those aforementioned reasons, using BFM alone is usually not the best way for determining the actual epilayer thickness. Therefore an additional real-time growth rate monitoring technique needs to be employed. HRXRD is one of the most reliable and accurate techniques in finding the actual epilayer thickness. However, other than a few MBE systems with *in situ* HRXRD installed which are very expensive [85, 86, 87], generally HRXRD can only be done *ex situ*. By measuring the intensity oscillation period of the selected streaks or spots with the lattice constant of the epilayer being known [88], RHEED can be very useful as a precise growth rate acquisition technique as one oscillation period corresponds to one ML being grown. Nonetheless, this growth rate fitting method usually works only when the substrate is stationary. For many growths where the substrate is set to rotation to minimize the thickness gradient across the substrate, the RHEED camera is no longer looking at the same spot and same wafer orientation over time, and the rotation artifact added to the oscillation makes it complicated to analyze and extract growth rate information. Here is where the optical reflectance fitting becomes useful. Breiland *et al*. [89] developed a virtual interface method for extracting growth rate from epitaxial growths using *in situ* normal incidence optical reflectance. In their work, any structure with multiple layers was reinterpreted as the top layer being grown, while the rest were simplified as a virtual substrate with an effective refractive index and extinction coefficient on its own. By derivations using transfer matrix method with boundary conditions based on Maxwell's equations, it can be shown that the reflectance vs time can be expressed as

$$\mathcal{R}(t) = \frac{\mathcal{R}_\infty - 2\sqrt{\mathcal{R}_\infty \mathcal{R}_\mathrm{i}} e^{-\gamma t} \cos(\delta t - \sigma - \varphi) + \mathcal{R}_\mathrm{i} e^{-2\gamma t}}{1 - 2\sqrt{\mathcal{R}_\infty \mathcal{R}_\mathrm{i}} e^{-\gamma t} \cos(\delta t - \sigma + \varphi) + \mathcal{R}_\infty \mathcal{R}_\mathrm{i} e^{-2\gamma t}} \tag{2.33}$$

with $\mathcal{R}_\infty$, φ, $\mathcal{R}_\mathrm{i}$, σ, γ and δ defined as

$$\mathcal{R}_\infty = \frac{(1-n)^2 + k^2}{(1+n)^2 + k^2} \tag{2.34}$$

$$\varphi = \tan^{-1}\left(\frac{2k}{n^2+k^2-1}\right) \tag{2.35}$$

$$\mathcal{R}_{\text{i}} = \left|\sqrt{\mathcal{R}_{\text{i}}}e^{i\sigma}\right|^2 = \frac{(n-n_s)^2+(k-k_s)^2}{(n+n_s)^2+(k+k_s)^2} \tag{2.36}$$

$$\sigma = \tan^{-1}\left[\frac{2(nk_s-n_sk)}{n^2-n_s^2+k^2-k_s^2}\right] \tag{2.37}$$

$$\gamma = \frac{4\pi kG}{\lambda} \tag{2.38}$$

$$\delta = \frac{4\pi nG}{\lambda} \tag{2.39}$$

where n and k are the refractive index and extinction coefficient of the top layer being deposited; n_s and k_s are the refractive index and extinction coefficient of the virtual substrate; λ is the wavelength. The optical reflectance fitting method works excellently well for growth rates in the order of $\sim$1Å/s and epilayer thickness in the order of $\sim$0.1–10μm. It is adopted for measuring the thickness of LT GaAs which will be discussed in Chapter 4. The reflectance fitting method also has some limitations. The epilayer has to be sufficiently thick, preferably several thousand Å or more, in order to acquire enough oscillation periods for growth rate fitting. Therefore it is usually not applicable to structures with multiple heterogeneous and thin epilayers, e.g. SL. In addition, the n and k of binary compounds are very well known, but the growth rate fittings of ternary and quaternary compounds are more complicated as their n and k vary with group III compositions.

2.2.8 ECV Profiling and Flux Calibration of Dopant Cells

ECV profiling is a common technique in determining the active carrier concentration profile in III-V epilayers. ECV operates by creating a Schottky contact between the electrolyte and semiconductor and applying a voltage bias to form a depletion region within. By measuring the capacitance using alternative current (AC) analysis, the doping concentration can be calculated. In general, for p and n-type compounds, forward and reverse bias voltages are applied for etching respectively, while the reverse bias region alone is used for measuring the inverse square of capacitance, $1/\mathcal{C}^2$, versus the external voltage applied to the depletion zone, V. For n-type epilayer with a low concentration of $< 5\times10^{18}$ cm^{-3}, halogen lamp illumination is often added to assist etching. Decent $1/\mathcal{C}^2$ vs V and profile shape is necessary for accurate concentration calculation, while the method requires reasonably low contact resistance of the electrodes with the wafer, usually $<$ 1kΩ. Eutectic

of Ga-In for p-type and Ga-Sn for n-type epilayer are usually used to help achieve good ohmic contact, but that still nevertheless dominantly dependent on the polarity of the epitaxial structure itself. For electrolytes, Ethylenediaminetetraacetic acid (EDTA) [90] and basified EDTA [78, 91, 92] are commonly used for etching GaAs, while ammonium tartrate ($(NH_4)_2C_4H_4O_6$) [93, 94] is a typical etchant for InGaAs and InAlAs. However, $(NH_4)_2C_4H_4O_6$ has the shortcomings of rapid volatility and short shelf life. For all grown wafers presented in this project, EDTA [91] mixed with 0.2M NaOH was used as the ECV electrolyte. According to Faraday's equation of electrolysis, the etch depth $\mathtt{x}_{\text{etch}}$ is given by

$$\mathtt{x}_{\text{etch}} = \frac{Q}{q\mathfrak{v}} \frac{\mathcal{M}_{\text{mol}}}{N_{\text{A}}\varrho} \frac{1}{\mathcal{A}} \tag{2.40}$$

where Q and q are the total measured charge and elementary charge respectively, $\mathfrak{v}$ is the number of valency electrons per unit molecule, $\mathcal{M}_{\text{mol}}$ and ϱ are the molar mass and density of the etched epilayer, N_{A} is the Avogadro number and $\mathcal{A}$ is the measurement area. By considering the Schottky contact as a plate capacitor, $\mathcal{C}$ is related to the depletion width $\mathtt{x}_{\text{depletion}}$ by

$$\mathcal{C} = \frac{\varepsilon_0 \varepsilon_r \mathcal{A}}{\mathtt{x}_{\text{depletion}}} \tag{2.41}$$

where ε_0 and ε_r are the free space permittivity and dielectric constant respectively. The relation of $1/\mathcal{C}^2$ vs V can be described by Mott Schottky equation:

$$1/\mathcal{C}^2 = -\frac{2}{q\varepsilon_0\varepsilon_r \mathfrak{n}\mathcal{A}^2}(V - V_{\text{fb}}) \tag{2.42}$$

where V_{fb} is the flat-band potential. The carrier concentration $\mathfrak{n}$ is inversely proportional to the slope of $1/\mathcal{C}^2$ vs V:

$$\mathfrak{n} = -\frac{2}{q\varepsilon_0\varepsilon_r \mathcal{A}^2 \frac{d(1/\mathcal{C}^2)}{dV}} \tag{2.43}$$

The relation between the dopant flux and cell temperature is deduced based on the calibration method as described below. A staircase structure is grown for each of those dopant cells: Si, Be and C. Each structure consists of several GaAs epilayers with different dopant cell temperatures. After the growth, ECV is performed to measure the doping concentration, which corresponds to dopant flux ϕ_d, vs depth, which corresponds to different epilayers. Fig. 2.8 illustrates the ECV profiles, plots and fittings of $\ln(\phi_d)$ vs $1000/(T + 273.15)$. For Si and Be cells, by assuming that the dopant flux follows an Arrhenius-like relation vs the cell temperature, a plot of $\ln(\phi_d)$ vs cell temperature is used to get the coefficients via linear fit. Those calibration coefficients are then used to set the cell temperatures corresponding to different doping concentrations. The calibration steps

for C cell are similar to that of Si and Be except the dopant flux is assumed to follow an Arrhenius-like relation vs the cell current.

2.3 Substrate Temperature Monitoring in MBE

2.3.1 Conventional Pyrometry

Optical pyrometry is a popular method for monitoring the wafer temperature, where the temperature is determined from the thermal radiation emitted by the substrate. According to Planck's Law, the spectral radiance $\mathcal{J}$ can be expressed as a function of wavelength λ and temperature T_g:

$$\mathcal{J}(\lambda, T_g) = \frac{2\mathcal{E}hc^2}{\lambda^5} \frac{1}{e^{\frac{hc}{\lambda k_B T_g}} - 1} \tag{2.44}$$

where h is the Planck constant, c is the speed of light in vacuum and $\mathcal{E}$ is the surface emissivity, which is a function of λ and T_g. In practical use, the spectral intensity I, usually in arbitrary unit (a.u.), would be measured instead, which is given by

$$I(\lambda, T_g) = \frac{\mathcal{G}\mathcal{E}}{\lambda^5} \frac{1}{e^{\frac{hc}{\lambda k_B T_g}} - 1} \tag{2.45}$$

where $\mathcal{G}$ is a geometric factor that is dependent on the effective spot size that the pyrometer viewing on the radiation surface and the solid angle covered by the pyrometer lens, as well as attenuation and sensitivity. For a surface with $\mathcal{E}$ being unknown, it can be determined by a technique called "reflectance-correcting pyrometry" [95]. For thermal equilibrium where the emitted and absorbed radiations being equal to each other, the sum of the reflectance $\mathcal{R}$, transmittance $\mathcal{T}$ and $\mathcal{E}$ equals unity, i.e.

$$R(\lambda, T_g) + \mathcal{T}(\lambda, T_g) + \mathcal{E}(\lambda, T_g) = 1 \tag{2.46}$$

By choosing λ such that $\mathcal{T}(\lambda, T_g) = 0$,

$$\mathcal{E}(\lambda, T_g) = 1 - R(\lambda, T_g) \tag{2.47}$$

thus $\mathcal{E}$ can be calculated from the $R(\lambda, T_g)$. The SVT pyrometer used in this project measures two wavelengths: 470 nm and 950 nm. While it is true that $\mathcal{T}(\lambda, T_g) = 0$ for small bandgap substrates, such as InAs, and large bandgap substrates at high temperatures, such as GaAs, for the two aforementioned λ, it is invalid for large bandgap substrates at

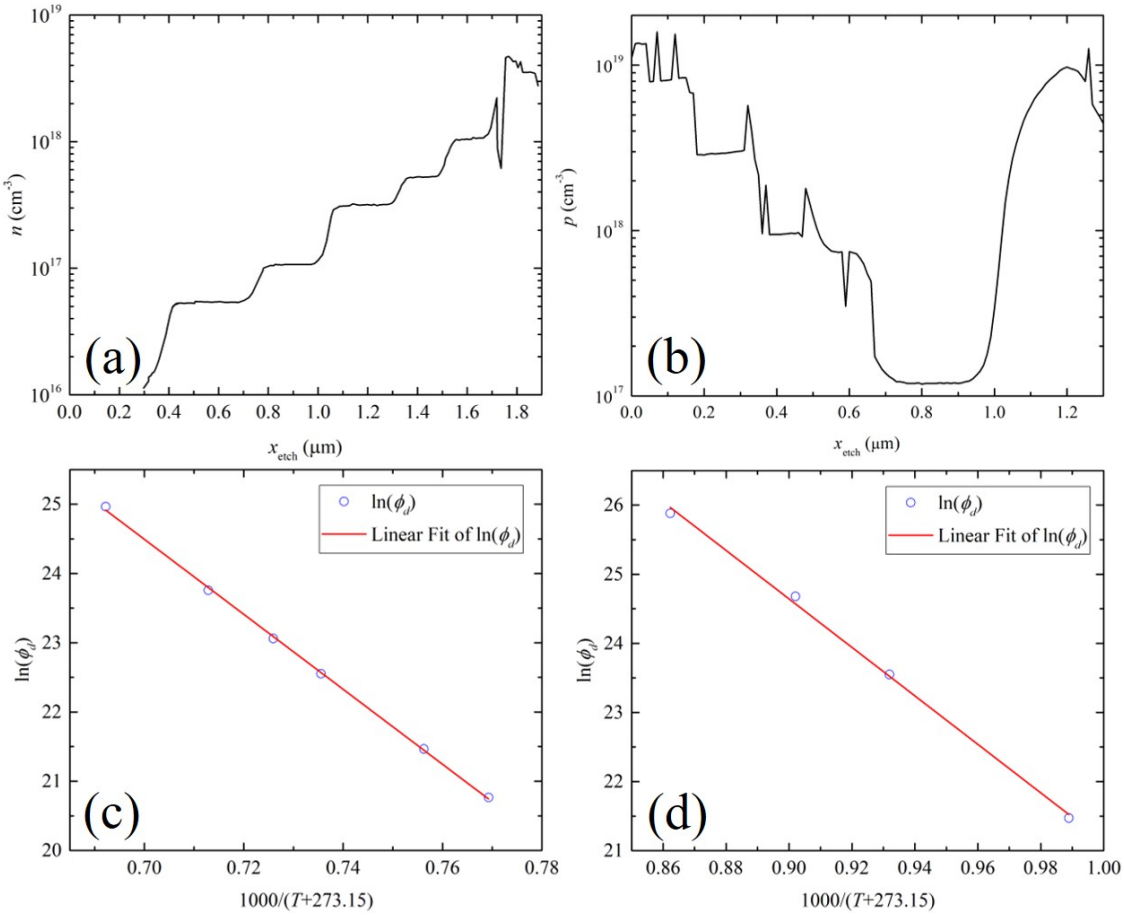

Figure 2.8: ECV profile (black line) of (a) GaAs:Si staircase structure and (b) GaAs:Be staircase structure; $\ln(\phi_d)$ vs $1000/(T + 273.15)$ (blue circle) with linear fit (red line) for (a) GaAs:Si staircase structure and (b) GaAs:Be staircase structure.

low temperatures, e.g. GaAs is transparent to 950 nm below 200°C. In addition, even if an accurate measurement of $\mathcal{R}$ and thus $\mathcal{E}$ has been conducted, in some scenarios $\mathcal{G}$ might still being unknown or cannot be calibrated with absolute values. Therefore from a practical perspective, it is more convenient to pre-calibrate the pyrometer with other temperature measurement techniques. In particular, for this present work, the SVT pyrometer is cross-calibrated with BET, where $\mathcal{G}$ is usually calibrated at high temperature after oxide desorption of the wafer.

Pyrometry works for most substrates, both semi-insulating (SI) and doped. However, there are a few drawbacks associated with this technique. Unless the substrate is indium-mounted on an opaque wafer such as molybdenum, the pyrometer wavelength must be chosen carefully to avoid the spectral region where the wafer is transparent. This restriction typically narrows down the available signal level at the optimum growth temperature. Si photodiode-based pyrometers are used for GaAs or InP substrate temperature measurements with the sensing wavelength window at 950 nm. Both InP and GaAs are still transparent to this wavelength at room temperature, but thanks to bandgap reduction with increasing temperature, it becomes strongly absorbed above 280°C for GaAs and above 180°C for InP. Nonetheless, since at 300°C, the blackbody emission peaks at 5.06 μm and there is still too little light (only 2×10^{-6} of the maximum intensity) at 950 nm, the pyrometer would not be very useful for low temperature measurement. Typically, temperatures above 450°C are necessary for a usable signal to noise ratio in Si sensor-based pyrometers. Another issue is that the substrate is not the only source of thermal radiation in an MBE chamber. There are other sources such as effusion cell orifices [22], ion-gauge filaments and heated viewports, as well as scatter thermal radiation in the system which add as background signals and may result in significant errors to the temperature reading even above 500°C. This issue is well illustrated for the In calibration growth in Fig. 2.5, where the pyrometer reading suddenly increased by more than 60°C when the Al and Sb shutters were opened. Light interference is another problem for commercial single or dual wavelength pyrometers when a layer is depositing on a wafer. It changes the wafer emissivity during the growth and brings another source of error into the measured temperature [18] unless a reflectance-correcting pyrometry method is employed [95]. In addition, most pyrometers don't have enough sensitivity to measure temperatures below 450°C, and to go that low, researchers end up collecting the light from fairly large areas, which means it does not work for small substrates. Sometimes because of their cost, smaller wafers are desirable.

2.3.2 Band Edge Thermometry

The aforementioned problems can be largely circumvented with BET, another contactless temperature sensing technique [19, 20, 21], where the temperature is determined by measuring the position of the absorption band edge for the substrate. This is achieved by acquiring the light transmission through the wafer using a suitable spectrometer. Typically, the thermal radiation from the substrate heater or a halogen lamp in a single or double pass geometry is used as a source of light. With appropriate correction for variation in substrate thickness, BET calibration can be reliably transferred between different deposition systems. On the other hand, the measurement of BET is not affected by scattered radiation or substrate size, and with an external light source, it can reliably measure any temperature of practical interest. For GaAs, InP or Si, turn-key commercial solutions are available, while more customized solutions can be assembled using compact high-performance 0.9–1.7 μm InGaAs array spectrometers coupled to the MBE system viewport via low-attenuation infrared optical fiber. In this work, the temperature vs band edge relations of several substrate materials: SI-GaAs, SI (Fe-doped) and n^+(S) InP, were calibrated in a vacuum chamber where the thermocouple had direct contact with the substrate. The transmission spectrum was acquired under different temperatures for each substrate. The temperature was assumed to follow an empirical cubic polynomial relation vs the band edge wavelength λ_c, i.e.

$$T_{\mathrm{BET}} = p_0 + p_1\lambda_c + p_2\lambda_c^2 + p_3\lambda_c^3 \tag{2.48}$$

Coefficients p_0, p_1, p_2, p_3 were determined from the calibration. For the MBE growths in this work, transmission spectrum and λ_c were acquired by the NIR spectrometer and analyzed by a LabVIEW code, where T_{BET} was calculated by using Eq. 2.48. Fig. 2.9 illustrates the BET traces of a SI GaAs(001) substrate, i.e. the transmittance spectrum, acquired by the raw radiation spectrum from the heater through the substrate divided by a reference spectrum directly from the heater without the substrate. Combination of both BET and 950nm pyrometry typically resolves most of the temperature measurement problems for larger bandgap materials discussed above, since the 950 nm pyrometry signal can be easily calibrated with BET using a SI GaAs substrate at high temperature (e.g. 600°C), and used subsequently to correct the BET calibration curve for doped GaAs wafers. Nonetheless, BET has its own limitations. The accuracy of BET relies on materials with a very reproducible absorption edge such as SI GaAs and InP in which their absorption edge locate within the near-infrared (NIR) spectral range of 700–1700 nm. However, this is not the case for doped substrates and small bandgap semiconductors such as InAs (0.35 eV) and GaSb (0.726 eV). Implantation of mid-infrared detectors that cover spectral range $>$ 2000 nm such as Fourier spectrometer may be a potential solution, but those devices

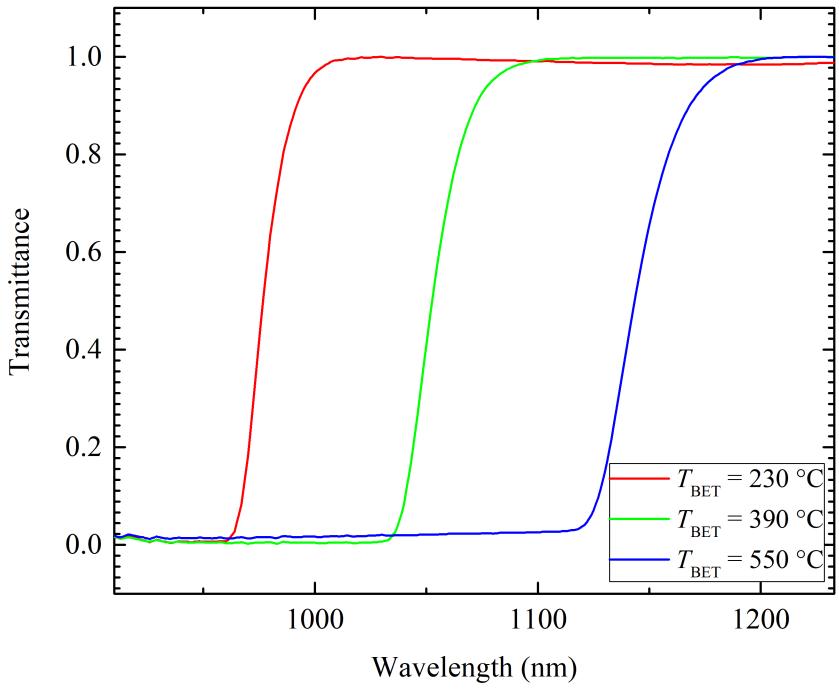

Figure 2.9: Illustrative BET traces of a SI GaAs(001) substrate at temperatures 230°C (red), 390°C (green) and 550°C (blue).

are usually bulky and expensive, not to mention those small bandgap materials have their absorption edge shapes vary strongly with carrier concentration and growth temperature.

2.3.3 Nomarski Microscopy and Black-Box Imaging

Nomarski microscopy, also known as differential interference contrast microscopy (DICM), is used to analyze raw, epitaxially grown or processed semiconductor wafers, or even bio-organic tissues and living bacteria. With the use of a Wollaston prism, the light beam generated from a lamp is separated into two orthogonally polarized components which travel to the sample surface before recombination. The image contrast can be altered by adjusting the offset phase, which changes the position at zero optical path difference by an additional polarizer [96]. The contrast is recorded by the shear distance represented by different intensities or colors and the surface morphology is displayed with a shadow-like 3D appearance, therefore it is more visible for observing semiconductor defects than conventional optical microscopy. For the grown wafers presented in this work, Nomarski images were acquired at 5× and 40× magnifications with an exposure time of ∼50–200 ms. Each acquired image has 2592 × 1944 pixels. For 40× magnification, this gives resolution as fine as ∼0.1 μm. In other words, defects with size as small as ∼0.1 μm can be observed. For any Nomarski image displayed in this work, when there are no observable defects in the 40× magnification, the corresponding grown wafer is considered as having high epitaxial quality and smooth morphology. Apart from Nomarski imaging, a conventional digital camera is another convenient tool that gives quick access to details about the overall smoothness and major defects of the wafer surface. The digital camera images, with each wafer placed inside a home-built black-box to minimize external stray lights, were taken with adjustable apertures of f/16, f/32 or f/36, exposure time of 0.4–0.5 s and ISO speed of 200–1600 depending the surface morphology to optimize the image quality.

2.4 Terahertz Photoconductive Antennas

2.4.1 Time-resolved Pump-Probe Technique

Pump-probe measurement is a common technique in photonics to acquire information on ultrafast phenomena. Fig. 2.10 shows a typical setup for transmission pump-probe measurement, where a femtosecond pulse laser acts as the excitation source. The incident laser beam is split into pump and probe beams. The pump pulse hits the sample first

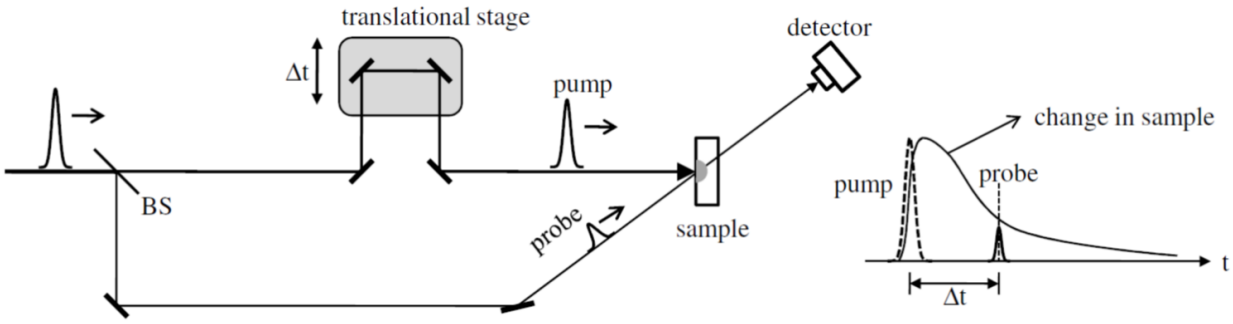

Figure 2.10: Schematic of a typical setup of a time-resolved pump-probe technique. BS: beam-splitter, Δt: time-delay between the pump and probe pulse. Figure adopted and reprinted from Ref. [23].

and generates some ultra-short, temporary optical excitations within the sample which cause transient current or lattice vibrations; the probe pulse hits the sample later and the transmission is measured, where the time-delay between the two pulses is adjustable with the use of a translational stage in the pump line. The plot of differential transmission (DT) vs time-delay is a common tool to analyze the pump-probe measurement data, in which DT is given by $\Delta\mathcal{T}/\mathcal{T}_0 = (\mathcal{T} - \mathcal{T}_0)/\mathcal{T}_0$, where $\Delta\mathcal{T}$ is the change in transmission induced by the pump pulse and $\mathcal{T}_0$ is the transmission without the pump pulse. As an alternative, reflection measurement geometry is also widely used, where the differential reflection (DR) vs time-delay is analyzed instead.

2.4.2 Terahertz Time-Domain Spectroscopy

The setup for THz time-domain spectroscopy is very similar to that of the pump-probe technique. An illustrative schematic is shown in Fig. 2.11. The optical input beam is split into two components. The pump pulse illuminates the emitter and generates the THz pulse, while the probe pulse, after going through a translational stage, illuminates the detector which receives the THz pulse on its other side. In a THz TDS, the measurement is done with and without a sample, in which the amplitude and phase of both cases are compared. By analyzing the THz signal in the frequency domain, information of the sample such as absorption and dispersion is acquired. The THz emitter and detector are made of PCAs attached to silicon lenses for collimating the output or input THz wave. A THz TDS system can be operated with two kinds of optical sources: femtosecond laser pulse or photomixing. Refer to Fig. 2.12, a femtosecond laser pulse excites the PCA and generates broadband THz radiation via transient photoconductive switching; on the other hand, photomixing

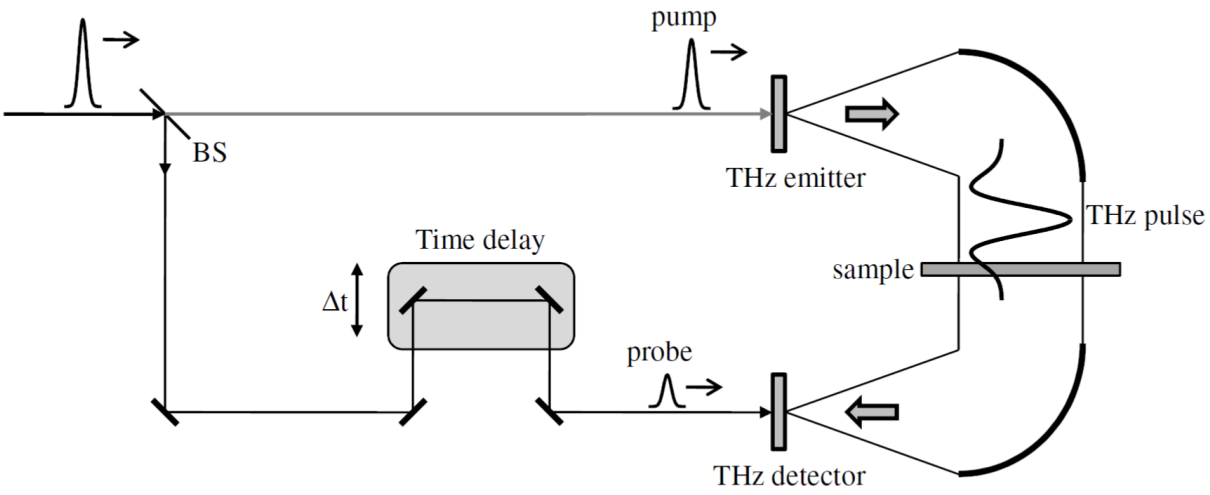

Figure 2.11: Schematic of a typical setup of THz TDS using femtosecond optical pulses. BS: beam-splitter, Δt: time-delay between the pump and probe pulse. Figure adopted and reprinted from Ref. [23].

is the superposition of two laser beams with different frequencies that forms an optical beat, which generates continuous wave (CW) THz radiation at the beat frequency. A PCA is somewhat similar to a Hertzian dipole antenna except it requires optical excitation to operate. The schematic of a PCA used as a THz emitter is shown in Fig. 2.13, where a pair of metal electrodes are deposited on a photoconductive semiconductor substrate. When the gap between the electrodes is exposed by a femtosecond pump pulse with photon energy larger or equal to the semiconductor bandgap, electron-hole pairs are generated, resulting in a sudden boost of the conductivity inside the material. A direct current (DC) bias that applied between the electrodes accelerates the charge carriers towards the polarities, but the carriers would be immediately trapped by the defect sites in the semiconductor, and hence bringing the conductivity back to its initial value. The duration of such a process can be quantified by a carrier lifetime. Therefore the transient current produced within the process generates the THz radiation. On the other hand, the schematic of a PCA based THz detector, as shown in Fig. 2.13(b), is almost identical to that of a THz emitter except the working mechanism is opposite: a photocurrent is produced upon incoming optical excitation and THz pulse. In a THz TDS measurement, the photocurrent that is acquired at various time-delay between the optical pump and probe pulse gives the THz signal that can be mapped into the frequency domain via Fourier transform. For THz emission and detection, the carrier lifetime of the PCA material should be in the order of sub-picosecond [23]. A THz pulse with shorter carrier lifetime affords a broader spectrum.

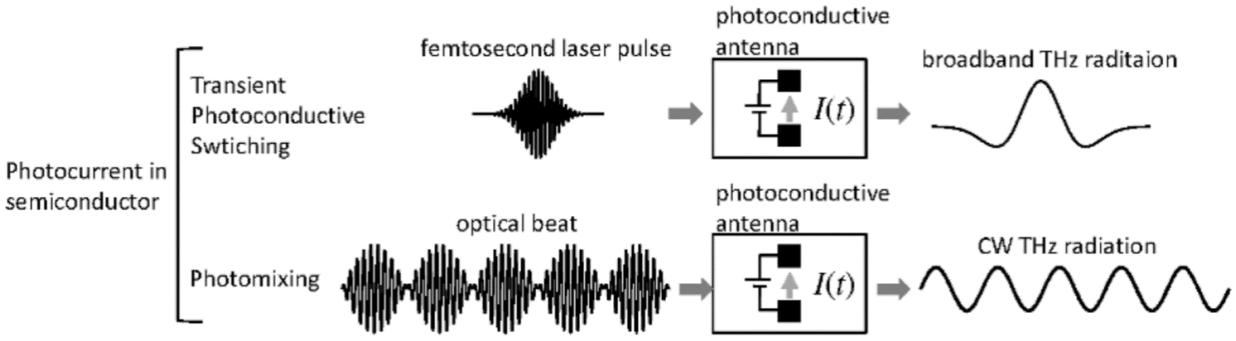

Figure 2.12: THz generation from PCA by femtosecond laser pulse (top) and photomixing (bottom). Figure adopted and reprinted from Ref. [23].

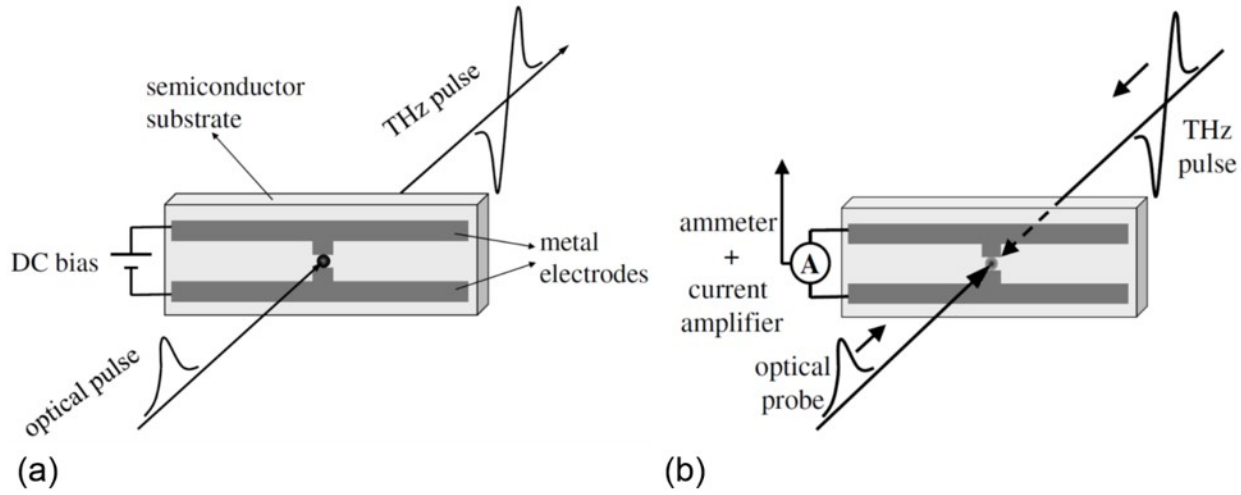

Figure 2.13: Schematics of a PCA used in (a) THz pulse generation (b) THz pulse detection. Figure adopted and reprinted from Ref. [23].

A high-quality PCA material should also have high carrier mobility, especially for THz emitter as it affects the emission power [97]. Aside from these, dark resistivity is another crucial factor that must be taken into account. This is particularly important for a THz detector, as high dark resistivity significantly reduces the detected noise [97]. Lastly, the material thickness should be appropriate, which determines the absorption efficiency of the input optical beam [51]. All of the aforementioned factors are to be considered when one designs a PCA structure. Various PCA materials have been being studied over the past 30 years, such as LT GaAs [98], self-assembled ErAs islands embedded GaAs [99], Fe-implanted InGaAs [100] and Be-doped LT InGaAs-InAlAs SL [51, 60, 101].

2.5 Low Temperature Grown Semiconductor Materials

2.5.1 Low Temperature GaAs

The structural, optical and electrical properties of MBE grown materials strongly depend on the growth temperature. For instance, to obtain stoichiometric, single-crystalline epitaxial layers, the typical growth temperature is in the range of ∼400–500°C for InAs, ∼600°C for GaAs and ∼600–700°C for AlGaAs. On the other hand, when the temperature is much lower than the "standard" at ∼200–300°C, the sticking coefficient of As increases. Up to 2% excess As can be incorporated into the GaAs layer, where the excess As amount increases with decreasing growth temperature [11, 12]. The excess As atoms become different types of point defects, including As antisites (As_{Ga}, where As atom locates on a Ga site), As interstitials and Ga vacancies (V_{Ga}). Upon annealing, the As point defects turn into precipitates in clusters with the density and size dependent on the annealing temperature. Fig. 2.14 shows the transmission electron microscopy (TEM) images of LT GaAs annealed at 500°C for 30 s and 900°C for 30 s. At lower annealing temperature, the As precipitates are densely packed and small in size, while the opposite case is observed at a higher temperature. In the 1990s, there were a large number of investigations of MBE growth of semiconductors at such low substrate temperatures, which lead to discoveries of many useful optoelectronic properties for semiconductors grown in such a condition. The role of As precipitates on carrier lifetime and resistivity can be explained by the Schottky barrier model [11, 12]. Referring to Fig. 2.15, a depletion region is formed around each As precipitate, in which those clusters work as electron traps. The resistivity of the material depends on the amount of excess As embedded, precipitate size, depletion radius and spacing, while the carrier lifetime, τ_c, of LT GaAs is inversely proportional to the As defect

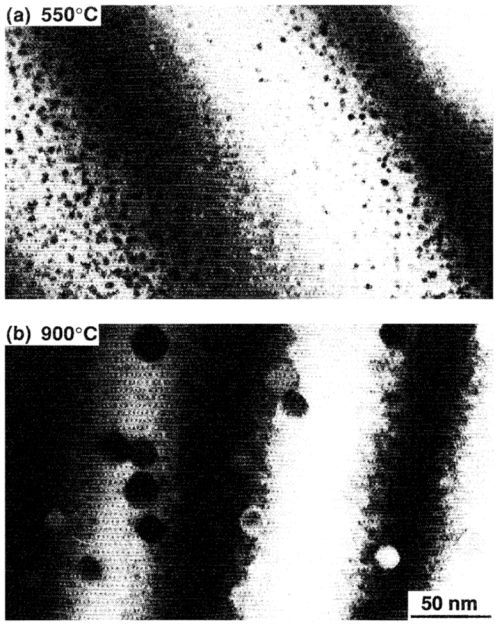

Figure 2.14: TEM images of two samples from the same LT GaAs epitaxial layer annealed at (a) 500°C for 30 s and (b) 900°C for 30 s. Figure adopted and reprinted from Ref. [12].

density, $\mathfrak{n}_{\mathrm{As}}$, according to Shockley-Read-Hall recombination theory [60, 102], i.e.

$$\tau_c = \frac{1}{\sigma \upsilon_{\mathrm{th}} \mathfrak{n}_{\mathrm{As}}} \tag{2.49}$$

where σ and υ_{th} are the carrier capture cross-section and mean thermal carrier velocity respectively. For instance, if the As defect density is very high such that its depletion region overlaps with its adjacent neighbor, the electrons would become easier to be captured and the material would exhibit a shorter carrier lifetime. Although as-grown LT GaAs is a relatively conductive material with resistivity of only $\rho \sim 10\ \Omega$cm, annealed LT GaAs at ~600°C is semi-insulating with $\rho \sim 10\ \mathrm{M}\Omega$cm. Along with reasonably high carrier mobility of $\mu_n \sim 200\ \mathrm{cm^2V^{-1}s^{-1}}$ and extremely short carrier lifetime of $\tau_c \sim 0.2$ ps [103], these are the properties that make LT GaAs an excellent photoconductive transient switch for THz PCA devices. Over the last 20 years, numerous GaAs based THz systems, both optical pulse [104, 105, 106] and photomixer driven [107], have been reported, with the maximum detection bandwidth (BW) of > 20 THz [105].

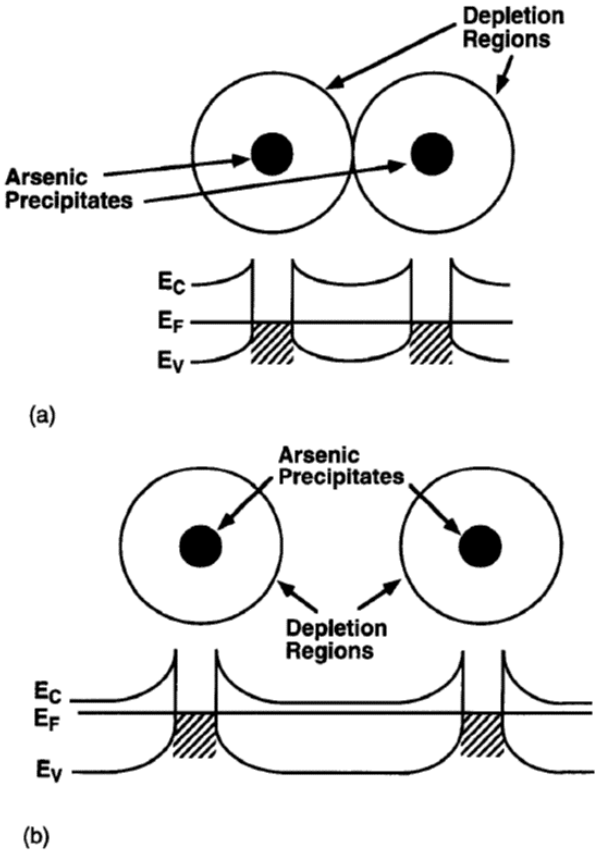

Figure 2.15: Depletion regions around As precipitates such that (a) they just overlap and (b) there is a spacing between them. Figure adopted and reprinted from Ref. [11].

2.5.2 Low Temperature InGaAs-InAlAs Superlattice

Although LT GaAs is a widely used PCA material with benefits from its sub-picosecond carrier lifetime, high mobility and resistivity, there are limitations of its applications. LT GaAs has a bandgap of ∼1.42 eV at room temperature, which corresponds to a wavelength of 870 nm. To generate THz radiation, input ultra-short optical pulse width of $\ll$ 1ps is required. Typically, 780 nm lasers are used to excite LT GaAs, for example, Ti: Sapphire mode-locked oscillators, but those lasers are usually expensive and bulky. Therefore the cheaper and compact 1550 nm telecom lasers emerge as a better alternative. In addition, The fiber optic components for 1550 nm are also much more portable and low-cost compared to those at 780 nm, which give more flexibility to deploy those THz devices for industrial applications. This is the reason why since the early 2000s, researchers have been studying $In_{0.53}Ga_{0.47}As$ on InP substrates as a better option of THz PCA material. With its bandgap energy at 0.75 eV, InGaAs is able to be excited by 1550 nm telecom laser and this significantly suppresses the building cost of a THz TDS system. Sartorius *et al*. studied the carrier concentration of InGaAs under different growth temperatures [51]. similar to the case of GaAs, InGaAs that is grown under LT turns non-stoichiometric with excess As defects. However, unlike LT GaAs, the defect states in InGaAs are incorporated in a way that the Fermi level is very close to the condition band, which in fact increases the conductivity of the material. In the LT regime ($<$ 200°C), InGaAs showed highly conductive behavior with its carrier concentration up to $\sim 10^{18}$ cm^{-3}, which was quite different from the highly resistive LT GaAs.

In order to pin down the Fermi level to a mid-gap position, several InGaAs samples were prepared with different Be doping levels to compensate for the n-type conduction by As_{Ga} defects. The carrier concentration vs Be concentration is shown in Fig. 2.16, where a transition from n to p-type was observed with increased Be doping. Since the adjustment of the doping level to get a zero net carrier concentration was extremely difficult, the authors showed that the insertion of InAlAs layers between InGaAs layers is an effective solution to increase the dark resistivity. Fig. 2.17 shows the schematic of the InGaAs-InAlAs SL and the respective band diagram, where 100 periods of lattice-matched, 12 nm InGaAs layers plus 8 nm InAlAs layers were grown on an InP substrate. Compared with InGaAs, InAlAs has a higher bandgap of 1.46 eV, which cannot be excited by 1550 nm input and does not contribute to photoconductivity. Nonetheless, the essence of LT InAlAs is its high concentration of deep electron traps, where electrons excited in the InGaAs photoconductive layers are trapped within the InAlAs layers via tunneling. The bulk LT InGaAs had sheet resistance of less than 100 Ω/sq, while with the insertion of InAlAs and doping it was dramatically increased to 1 MΩ/sq. This number corresponds

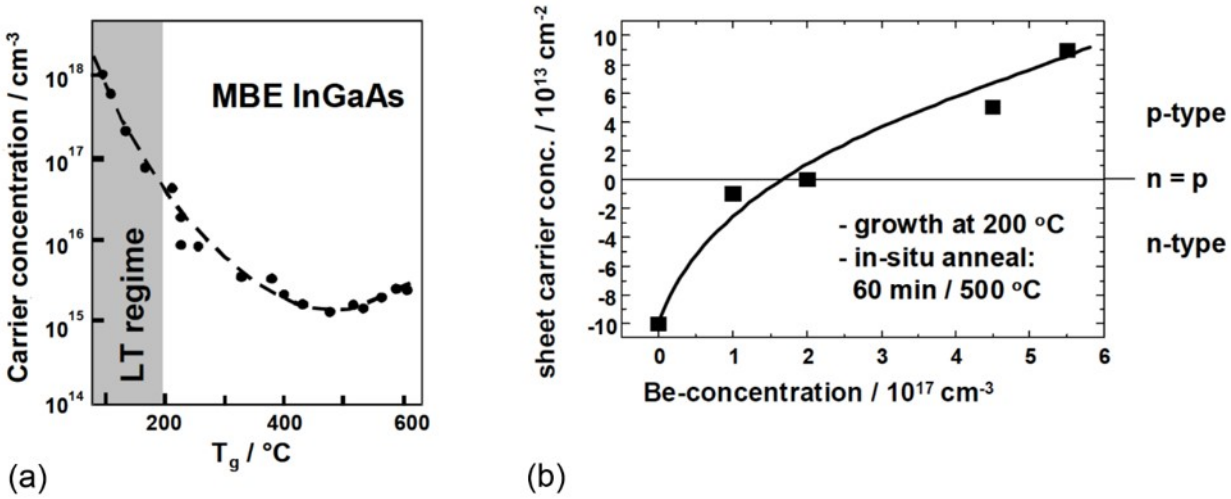

Figure 2.16: (a) Carrier concentration of InGaAs under different growth temperatures; (b) Be doping vs carrier concentration. Figure adopted and reprinted from Ref. [51].

to a resistivity of 1.2×10^5 Ω/sq, which is much smaller than that of LT GaAs (10 MΩ/sq) but already sufficient for THz device applications. Using a 1550 nm, 100 fs optical pulse width, 100MHz repetition rate fiber ring laser as the source, LT InGaAs-InAlAs SL as the PCA target, THz pulse width of < 750 fs and spectral bandwidth extended up to 3 THz were achieved.

To further improve the dynamic range, Dietz *et al.* demonstrated another 1550 nm pulsed laser driven THz TDS system with a strip-line high mobility MLHS emitter and a 130°C grown, 100 periods LT InGaAs-InAlAs SL structure with Be doping concentration of 4×10^{18} cm^{-3} used as the detector [58]. Refer to Fig. 2.18, a 90 dB dynamic range and 6 THz BW were obtained. This, up to date, is the best performance record for pulsed fiber laser operated, LT InGaAs-InAlAs SL based THz TDS system. However, very little details about the MBE growth conditions are revealed in the aforementioned reports, especially not much is being told how to grow the SL at 130°C without losing single crystallinity. MBE optimizations of InGaAs-InAlAs SL needs to be established to achieve similar THz TDS performance. This work attempted to determine the appropriate conditions to grow InGaAs-InAlAs SL. In particular, in order to optimize the growth temperature precisely, pyrometry, BET and ISP were used as temperature monitoring tools. Furthermore, as already mentioned in Chapter 1, by assuming carbon would act as a p-dopant in InGaAs as it does in GaAs, the sheet resistance of C-doped InGaAs-InAlAs SL was optimized and the results were compared to the Be-doped counterparts.

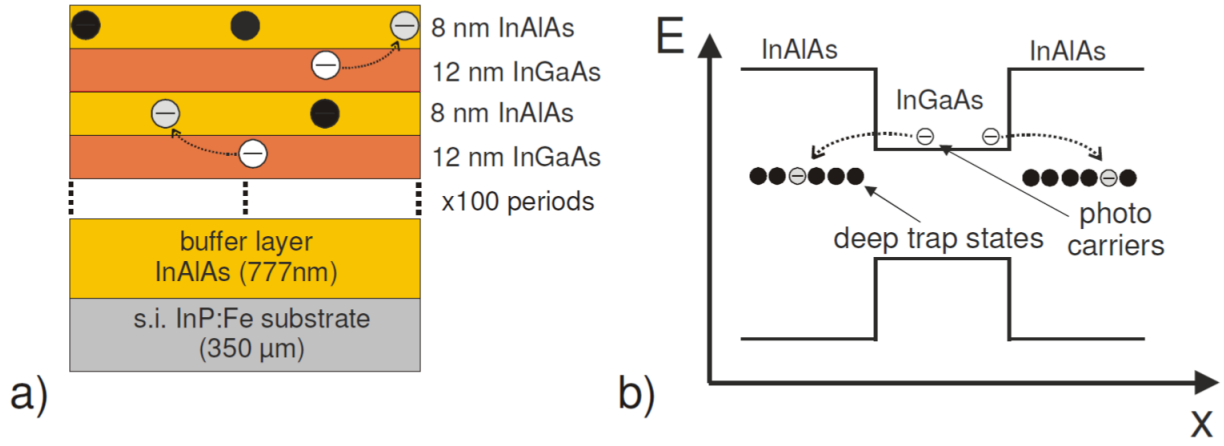

Figure 2.17: (a) Schematic of InGaAs-InAlAs SL, with 100 periods of a 12 nm InGaAs and 8 nm InAlAs layers. Cluster-induced defects act as electron traps in the InAlAs layers. (b) Schematic of the respective energy band diagram. Figure adopted and reprinted from Ref. [56].

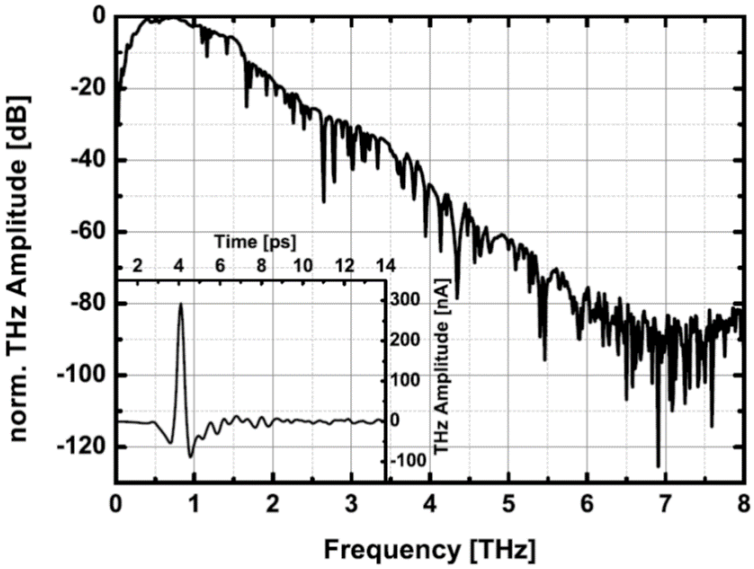

Figure 2.18: Fast Fourier transform (FFT) spectrum obtained for a high mobility MLHS emitter at 120 V bias and 25 mW optical excitation and an MLHS detector at 16 mW optical excitation. The corresponding THz pulse trace is shown in the inset. Figure adopted and reprinted from Ref. [58].

2.6 InAlGaAs as a Photonic Power Converter Material

MJ is one of the most effective methods to boost the efficiency of photovoltaic devices above the values presently achievable. For instance, an III-V semiconductor-based, cell size ranged ∼1–10mm^2, SJ PPC device typically gives an output voltage of only ∼1V, but with the use of an MJ architecture of subcells, the output voltage can be raised up to 30V, with the voltage scaling linearly with the number of subcells. Wilkins *et al*. show the current-voltage characteristics for PPC of up to 20 junctions with power conversion efficiency more than 60% [65]. Tunnel diode (TD) serves as an essential part of an MJ cell which interconnects adjacent subcells. A high-performance TD based PPC needs high transparency to minimize optical losses, high peak tunnel current for effective operation under high solar concentration and low differential resistance to reduce parasitic voltage loss [108]. Conventional PPCs are usually based on GaAs and operated under 850 nm, which is well suited for short-distance over-fiber power transfer but attenuates quickly when it switches to longer distance [62]. For this reason, researchers have redirected their focus in designing PPCs that absorb 1310 nm of light corresponding to the telecom o-band, in which the attenuation of light through the fiber is significantly alleviated. This can be achieved by using the lattice-matched quaternary InAlGaAs. Fig. 2.19 labels the approximate positions of the optimum bandgaps with the vertical dashed line showing the available bandgap for InAlGaAs lattice-matched to InP, ranges from ∼0.75–1.46 eV for lattice-matched InGaAs and InAlAs bandgap respectively, which can all be grown by MBE with excellent epitaxial quality. Thanks to this feature of tunable bandgap, the InAlGaAs based PPC has more design flexibility to work with various pumping wavelengths [68, 69], of which 1310 nm is within. Fig. 2.20 shows the conceptual schematics of an InAlGaAs based SJ and MJ devices, with the later device having each subcell thickness engineered in a way such that all of them receive an equal amount of the incident light and produce the same current. In a typical MJ device, the TD serves as a series connection between adjacent subcells. The absorbed photons are mainly from the laser and are partially emitted by other subcells through luminescent coupling. Fig. 2.21 illustrates a J-V characteristic plot of o-band power converters with 1–10 junctions and illumination intensity of 1 Wcm^{-2}, with the efficiency increases from 57% for 1 junction up to 58.5% for 10 junctions. Such an increase is mainly due to the luminescent coupling and compared with their thicker counterparts, thinner subcells have slightly larger voltage.

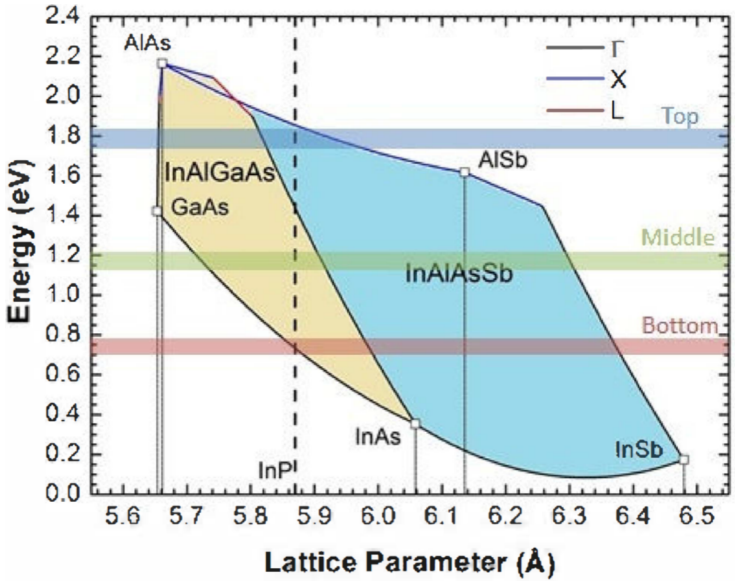

Figure 2.19: Bandgap vs lattice parameter plot for As and Sb based III-V compounds. Figure adopted and reprinted from Ref. [109].

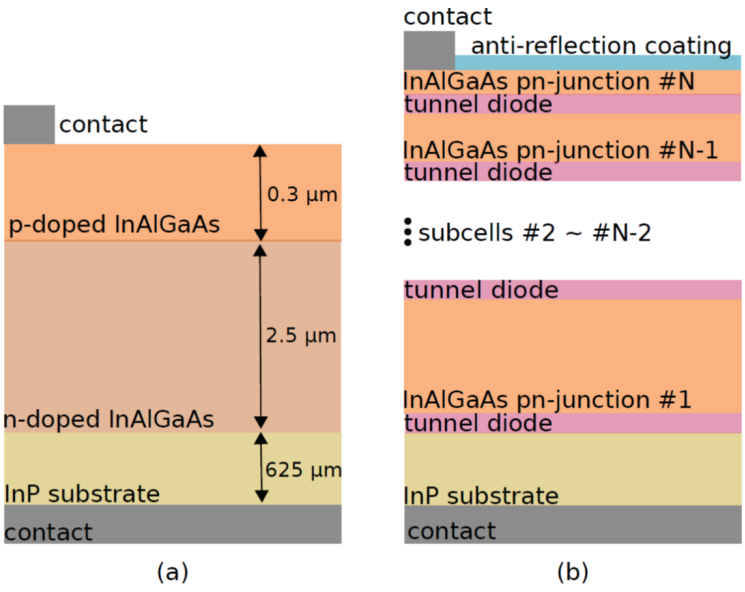

Figure 2.20: Conceptual schematics (not to scale) of the InAlGaAs (a) SJ and (b) MJ devices. Figure adopted and reprinted from Ref. [62].

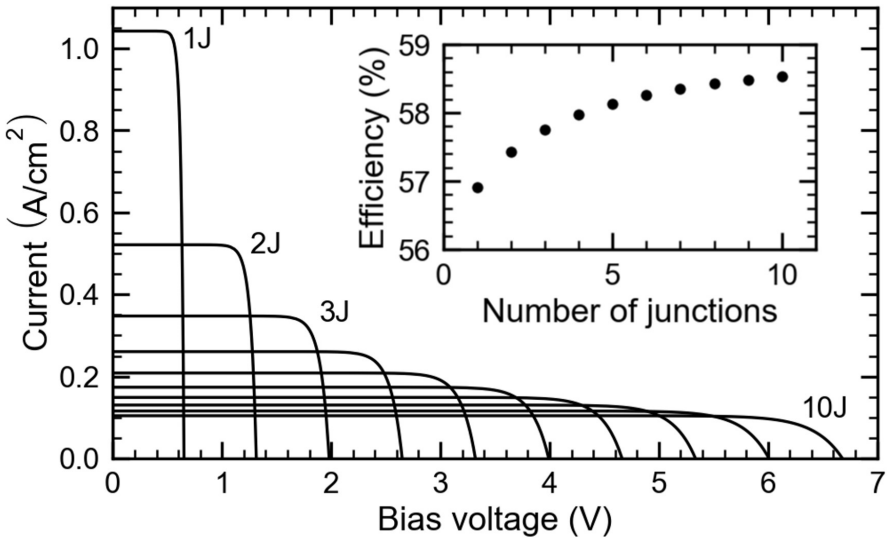

Figure 2.21: Theoretical J-V characteristics for PPCs with 1 to 10 junctions. The inset shows the efficiency as a function of the number of junctions. Calculations are done using an extended and detailed balance model in the radiative limit. Incident illumination is centered at 1319 nm with an intensity of 1 Wcm^{-2}. The active layer has a bandgap of 0.867 eV. Figure adopted and reprinted with permission from SUNLAB, University of Ottawa.

Chapter 3

Integrated Spectral Pyrometry

3.1 Prior-Growth Calibration

Fig. 3.1 shows the schematic of the wafer used for ISP calibration. A quarter-2-inch (Q2") InAs wafer was In-mounted on a full-3-inch (full 3") SI GaAs substrate, where the latter one was mostly covered by a Mo plate with the exception of a very small gap next to the edge of the InAs substrate. The thermal radiation was collected by the InGaAs NIR spectrometer through a bi-convex lens of 25.4 mm focal length and an optical fiber mounted on the bottom viewport of the MBE GM. The focusing optics was designed to collect light from a spot of approximately 10 mm in diameter, which could be shifted between the exposed GaAs region for BET measurements and the centre of the InAs substrate for pyrometry measurements. Since the two wafers were in contact, the GaAs temperature determined by T_{BET} was essentially the same as the InAs temperature. A LabVIEW code was written to log the data for both the BET and ISP measurements. The spectrometer integration time was kept at 1 s for the BET part and 0.2 s for the ISP part to obtain enough intensity without saturating the detector array at any point throughout the entire calibration. T_{BET} was acquired vs T_c, stepping up from 370 to 400°C, then to 440°C and finally to 590°C in 30°C steps, as presented in Fig. 3.2(a). The noise appears at time $t < 1200$ s was attributed to the weak BET signal for $T_{\mathrm{BET}} < 330$°C, which resulted in incorrect locating of the band edge wavelength. Other than that, T_{BET} followed a smooth, step-wise increase pattern similar to that of T_c. The ISP measurement is shown in Fig. 3.2(b). Instead of one or two wavelengths as is done with a typical pyrometer, the entire emission spectrum of InAs was acquired and the integrated intensity over the spectrum, I_{InAs}, was measured vs T_c with the aforementioned temperature range and step size, but this time with T_c stepping down.

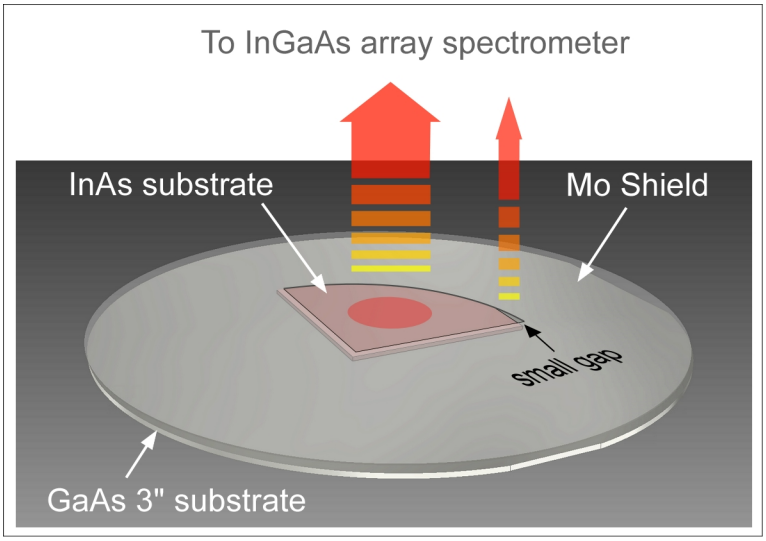

Figure 3.1: Schematic of the calibration system consisting of a Q2" InAs substrate, In-mounted to a 3" GaAs substrate, with the latter mostly covered by a Mo plate, which leaves only a small gap near the InAs edge for BET measurement of GaAs.

The fluctuation of I_{InAs} reading originates from the substrate wobbling during rotation. The calibration data extracted from Fig. 3.2(a) and (b) was analyzed by mapping each averaged T_{BET} and I_{InAs} data point with the same T_c as a pair and introducing a simple exponential function:

$$I_{\text{InAs}}(T_{\text{BET}}) = C_1 e^{-\frac{C_2}{T_{\text{BET}}+273.15}} \tag{3.1}$$

where C_1, C_2 are calibration coefficients. Fig. 3.3(a) shows the plot of $\ln(I_{\text{InAs}})$ vs $1000/(T_{\text{BET}} + 273.15)$ and the linear fitting by using Eq. 3.1. ISP ensures high precision of temperature calibration by taking advantage of BET which is unaffected by substrate emissivity or stray light from other sources. Although any data point for $T_{\text{BET}} < 290°\text{C}$ was hardly measurable in the calibration, the fitting was precise enough that it could be safely extrapolated to temperature as low as 200°C. Once C_1 and C_2 are determined, the same spectrometer can be used to measure the temperature of any other InAs wafer, T_{ISP}, by acquiring its I_{InAs} as:

$$I_{\text{InAs}}(T_{\text{ISP}}) = I_{\text{all}}(T_{\text{ISP}}) - \sum_j I_j = C_1 e^{-\frac{C_2}{T_{\text{ISP}}+273.15}} \tag{3.2}$$

Here a summation term is added, where I_j is the extra radiation from a particular source other than the InAs wafer. For substrate spectrum acquisition, I_j can be compensated

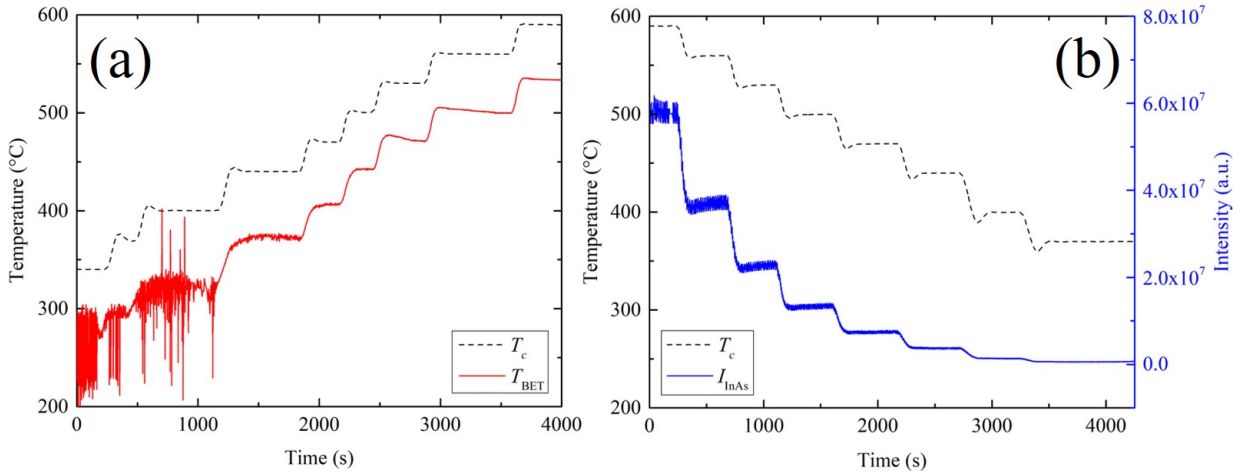

Figure 3.2: (a) T_c (dash black) and T_{BET} (solid red) of the small exposed GaAs region acquired during the prior growth calibration; (b) T_c (dash black) and I_{InAs} (solid blue) of the InAs substrate during the prior growth calibration.

by measuring the difference of the measured ISP signal, I_{all}, between the cases where an effusion cell shutter is opened and closed or a viewport heater is turned on and off, which can potentially be incorporated into a temperature measurement and control feedback loop during any epitaxial growth. For comparison, a simulated blackbody radiation plot is also added in Fig. 3.3(a) with the responsivity, shown in Fig. 3.3(b), of the InGaAs spectrometer taken into account, where it is normalized such that it has the same value as the ISP linear fit at 600°C. The blackbody has its slope deviated from the ISP linear fit, which can be explained by the fact that as the substrate radiation increases exponentially with temperature, it is possible that the InGaAs photodetector array response becomes nonlinear at high substrate temperature, where the detected signal is no longer proportional to the incident intensity.

3.2 Si-Doped InAs Growth

An In-free mounted, single-side polished, Q2" InAs wafer was used for this growth. The growth involved three stages. In stage (i), the oxide was desorbed under As Op for 1600 s at a substrate temperature of 500°C, as measured with calibrated ISP. Afterwards, the wafer was ramped down to 350°C for stages (ii) and (iii), where at (ii) a 2000Å InAs layer with Si doping concentration of 1×10^{18} cm^{-3} was grown, followed by (iii) a 10,000Å InAs

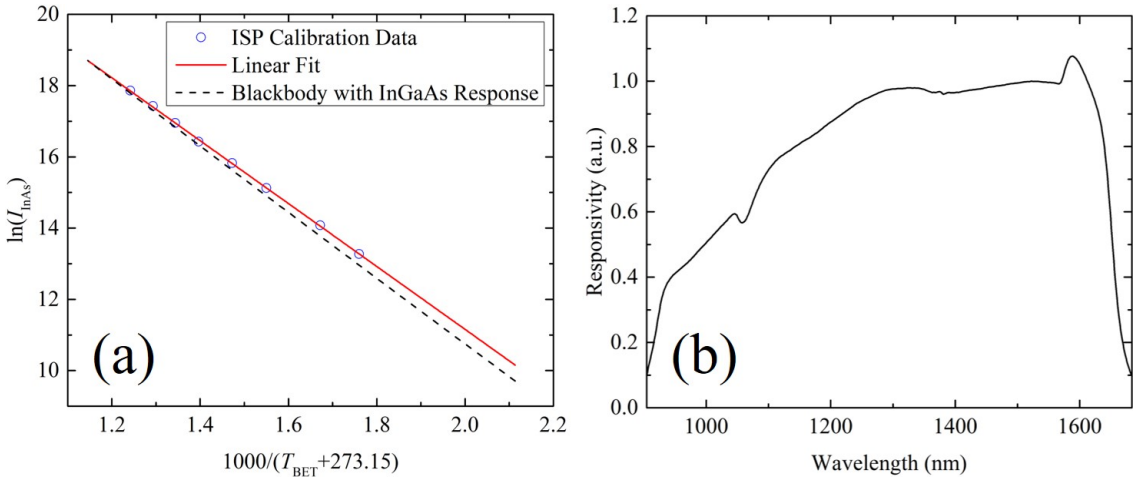

Figure 3.3: Plot of $\ln(I_{\mathrm{InAs}})$ vs $1000/(T_{\mathrm{BET}}+273.15)$ data (blue circle), its linear fit with Eq. 3.1 (red line) and a simulated blackbody plot with the responsivity of the InGaAs spectrometer taken into account (dash black line); (b) responsivity of the 900–1700 nm InGaAs NIR spectrometer (black).

layer with Si doping concentration of 5×10^{19} cm^{-3}. Fig. 3.4(a) shows ISP temperature monitoring of the Si-doped InAs growth. At $t < 700$ s, the ISP signal was too weak and suffering from small signal to noise ratio that the T_{ISP} reading was even larger than T_c, but other than that, T_{ISP} exhibited a similar trace as T_c and always maintained 50 to 80°C lower than T_c, which showed that the ISP calibration was reliable. The temperature measured by an SVT pyrometer, T_{pyro}, was also displayed as a comparison. Throughout the entire growth $T_{\mathrm{pyro}} > 420$°C, and its trace was significantly different from that of T_c, which indicated the standard pyrometer failed to measure the correct substrate temperature. The only exception was at stage (i), where the oxide desorption took place and $T_{\mathrm{pyro}} \approx T_{\mathrm{ISP}}$. The comparison shows ISP's accuracy over conventional pyrometry, in which ISP allows temperature measurement as low as 200°C. The procedure of stray light compensation is illustrated in Fig. 3.4(b), which is a zoom-in display of T_{ISP} and I_{all} at stages (ii) and (iii). At the beginning of stage (ii), the In and Si cell shutters were opened. Due to the extra radiation from these two cells, the reading of I_{all} increased by an amount of $I_{\mathrm{In}} + I_{\mathrm{Si}}$, which also resulted in an increase of T_{ISP} reading from 350°C to 370°C. By simply measuring this step-up and input $\sum_j I_j = I_{\mathrm{In}} + I_{\mathrm{Si}}$ into the LabVIEW code for ISP calculation based on Eq. 3.2, such extra radiation can be immediately compensated and T_{ISP} restored back to 350°C. Similar procedures were done at stage (iii) where I^*_{Si} was larger than the previous I_{Si} due to heavier doping concentration and thus hotter cell temperature, and for As cell

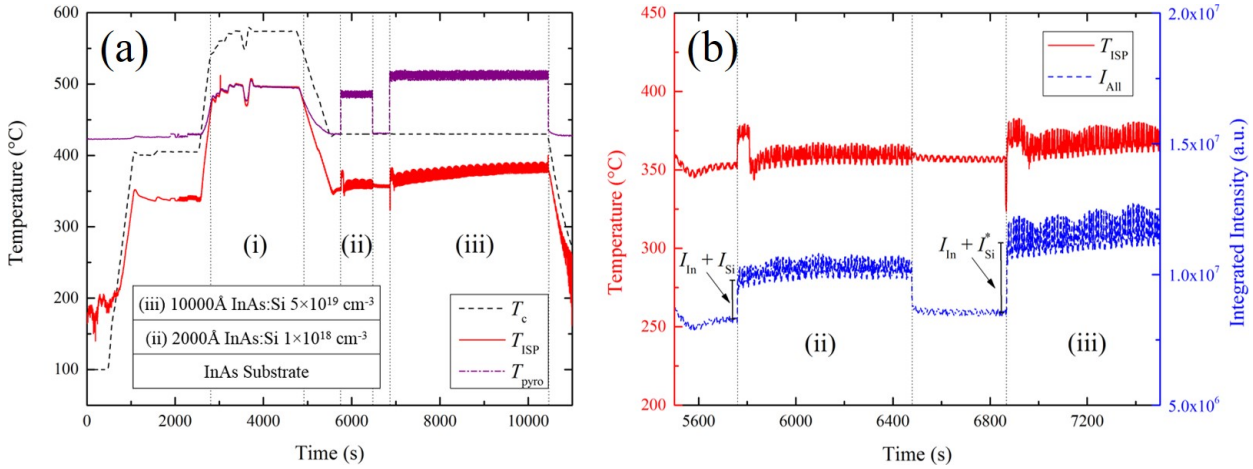

Figure 3.4: (a) T_c (dash black), T_{ISP} (solid red) and T_{pyro} (dash-dot purple) of an InAs:Si growth on InAs(001) substrate. The growth involved 3 stages: (i) oxide desorption, (ii) 2000Å InAs:Si with doping concentration of 1×10^{18} cm^{-3} and (iii) 10000Å InAs:Si doping concentration of 5×10^{19} cm^{-3}. The inset shows the schematic of the growth; (b) a zoom-in display of T_{ISP} (solid red) and I_{all} (dash blue) from $t = 5500$ s to $t = 7500$ s.

and viewport heaters which were pre-measured earlier. The fluctuation of the I_{all} and T_{ISP} readings at stage (ii) and (iii) were possibly originated from substrate rotation which wobbled the amount of scattered radiation from In and Si cell to arrive at the spectrometer. On the other hand, the continuous increase of T_{ISP} during stage (iii) would probably be attributed to induced radiative heating effect from the hot Si cell. Nonetheless, they did not affect the ISP temperature monitoring significantly.

3.3 ISP vs Blackbody Fitting

Blackbody temperature measurement was proposed and commercialized back in 2008 [110]. By fitting the radiation spectrum acquired by the NIR spectrometer with a blackbody function, such a method has the capability of measuring substrate temperature as low as 225°C, which provides another possibility of temperature monitoring of narrow bandgap materials at LT regime. However, as mentioned in previous sections, the problem of the background radiation can be particularly severe for these materials, which makes such a method not very reliable. To further demonstrate the issue in blackbody temperature measurement, it is reasonable to estimate the actual radiation from the substrate and a heated effusion cell used for growth. Suppose they have temperatures of 350 and 1000°C

respectively and are given by the same blackbody form of

$$I_{\text{sub}}(\lambda, T_{\text{sub}} = 350^{\circ}\text{C}) = \frac{\mathcal{B}_{\text{sub}}}{\lambda^5} \frac{1}{e^{\frac{hc}{\lambda k_B T_{\text{sub}}}} - 1} \tag{3.3}$$

$$I_{\text{cell}}(\lambda, T_{\text{cell}} = 1000^{\circ}\text{C}) = \frac{\mathcal{B}_{\text{cell}}}{\lambda^5} \frac{1}{e^{\frac{hc}{\lambda k_B T_{\text{cell}}}} - 1} \tag{3.4}$$

where $\mathcal{B}_{\text{sub}}$ and $\mathcal{B}_{\text{cell}}$ are coefficients dependent on the geometry of the substrate and the cell respectively. Their integrated intensities are given by

$$I_{\text{sub,ISP}}(T_{\text{sub}} = 350^{\circ}\text{C}) = \int_{\lambda=904\text{nm}}^{\lambda=1684\text{nm}} I_{\text{sub}}(\lambda, T_{\text{sub}} = 350^{\circ}\text{C}) d\lambda \tag{3.5}$$

$$I_{\text{cell,ISP}}(T_{\text{cell}} = 1000^{\circ}\text{C}) = \int_{\lambda=904\text{nm}}^{\lambda=1684\text{nm}} I_{\text{cell}}(\lambda, T_{\text{cell}} = 1000^{\circ}\text{C}) d\lambda \tag{3.6}$$

The problem is how to make a reasonable guess for coefficients $\mathcal{B}_{\text{sub}}$ and $\mathcal{B}_{\text{cell}}$ that resembles a real growth scenario. Refer to the InAs:Si growth in the last section, the In cell was kept at 807°C, while the Si cell was at 1139.4°C in stage (ii) and 1287.3°C in stage (iii). Now suppose $\mathcal{B}_{\text{sub}} = 7 \times 10^{-19}$ a.u., $\mathcal{B}_{\text{cell}} = 4 \times 10^{-21}$ a.u. and only 1% of the effusion cell radiation arrives at the spectrometer, we will obtain

$$I_{\text{sub,ISP}}(T_{\text{sub}} = 350^{\circ}\text{C}) = 8.6 \times 10^{6}\text{a.u.} \tag{3.7}$$

$$I_{\text{sub,ISP}}(T_{\text{sub}} = 350^{\circ}\text{C}) + I_{\text{cell,ISP}}(T_{\text{cell}} = 1000^{\circ}\text{C}) = 1.0 \times 10^{7}\text{a.u.} \tag{3.8}$$

which are similar to the ISP values in Fig. 3.4 for the 1st InAs:Si epilayer, despite only one cell is considered in the modeling while there were more than one cell used in the growth. Fig. 3.5 shows $I_{\text{sub}}(\lambda, T_{\text{sub}} = 350^{\circ}\text{C})$ and $I_{\text{cell}}(\lambda, T_{\text{cell}} = 1000^{\circ}\text{C})$ at wavelength range of 0–20000 nm, with the inset at the NIR range of ∼900–1700 nm. It is clear that even with the huge coefficient difference and only a very small portion of it scattered into the spectrometer, the radiation from the cell is still much larger than that from the substrate, which will affect its reading significantly. To conclude, since it does not distinguish the radiation emitted from the substrate and the cell, the blackbody fitting method has very limited precision especially when hot effusion cell is used. In contrast, ISP can solve this problem by compensating the extra radiation as described in the previous section.

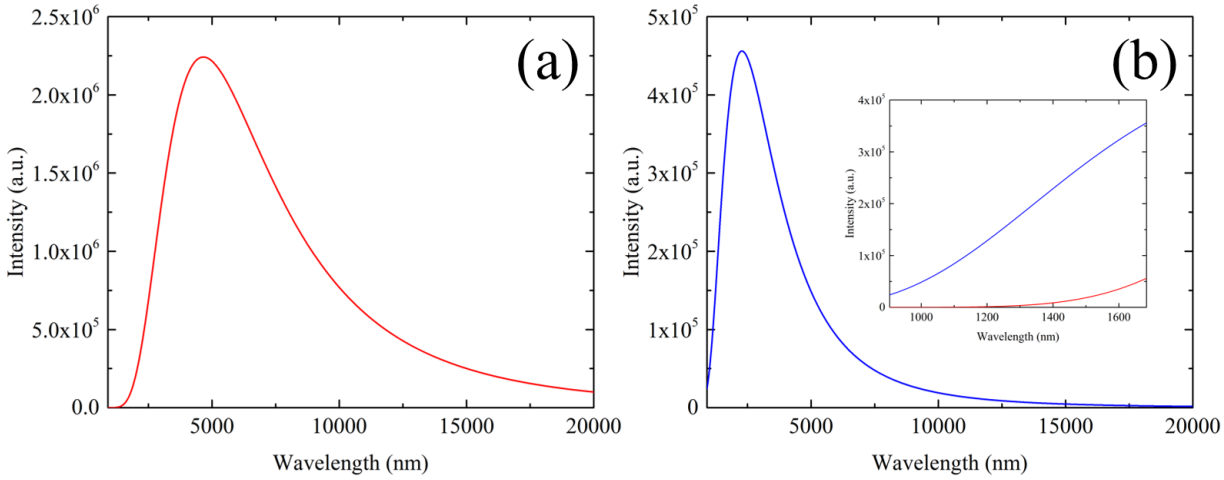

Figure 3.5: Illustrative blackbody radiation curves of the (a) substrate at 350°C and (b) effusion cell at 1000°C. The inset in (b) shows the zoom-in of the curves at the NIR spectrometer range.

3.4 Narrow Bandgap Metamorphic Buffer Growth

For this growth, a full 3" SI GaAs substrate was used. Fig. 3.6 shows a schematic illustrating the four stages of the growth. In stage (i), the native oxide was desorbed for 500 s at a substrate temperature of 630°C . Stage (ii) involved the growth of a GaAs smoothing layer and an AlSb nucleation buffer, whereby the substrate temperature was ramped from 580°C to 620°C while growing GaAs and followed by two steps down to 500°C for AlSb growth and 475°C for thin GaSb layer growth. Stage (iii) was the growth of a thick narrow bandgap metamorphic buffer consisting of the AlInSb layer sequence. At the beginning of this stage, T_c was lowered to 470°C and T_{BET} was measured to be 420°C. T_c was kept the same till the end of this deposition process. The active region was deposited in stage (iv), which consisted of Te δ-doping layers, an $Al_{0.12}In_{0.88}Sb$-InSb quantum well and finally an InSb cap. T_c was further ramped down to 380°C and held at that temperature until the end of the growth. Refer to Fig. 3.7, at stage (i) and (ii), the growth temperature was accurately measured by BET, while part of the ISP signal was originated from the substrate heater radiation transmitting through the GaAs wafer, which made T_{ISP} higher than the actual substrate temperature. When it came to stage (iii), as the metamorphic buffer became thicker, the substrate turned opaque in the NIR range and the GaAs band edge disappeared at $t \approx 13000$ s. Once T_{BET} lost its trace, the only measurement tool left was ISP. In normal circumstances, unless the pyrometer was properly calibrated with the emissivity of the epitaxial material, one could only monitor the growth by estimating the

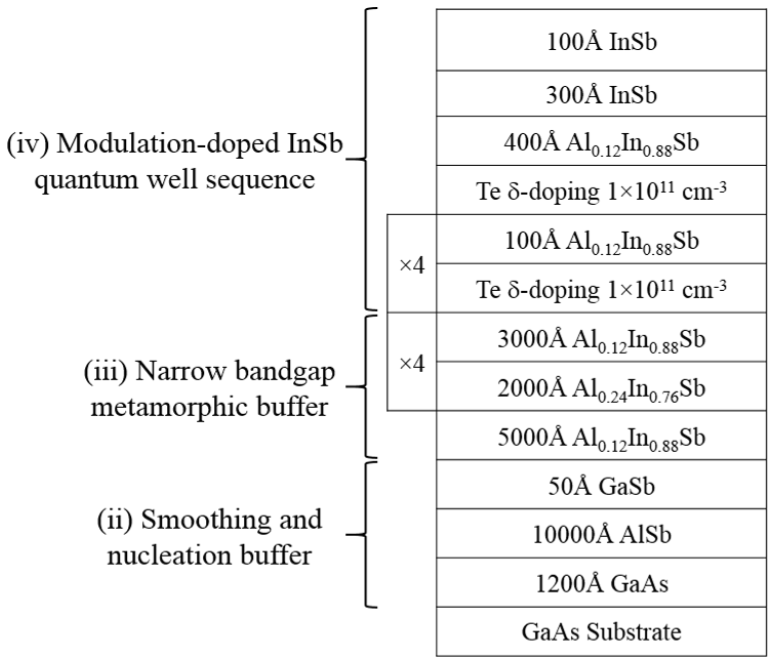

Figure 3.6: Schematic of the narrow bandgap metamorphic buffer structure. The growth involved four stages: (i) oxide desorption (not shown above), (ii) smoothing and nucleation buffer, (iii) narrow bandgap metamorphic buffer, and (iv) modulation-doped InSb quantum well sequence.

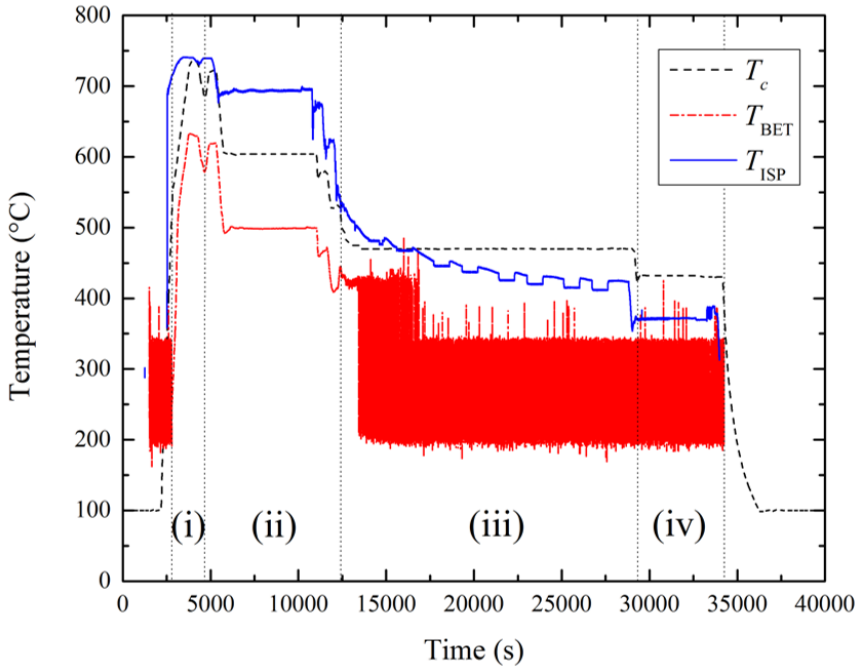

Figure 3.7: Thermocouple temperature T_c (dash black), substrate temperatures measured by BET (T_{BET}, dash-dot red) and ISP (T_{ISP}, solid blue) acquired during the metamorphic multilayer growth. The growth involved 4 stages: (i) oxide desorption, (ii) smoothing and nucleation buffer, (iii) narrow bandgap metamorphic buffer and (iv) modulation-doped InSb quantum well sequence.

temperature difference between the thermocouple and the substrate. Our ISP calibration was done for InAs wafer which in principle should not be used for monitoring this growth. However, although its reading was around 500°C at $t \approx 13000$ s which was supposed to be incorrect, T_{ISP} gradually dropped and eventually reached 420°C at $t \approx 23000$ s, which was the same as the last readable BET signal. Since we were keeping the substrate heater temperature T_c constant during this period, which showed the T_{ISP} reading here was reliable. For the $Al_{0.12}In_{0.88}Sb$ and InSb layers at $t > 29000$ s, T_{ISP} showed readings of 370–390°C which was close to the target growth temperature of 380°C. In fact, such result was within our expectation and it could be explained by the fact that the GaAs substrate, the binary (InSb) and ternary ($Al_{0.12}In_{0.88}Sb$) materials used in this growth shared an emissivity of ∼0.58–0.67 [111], which is similar to that InAs. This indicates that our ISP technique, even initially calibrated for InAs wafers, can still get reasonable temperature value for other materials with similar emissivities. For instance, if the pyrometer shows $T_{\text{ISP}} = 400$°C for

InAs, it would show $T_{\mathrm{ISP}} = 394.7°\mathrm{C}$ to $T_{\mathrm{ISP}} = 402.5°\mathrm{C}$ for other wafers with emissivity difference of $\pm 5\%$ from that of InAs even with the same calibration coefficients, which are only tiny changes. While a full ISP calibration for each individual wafer material is beyond the scope of this work, one can adjust the calibration coefficient by multiplying the ratio of the emissivity of the material grown to that of the material calibrated, which would still reasonably improve the reliably of the temperature measurement.

Chapter 4

LT GaAs Based PCAs

4.1 MBE Growth, Annealing and Characterizations

Several batches of LT GaAs samples were grown on GaAs(001) substrates with As_4 using the Veeco GEN10 MBE system. Except for earlier samples G0238 and G0239 which were grown on quarter-3-inch (Q3") wafers, the rest were grown on full 3" wafers. Those samples are structurally identical, as shown in Table 4.1, where after oxide desorption at 630°C, a GaAs buffer layer of 1000Å was grown with increasing temperature from 580 to 620°C and stabilized at 620°C for another 1000Å, followed by a 3000Å AlAs layer and 100Å GaAs cap layer, both at 590°C. Afterwards, the wafer temperature was ramped down for the 15,000Å LT GaAs deposition at 230–280°C which varied among samples. The growth morphology was monitored by RHEED, while the substrate temperature was monitored by the BET spectrometer and the SVT pyrometer. The wafer was illuminated by a pair of LEDs at 470 and 950 nm respectively and the reflected light beams were collected by the SVT camera as a function of time. The AlAs was deposited for two purposes. With its refractive index different from that of GaAs, the reflected 470 and 950 nm beams exhibited a sinusoidal-like pattern vs time due to interference. By fitting such oscillation curves using the virtual substrate model described in Chapter 2, the SVT camera can be used to monitor the growth rate of LT GaAs layer which was deposited later. In addition, during the THz TDS testing of the processed LT GaAs wafers with PCAs, the AlAs layer also served as a reflective mirror for the 780 nm incident laser, which resulted in more carrier photo-excitation and thus a stronger THz signal. All LT GaAs samples were grown with As Op of ∼3–4 with the exception of G0266–G0269, in which the As valve opening was purposely adjusted at different values to study its effect on the amount of excess As

Name	Material	Thickness (Å)
Substrate	SI GaAs(001)	
1st Buffer Layer	GaAs	1000
2nd Buffer Layer	GaAs	1000
Reflectance Layer	AlAs	3000
Cap Layer	GaAs	100
Low Temperature Layer	LT GaAs	15000

Table 4.1: Growth schematic for all LT GaAs samples: G0238, G0239, G0266, G0267, G0268, G0269, G0286, G0287, G0288, G0289, G0323, G0324, G0326, G0327, G0503 and G0504.

embedded into the LT GaAs epilayer. All as-grown samples were *ex situ* characterized by Nomarski microscopy, black-box imaging and HRXRD. Afterwards, most of those wafers were cleaved into four Q3" pieces with each piece either reloaded into the Veeco GEN10 MBE system for *in situ* annealing in the GM or *ex situ* annealing by using a rapid thermal annealer (RTA) with N_2 supplied. Each cleaved wafer was labelled with a letter, either "A", "B", "C" or "D" which represents *in situ* annealing, or "E", "F", "G" or "H" which represents *ex situ* annealing. All pieces were ramped up and stabilized at their target temperatures for 10 minutes of annealing. Unlike MBE GM, since the RTA device does not have As gas supply, the wafers annealed at higher temperatures of 600 and 610°C had the risk of As desorption. A compensative measure was applied by contacting the LT GaAs surface with a piece of GaAs control wafer that was back-coated with SiO_2, while the ungrown back surface of the sample was covered by a piece of a Si wafer. The growth and annealing conditions are summarized in Tables 4.2 and 4.3.

Representative *in situ* growth parameters during LT GaAs deposition of the LT GaAs wafers, including the 470 and 950 nm SVT reflectance, BFM reading, T_c and T_{BET} are shown in Figs. 4.1 and 4.2. At LT, radiative heating of the substrate from the effusion cells becomes increasingly significant [112, 113, 114], hence T_c had to be continuously adjusted to keep T_{BET} constant. The constant 470 nm reflectance after damping indicated high epitaxial quality for all wafers, with an exception that it dropped a little bit by the end of deposition of G0327, which was grown at 230°C, the lowest growth temperature among all samples. This was consistent with the observation in RHEED. Fig. 4.3 shows the RHEED images of G0288, G0287, G0323, G0324, G0326 and G0327 at the end of LT GaAs deposition, which were grown from 280 to 230°C with decreasing step of 10°C. In fact, in this scenario RHEED is an even better indicator of epitaxial quality than the 470 nm reflectance. For G0288 which was grown at 280°C as shown in Fig. 4.3(a), the RHEED pattern was still streaky which indicated high single-crystalline epitaxial quality; as the

Growth No.	T_g (°C)	T_a (°C)	Anneal Method
G0238	270	600	*in situ* (MBE)
G0239	280	550	*in situ* (MBE)
G0266	270	N/A	N/A
G0267	270	N/A	N/A
G0268	270	N/A	N/A
G0269E	270	375	*ex situ* (RTA)
G0269F	270	450	*ex situ* (RTA)
G0269G	270	525	*ex situ* (RTA)
G0269H	270	600	*ex situ* (RTA)
G0286A	270	450	*in situ* (MBE)
G0286B	270	460	*in situ* (MBE)
G0286C	270	600	*in situ* (MBE)
G0286D	270	610	*in situ* (MBE)
G0287E	270	450	*ex situ* (RTA)
G0287F	270	460	*ex situ* (RTA)
G0287G	270	600	*ex situ* (RTA)
G0287H	270	610	*ex situ* (RTA)
G0288A	280	450	*in situ* (MBE)
G0288B	280	460	*in situ* (MBE)
G0288C	280	600	*in situ* (MBE)
G0288D	280	610	*in situ* (MBE)
G0289E	280	450	*ex situ* (RTA)
G0289F	280	460	*ex situ* (RTA)
G0289G	280	600	*ex situ* (RTA)
G0289H	280	610	*ex situ* (RTA)

Table 4.2: Growth and anneal summary of G0238, G0239, G0266, G0267, G0268, G0269, G0286, G0287, G0288 and G0289, which shows the growth no., growth temperature (T_g) of the 15000Å LT GaAs layer, annealing temperature (T_a) and annealing method.

Growth No.	T_g (°C)	T_a (°C)	Anneal Method
G0323E	260	450	*ex situ* (RTA)
G0323F	260	460	*ex situ* (RTA)
G0323G	260	600	*ex situ* (RTA)
G0323H	260	610	*ex situ* (RTA)
G0324E	250	450	*ex situ* (RTA)
G0324F	250	460	*ex situ* (RTA)
G0324G	250	600	*ex situ* (RTA)
G0324H	250	610	*ex situ* (RTA)
G0326E	240	450	*ex situ* (RTA)
G0326F	240	460	*ex situ* (RTA)
G0326G	240	600	*ex situ* (RTA)
G0326H	240	610	*ex situ* (RTA)
G0327E	230	450	*ex situ* (RTA)
G0327F	230	460	*ex situ* (RTA)
G0327G	230	600	*ex situ* (RTA)
G0327H	230	610	*ex situ* (RTA)
G0503F	270	460	*ex situ* (RTA)
G0503G	270	600	*ex situ* (RTA)
G0504F	240	460	*ex situ* (RTA)
G0504G	240	600	*ex situ* (RTA)

Table 4.3: Growth and anneal summary of G0323, G0324, G0326, G0327, G0503 and G0504, which shows the growth no., growth temperature (T_g) of the 15000Å LT GaAs layer, annealing temperature (T_a) and annealing method.

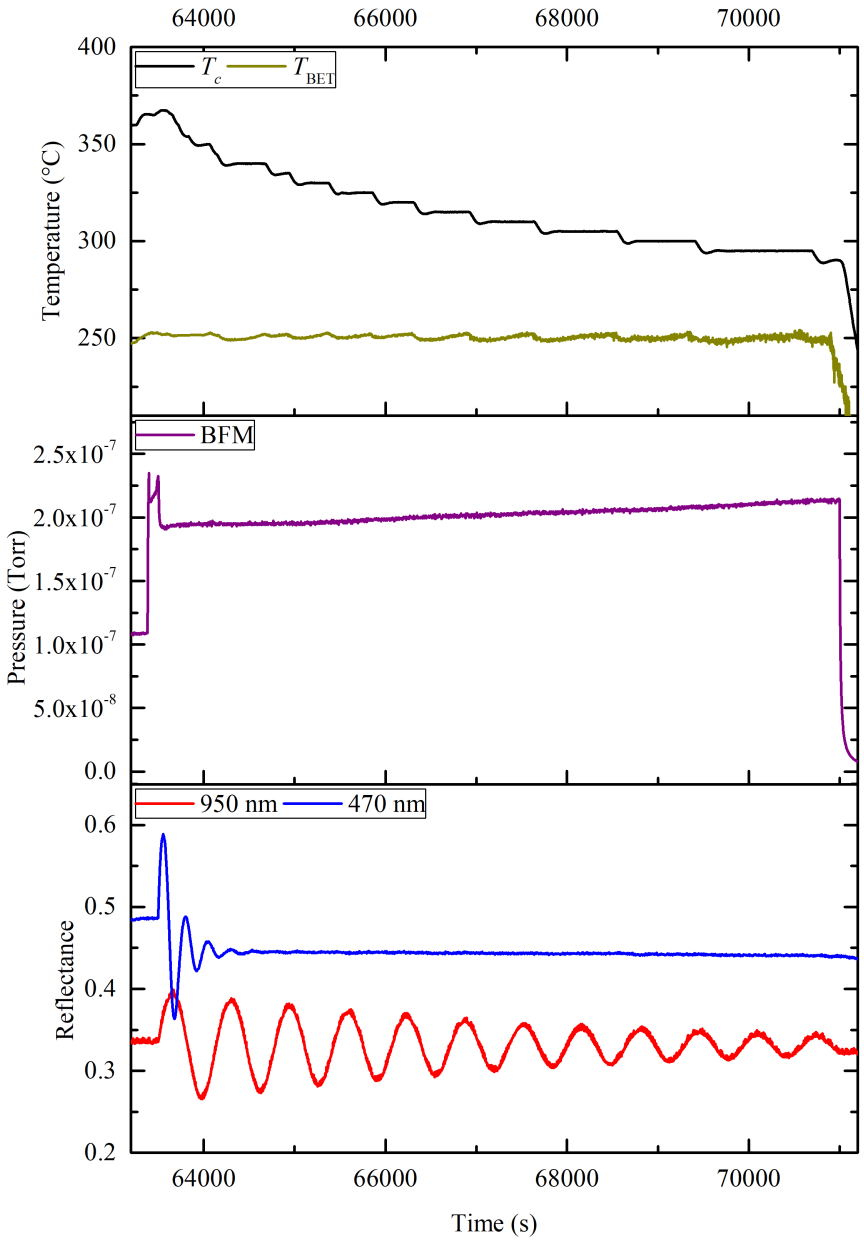

Figure 4.1: *In situ* growth parameters during LT GaAs deposition of G0324. From top to bottom: T_c (black) and T_{BET} (dark yellow); BFM (purple) pressure; 950 nm (red) and 470 nm (blue) reflectance.

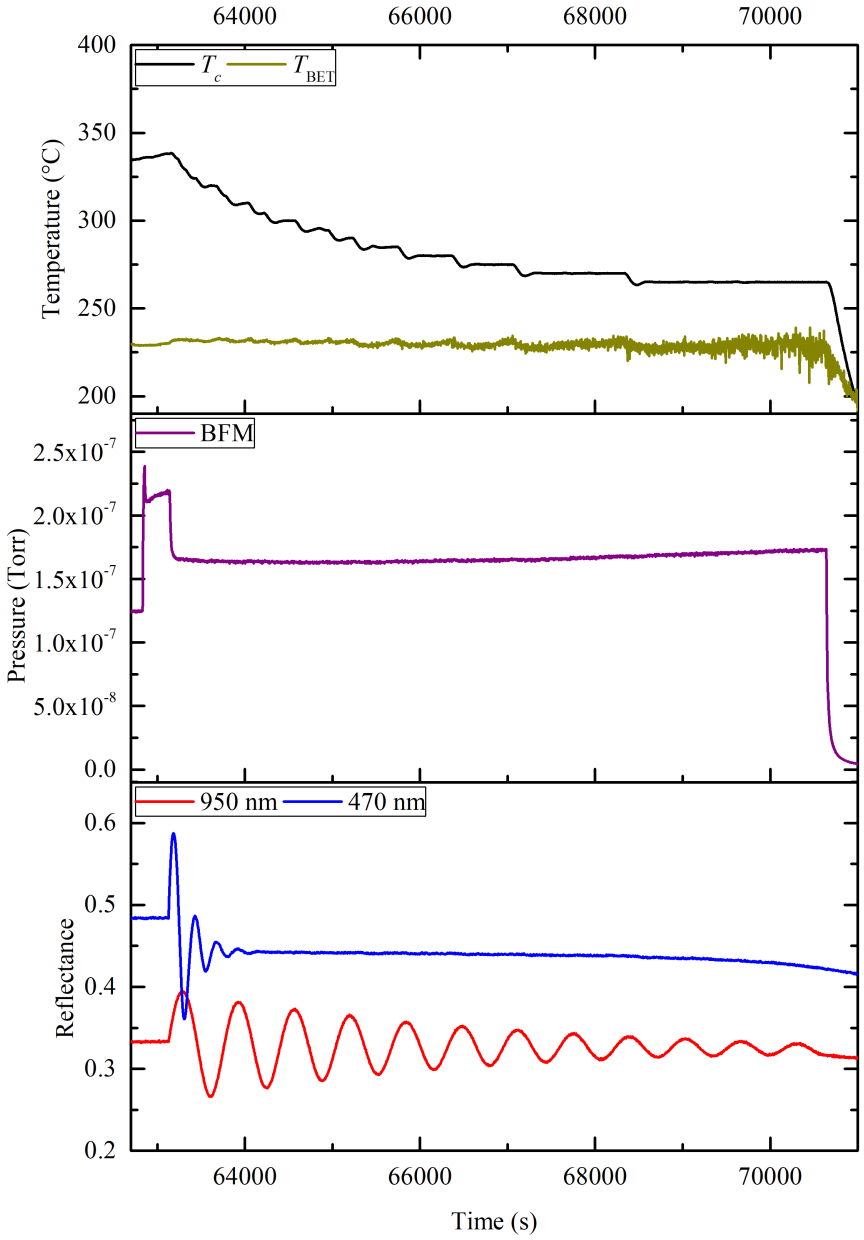

Figure 4.2: *In situ* growth parameters during LT GaAs deposition of G0327. From top to bottom: T_c (black) and T_{BET} (dark yellow); BFM (purple) pressure; 950 nm (red) and 470 nm (blue) reflectance.

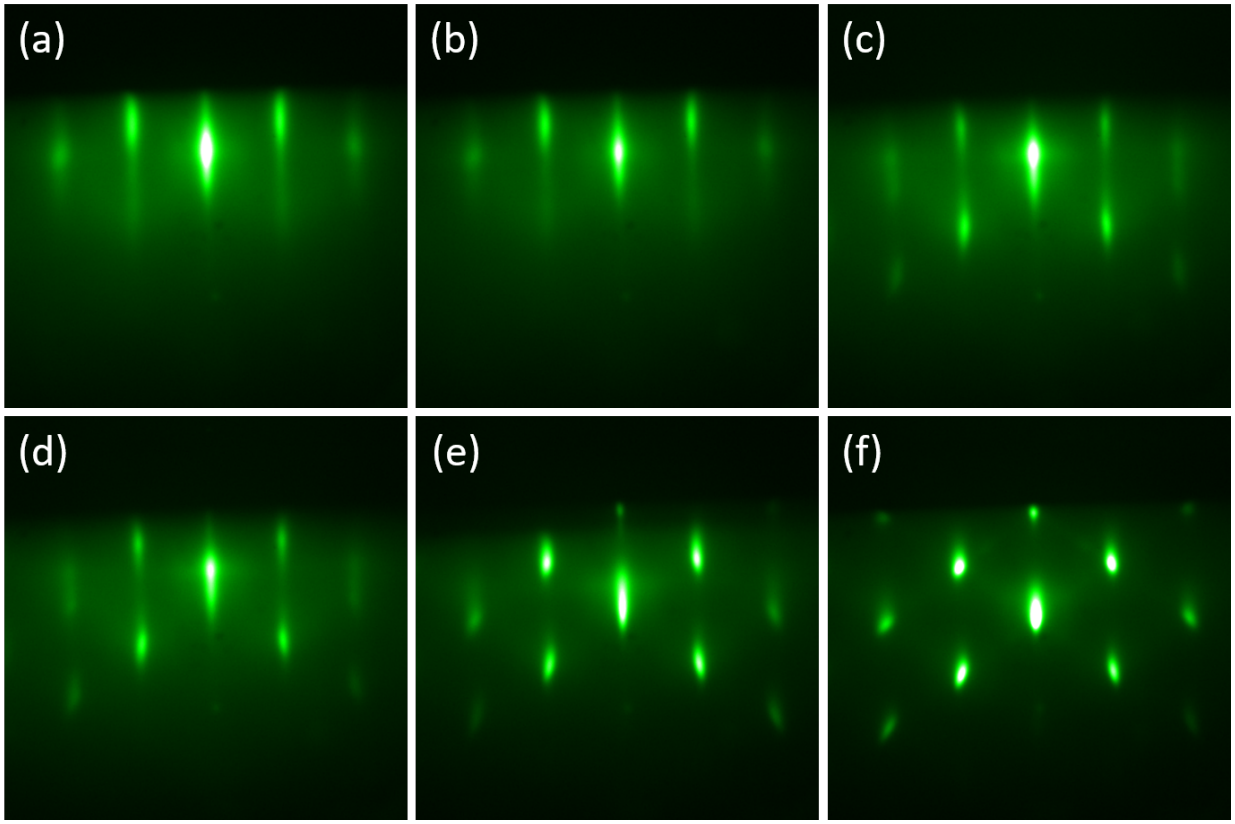

Figure 4.3: Representative RHEED images at the end of LT GaAs deposition of (a) G0288, (b) G0287, (c) G0323, (d) G0324, (e) G0326 and (f) G0327.

growth temperature decreased, the RHEED pattern got less and less streaky; for G0327 which was grown at 230°C, the RHEED pattern became entirely spotty as shown in Fig. 4.3(f), which indicated that the epilayer was considerably roughened at the end of the LT GaAs deposition.

The representative 5× and 40× magnified Nomarski images of G0324, G0326 and G0327, with the as-grown sample before cleaving and the cleaved, annealed pieces, are shown in Figs. 4.4–4.6. For each image, one to a few point defects, with the shiny white colour due to reflection from the illumination of the microscope lamp, were used to assist adjustment of the focusing on the wafer surface. Before annealing, all samples exhibited smooth surface morphology which indicated decent single-crystalline epitaxial quality. The morphologies of most annealed samples remain the same high quality except G0327G where barely noticeable, densely and regularly distributed tiny bumps in the size of $\sim 1\mu$m are

seen (see Fig. 4.5(b)). This is probably due to the lowest growth temperature of 230°C and high annealing temperature of 600°C of the sample. The low growth temperature resulted in a large amount of excess As incorporated inside the LT GaAs epilayer, while annealing at high temperature resulted in significant precipitation of excess As, which possibly caused slight distortion of the epitaxial quality. Among this batch of samples, G0324, G0326 and G0327 also show some sites with lattice relaxation, indicated by the straight lines on the wafer surface in Fig. 4.6. This can be attributed to the lattice mismatch between the highly non-stoichiometric LT GaAs and the GaAs substrate of these three growths, while G0323 was grown at a relatively higher temperature, had smaller lattice mismatch issue and did not encounter such a problem. Such relaxation only exist in part but not the entire wafer; most of each wafer was still grown lattice-matched. The representative black-box images of G0503 are shown in Fig. 4.7. The shadow line is just a reflection from the black-box ceiling. Although there were apparently many point defects on the surface, the morphology under Nomarski microscope was as smooth as most of the other samples.

HRXRD TA coupled scans were done on all LT GaAs samples. Fig. 4.8(a) presents the HRXRD scan of G0266–G0269, grown at different As valve openings: 145, 102, 180 and 210 mil, which corresponds to As Op of 2.9, 1.8, 3.4 and 4.5 respectively with the LT GaAs peak positions summarized in Table 4.4. The result reveals that the LT GaAs peak shifts less as P_{min} gets larger and unlikely to have a further shift for $P_{\text{min}} > 4$, which means the amount of excess As embedded had already saturated with this growth temperature. Fig. 4.8(b) shows the LT GaAs peak moving towards the substrate peak with increasing annealing temperature at 75°C intervals. The LT GaAs peak merges with the substrate peak at 600°C, which indicates full relaxation. The result here is consistent with numerous reports in the past which confirms the amount of As pressure affects the structural properties of LT GaAs [102, 115, 116, 117, 118]. For example, Yano *et al*. grew several GaAs samples at 250°C with the As shutter repeatedly opened for 1 s and closed for 0, 0.5, 1 and 1.5 s respectively during the MBE growth [102, 118], hence the effective As Op increased as the duration of closed shutter decreased. HRXRD and pump-probe measurement results indicated that the more As that was embedded, the larger the GaAs lattice constant and the shorter the carrier lifetime that were obtained.

The HRXRD scans of G0286–G0289, G0323, G0324, G0326 and G0327, and the 32 pieces of annealed Q3" LT GaAs samples cleaved from these 8 samples are shown in Figs. 4.9 and 4.10. The LT GaAs peak positions are summarized in Tables 4.5 and 4.6. There is a significant shift of the LT GaAs peak position in HRXRD for the as-grown wafers by changing the growth temperature by 10°C, which indicates growth temperature is a more dominant factor than As Op for the amount of excess As embedded. The pieces with lower annealing temperatures at 450–460°C still have LT GaAs peaks distinguishable from

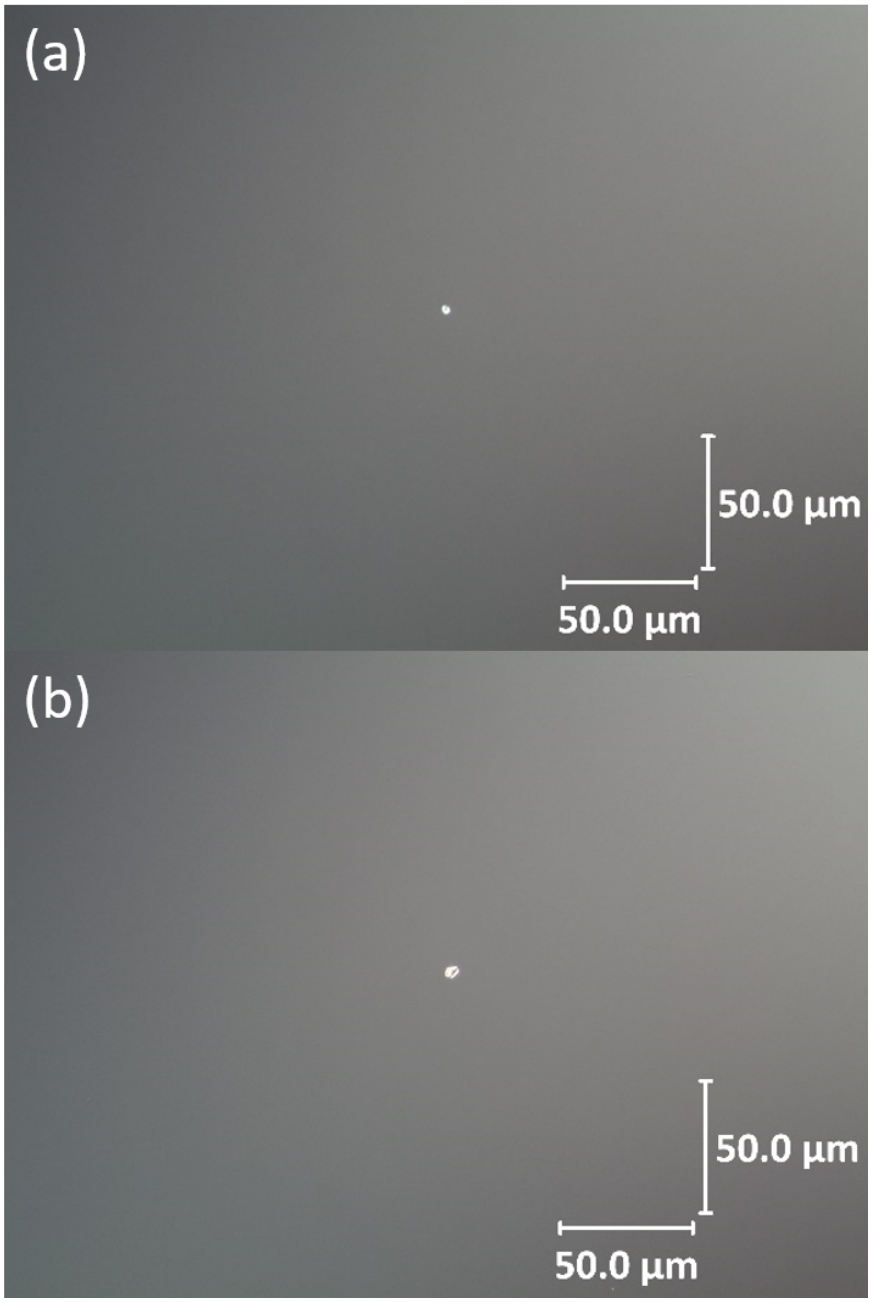

Figure 4.4: Nomarski images at 40× magnification of sample G0326, with conditions (a) as-grown and (b) G0326F, annealed at 460°C.

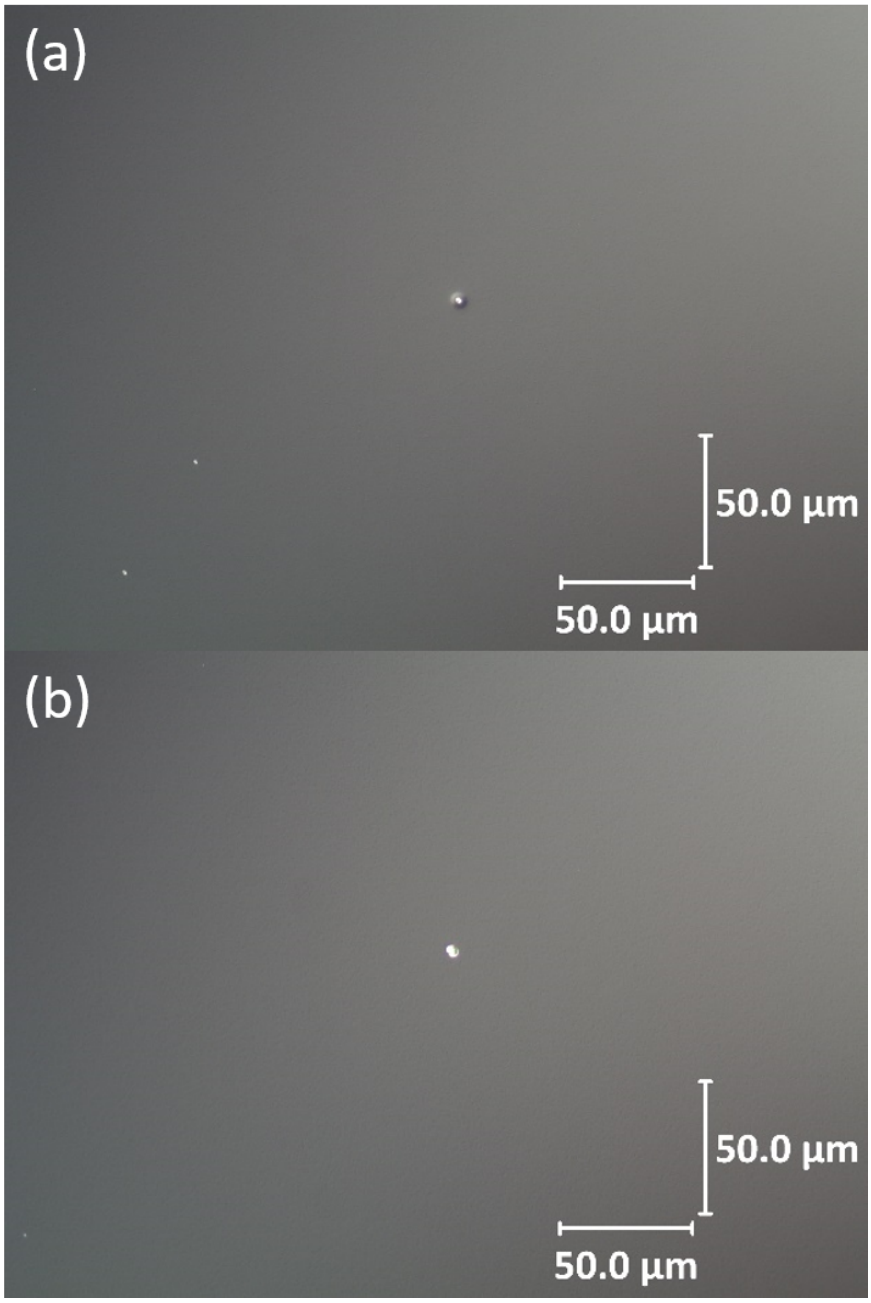

Figure 4.5: Nomarski images at 40× magnification of sample G0327, with conditions (a) as-grown and (b) G0327G, annealed at 600°C.

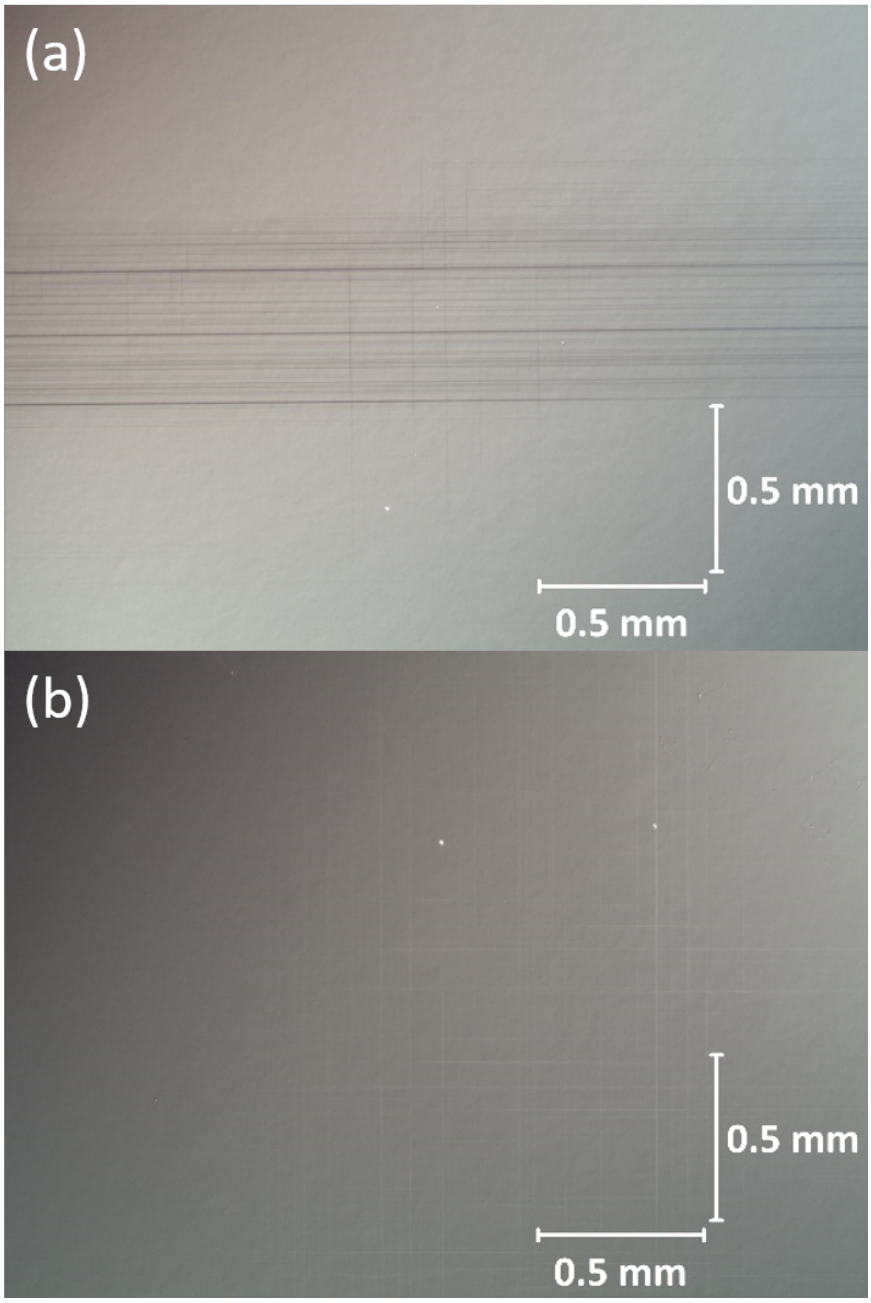

Figure 4.6: Nomarski images of some relaxation sites at 5× magnification of (a) G0324, as-grown and (b) G0326E, annealed at 450°C.

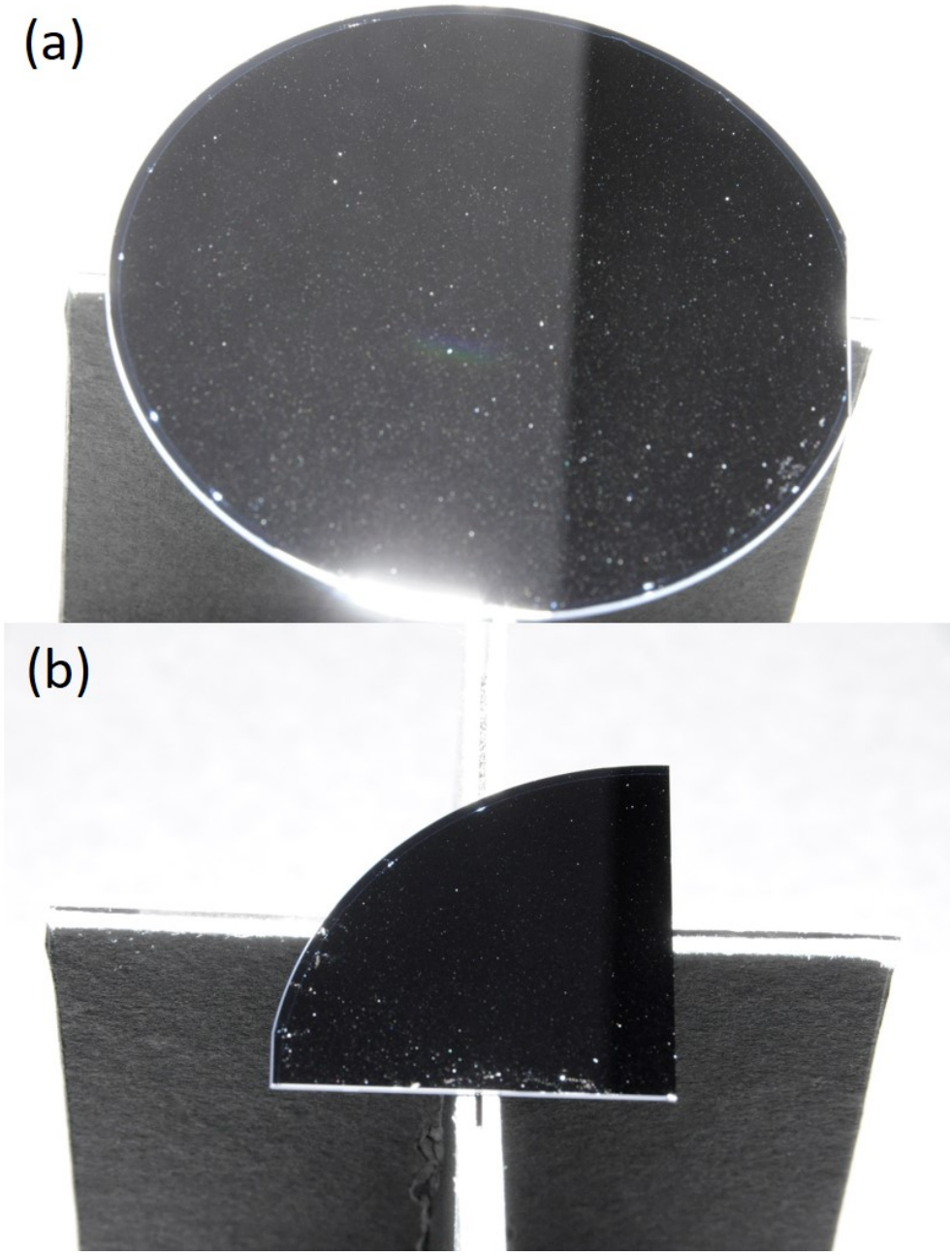

Figure 4.7: Black-box images with an exposure time of 5 ms of sample G0503, with conditions (a) as-grown and (b) G0503F, annealed at 460°C.

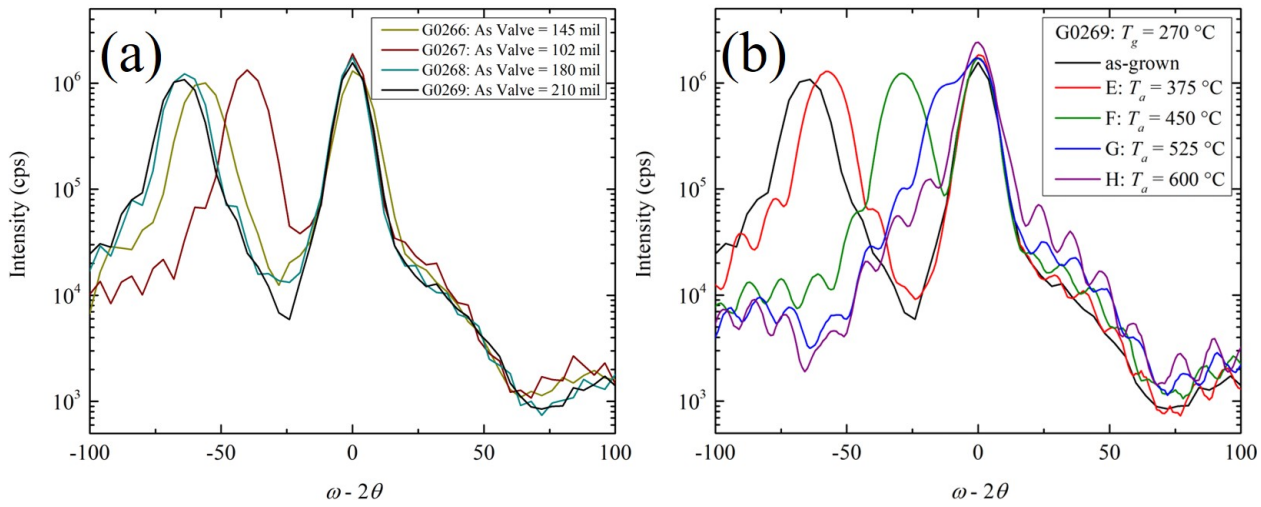

Figure 4.8: HRXRD TA coupled scans of (a) as-grown G0266 (dark yellow), G0267 (brown), G0268 (cyan) and G0269 (black) grown at the same temperature but different As valve openings; (b) as-grown G0269 (black) and annealed G0269E (red), G0269F (dark green), G0269G (blue) and G0269H (purple) at different annealing temperatures.

the GaAs(001) substrate peak, which indicates partial relaxation of the LT GaAs lattice; while for higher annealing temperature at 600–610°C, the LT GaAs peak merges with the substrate peak, which indicates full relaxation via As precipitation [11, 12]. The results in Table 4.5 concludes that there is no observable difference between the LT GaAs position by *in situ* annealing inside the MBE GM with As soak and *ex situ* annealing in RTA with N_2. For cost-saving and convenience, RTA was used for most LT GaAs wafers presented in this chapter.

4.2 Growth Rate from SVT Reflectance Fitting

Thickness determination by Pendellösung fringe fitting in HRXRD is very precise for epilayer thickness up to a few thousand Å. However, when the epilayer exceeds 1μm, the uncertainty of fitted thickness gets larger and such a method becomes less reliable. For all the structures with LT GaAs epilayer of target thickness of 1.5μm in this chapter, HRXRD was mainly used only for studying the correlation between the LT GaAs peak position and excess As incorporation, but for thickness calculation, SVT reflectance fitting was applied instead, as shown in Fig. 4.11, where both LT GaAs and AlAs are fitted at 950 and 470 nm. For GaAs, 950 nm shows very nice sinusoidal-like reflectance data and fitting pattern,

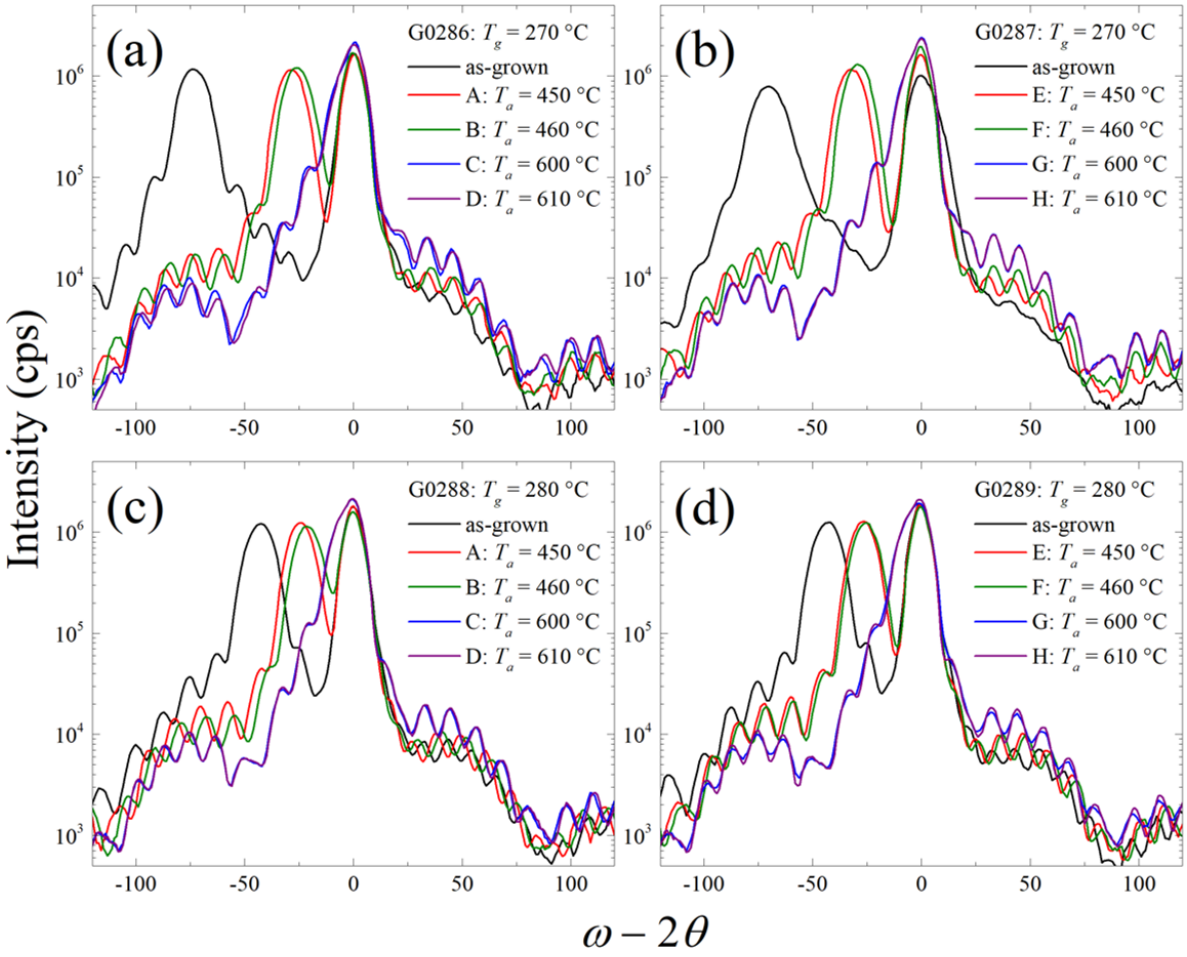

Figure 4.9: HRXRD TA coupled scans of (a) G0286, (b) G0287, (c) G0288 and (d) G0289, as-grown (black) and annealed at 450°C (red), 460°C (dark green), 600°C (blue) and 610°C (purple).

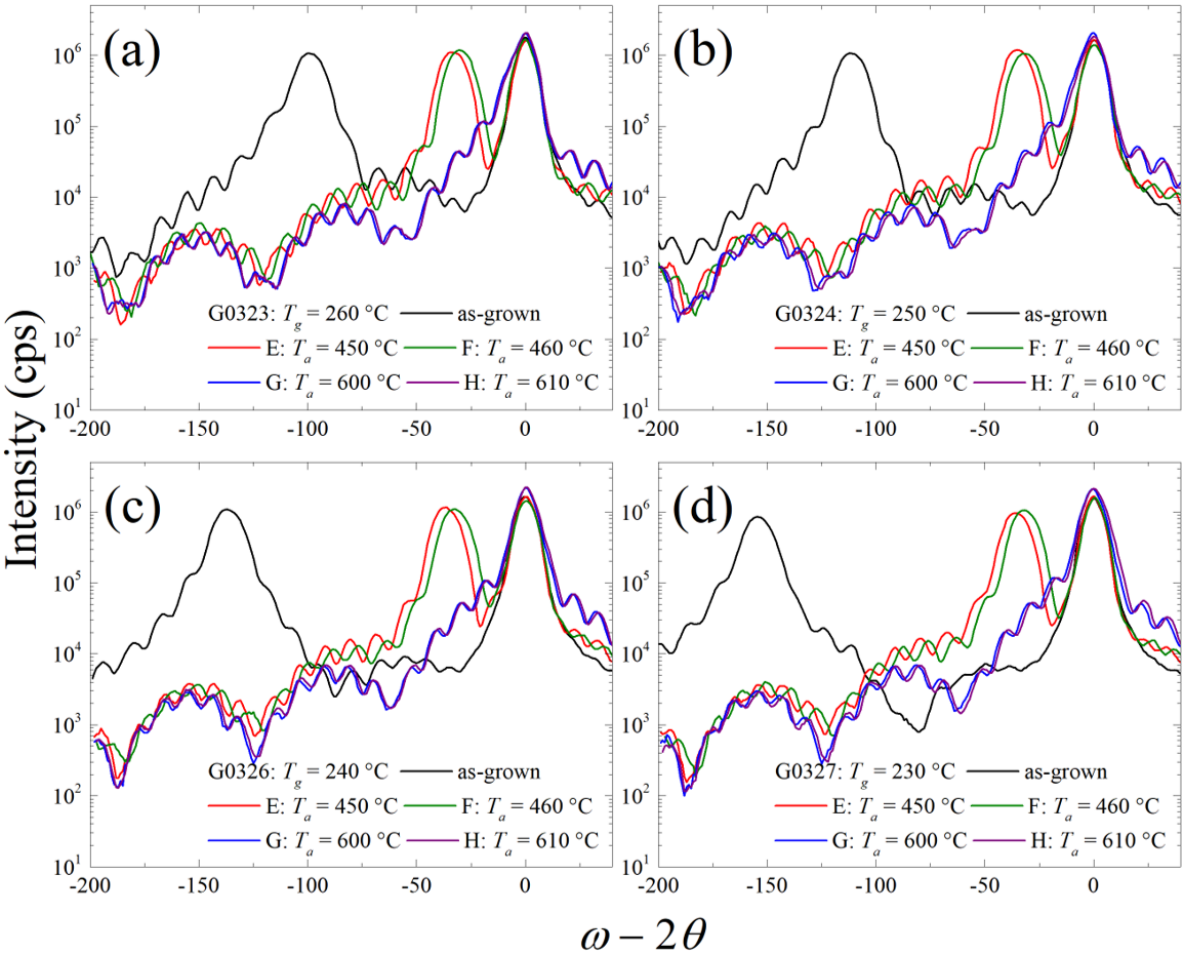

Figure 4.10: HRXRD TA coupled scans of (a) G0323, (b) G0324, (c) G0326 and (d) G0327, as-grown (black) and annealed at 450°C (red), 460°C (dark green), 600°C (blue) and 610°C (purple).

Growth No.	As Valve (mil)	T_g (°C)	T_a (°C)	$\omega_{\text{LT-GaAs}}$ (")
G0266	145	270	as-grown	-58
G0267	102	270	as-grown	-40
G0268	180	270	as-grown	-64
G0269	210	270	as-grown	-66
G0269E	210	270	375, *ex situ*	-58
G0269F	210	270	450, *ex situ*	-29
G0269G	210	270	525, *ex situ*	-12
G0269H	210	270	600, *ex situ*	fully relaxed

Table 4.4: HRXRD summary of as-grown G0266, G0267, G0268 and G0269; annealed G0269E, G0269F, G0269G and G0269H, which shows the growth no., As valve opening, growth temperature (T_g) for the 15000Å LT GaAs layer, annealing temperature (T_a) and LT GaAs peak position ($\omega_{\text{LT-GaAs}}$).

Growth No.	as-grown	$T_a = 450$°C	$T_a = 460$°C	$T_a = 600$°C	$T_a = 610$°C
G0286 ($T_g = 270$°C, *in situ* anneal)	-74	-29	-26	fully relaxed	fully relaxed
G0287 ($T_g = 270$°C, *ex situ* anneal)	-70	-32	-29	fully relaxed	fully relaxed
G0288 ($T_g = 280$°C, *in situ* anneal)	-43	-24	-21	fully relaxed	fully relaxed
G0289 ($T_g = 280$°C, *ex situ* anneal)	-43	-27	-26	fully relaxed	fully relaxed

Table 4.5: Summary of the LT GaAs peak position of G0286, G0287, G0288 and G0289, as-grown and annealed at temperature T_a = 450, 460, 600, 610°C.

Growth No.	as-grown	$T_a = 450$°C	$T_a = 460$°C	$T_a = 600$°C	$T_a = 610$°C
G0323 ($T_g = 260$°C, *ex situ* anneal)	-100	-33	-30	fully relaxed	fully relaxed
G0324 ($T_g = 250$°C, *ex situ* anneal)	-112	-35	-32	fully relaxed	fully relaxed
G0326 ($T_g = 240$°C, *ex situ* anneal)	-137	-37	-33	fully relaxed	fully relaxed
G0327 ($T_g = 230$°C, *ex situ* anneal)	-154	-36	-32	fully relaxed	fully relaxed

Table 4.6: Summary of the LT GaAs peak position of G0323, G0324, G0326 and G0327, as-grown and annealed at temperature T_a = 450, 460, 600, 610°C.

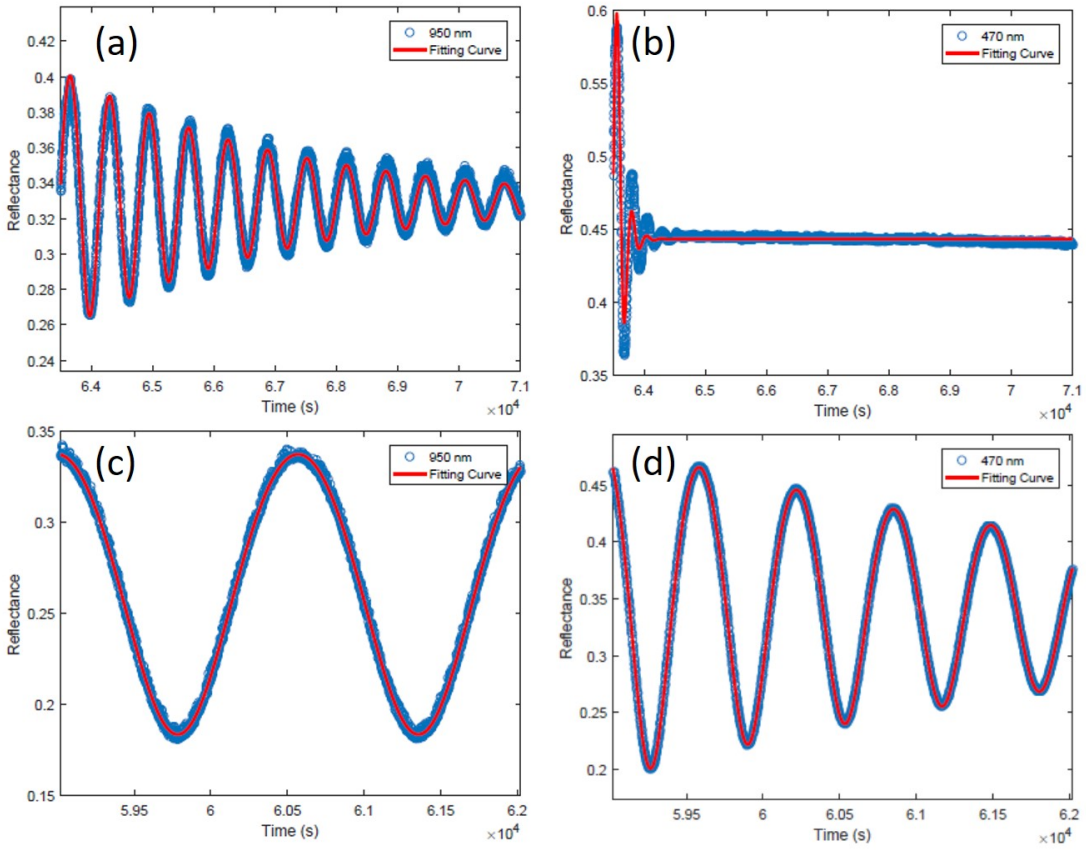

Figure 4.11: SVT reflectance data (blue circle) and fitting curve (red) for G0324 with (a) LT GaAs at 950 nm, (b) LT GaAs at 470 nm, (c) AlAs at 950 nm and (d) AlAs at 470 nm.

while the flat line after damping at 470 nm reveals epitaxial quality but unsuitable for quantitative growth rate fitting purpose. On the other hand, both 950 and 470 nm exhibit excellent fitting, nonetheless, 470 nm is preferred since it counts more periods than 950 nm. The fitted growth rates of GaAs at 950 nm, AlAs at 470 nm as well as their estimated thicknesses of G0238–G0504 are summarized in Table 4.7. All growths exhibit excellent fittings with R-square values of > 0.99. To summarize, the fitted LT GaAs thicknesses of earlier growths G0238–G0289 were a bit off, thinner than the target by up with 6.5%, but the precision improved for later growths G0323–G0504 with errors less than 3.5%. Such precision improvement was probably benefited from the reconfiguration of the Ga cell between those two sequences of growths in which its flux stability was considerably improved.

Growth No.	$G_{\text{LT-GaAs}}$ at 950nm (Å/s)	G_{AlAs} at 470nm (Å/s)	$d'_{\text{LT-GaAs}}$ (Å)	d'_{AlAs} (Å)
G0238	1.90	1.00	14238.60	3013.43
G0239	1.88	1.00	14094.45	3005.66
G0266	1.88	1.01	14075.11	3018.99
G0267	1.87	1.01	14034.56	3016.72
G0268	1.89	1.00	14150.09	2991.70
G0269	1.88	0.99	14137.46	2972.82
G0286	1.88	0.97	14106.49	2906.13
G0287	1.88	0.97	14068.42	2897.46
G0288	1.88	0.96	14125.79	2866.54
G0289	1.89	0.95	14171.56	2862.10
G0323	1.96	0.98	14672.56	2952.84
G0324	1.96	0.99	14722.60	2975.32
G0326	1.98	1.00	14846.51	3002.06
G0327	1.98	0.99	14861.26	2979.58
G0503	1.93	1.00	14460.00	3005.89
G0504	1.97	1.00	14783.45	3012.23

Table 4.7: Summary of the SVT reflectance fitted growth rate of LT GaAs at 950 nm ($G_{\text{LT-GaAs}}$) and AlAs at 470 nm (G_{AlAs}), fitted thickness of LT GaAs ($d'_{\text{LT-GaAs}}$) and AlAs (d'_{AlAs}) for samples G0238, G0239, G0266, G0267, G0268, G0269, G0286, G0287, G0288, G0289, G0323, G0324, G0326, G0327, G0503 and G0504.

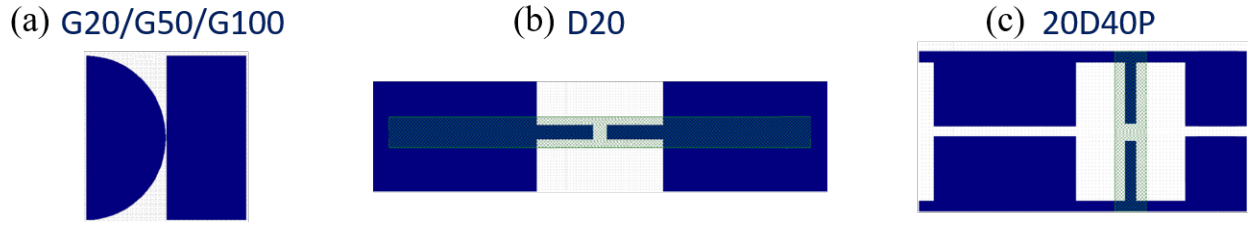

Figure 4.12: Pattern details for THz (a) Tx type G20/G50/G100, (b) Rx type D20 and (c) 20D40P. The blue areas are the target positions for metal deposition and the green area is the target position for the LT GaAs gap. Figure adopted and reprinted with permission from Nanofabrication Group, University of Waterloo and TeTechS Inc.

4.3 Photoconductive Antenna Processing

For the annealed Q3" wafers, three types of PCAs for transmitters (Tx)s, named G20, G50 and G100, and two types of PCAs for receivers (Rx)s, named 20D40P and D20, were applied for processing. The pattern details of antenna type G20/G50/G100, 20D40P and D20 are shown in Fig. 4.12. For Tx, G20, G50 and G100 have a similar pattern: a pair of antennas with one of them in rectangular while another one of semi-circular shape. The only difference between these antennas is their LT GaAs gap width. For Rx, 20D40P comes with a very specific repetitive pattern of equally spaced square cavities, with one of them having a pair of dipoles and LT GaAs gap within, while D20 has a more regular planar dipole geometry. Standard clean-room processing procedures such as metal patterning, photolithography and reactive ion etching (RIE) were applied to fabricate those antennas. The illustrative optical microscopic images of Rx type D20 on G0287H, 20D40P on G0327G and G0289E, and scanning electron microscopic (SEM) image of 20D40P on G0238 are shown in Fig. 4.13. The final device photos of G20 and G50 on G0287G, D20 on G0287F and 20D40P on G0289E are shown in Fig. 4.14.

4.4 THz TDS Measurement

The schematic of the optical setup of the THz TDS measurement of the two batches of LT GaAs based PCAs is shown in Fig. 4.15. A pumping laser of 780 nm wavelength, 100 MHz pulse frequency and 80 fs pulse width was used to excite the LT GaAs based Tx and Rx. The detected photocurrent in Rx was fed into the pre-amplifier with an adjustable gain of 5–500 nA/V, which was then fed into the lock-in amplifier then to the computer.

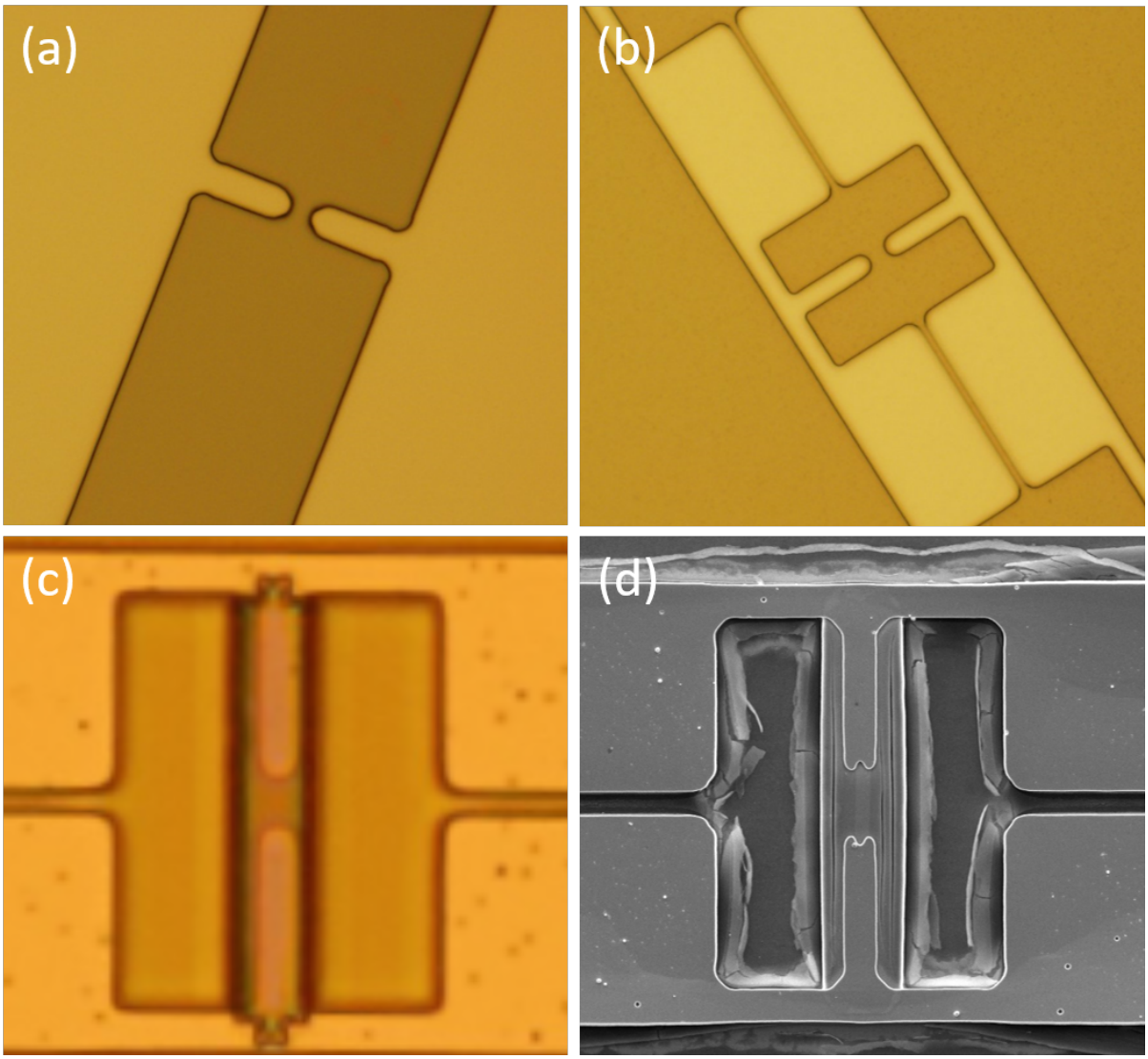

Figure 4.13: Illustrative PCA processing images for THz Rx type D20 and 20D40P, with optical microscopic images of samples (a) D20 on G0287H, (b) 20D40P on G0327G, (c) 20D40P on G0289E and (d) SEM image of 20D40P on G0238. Figure adopted and reprinted with permission from Nanofabrication Group, University of Waterloo and TeTechS Inc.

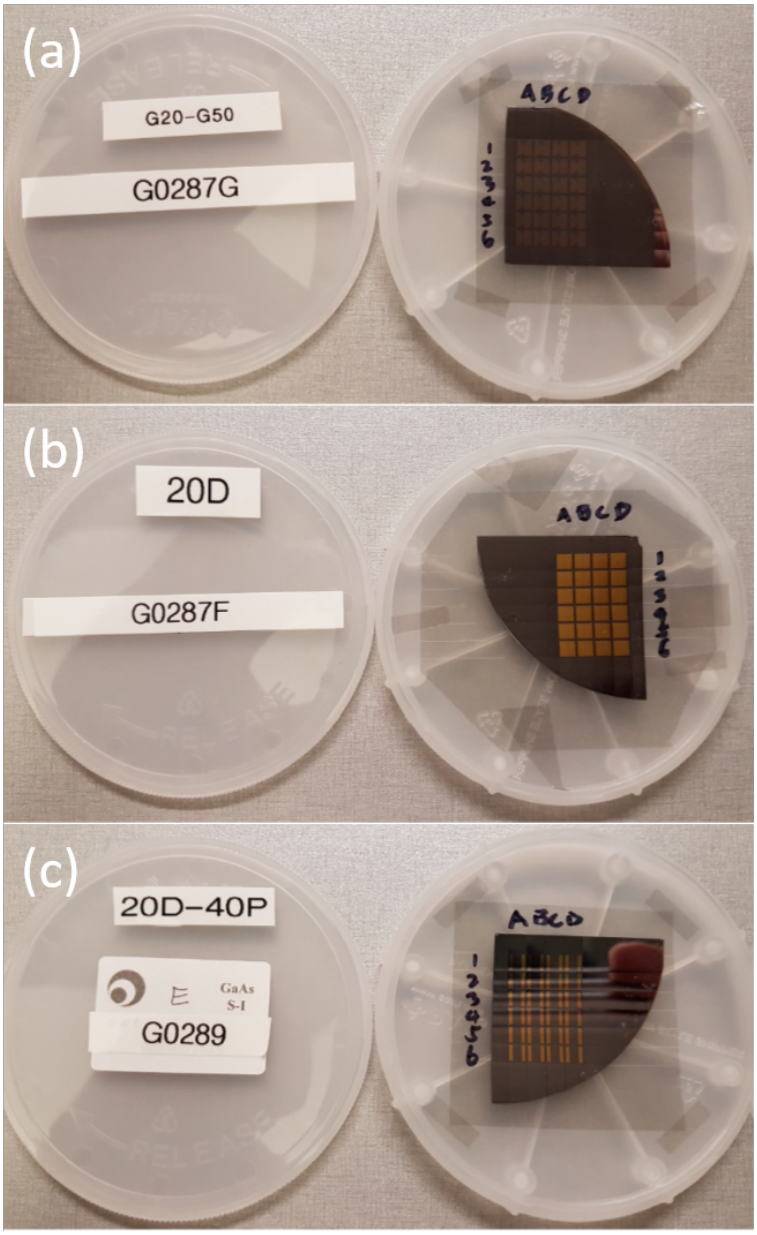

Figure 4.14: Photo of sample (a) G0287G deposited with G20 and G50 THz Tx, (b) G0289E deposited with 20D40P THz Rx and (c) G0287F deposited with D20 THz Rx. Figure adopted and reprinted with permission from Nanofabrication Group, University of Waterloo and TeTechS Inc.

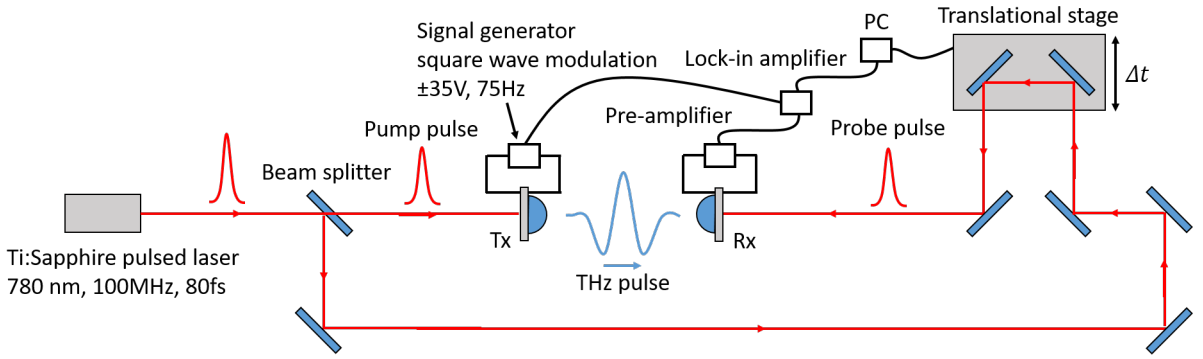

Figure 4.15: Optical setup of the 780 nm pumped THz TDS measurement, with both Tx and Rx LT GaAs based. Δt: time-delay between pump and probe pulse; PC: computer.

The signal generator produced a square wave of peak-to-peak voltage $V_{\text{pp}} = 70$ V at 75 Hz, which served as the bias voltage of Tx. A reference output of the signal generator was fed into the lock-in amplifier to filter noise. A LabVIEW code was used to operate the THz TDS scan, with the speed of the translational stage during a scan at 0.02–0.04 mm/s, scanning range of 9–12 mm and duration of 300 s. A MATLAB code was used to generate the time and frequency domain data. Repetitive THz TDS measurements were done with a variety of combinations of Tx and Rx. Due to various reasons such as changing of the setup and the switching of optical components during the whole measurement process, for better consistency, only the THz TDS measurements with the same setup and components are presented in this chapter. The illustrative photocurrent measured in the Rx, presented in both temporal and spectral domain, are shown in Figs. 4.16 and 4.17. The corrected THz amplitude, which is essentially the photocurrent measured in the Rx for this study, was obtained by multiplying the voltage acquired in the lock-in amplifier by the gain (unit: nA/V) in the pre-amplifier. Table 4.8 summarizes the THz TDS results with a focus of the four annealed samples from G0269 used as Tx and Rx. The data set with G0269A as Rx had no THz pulse detected and the exact reason is unknown, possibly due to bad contact of antennas with LT GaAs, or the dark resistance of device annealed at 375°C was too low and could not give sufficient photoconductive transient upon excitation. When the Tx was fixed and the Rx varied from G0269B to G0269D with increasing annealing temperature, the full-width-half-maximum (FWHM) of the Rx detected THz pulse in the temporal domain increased from 0.86 to 1.53 ps. In contrast, when the Rx was fixed and the Tx varied from G0269A to G0269D, the FWHM remained around 0.60–0.67 ps. This serves as a very clear example that the detected THz pulse width strongly depends on the annealing temperature of Rx but insensitive to that of Tx [119]. Nonetheless, the drastic

Tx Antenna Type	Tx Growth No.	Rx Antenna Type	Rx Growth No.	THz Amp. (nA)	FWHM (ps)	BW (THz)
G100	G0239	D20	G0269B	13.61	0.86	0.9005
G100	G0239	D20	G0269C	23.67	1.06	0.7449
G100	G0239	D20	G0269D	40.89	1.53	0.4601
D20	G0269A	20D40P	G0238	7.14	0.67	1.1537
D20	G0269B	20D40P	G0238	12.10	0.63	1.1648
D20	G0269C	20D40P	G0238	17.29	0.66	1.1778
D20	G0269D	20D40P	G0238	20.37	0.63	1.1685
G100	G0269A	20D40P	G0238	0.85	0.66	1.4022
G100	G0269B	20D40P	G0238	1.48	0.63	1.3509
G100	G0269C	20D40P	G0238	4.94	0.60	1.4875
G100	G0269D	20D40P	G0238	5.72	0.63	1.4905

Table 4.8: Summary table of the 780 nm THz TDS measurements with G0238, G0239, G0269A, G0269B, G0269C and G0269D used as Tx and Rx. The antenna type and growth no. of Tx and Rx, corrected THz amplitude, FWHM and BW are presented.

difference of FWHM between using D20 and 20D40P as Rx indicates that the antenna type is still the most dominant factor in determining the THz pulse width. The THz amplitude, on the other hand, increased vs annealing temperature when G0269A-D was served either as Tx or Rx, which indicated that the carrier mobility of in both semiconductors would affect the detected THz signal strength.

The THz TDS results summarized in Table 4.9 has the FWHM of the THz pulse sorted in ascending order. All Tx devices were grown at relatively high temperatures of 270–280°C and annealed at 600°C, hence their performance was mostly dominated by the antenna type, G20 or G100. For Rx devices, the growth temperatures ranged from 240 to 270°C; the annealing temperatures consisted of a relatively low regime of 450–460°C and a relatively high regime of 600–610°C. The effect of antenna type on the THz amplitude can be studied by comparing the three sets of THz TDS: 0032–0188, 0032–0134 and 0128–0134, with the same Rx growth temperature of 270°C and similar annealing temperature of 450–460°C. From 0032–0134 and 0128–0134, it is clear that G20 gave ∼2.2 times stronger THz signal than G100. On the other hand, from 0032–0188 and 0032–0134, D20 drove significantly more photocurrent than 20D40P by ∼70 times. There is no clear correlation between the detected THz amplitude and the Rx growth or annealing temperature though. In addition, there is no clear correlation between the FWHM and the Tx antenna type either, the Rx antenna type plays a huge role here, however. All measurement sets with D20 as the Rx show considerably wider FWHM of > 0.5 ps than their 20D40P counterparts with FWHM ∼0.33–0.43 ps. The only exception here is 0127–0134 with FWHM of 0.3833 ps, but its 20dB BW is only 1.7582 THz, considerably lower than many of those with 20D40P as Rx which show ∼2 THz or broader BW. Empirically, a Rx with a lower growth temperature should give a shorter THz pulse width, but such trend is not very clear in

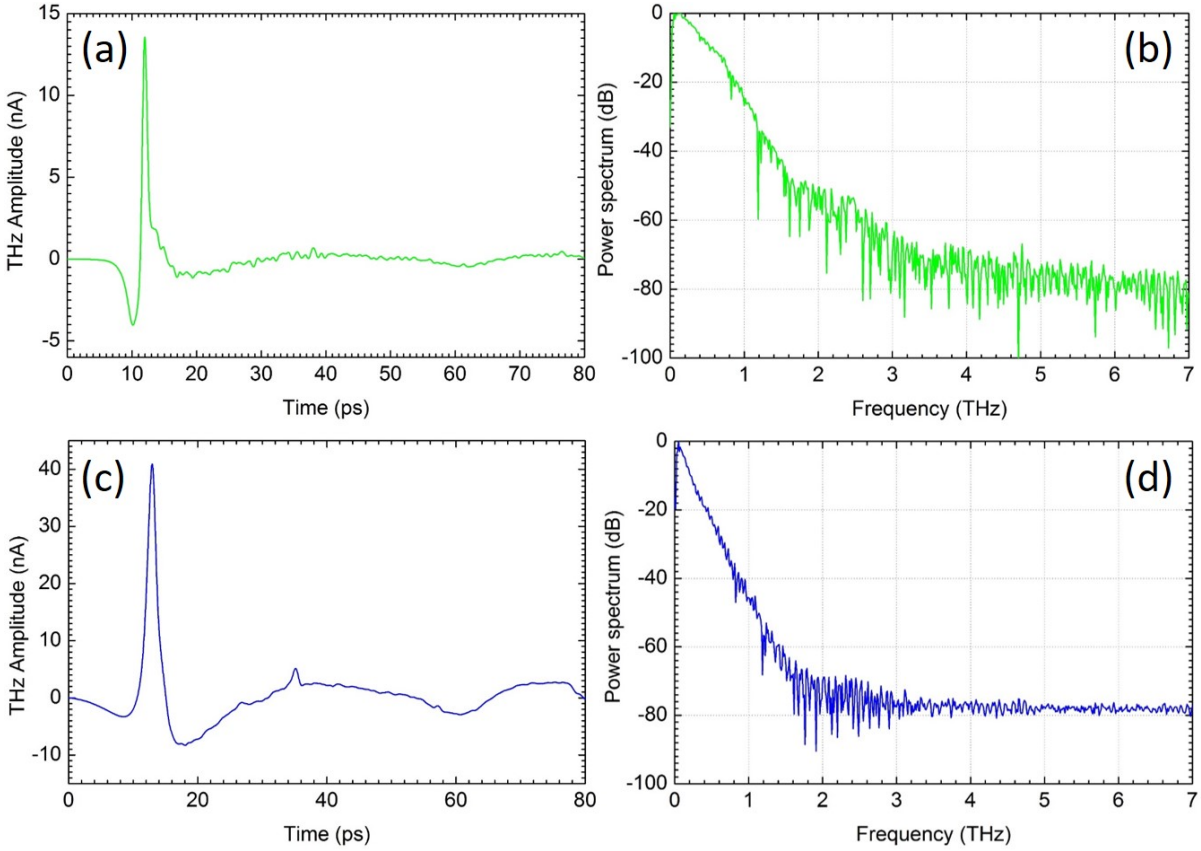

Figure 4.16: Photocurrent response in a 780 nm pumped THz TDS system with LT GaAs based Tx of antenna type G100, growth no. G0239 and Rx of antenna type D20, for Rx growth no. G0269B in (a) temporal and (b) spectral domain; for Rx growth no. G0269D in (c) temporal and (d) spectral domain. Figure adopted and reprinted with permission from Nanofabrication Group, University of Waterloo and TeTechS Inc.

Tx			Rx			TDS Results		
Sample No.	Antenna Type	Growth No.	Sample No.	Antenna Type	Growth No.	THz Amp. (nA)	FWHM (ps)	BW (THz)
0032	G100	G0239	0099	20D40P	G0324F	3.42	0.3333	2.4100
0032	G100	G0239	0109	20D40P	G0326E	0.57	0.3417	2.4832
0143	G20	G0503G	0145	20D40P	G0503F	5.13	0.3500	2.0440
0032	G100	G0239	0103	20D40P	G0326F	1.09	0.3583	2.2049
0127	G20	G0287G	0134	D20	G0287F	3.37	0.3833	1.7582
0032	G100	G0239	0101	20D40P	G0324H	2.02	0.4083	2.0437
0032	G100	G0239	0100	20D40P	G0324G	6.22	0.4333	1.9045
0032	G100	G0239	0188	20D40P	G0287E	0.30	0.4333	1.5462
0128	G20	G0287G	0134	D20	G0287F	21.07	0.5000	1.4723
0032	G100	G0239	0134	D20	G0287F	9.48	0.5083	1.4943
0128	G20	G0287G	0067	D20	G0287H	5.20	0.9833	0.7691

Table 4.9: Summary table of the 780 nm THz TDS measurements with different combinations of Tx and Rx. The Tx and Rx sample no., antenna type, growth no., corrected THz amplitude, FWHM and BW are presented.

this set of study. A higher annealing temperature may increase the FWHM slightly, as indicated by comparing the data sets with FWHM < 0.3 ps and > 0.4 ps, but again such trend is not very significant especially for those with 20D40P as Rx. The only set that shows a clear effect of a higher annealing temperature resulted in a longer carrier lifetime is 0128–0067. It has FWHM $= 0.9833$ ps which is more than double of those of the rest, and its BW $= 0.7691$ THz is less than half of those of the rest. Overall, our THz TDS results have bandwidth comparable to those LT GaAs based PCA devices reported in recent years [46, 120]. To investigate the effect of growth and annealing temperatures on carrier lifetime, time-resolved pump-probe measurements of the change of reflectance vs time-delay is a more reliable tool [60, 119, 121]. The improvement in overall FWHM and BW from Table 4.8 to Table 4.9 is not due to growth temperature, annealing temperature or antenna type, but the difference in processing techniques such as the type of photoresist chemical used or the duration of RIE. The PCA devices presented in the latter table were processed and tested approximately two years later than those in the former table, in which a lot of advancements had been made in antenna fabrication for faster photoconductive transients.

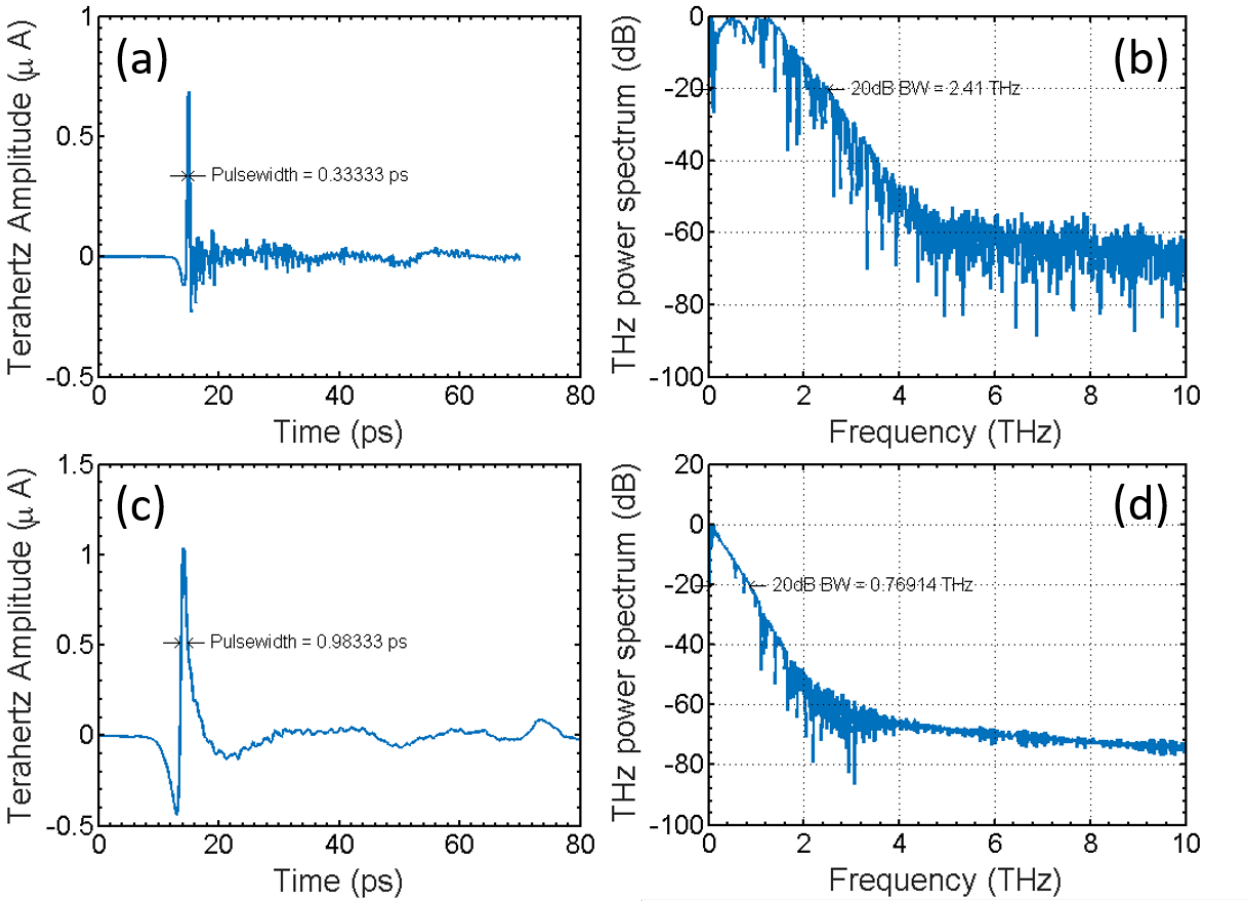

Figure 4.17: Photocurrent response in a 780 nm pumped THz TDS system, with LT GaAs based Tx no. 0032 and Rx no. 0099. in (a) temporal and (b) spectral domain; with LT GaAs based Tx no. 0128 and Rx no. 0067 in (c) temporal and (d) spectral domain. Figure adopted and reprinted with permission from Nanofabrication Group, University of Waterloo and TeTechS Inc.

Chapter 5

InGaAs-InAlAs Superlattice Based PCAs

5.1 MBE Growth, Annealing and Characterizations

Multiple lattice-matched InGaAs-InAlAs SL structures were grown at various parameters. The schematic of LT InGaAs-InAlAs SL with 3D Be doping, named G0123, G0134, G0296, G0297, G0301, G0302, G0400, G0541, G0542, G0688 and G0689, are shown in Table 5.1. The schematic of undoped middle temperature (MT) InGaAs-InAlAs SL, named G0248, G0362, G0363 and G0388, are shown in Table 5.2. The schematics of LT InGaAs-InAlAs SL with C as the dopant, either δ or conventional 3D doping, named G0430, G0431, G0457, G0458, G0467, G0477 and G0479, are shown in Table 5.3. The summary of the growth parameters of all Be-doped LT and undoped MT growths in this study are shown in Table 5.4, while that for all C-doped LT growths are shown in Table 5.5. Overall, the Be and C-doped LT SLs were grown at target temperature of 260–270°C, while the MT ones were grown at 400°C. All samples were grown with As Op of ∼2-4. Except for G0688 and G0689 which were grown on full 3" InP(001) substrates, the rest were grown on Q3" substrates. All annealing were done *in situ* in the MBE GM for 60 min, with an annealing temperature of 500°C applied for earlier growths and increased to 540°C since G0400. It could not be further increased to minimize In desorption. The bowing factors of the ternary compounds were also adjusted twice throughout this sequence of growths. Target In compositions of 0.526 for InGaAs and 0.53 for InAlAs had been used since G0400. They were expected to give the best lattice-matching conditions. The structural schematic reported in [51, 60] was adopted for the samples presented in this chapter, which contain 100 periods of SL

Name	Material	Thickness (Å)	Repeat
Substrate	SI (Fe-doped) InP(001)		
Buffer	InAlAs	2000	
Well	InGaAs:Be	120	100
Barrier	InAlAs:Be	80	100
Top Contact	InGaAs:Be	120	

Table 5.1: Growth schematic of Be-doped LT InGaAs-InAlAs SL G0123, G0134, G0296, G0297, G0301, G0302, G0400, G0541, G0542, G0688 and G0689.

Name	Material	Thickness (Å)	Repeat
Substrate	SI (Fe-doped) InP(001)		
Buffer	InAlAs	2000	
Well	InGaAs	120	100
Barrier	InAlAs	80 or 20	100
Top Contact	InGaAs	120	

Table 5.2: Growth schematic of undoped MT InGaAs-InAlAs SL G0248, G0362, G0363 and G0388.

with target thicknesses of 120 Å for InGaAs and 80 Å for InAlAs. The only exception is G0388, where InAlAs thickness of 20 Å was grown instead which is expected to give stronger THz signal when it is fabricated as Tx [57].

The *in situ* growth parameters of illustrative SLs are shown in Figs. 5.1–5.3. The main challenge of growing InGaAs based structure is the difficulty of substrate temperature monitoring. Similar to the case of LT GaAs growth, radiative heating on substrates also occurs during the growth of lattice-matched InGaAs on InP, which increases dramatically as the layer becomes thicker [113]. Same as Chapter 4, for LT InGaAs-InAlAs SL growths, T_c was continuously adjusted to keep T_{BET} constant, as illustrated in Fig. 5.2. However, unlike LT GaAs growth which still showed decent and clean BET signal throughout the entire epitaxy, InGaAs deposition would distract the BET reading over time due to the small bandgap nature of InGaAs, in which the wafer turned opaque gradually as the layer grew thicker and the band edge in the 900–1700 nm transmittance spectrum would eventually fade away. Illustrated in Figs. 5.1 and 5.2, where the BET graph showed an identifiable temperature at the beginning of the SL deposition, such reading became noisy over time and eventually unreadable. The strong fluctuation is attributed to the distortion of the 900–1700 nm transmittance spectrum, which was more severe in the case of C-doped SL. Unlike conventional effusion cells which operate by melting elements in

Name	Material	Thickness (Å)	Repeat
Substrate	SI (Fe-doped) InP(001)		
Buffer	InAlAs	2000	
Well	InGaAs	120	100
Barrier	InAlAs	80	100
δ-Doping	C		100
Top Contact	InGaAs	120	

Name	Material	Thickness (Å)	Repeat
Substrate	SI (Fe-doped) InP(001)		
Buffer	InAlAs	2000	
Well	InGaAs:C	120	100
Barrier	InAlAs:C	80	100
Top Contact	InGaAs:C	120	

Table 5.3: Growth schematics of C-doped LT InGaAs-InAlAs SL G0430, G0431, G0457, G0458, G0467 (top); G0477 and G0479 (bottom).

Growth No.	w_{InGaAs}	w_{InAlAs}	Dopant	Concentration (cm^{-3} or cm^{-2})	T_g (°C)	T_a (°C)
G0123	0.530	0.520	Be	4.00×10^{18}	260–270	500
G0134	0.530	0.520	Be	4.00×10^{18}	260–270	500
G0164	0.530	0.520	Be	4.00×10^{18}	260–270	500
G0249	0.530	0.520	Be	4.00×10^{18}	260–270	500
G0296	0.534	0.546	Be	2.37×10^{18}	260–270	500
G0297	0.534	0.546	Be	1.27×10^{18}	260–270	500
G0301	0.534	0.546	Be	6.00×10^{17}	260–270	500
G0302	0.534	0.546	Be	3.00×10^{17}	260–270	500
G0400	0.526	0.530	Be	4.00×10^{18}	260–270	540
G0541	0.526	0.530	Be	4.00×10^{18}	260–270	540
G0542	0.526	0.530	Be	4.00×10^{18}	260–270	540
G0688	0.526	0.530	Be	4.00×10^{18}	260–270	540
G0689	0.526	0.530	Be	8.00×10^{18}	260–270	540
G0248	0.530	0.520	None	N/A	400	N/A
G0362	0.526	0.530	None	N/A	400	N/A
G0363	0.526	0.530	None	N/A	400	N/A
G0388	0.526	0.530	None	N/A	400	N/A

Table 5.4: Growth and anneal summary of all undoped MT and Be-doped LT InGaAs-InAlAs SL structures, which shows the growth no., target In composition of InGaAs (w_{InGaAs}) and InAlAs (w_{InAlAs}), dopant type, doping concentration, growth temperature (T_g) and annealing temperature (T_a).

Growth No.	w_{InGaAs}	w_{InAlAs}	Dopant	$\mathcal{I}_c$ (A)	t (s)	T_g (°C)	T_a (°C)
G0430	0.526	0.530	C–δ	54.53	79.7	260–270	540
G0431	0.526	0.530	C–δ	54.53	19.9	260–270	540
G0457	0.526	0.530	C–δ	56.41	60.0	260–270	540
G0458	0.526	0.530	C–δ	57.17	60.0	260–270	540
G0458	0.526	0.530	C–δ	57.17	60.0	260–270	540
G0477	0.526	0.530	C	56.41	79.6	260–270	540
G0479	0.526	0.530	C	57.49	79.6	260–270	540

Table 5.5: Growth summary of all C-doped LT InGaAs-InAlAs SL structures, which shows the growth no., target In composition of InGaAs (w_{InGaAs}) and InAlAs (w_{InAlAs}), dopant type, carbon cell filament current ($\mathcal{I}_c$), doping duration (t), growth temperature (T_g) and annealing temperature (T_a).

crucibles, the carbon cell ejects atoms by heating up a filament entirely made of carbon via a huge electrical current passing through it. Depending on the target flux and doping concentration, the current was 45–60 A and the voltage was 9–10 V which corresponded to an electrical power of ∼400–600 W. The filament was heated up to 1500°C during growth and as a side effect, tremendous radiation was emitted from the filament, which severely distorted the transmittance spectrum and boosted the BET reading. Fig. 5.3 shows the spikes on the BET graph originated from this sudden increase of reading during carbon δ-doping. For undoped MT and Be-doped LT growths, the substrate was kept rotating and either In/Ga or In/Al were kept open during the entire InGaAs-InAlAs SL deposition. However, for C-doped LT growths, in order to compensate the tremendous heating from the carbon filament, all group III shutters were closed for As soak for 1–2 minutes after each period of SL deposited to cool down the wafer back to its target temperature. Furthermore, for growths G0430, G0431, G0457, G0458 and G0467, the substrate rotation was paused before δ-doping and the rotation was restored afterwards. Those additional steps made the C-doped SL growth duration approximately 2–3 times longer than the undoped and Be-doped ones. Apart from T_{BET}, Fig. 5.1 also shows the T_{pyro} and the T_{ISP} traces for comparison. From Fig. 5.1, even with the SVT pyrometer temperature pre-calibrated with BET for the bare InP substrate right after oxide desorption at 500°C, the two readings already showed significant inconsistency when the wafer temperature dropped by ∼75–100°C, where T_{pyro} read 450°C, higher than T_{BET} by ∼25°C before the latter one lost the trace. On the other hand, the bare InP substrate was transparent to the substrate heater at the beginning such that T_{ISP} had an unreal reading of 540°C. However, T_{ISP} kept dropping as the SL layers were piling up and the wafer gradually turned opaque. Although the ISP coefficients were calibrated with the customized InAs-GaAs composite substrate as described in Chapter 3, thanks to the similarity of emissivity among most group III-V

compounds, T_{ISP} dropped to a value similar to T_{pyro} by the end of the 2 μm SL deposition. The rapid up-and-down trace in the SVT reflectance, particularly 470 nm, originated from the repetitive, short and thin InGaAs and InAlAs depositions, with growth durations of 47.9 and 32 s per SL period respectively .

Figs. 5.4–5.7 show representative Nomarski and black-box images of the InGaAs-InAlAs structures in this study. Most LT and MT grown SL growths, whether doped or undoped, exhibited smooth morphology or barely visible bumps under Nomarski. For black-box images, besides the irregularly distributed point defects on the top, those wafers had mirror-smooth surface. Generally, the average SVT reflectance readings of an SL period, particularly 470 nm, serve as indicators of the epitaxial quality. In this study, the average SVT reflectance over time varied from growth to growth. Most growths had the reflectance decreased over time as illustrated in Fig. 5.2, while a few remained constant as in Fig. 5.1, or increased as in Fig. 5.3. However, optical reflectance is not always a good indicator of surface smoothness when the growth qualities of two or more growths are similar to each other. Fig. 5.4 shows G0296 is mirror-smooth while G0458 has some very minor bumps, contrary to Figs. 5.2 and 5.3, which have average 470 nm reflectance decreasing and increasing with time respectively. This indicates that instead of surface roughness, the change of average 470 nm reflectance was more likely due to the lattice mismatch between the InGaAs-InAlAs SL layer and the InP substrate, which resulted in epitaxial relaxation during growth where the surface could be convexly or concavely curved. Most LT grown SL do not have apparent difference before and after annealing, but there are a few exceptions as illustrated by the Nomarski and black-box images in Figs. 5.5 and 5.7, where G0689 had relaxation lines appeared and G0479 converted from a mirror smooth to a hazy surface after annealing. This is understandable, as an annealing temperature of $\sim$540°C was used in order to achieve higher dark sheet resistance. However, as a trade-off, this is also the critical temperature where In desorption starts to occur, which resulted in surface degrading.

The representative HRXRD scans are shown in Figs. 5.8–5.11. All SL structures had the same target InGaAs and InAlAs thicknesses of 120Å and 80Å per period in SL respectively, with the exception of G0388, where the InAlAs was only 20Å thick. Such a difference is clearly shown in Fig. 5.8(b), where the average separation between adjacent SL satellite peaks is obviously wider than all the other growths. The InGaAs and InAlAs layers for all growths in this study were targeted to be lattice-matched to the InP substrate. However, in practical MBE growths, there is almost always unintentional lattice-mismatch. For the HRXRD graphs illustrated here, Figs. 5.8(b)–(d), 5.9(b), 5.10(a)–(c), G0362, G0363 and G0388 in Fig. 5.11 are better growths. They are either lattice-matched or with only minor lattice-mismatch. Each of them has the 0^{th} order satellite peak either

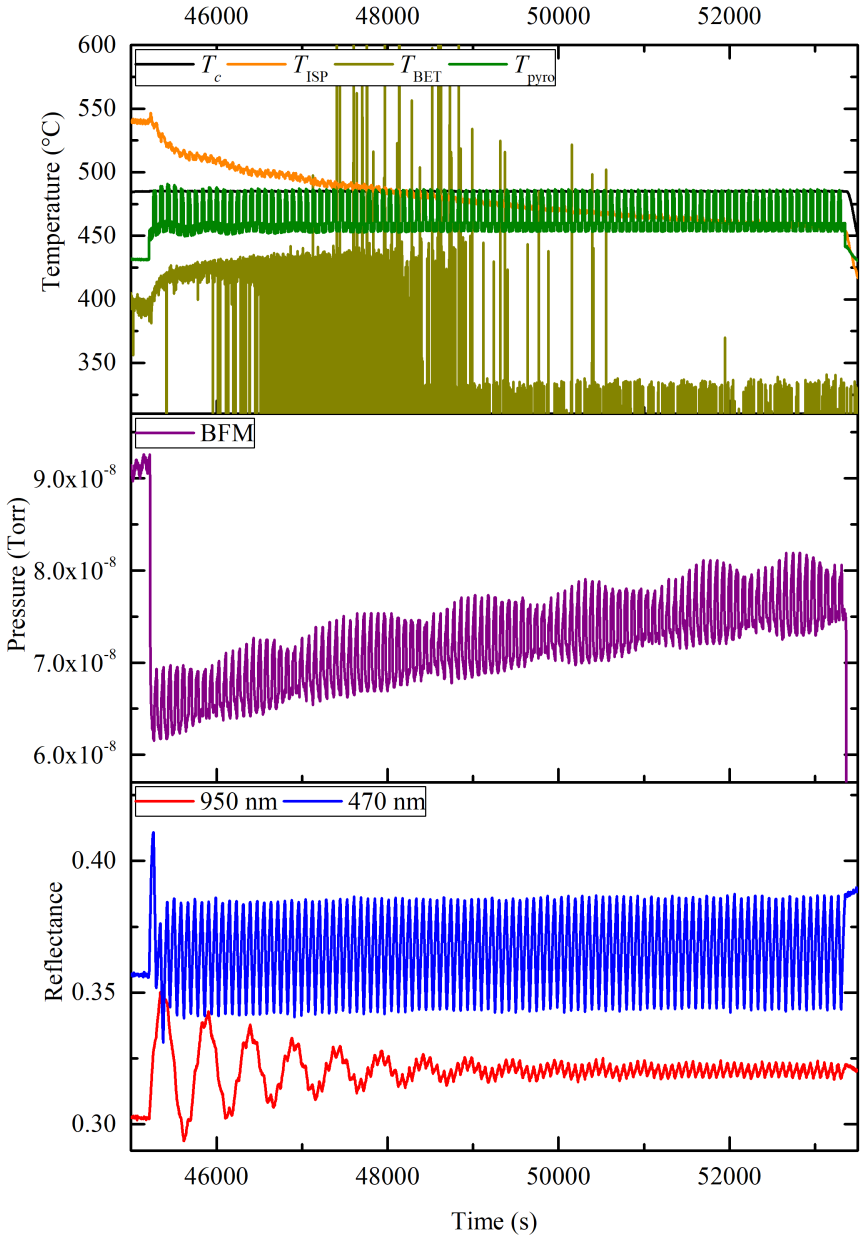

Figure 5.1: *In situ* growth parameters during InGaAs-InAlAs SL deposition of G0248. From top to bottom: T_c (black), T_{BET} (dark yellow), T_{ISP} (orange) and T_{pyro} (dark green); BFM (purple) pressure; 950 nm (red) and 470 nm (blue) reflectance.

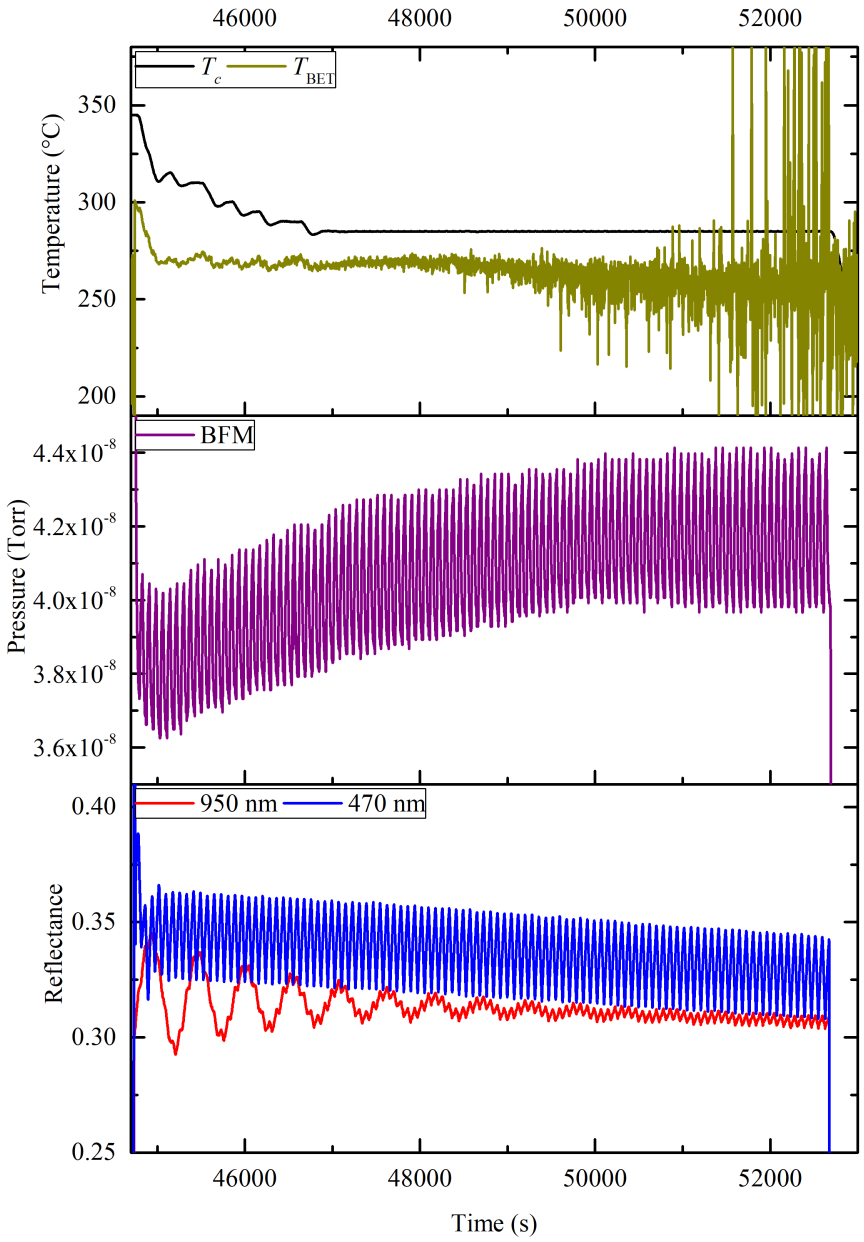

Figure 5.2: *In situ* growth parameters during InGaAs-InAlAs SL deposition of G0296. From top to bottom: T_c (black) and T_{BET} (dark yellow); BFM (purple) pressure; 950 nm (red) and 470 nm (blue) reflectance.

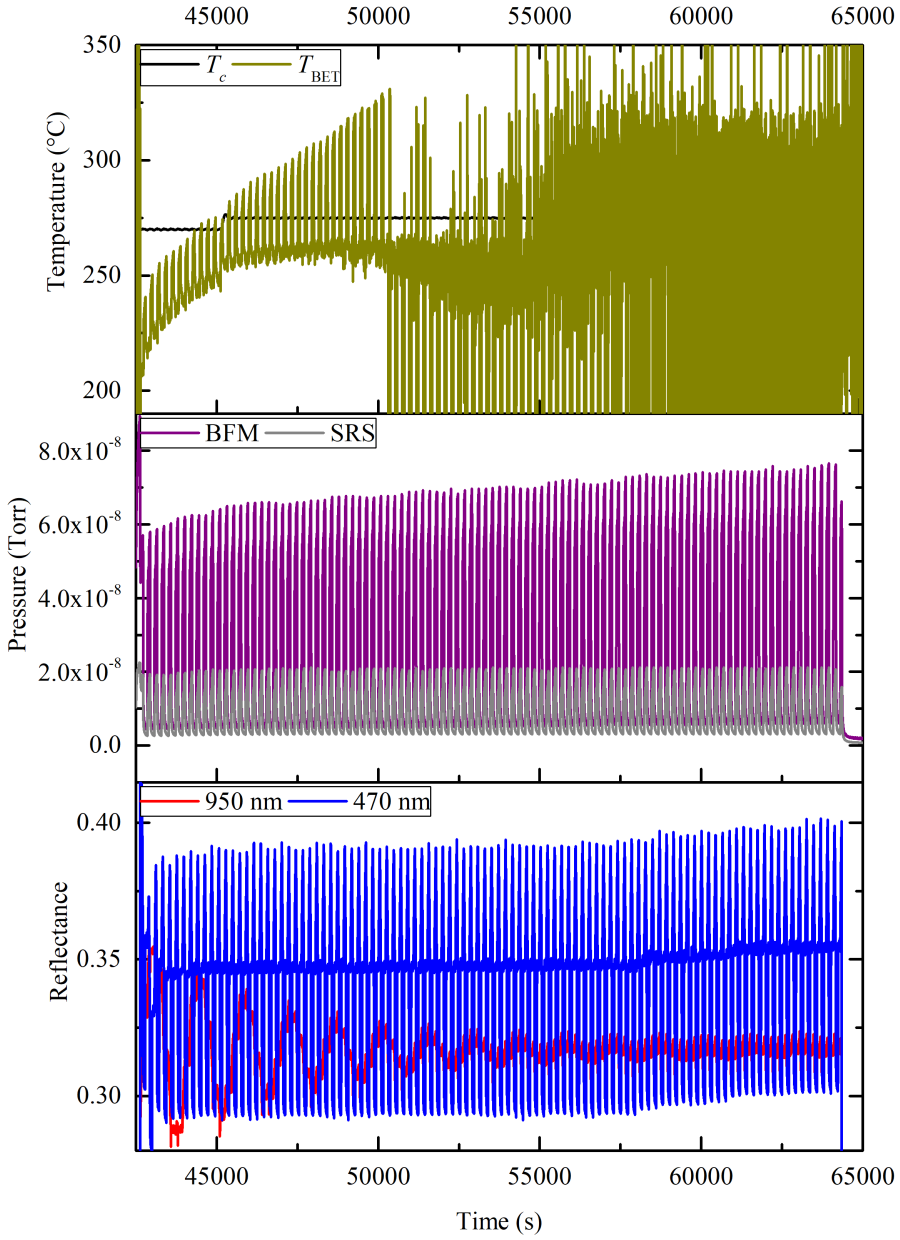

Figure 5.3: *In situ* growth parameters during InGaAs-InAlAs SL deposition of G0458. From top to bottom: T_c (black) and T_{BET} (dark yellow); BFM (purple) and SRS (gray) pressure; 950 nm (red) and 470 nm (blue) reflectance.

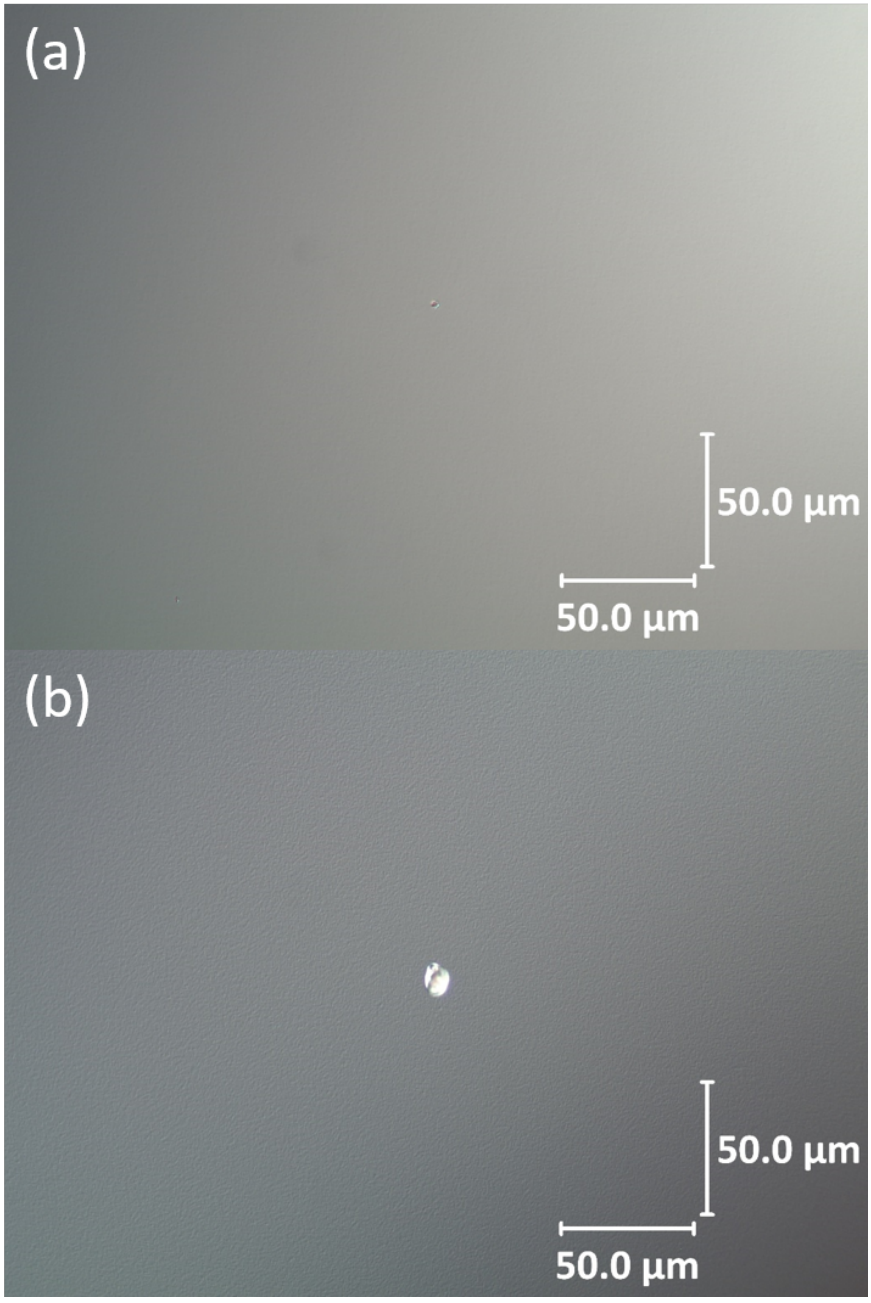

Figure 5.4: Nomarski images at 40× magnification of sample (a) G0296 and G0458.

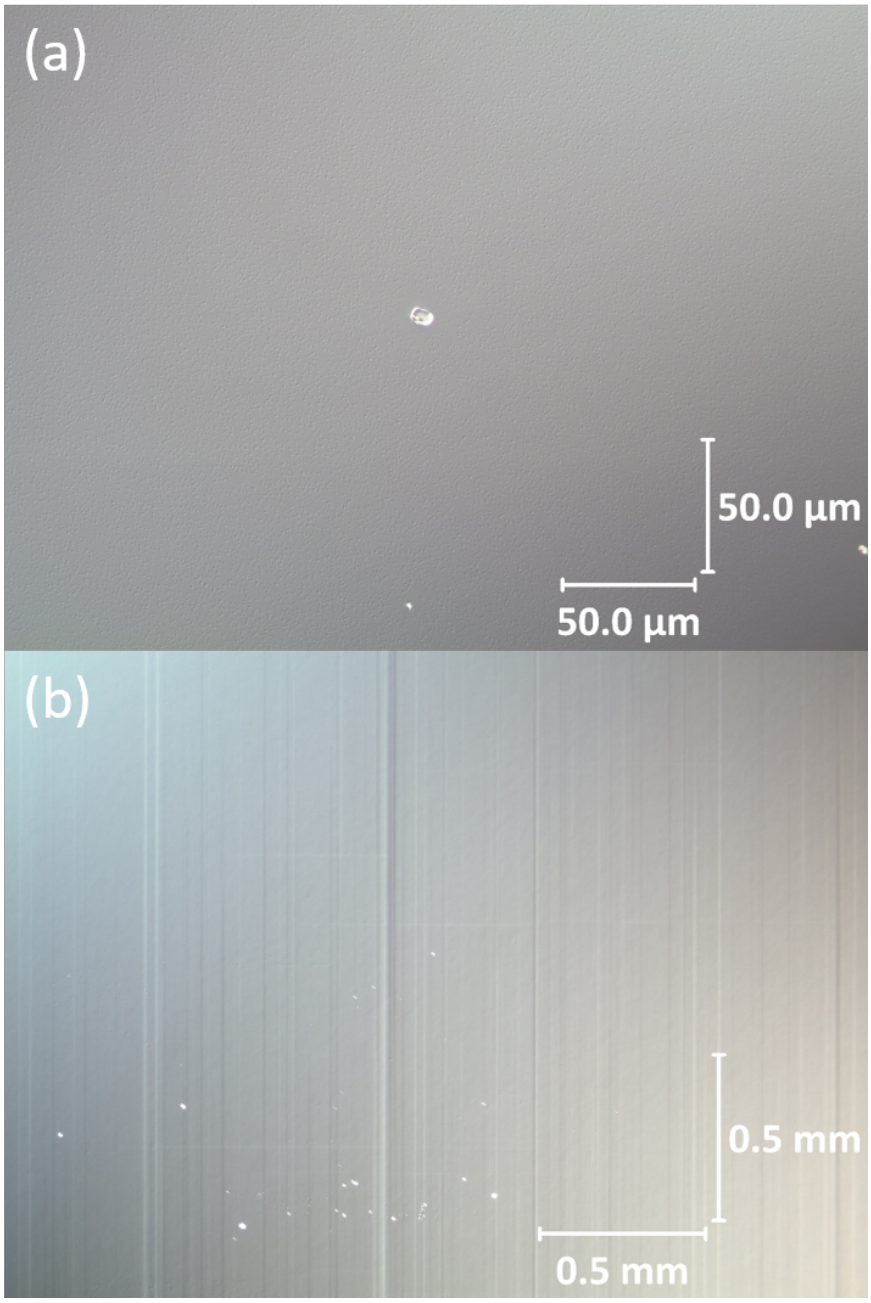

Figure 5.5: Nomarski images of sample a relaxation site of G0689 at (a) 40× and (b) 5× magnification.

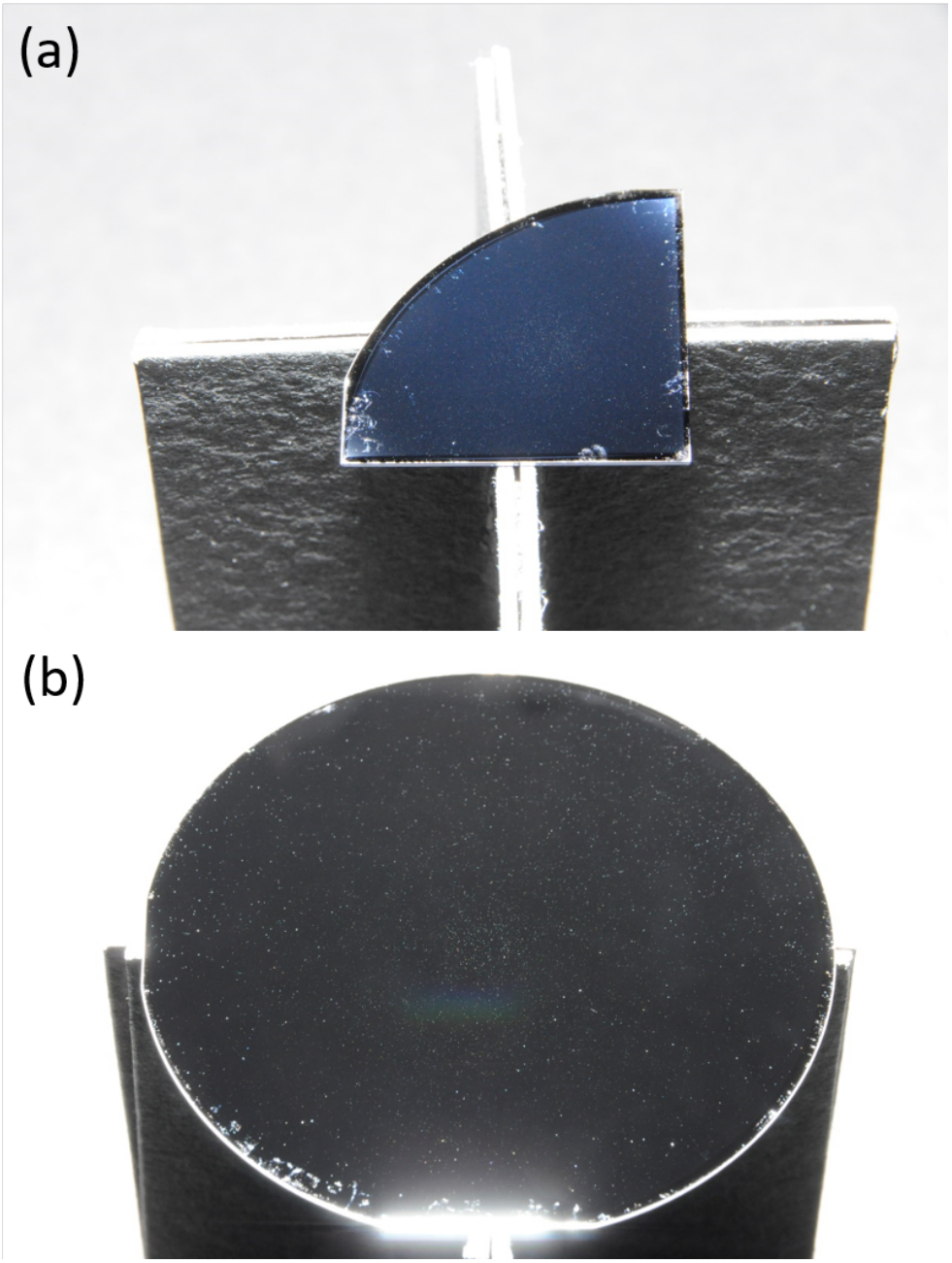

Figure 5.6: Black-box images with an exposure time of 5 ms of sample (a) G0541 and (b) G0689.

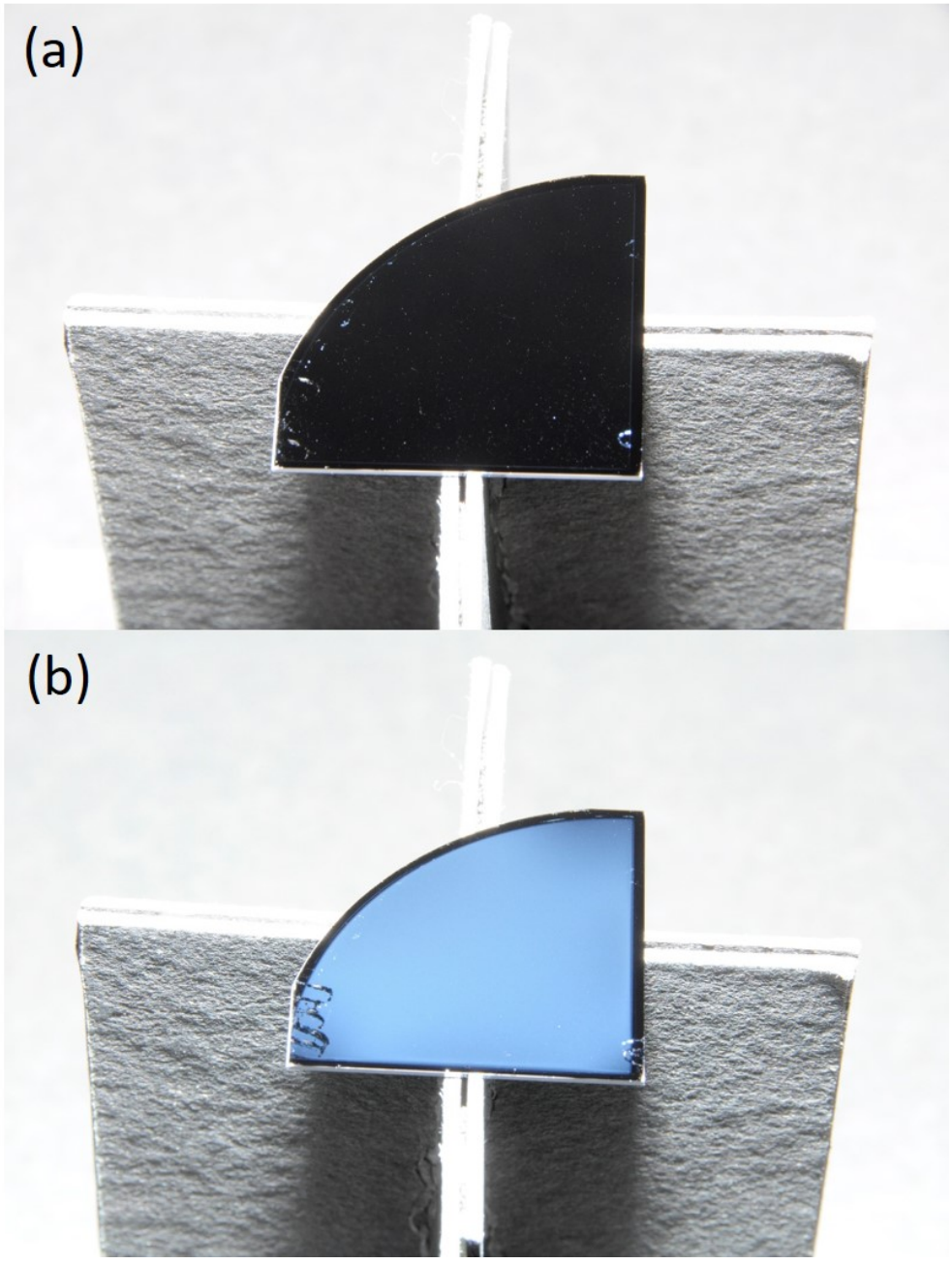

Figure 5.7: Black-box images with an exposure time of 5 ms of (a) as-grown and (b) annealed G0479.

merges with the substrate peak or just with very little separation from each other. In particular, Fig. 5.9(b) shows a shoulder-like peak at the right of the substrate peak, which is clearly attributed to the 2000Å InAlAs buffer. On the other hand, some growths had flux drift issues, which altered their HRXRD profiles in various ways. Those include: 0^{th} order satellite peak with significant compressive strain as illustrated in Fig. 5.9(a); 0^{th} order satellite peaks with significant tensile strains as illustrated in Fig. 5.10(d) and G0248 in Fig. 5.11; split satellite peaks in Fig. 5.9(d) which indicated there could be two different periods in the SL stack; poor peak and fringe profile as illustrated in Fig. 5.9(c). Fortunately, provided that the InGaAs material can still be excited by a 1550 nm laser, the precision of thickness and composition or period consistency of InGaAs-InAlAs SL are not the most crucial factors which affect the THz PCA performance. In fact, even with an In flux drift of 0.5% can make a noticeable InGaAs peak shift of 20". Table 5.6 provides an HRXRD summary of all SLs. Except for all MT samples which were not annealed, all LT samples show peak shift of the 0^{th} order satellite towards positive upon annealing, which indicate As precipitation. Unlike LT GaAs, the 0^{th} order satellite peak of InGaAs-InAlAs SL is dependent on the group III compositions, which adds complexity to direct comparison of the peak positions among different samples. Nonetheless, most samples have SL period with only ∼1-2% deviation from the target of 200Å, which indicate in overall, the majority of the SLs presented in this work were still reasonably grown on-target.

5.2 Four-Point-Probe Measurement

4pp measurement was conducted to find the sheet resistance, R_{sheet} of selective Be or C-doped InGaAs-InAlAs SL samples. For G0430, G0431, G0457, G0458, G0467, G0477, G0479 and G0541, 4pp scans were taken along 5 different azimuth angles of $\vartheta = 0°$, 22.5°, 45°, 67.5 and 90° on the Q3" SI InP(001) wafer with 5 mm spacing between adjacent measurement sites, as illustrated in Fig. 5.12(a). For G0688 and G0689 which were grown on full 3" wafers, 4pp scans were taken along $\vartheta = 0°$, 45°, 90° and 135°, again with 5 mm spacing between adjacent measurement sites, as illustrated in Fig. 5.12(b). The arrows indicate the scan directions which began at radial position $s = 0$ mm for Fig. 5.12(a) and s = -30 mm for Fig. 5.12(b) and ended at $s = 30$ mm for both. The averaged R_{sheet} with its standard deviation of multiple measurements, as well as the resistance of PCA types G20, G50, D20 of certain samples are shown in Table 5.7. Overall, the C-doped SL samples have R_{sheet} in the order of kΩ/sq, much lower than that of the Be-doped counterparts which are in the order of MΩ/sq. In particular, the δ-doped samples have $R_{\text{sheet}} \approx 1 - 20\text{k}\Omega/\text{sq}$, even lower than that of the 3D-doped ones which are ∼ 100kΩ/sq. All the C-doped InGaAs-

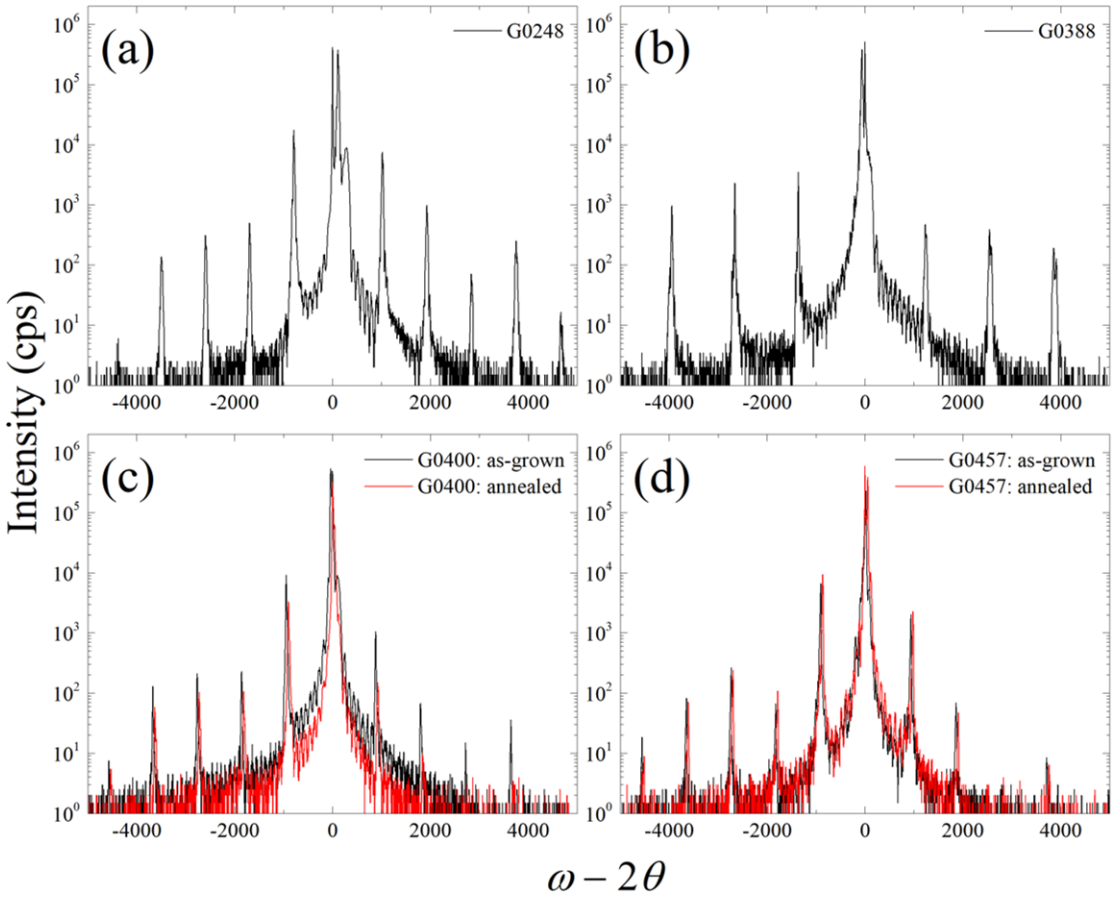

Figure 5.8: HRXRD TA coupled scans of as-grown (black) and annealed (red) InGaAs-InAlAs SL samples (a) G0248 and (b) G0388, both MT grown and undoped; (c) G0400 and (d) G0457, both LT grown, Be and C doped respectively.

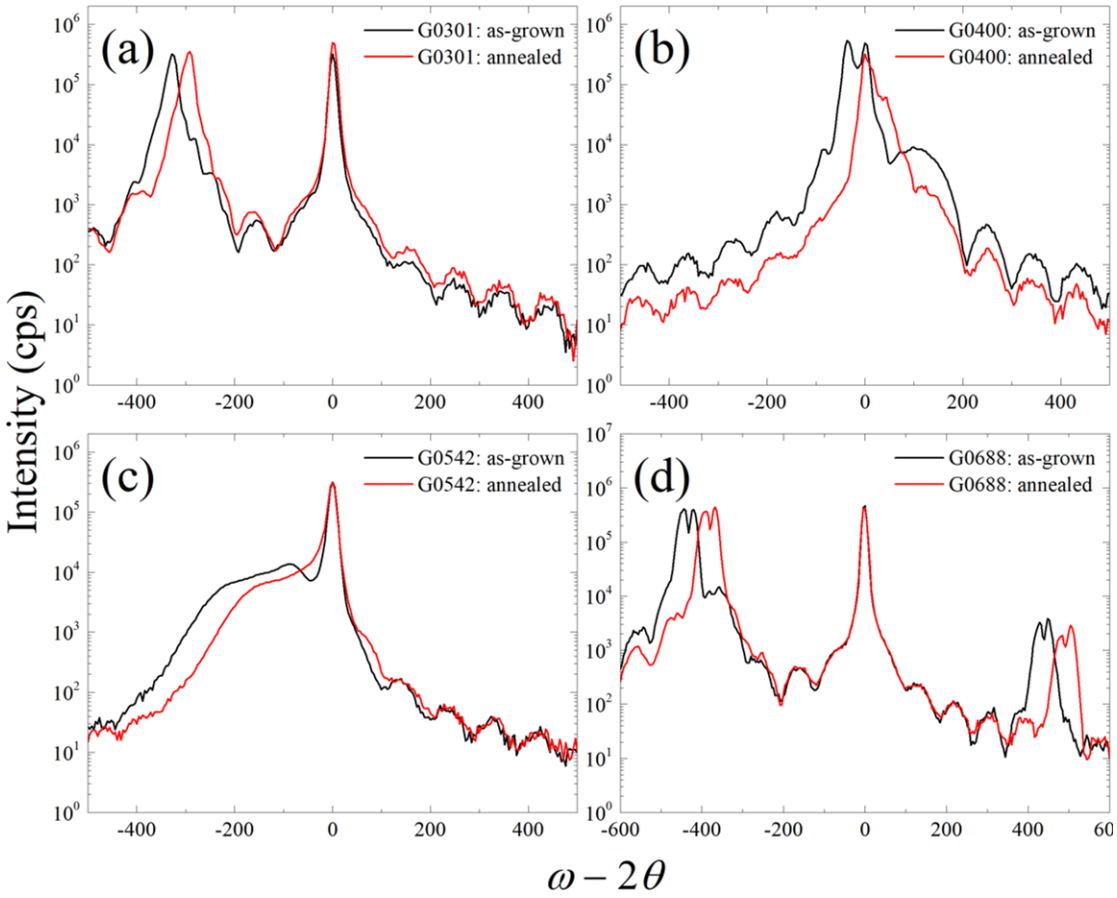

Figure 5.9: HRXRD TA coupled scans of Be-doped LT InGaAs-InAlAs SL samples (a) G0301, (b) G0400, (c) G0542 and (d) G0688, as-grown (black) and annealed (red).

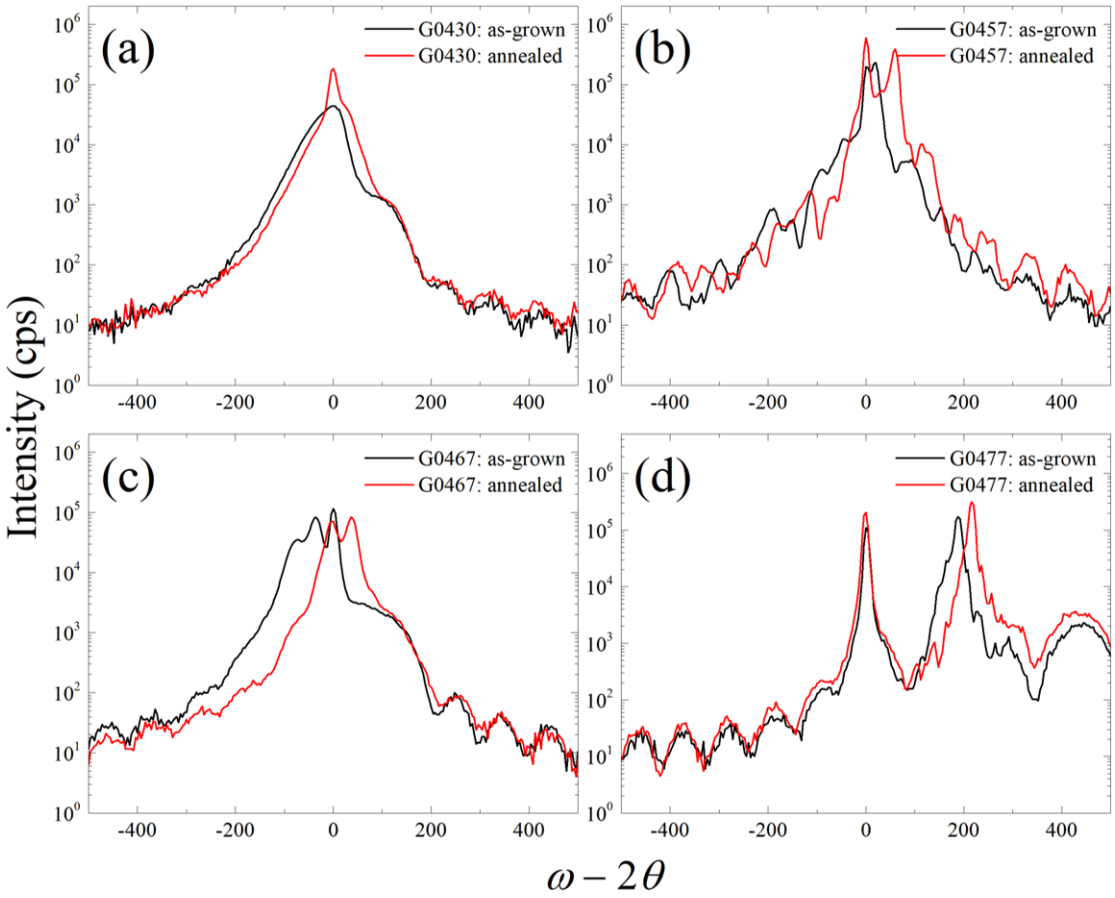

Figure 5.10: HRXRD TA coupled scans of C-doped LT InGaAs-InAlAs SL samples (a) G0430, (b) G0457, (c) G0467 and (d) G0477, as-grown (black) and annealed (red).

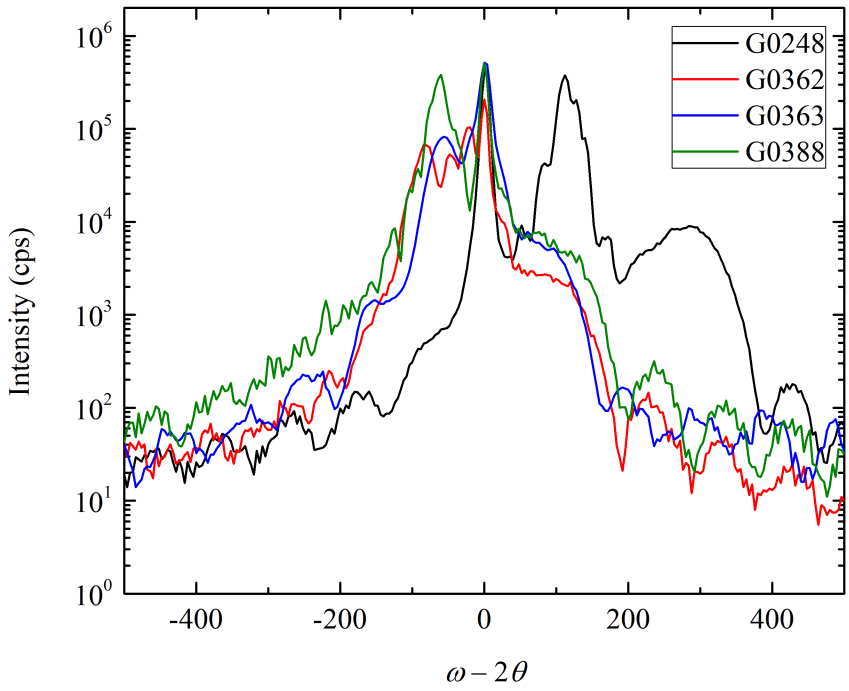

Figure 5.11: HRXRD TA coupled scans of undoped MT InGaAs-InAlAs SL samples G0248 (black), G0362 (red), G0363 (blue) and G0388 (dark green).

Growth No.	$\langle\Delta\omega\rangle$ (")	Λ (Å)	$\omega_{\text{SL0,as-grown}}$ (")	$\omega_{\text{SL0,annealed}}$ (")	Note
G0123	910	200.90	-492	-416	rough
G0134	869	211.62	-240	-184	
G0164	850	216.31	72	188	rough
G0248	905	202.75	112	N/A	
G0296	980	186.44	-220	-196	
G0297	950	192.25	-440	-392	
G0301	930	198.02	-328	-296	
G0302	933	197.20	-304	-280	
G0362	923	198.22	0	N/A	split
G0363	927	198.05	0	N/A	split
G0388	1304	141.99	0	N/A	split
G0400	915	201.29	-36	0	
G0430	912	202.19	0	0	rough
G0431	904	204.12	0	64	
G0457	916	200.53	20	60	
G0458	929	198.14	40	68	
G0467	926	197.77	36	40	split
G0477	922	198.61	188	216	
G0479	924	199.14	188	212	
G0541	912	200.97	-44	32	rough
G0542	916	200.64	-88	0	rough
G0688	865	211.36	-432	-380	split
G0689	869	210.75	-444	-392	

Table 5.6: HRXRD summary of all InGaAs-InAlAs SL samples, which shows the average separation between adjacent SL satellite peaks ($\langle\Delta\omega\rangle$), SL period thickness ($\Lambda$), as-grown 0^{th} order SL peak position ($\omega_{\text{SL0,as-grown}}$) and annealed 0^{th} order SL peak position ($\omega_{\text{SL0,annealed}}$).

InAlAs SL samples exhibit low resistances which are too conductive for any practical THz PCA applications.

Fig. 5.13 shows the 3D plots of R_{sheet} vs perpendicular positions X, Y for G0688 and G0689, where $s = \sqrt{X^2 + Y^2}$, with both samples exhibit lower reading towards the peripheral wafer edge. For G0689, since there was an unintentional movement of the wafer slightly away from the centre of the 4pp rotational stage when it was rotated to different azimuths, the 4pp data was skewed and the resistance profile is not as good quality as that of G0688. The 4pp profile is most likely due to the temperature gradient across the full 3" InP wafer surface, in which the temperature between the centre and the edge is estimated to be ~5–10°C. According to the work of Sartorius *et al.* in [51] as shown in Fig. 2.16, the intrinsic carrier concentration of InGaAs is $\sim 10^{15}$–10^{16} cm^{-3} for normal temperature growth above 400°C. However, it changes to n-doped in the LT regime and this concentration is very sensitive to the growth temperature, which results in different carrier compensations between the centre and the edge and this explains their difference in sheet resistance. Nonetheless, in Ref. [51] the InGaAs carrier concentration raised to $\sim 10^{17}$–10^{18} cm^{-3} only when the temperature was below 200°C. On the other hand, based on the 4pp data, the InGaAs-InAlAs SL samples presented in this work had n-type carrier concentration at least in the order of $\sim 10^{18}$–10^{19} cm^{-3} or above with growth temperature of 260–270°C measured by BET. The temperature monitoring method was unstated in Ref. [51] so their carrier concentration data cannot be directly compared with ours. Nonetheless, it is clear that the intrinsic InGaAs carrier concentration in the LT regime varies among different MBE systems. Overall, this indicates that in our samples the n-type LT InGaAs was not fully compensated even with Be doping concentration as high as 8×10^{18} cm^{-3} which suggests that heavier doping is needed. It would be beneficial if we know the exact wafer temperature profile, which helps carrier compensation of the InGaAs-InAlAs SL with different intrinsic carrier concentrations at different growth temperatures. The best way to do such temperature mapping is to use a NIR charge-coupled device (CCD) camera as a single-wavelength pyrometer [122]. Even if such equipment is unavailable, alternatively a compromising approach similar to what described in the ISP calibration part in Chapter 3 can be applied, where the detection spot of ~1 cm diameter of the InGaAs spectrometer can be adjusted to look at different positions of the full 3" wafer and measure the BET temperature. The bell-shape R_{sheet} profile is only observable for full 3" wafers G0688 and G0689. For all the other Q3" wafers, whether Be or C-doped, there is no clear correlation between R_{sheet} and the 4pp scan position, as illustrated by G0477 in Fig. 5.14. This can be explained as follows. The Q3" wafer is sandwiched by a pair of Mo inserts, with each of them having a cavity of Q3" shape, one slightly larger and another smaller than that of the Q3" wafer respectively. The insert above the wafer has two pairs of tiny "fingers"

of ∼3 mm long locating along the two straight edges and pointing towards the cavity. Hence, due to its complex geometry, the temperature profile of the Q3" wafer is much more complicated than that of the full 3" case, which is essentially radial symmetric. In addition, same as G0688, an unintentional movement could also happen for the Q3" wafer during measurement at different azimuths which can also skew the 4pp data and make it more complicated to interpret. Therefore the substrate stability during measurement needs to be improved to give more reliable 4pp data.

The standard deviations of the 4pp measurements are large for C-doped samples especially for G0477 which is close to 50%. To further understand such a difference between Be and C doping, two staircase structures were grown, one with GaAs on GaAs(001) and another with InGaAs on InP(001). Each structure consisted of several GaAs epilayers with different C filament currents corresponding to different target doping concentrations. Fig. 5.15 shows the ECV profiles of those two staircases. Unexpectedly, even with the same current applied, the InGaAs staircase has considerably lower doping concentration than that of GaAs. This is probably due to the fundamental difference between the two dopants: while Be is a group II alkali earth metal and works well as a p-dopant for all III-V elements, C is an amphoteric group IV element. When it is embedded in a group V site, it acts as an acceptor; However, when it is embedded in a group III site, it acts as a donor. Although in the case of GaAs grown at normal temperature, an As site being occupied by C is more dominant, it might not be the same case for LT growth of InGaAs, where the As sticking coefficient increases and those As sites are overcrowded with excess As incorporating as interstitial and antisites. It is possible that C tends to go onto a Ga site instead of an As site in the LT regime, which still requires more investigations. Furthermore, the ECV profile steps at $\sim 10^{19}$ cm^{-3} of InGaAs:C are not as sharp as those of GaAs:C, which indicates that further increasing the dopant flux did not increase the p-doping concentration as predicted. Overall, this suggests that carbon does not work very well as a p-dopant to compensate for the naturally n-type LT InGaAs.

In this stack of growths, G0689 has the highest average dark resistance of 17.69 MΩ/sq. The Be-doped InGaAs-InAlAs SL with the highest sheet resistance record up to date, which is $\sim$ 30 MΩ/sq, was reported by Globisch *et al.* in [61] with the sample grown at 130°C, Be-doped at 1.2×10^{19} cm^{-3} and annealed in a metalorganic vapor phase epitaxy (MOVPE) system in an As and P stabilized atmosphere at 600°C. G0689's sheet resistance is a bit lower but at least it is at the same order of magnitude with the best record. It is very likely that the sheet resistance can be further increased by heavier Be doping and hotter annealing. Practically these can create other issues though, as heavy Be doping has a tendency of cross-contaminating the GM, which can result in unintentional Be doping when growing other structures inside in same system. In addition, an annealing at a temperature

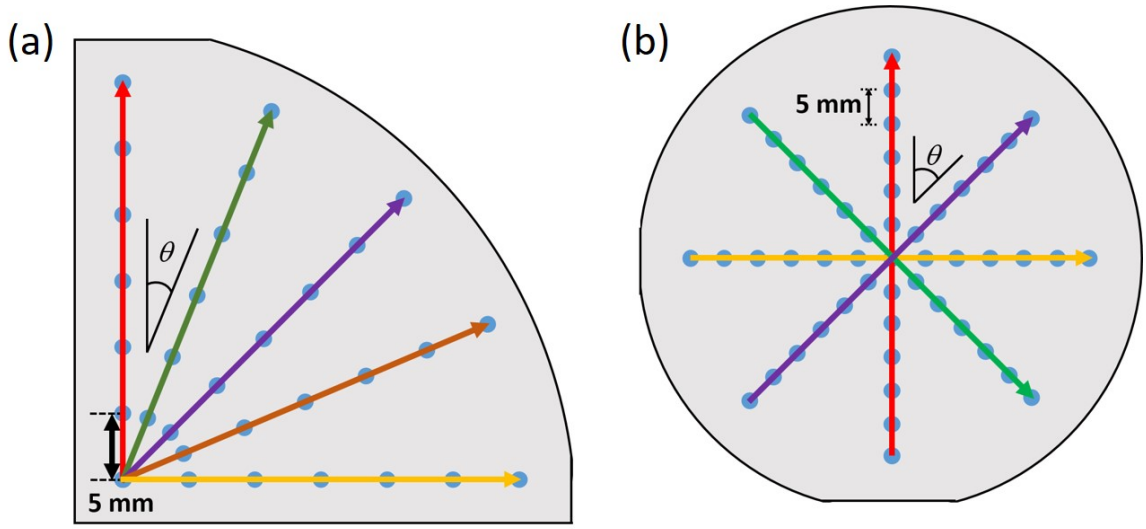

Figure 5.12: Sketches of 4pp measurement sites on the surface of Be or C-doped InGaAs-InAlAs SL grown on (a) Q3" SI InP(001) wafer for samples G0430, G0431, G0457, G0458, G0467, G0477, G0479 and G0541, with linear scans of azimuths $\vartheta = 0°$ (red), 22.5° (dark green), 45° (purple), 67.5° (brown) and 90° (orange); (b) on full 3" SI InP(001) wafer for samples G0688 and G0689, with linear scans of azimuths $\vartheta = 0°$ (red), 45° (purple), 90° (orange) and 135° (green).

above 600°C can result in quick In desorption and disrupt the crystalline quality. A MBE system dedicated to Be-doped growths, along with RTA with As and P supplied or control wafers to passivate undesired surface desorption might become necessary to carry out those procedures. The significant difference of R_{sheet} between G0541 and G0688 is unknown, given that their Be doping level, growth and annealing temperature were at least very close if not identical to each other. One possible explanation is their main difference as indicated in HRXRD, in which G0541 is reasonably lattice-matched, while G0688 has an unintentional compressive strain. However, the correlation between R_{sheet} and lattice strain requires further investigation. Last but not least, due to the gradual change of the conditions of the components inside GM from day to day, e.g. coating on the substrate heater, the substrate temperature can still vary from wafer to wafer even with the same T_c, material and geometry. One possible solution to improve the consistency of substrate temperature among those growths is to monitor the power output of the substrate heater as a function of time, which provides more info about how the substrate is being heated in order to fine-tune the heater as appropriate to give the desired substrate temperature.

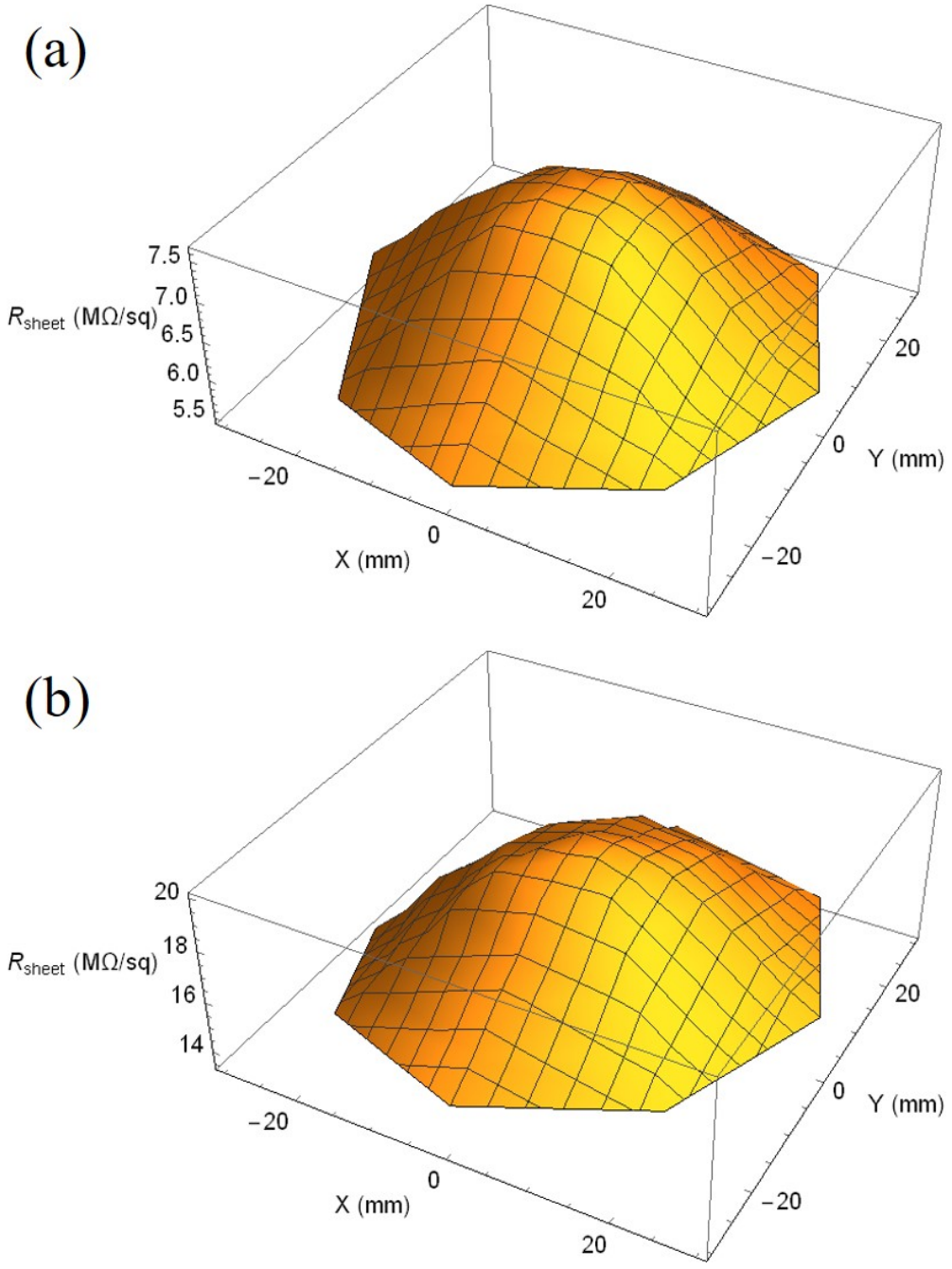

Figure 5.13: 3D plot of the 4pp sheet resistance profile (R_{sheet}) of (a) G0688 and (b) G0689.

Growth No.	Average R_{sheet} (Ω/sq)	R_{G20} (Ω)	R_{G50} (Ω)	R_{D20} (Ω)
G0400		0.88 ± 0.09 M		2.50 M
G0430	2.68 ± 0.22 k			25.99 ± 5.54 k
G0431	1.24 ± 0.95			3.20 ± 0.18 k
G0457	10.64 ± 1.74 k			
G0458	22.15 ± 12.07 k			
G0467	13.10 ± 4.15 k			
G0477	95.02 ± 45.08 k	34.46 ± 1.00 k	46.75 ± 1.28 k	
G0479	86.91 ± 22.48 k	31.80 ± 0.91 k	21.97 ± 0.91 k	
G0541	1.79 ± 0.30 M			
G0688	6.81 ± 0.65 M			
G0689	17.69 ± 1.82 M			

Table 5.7: Comparison of averaged 4pp sheet resistance (R_{sheet}) with PCA device resistance of PCA types G20, G50 and D20 of Be and C-doped InGaAs-InAlAs SL samples.

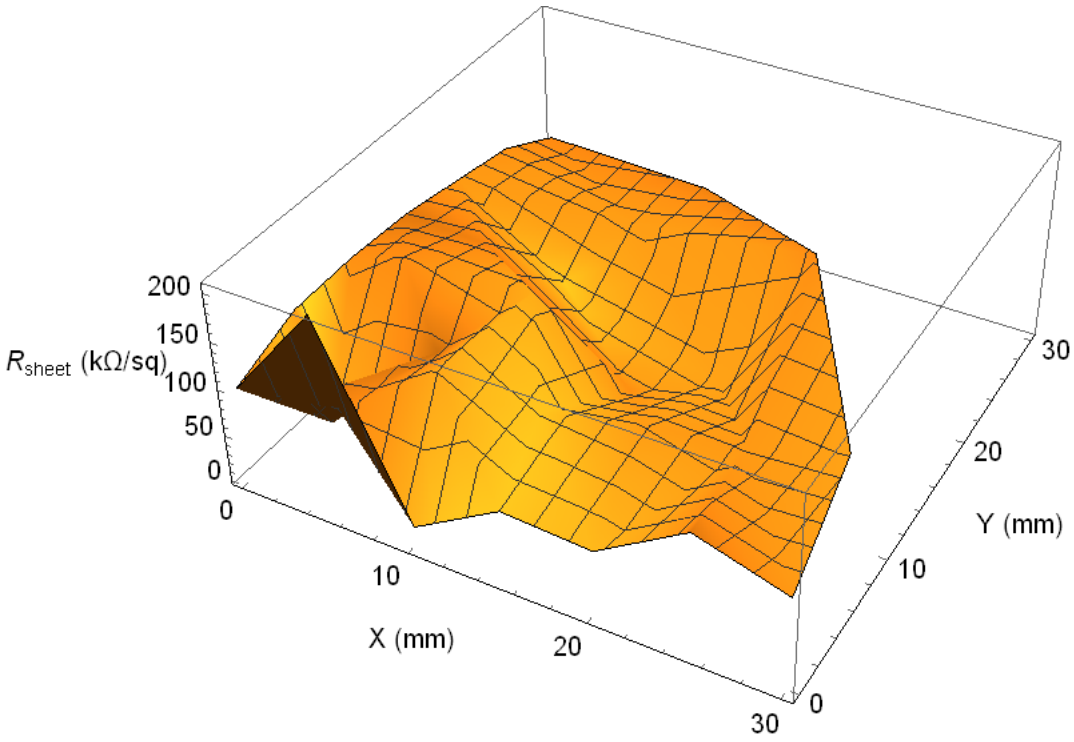

Figure 5.14: 3D plot of the 4pp sheet resistance profile (R_{sheet}) of G0477.

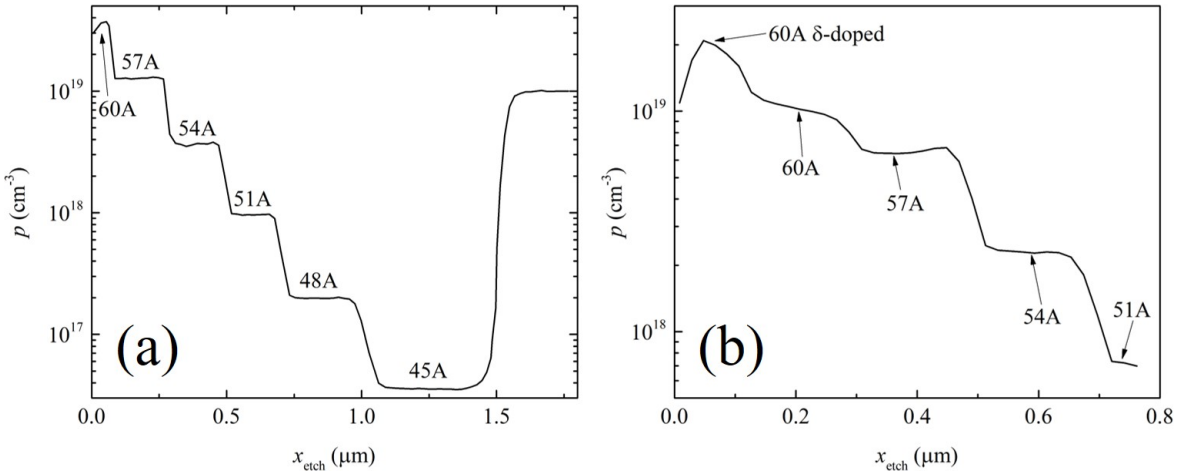

Figure 5.15: ECV profile of (a) GaAs:C and (b) InGaAs:C staircase structure.

5.3 THz TDS Measurement

Similar to LT GaAs based PCAs, standard clean-room processing procedures such as metal patterning, photolithography and RIE were applied to fabricate PCAs on the InGaAs-InAlAs SL samples. Three different Tx antennas: G20, G50, G100, with their geometries identical to each other except the size of the InGaAs-InAlAs SL gap for photo-excitation, were fabricated. On the other hand, due to the difficulty of processing 20D40P on InGaAs-InAlAs SL, only D20 antennas for Rx were prepared. Fig. 5.16 illustrates a SEM image of D20 antennas processed on sample G0542. The THz TDS setup, shown in Fig. 5.17, was similar to that in Fig. 4.15 in Chapter 4 except the pumping source was replaced with a 1550 nm telecom fiber laser. Besides, since InGaAs-InAlAs SL has dark resistance much lower than that of LT GaAs, a high bias voltage can result in burning the PCA. Therefore the square wave modulation was set to a lower bias of $V_{\text{pp}} = 20$ V across the Tx. THz TDS measurements were done with several combinations of Tx and Rx. In particular, the performance of LT InGaAs-InAlAs SL based Rx was compared with that of LT GaAs based Rx under 1550 nm excitation, with the later one operated via the two-step mid-gap defect states mediated excitation [71, 72, 73, 74, 75]. The representative THz TDS results, with the photocurrent measured in the Rx, presented in both temporal and spectral domain, are shown in Fig. 5.18. Overall, the Tx deposited on G0363 shows stronger THz amplitude than that of other Tx samples, which can possibly be explained by the fact that G0363 was MT grown while the rest were LT grown. Although it has long carrier lifetime and unsuitable to be used as Rx, MT grown InGaAs-InAlAs SL generates stronger THz wave

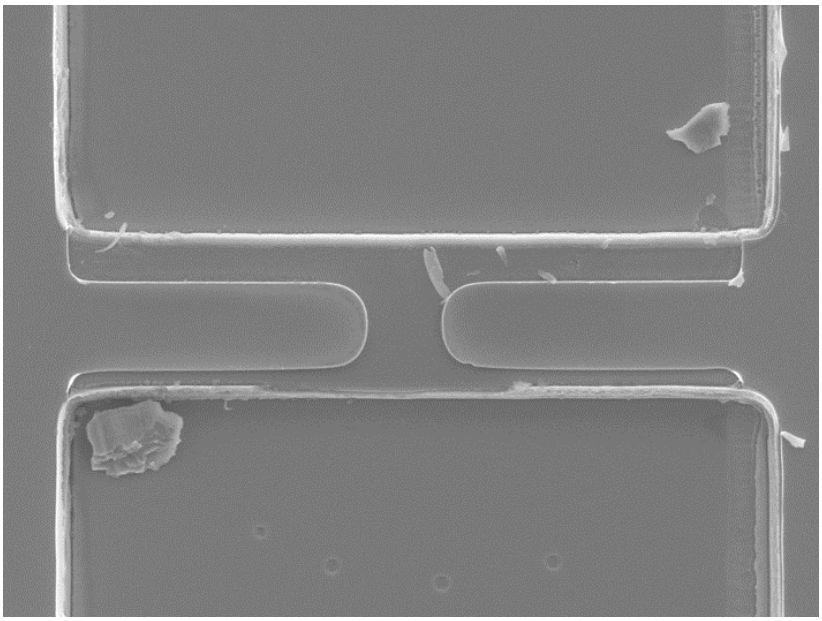

Figure 5.16: Illustrative PCA processing SEM image of THz Rx type D20 on sample G0542. Figure adopted and reprinted with permission from Nanofabrication Group, University of Waterloo and TeTechS Inc.

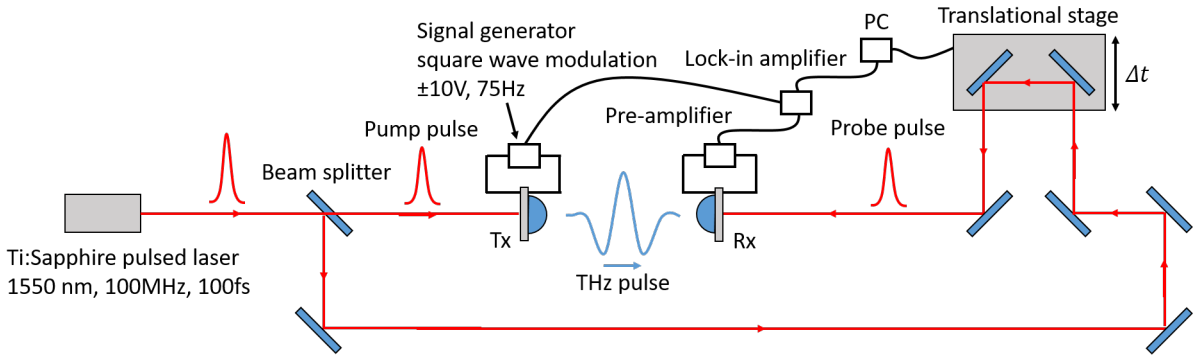

Figure 5.17: Optical setup of the 1550 nm THz TDS measurement, with Be-doped LT InGaAs-InAlAs SL based Tx and either Be-doped LT InGaAs-InAlAs SL or LT GaAs based Rx. Δt: time-delay between pump and probe pulse; PC: computer.

Tx			Rx			TDS Results		
Sample No.	Antenna Type	Growth No.	Sample No.	Antenna Type	Growth No.	THz Amp. (nA)	FWHM (ps)	BW (THz)
0150	G50	G0363	0125	D20, LT GaAs	G0287F	1.570	0.8333	0.9306
0150	G50	G0363	0062	D20, LT GaAs	G0287F	4.036	0.9667	0.8720
0025	G100	G0134	0084	D20, InGaAs	G0400	0.428	1.0000	0.7255
0150	G50	G0363	0152	D20, InGaAs	G0542	0.595	1.1500	0.5714
0075	G20	G0400	0066	D20, LT GaAs	G0287H	0.024	1.1667	0.6009
0075	G20	G0400	0066	D20, LT GaAs	G0287H	0.010	1.2333	0.5349

Table 5.8: Summary table of the 1550 nm pumped THz TDS measurements with different combinations of Tx and Rx. The Tx and Rx sample no., antenna type, growth no., corrected THz amplitude, FWHM and BW are presented.

and it is more suitable to be used as Tx than the LT grown counterpart as reported in [57]. On the other hand, it seems that the material choice is not a dominant factor of THz amplitude or pulse FWHM, but the annealing temperature in Rx plays an essential role in these quantities. G0287F, which is LT GaAs with a low annealing temperature of 460°C, exhibits shorter FWHM and broader THz BW; G0287H, also LT GaAs but with a higher annealing temperature of 610°C, exhibits longer FWHM and narrower THz BW; while G0400 and G0542, both InGaAs-InAlAs SL and annealed at ∼540°C, have both quantities intermediate.

All LT InGaAs-InAlAs SLs had the grow temperature purposely kept at 260–270°C, considerably higher than those grown at 130°C as reported in [57, 58, 60, 61]. Preliminary growths, which are not shown here, revealed that once the deposition begins, the epilayer surface turns amorphous very quickly if the growth temperature is < 200°C, measured by BET. Since very little detail about MBE growth conditions is mentioned in those reports,

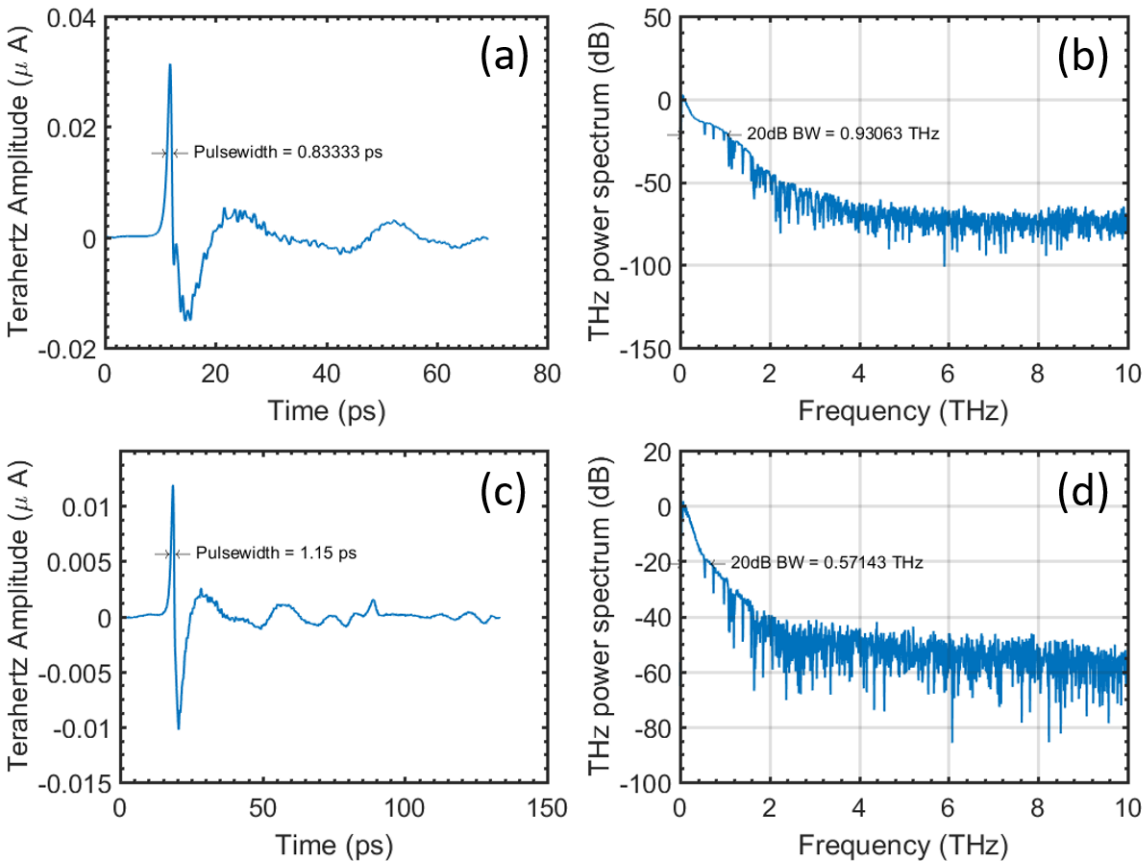

Figure 5.18: Photocurrent response in a 1550 nm pumped THz TDS system, with MT InGaAs-InAlAs SL based Tx no. 0150 and LT GaAs based Rx no. 0125 in (a) temporal and (b) spectral domain; with MT InGaAs-InAlAs SL based Tx no. 0150 and LT InGaAs-InAlAs SL based Rx no. 0152 in (c) temporal and (d) spectral domain. Figure adopted and reprinted with permission from Nanofabrication Group, University of Waterloo and TeTechS Inc.

especially the temperature measurement method which is not stated either, it is difficult to compare the results in this work with the aforementioned reports. Nonetheless, the 260–270°C growths still limited the excess As embedded and thus the THz BW, which concludes that further optimization is needed. To improve the 1550 nm pumped THz TDS performance, it is possible to further reduce the growth temperature of InGaAs-InAlAs SLs by ∼30–40°C, close to the lowest one for LT GaAs in Chapter 5, while maintaining single crystallinity to a certain degree. However, epitaxial roughness starts occurring at this temperature too, so precise flux calibration and flux stability are needed to grow the SL lattice-matched on InP and minimize roughening.

Chapter 6

InAlGaAs Based Photonic Power Converter

6.1 MBE Growth and Characterizations

Since the early 1980s, there had been several reports, mostly empirical, attempted to quantitatively correlate the InAlGaAs bandgap with its group III compositions [123, 124, 125]. In this work, the empirical expression in Ref. [123] is used. The bandgap of $In_wAl_vGa_uAs$ is written as a function of group III compositions u, v and w with $u + v + w = 1$:

$$E_g = 0.360 + 0.629u + 2.093v + 0.436u^2 + 0.577v^2 + 1.013uv \tag{6.1}$$

It is also assumed that $In_wAl_vGa_uAs$ obeys Vegard's law, in which its lattice constant varies linearly with those of the binary compounds InAs, AlAs and GaAs:

$$a_{\mathrm{InAlGaAs}} = wa_{\mathrm{InAs}} + va_{\mathrm{AlAs}} + ua_{\mathrm{GaAs}} \tag{6.2}$$

With the condition $a_{\mathrm{InAlGaAs}} = a_{\mathrm{InP}}$, Eqs. 6.1 and 6.2 can be solved together to find the group III compositions corresponding to different bandgap energies while InAlGaAs is lattice-matched to InP. All the ternary and quaternary epilayers presented in this chapter were targeted to be lattice-matched to InP, with the strongly tensile-strained $In_{0.3}Al_{0.7}As$ etch stop layer as the only exception. All growths were done under As Op of ∼2, substrate temperature at ∼460–490°C and a target growth rate of 2.5Å/s for all ternary and quaternary epilayers.

Before growing an MJ PPC device, a series of preliminary single p-n junction and tunnel diode samples were grown to optimize the thicknesses and doping concentrations for the

Name	Material	Thickness (Å)
Substrate	SI (Fe) InP(001)	
Quaternary Layer	$In_wAl_vGa_uAs$	10000
Cap Layer	$In_{0.526}Ga_{0.474}As$	100

Growth No.	Bandgap (eV)	u	v	w
G0341	1.30	0.117	0.356	0.527
G0343	1.20	0.181	0.291	0.528
G0345	0.92	0.357	0.111	0.532
G0389	0.78	0.448	0.019	0.533
G0501	0.90	0.371	0.097	0.532

Table 6.1: Growth schematic (top) and the relation between $In_wAl_vGa_uAs$ bandgap and Ga, Al, In compositions u, v, w (bottom) of calibration samples G0341, G0343, G0345, G0389 and G0501 for ellipsometry.

best PPC performance. Similar to typical solar cells, each p-n junction structure consists of an active region, also known as the absorber, which includes an emitter layer and a base layer. They are sandwiched by a front surface field (FSF) layer and a back surface field (BSF) layer with wider bandgap. On the other hand, a tunnel diode consists of a pair of heavily-doped p^{++} and n^{++} layers surrounded by cladding layers. To determine the most appropriate group III compositions in InAlGaAs for those layers in PPCs, several calibration structures with selective bandgaps: G0341, G0343, G0345, G0389 and G0501, all with Fe-doped SI InP(001) used as substrates, were grown for ellipsometry characterizations. The schematic, target compositions and bandgaps of those samples are shown in Table 6.1. The schematics of the 1st set of preliminary SJ devices: G0384, G0386, G0433 and G0448 are shown in Tables 6.2 and 6.3. They were all grown on Zn-doped p-type InP(001) substrates with various base and emitter target bandgaps for tests. For p-dopant, Be was used for G0384 and G0386 while C was used for G0433 and G0448. G0448 had its design based on the 1st batch of SJ structures but with a thicker base layer, a strongly tensile-strained $In_{0.3}Al_{0.7}As$ etch stop right after the FSF layer, and a Si δ-doping layer between the two $In_{0.526}Ga_{0.474}As$ cap layers.

After ellipsometry and preliminary device tests, the materials for different layers for all the growths onward are listed in the following: $In_{0.527}Al_{0.356}Ga_{0.117}As$ for FSF, BSF, p^{++}, n^{++} and buffer layers; the 1310 nm excitable $In_{0.532}Al_{0.097}Ga_{0.371}As$ for base and emitter; $In_{0.526}Ga_{0.474}As$ for initial buffer and cap layer; $In_{0.53}Al_{0.47}As$ for cladding and $In_{0.3}Al_{0.7}As$ for etch stop. The schematics of the 2nd set of SJ devices: G0587, G0588, G0589, G0623, G0664, G0665 and G0666 are shown in Tables 6.4 and 6.5. They were all grown on Zn-

Name	Material	Thickness (Å)	Doping (cm^{-3})
Substrate	p^+(Zn) InP(001)		
Initial Buffer	$In_{0.527}Al_{0.356}Ga_{0.117}As$:Be or C	1000	1×10^{18}
BSF	$In_{0.527}Al_{0.356}Ga_{0.117}As$:Be or C	500	5×10^{18}
Base	$In_wAl_vGa_uAs$:Be or C	6000	2×10^{16}
Emitter	$In_wAl_vGa_uAs$:Si	1000	-1×10^{18}
FSF	$In_{0.527}Al_{0.356}Ga_{0.117}As$:Si	4000	-5×10^{18}
Cap Layer	$In_{0.526}Ga_{0.474}As$:Si	500	-5×10^{18}

Growth No.	P-Dopant	Bandgap (eV)	u	v	w
G0384	Be	1.06	0.267	0.203	0.530
G0386	Be	0.98	0.319	0.150	0.531
G0433	C	0.90	0.371	0.097	0.532

Table 6.2: Growth schematic (top) and the relation between $In_wAl_vGa_uAs$ bandgap and Ga, Al, In compositions u, v, w (bottom) for single-junction (SJ) samples G0384, G0386 and G0433. BSF: Back surface field, FSF: Front surface field.

Name	Material	Thickness (Å)	Doping (cm^{-3})
Substrate	p^+(Zn) InP(001)		
Initial Buffer	$In_{0.527}Al_{0.356}Ga_{0.117}As$:C	1000	1×10^{18}
BSF	$In_{0.527}Al_{0.356}Ga_{0.117}As$:C	500	5×10^{18}
Base	$In_{0.532}Al_{0.097}Ga_{0.371}As$:C	25000	2×10^{16}
Emitter	$In_{0.532}Al_{0.097}Ga_{0.371}As$:Si	3000	-1×10^{18}
FSF	$In_{0.527}Al_{0.356}Ga_{0.117}As$:Si	4000	-5×10^{18}
Etch Stop	$In_{0.3}Al_{0.7}As$:Si	100	-2×10^{18}
Cap Layer	$In_{0.526}Ga_{0.474}As$:Si	220	-2×10^{18}
δ-Doping	Si		δ -1×10^{13} cm^{-2}
Cap Layer	$In_{0.526}Ga_{0.474}As$:Si	30	-2×10^{18}

Table 6.3: Growth schematic of single-junction (SJ) sample G0448. All layers have 3D doping displayed in cm^{-3} with the exception of the Si δ-doping layer which is in cm^{-2}. BSF: Back surface field, FSF: Front surface field.

Name	Material	Thickness (Å)	Doping (cm^{-3})
Substrate	p^+(Zn) InP(001)		
Initial Buffer	$In_{0.526}Ga_{0.474}As$:Be	1000	2×10^{18}
Cap Layer	$In_{0.526}Ga_{0.474}As$:Be	d_1	2×10^{19}
BSF	$In_{0.527}Al_{0.356}Ga_{0.117}As$:Be	500	5×10^{18}
Base	$In_{0.532}Al_{0.097}Ga_{0.371}As$:Be	d_2	2×10^{16}
Emitter	$In_{0.532}Al_{0.097}Ga_{0.371}As$:Si	1000	-1×10^{18}
FSF	$In_{0.527}Al_{0.356}Ga_{0.117}As$:Si	4000	-5×10^{18}
Etch Stop 1	$In_{0.3}Al_{0.7}As$:Si	100	-2×10^{18}
Cap Layer	$In_{0.526}Ga_{0.474}As$:Si	1000	-5×10^{18}

Growth No.	d_1	d_2
G0587	1000	40000
G0588	1000	7420
G0664	1000	2050
G0665	2000	5960
G0666	2000	11410

Table 6.4: Growth schematic (top), $In_{0.526}Ga_{0.474}As$ cap layer and $In_{0.532}Al_{0.097}Ga_{0.371}As$ base layer thickness d_1, d_2 (bottom) of single-junction (SJ) samples G0587, G0588, G0664, G0665 and G0666. BSF: Back surface field, FSF: Front surface field.

doped InP(001) substrates and structurally similar except for the base layer thicknesses, which are 40000, 7420, 2050, 5960 and 11410 Å respectively. The former two and the latter three have $In_{0.526}Ga_{0.474}As$ cap layer thicknesses of 1000 and 2000 Å respectively. G0589 and G0623, both grown on S-doped InP(001) substrates, are the inverted versions of G0588. These two are structurally similar except G0589 has two $In_{0.3}Al_{0.7}As$ etch stop layers with an $In_{0.526}Ga_{0.474}As$ layer between them, while G0623 only has one $In_{0.3}Al_{0.7}As$ etch stop layer. The schematic of the TD trial devices: G0624, G0625 and G0675 are shown in Table 6.6. They were all grown on S-doped InP(001) substrates and structurally similar except the p^{++} layers of G0624 and G0675 were Be-doped, while that of G0625's was C-doped. With their structures being identical, the only difference between G0624 and G0675 is that G0624 was grown at 480°C for the whole structure, while the substrate temperature of G0675 was purposely dropped from 480 to 460°C right after the tunnel interface which was between the 150Å n^{++}(Si) and p^{++}(Be) epilayers.

Finally, the schematic of the TJ PPC structure G0690 is shown in Table. 6.7, which can be considered as a combination of the SJ structures G0587 and G0588. The *in situ* growth parameters over time of samples G0345, G0433 and G0589, which were grown

Name	Material	Thickness (Å)	Doping (cm^{-3})
Substrate	n^+(S) InP(001)		
Initial Buffer	$In_{0.526}Ga_{0.474}As$:Si	1000	-2×10^{18}
Etch Stop	$In_{0.3}Al_{0.7}As$:Si	100	-2×10^{18}
Cap Layer	$In_{0.526}Ga_{0.474}As$:Si	1000	-5×10^{19}
Etch Stop	$In_{0.3}Al_{0.7}As$:Si	100	-2×10^{18}
FSF	$In_{0.527}Al_{0.356}Ga_{0.117}As$:Si	4000	-5×10^{18}
Emitter	$In_{0.532}Al_{0.097}Ga_{0.371}As$:Si	1000	-1×10^{18}
Base	$In_{0.532}Al_{0.097}Ga_{0.371}As$:Be	7420	2×10^{16}
BSF	$In_{0.527}Al_{0.356}Ga_{0.117}As$:Be	500	5×10^{18}
Cap Layer	$In_{0.526}Ga_{0.474}As$:Be	1000	2×10^{19}

Name	Material	Thickness (Å)	Doping (cm^{-3})
Substrate	n^+(S) InP(001)		
Initial Buffer	$In_{0.526}Ga_{0.474}As$:Si	1000	-2×10^{18}
Etch Stop	$In_{0.3}Al_{0.7}As$:Si	100	-2×10^{18}
FSF	$In_{0.527}Al_{0.356}Ga_{0.117}As$:Si	4000	-5×10^{18}
Emitter	$In_{0.532}Al_{0.097}Ga_{0.371}As$:Si	1000	-1×10^{18}
Base	$In_{0.532}Al_{0.097}Ga_{0.371}As$:Be	7420	2×10^{16}
BSF	$In_{0.527}Al_{0.356}Ga_{0.117}As$:Be	500	5×10^{18}
Cap Layer	$In_{0.526}Ga_{0.474}As$:Be	1000	2×10^{19}

Table 6.5: Growth schematics of single-junction (SJ) samples G0589 (top) and G0623 (bottom). BSF: Back surface field, FSF: Front surface field.

Name	Material	Thickness (Å)	Doping (cm^{-3})
Substrate	n^{+}(S) InP(001)		
Initial Buffer	$In_{0.526}Ga_{0.474}As$:Si	1000	-2×10^{18}
Cap Layer	$In_{0.526}Ga_{0.474}As$:Si	1000	-5×10^{18}
Cladding	$In_{0.53}Al_{0.47}As$:Si	300	-1×10^{18}
n^{++}	$In_{0.527}Al_{0.356}Ga_{0.117}As$:Si	150	-5×10^{19}
p^{++}	$In_{0.527}Al_{0.356}Ga_{0.117}As$:Be or C	150	2.68×10^{19}
Cladding	$In_{0.53}Al_{0.47}As$:Be	300	5×10^{18}
Buffer	$In_{0.527}Al_{0.356}Ga_{0.117}As$:Be	150	4×10^{17}
Etch Stop	$In_{0.3}Al_{0.7}As$:Be	100	2×10^{18}
Cap Layer	$In_{0.526}Ga_{0.474}As$:Be	1000	2×10^{19}

Growth No.	Dopant of p^{++}	T_g (°C)
G0624	Be	480
G0625	C	480
G0675	Be	$480 \rightarrow 460$

Table 6.6: Growth schematic of tunnel diodes (TDs) G0624, G0625 and G0675 (top), with G0625's p^{++} layer being C-doped (bottom). When the deposition was switched from n^{++} to p^{++} layer, G0675's growth temperature (T_g) was ramped down from 480 to 460°C.

Name	Material	Thickness (Å)	Doping (cm^{-3})
Substrate	p^+(Zn) InP(001)		
Initial Buffer	$In_{0.526}Ga_{0.474}As$:Be	1000	2×10^{18}
Cap Layer 1	$In_{0.526}Ga_{0.474}As$:Be	2000	2×10^{19}
Subcell 1: BSF	$In_{0.527}Al_{0.356}Ga_{0.117}As$:Be	500	5×10^{18}
Subcell 1: Base	$In_{0.532}Al_{0.097}Ga_{0.371}As$:Be	40000	2×10^{16}
Subcell 1: Emitter	$In_{0.532}Al_{0.097}Ga_{0.371}As$:Si	1000	-1×10^{18}
Subcell 1: FSF	$In_{0.527}Al_{0.356}Ga_{0.117}As$:Si	500	-5×10^{18}
TD: Cladding	$In_{0.53}Al_{0.47}As$:Si	300	-1×10^{18}
TD: n^{++}	$In_{0.527}Al_{0.356}Ga_{0.117}As$:Si	150	-5×10^{19}
TD: p^{++}	$In_{0.527}Al_{0.356}Ga_{0.117}As$:Be	150	2.68×10^{19}
TD: Cladding	$In_{0.53}Al_{0.47}As$:Be	300	5×10^{18}
Subcell 2: BSF	$In_{0.527}Al_{0.356}Ga_{0.117}As$:Be	500	5×10^{18}
Subcell 2: Base	$In_{0.532}Al_{0.097}Ga_{0.371}As$:Be	6480	2×10^{16}
Subcell 2: Emitter	$In_{0.532}Al_{0.097}Ga_{0.371}As$:Si	1000	-1×10^{18}
Subcell 2: FSF	$In_{0.527}Al_{0.356}Ga_{0.117}As$:Si	4000	-5×10^{18}
Etch Stop	$In_{0.3}Al_{0.7}As$:Si	100	-2×10^{18}
Cap Layer 2	$In_{0.526}Ga_{0.474}As$:Si	1000	-5×10^{18}

Table 6.7: Growth schematic of the twin junction (TJ) structure G0690, which consists of two subcells interconnected by a tunnel diode (TD). BSF: Back surface field, FSF: Front surface field.

on SI (Fe), p^+(Zn) and n^+(S) Q3" InP(001) substrates respectively, are shown in Figs. 6.1–6.3. Since those InAlGaAs calibration samples for ellipsometry were grown on SI InP substrates, the substrate temperature control approach and the temporal profile of temperature were quite similar to that of MT InGaAs-InAlAs SL in Chapter 5, where the thermocouple temperature T_c was continuously decreased to keep T_{BET} constant at 470°C, as shown in Fig. 6.1. T_{pyro} is also added into the graph for comparison, which was ∼10°C higher than T_{BET} during As soak but boosted to 540°C during InAlGaAs layer deposition due to the tremendous extra radiation from the group III cells when they were opened. On the other hand, BET did not work properly as the T_{BET} reading was even higher than that of T_c as seen in Fig. 6.2. Due to the absence of calibration coefficients for the p^+(Zn) InP substrate, the coefficients for SI InP were used which turned out did not give the correct value. Therefore, the only reliable temperature monitoring tool here was the SVT pyrometer, but similar to the case of SI substrate, the T_{pyro} reading made sense only during As soak without radiation from the group III cells. T_{ISP} is also added to the graph for comparison and its reading differs from T_{pyro} by only ±10°C. In most of the other growths, T_{ISP} reads higher than even the T_c since the epilayers are transparent to the substrate heater in the NIR range, which makes it unusable. However, in this scenario, the InAlGaAs deposition gradually decreased the T_{ISP} reading, which made it eventually assisted in substrate temperature monitoring, especially when the T_{BET} was completely inapplicable and T_{pyro} jumped by ∼50–60°C when the group III shutters were open. The temporal dependence of temperature of the n^+(S) InP substrate, shown in Fig. 6.3, was similar to that of SI InP, where both T_{BET} and T_{pyro} had reasonable readings with the difference between those two only up to ∼20°C. Even with constant As valve opening, the BFM reading increased over time as explained in Chapter 2, while the SRS and GM ion gauges gave more steady readings which were more reliable for As Op monitoring. Overall, all growths exhibited excellent epitaxial growth qualities with the 470 nm reflection either remained stable after damping or just dropped slightly, in which the latter one was not necessary attributed to wafer roughening but possibly curvature formation of the surface epilayer due to lattice relaxation. The Nomarski and black-box images of representative growths are shown in Figs. 6.4–6.7. Most growths in this study exhibit nice epitaxial quality as in Figs. 6.4(a) and 6.6(b), but a few of those have morphology issues. G0589 and G0623 show relaxation lines and hazy surfaces, due to the fact that one or two highly strained $In_{0.3}Al_{0.7}As$ epilayers were grown at the bottom of each structure which caused lattice relaxation for the rest of the structure. For G0690, the In flux was overshot which also caused lattice relaxation in this TJ device.

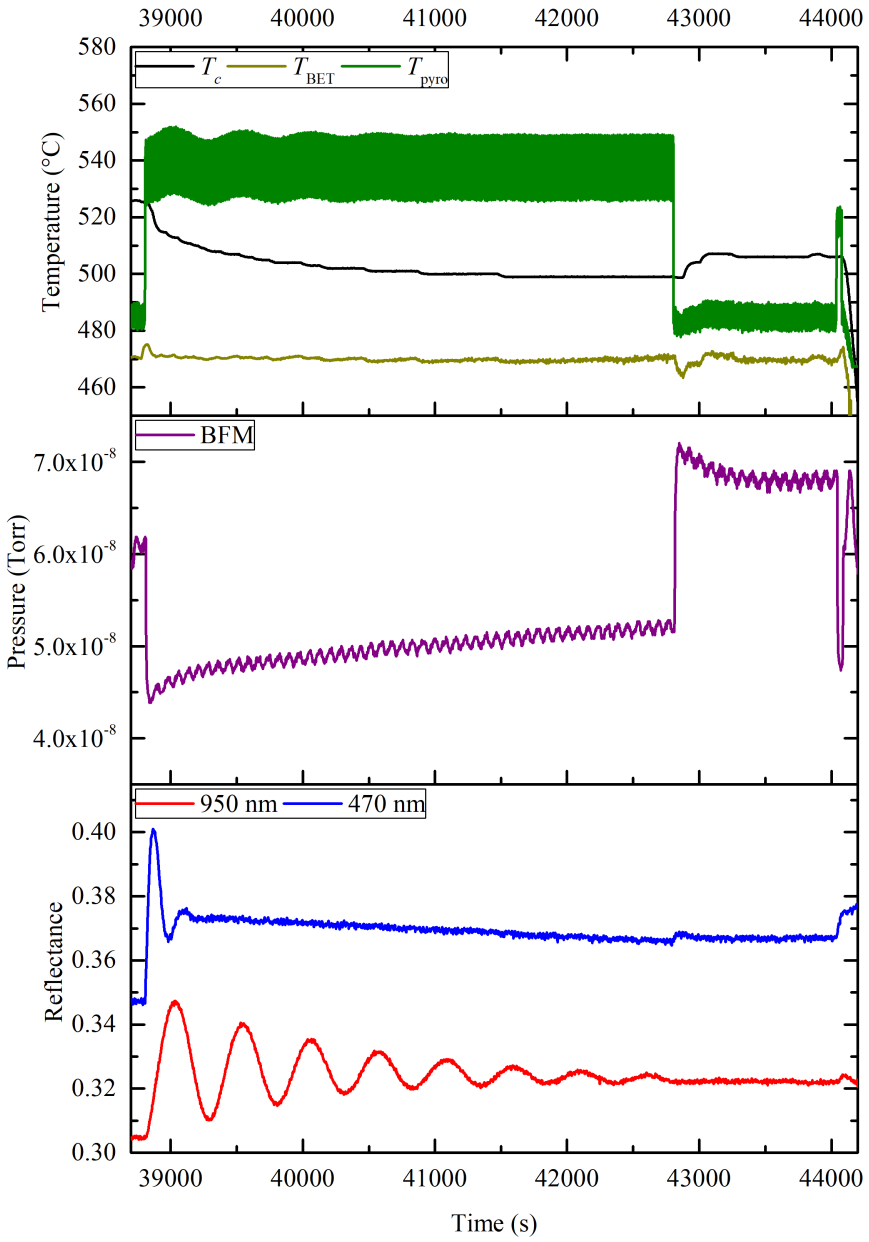

Figure 6.1: *In situ* growth parameters during $In_{0.532}Al_{0.111}Ga_{0.357}As$ and $In_{0.526}Ga_{0.474}As$ deposition of G0345. From top to bottom: T_c (black), T_{BET} (dark yellow) and T_{pyro} (dark green); BFM (purple) pressure; 950 nm (red) and 470 nm (blue) reflectance.

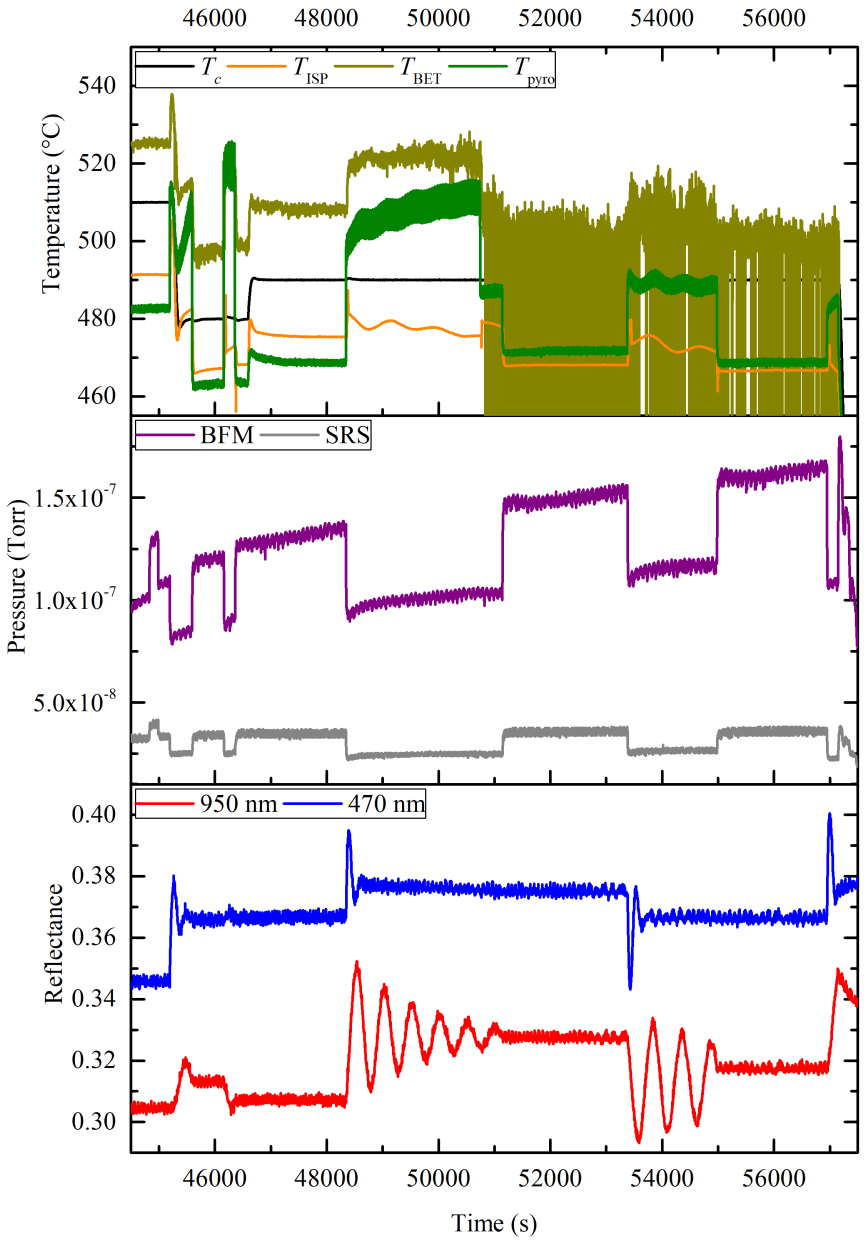

Figure 6.2: *In situ* growth parameters during p-n junction deposition of G0433. From top to bottom: T_c (black), T_{BET} (dark yellow), T_{ISP} (orange) and T_{pyro} (dark green); BFM (purple) and SRS (gray) pressure; 950 nm (red) and 470 nm (blue) reflectance.

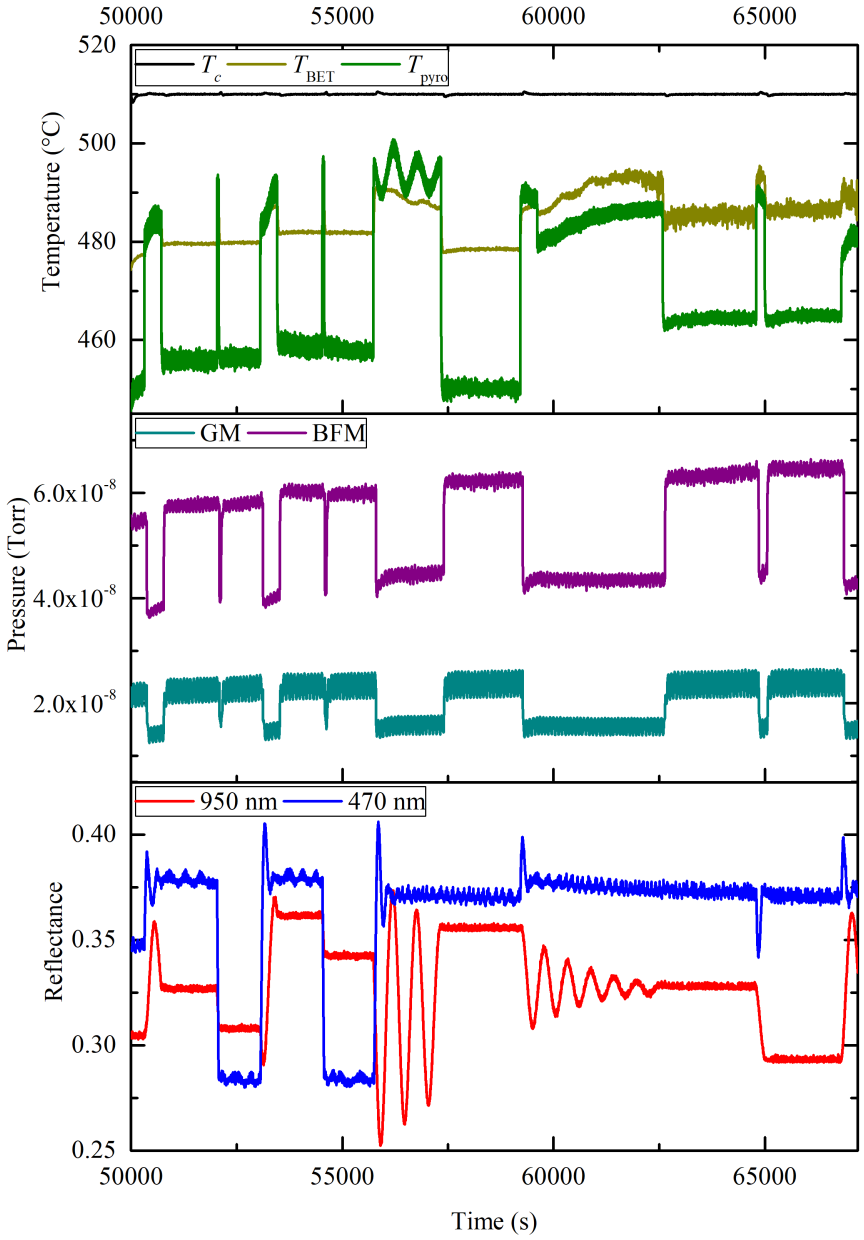

Figure 6.3: *In situ* growth parameters during p-n junction deposition of G0589. From top to bottom: T_c (black), T_{BET} (dark yellow) and T_{pyro} (dark green); BFM (purple) and GM (cyan) pressure; 950 nm (red) and 470 nm (blue) reflectance.

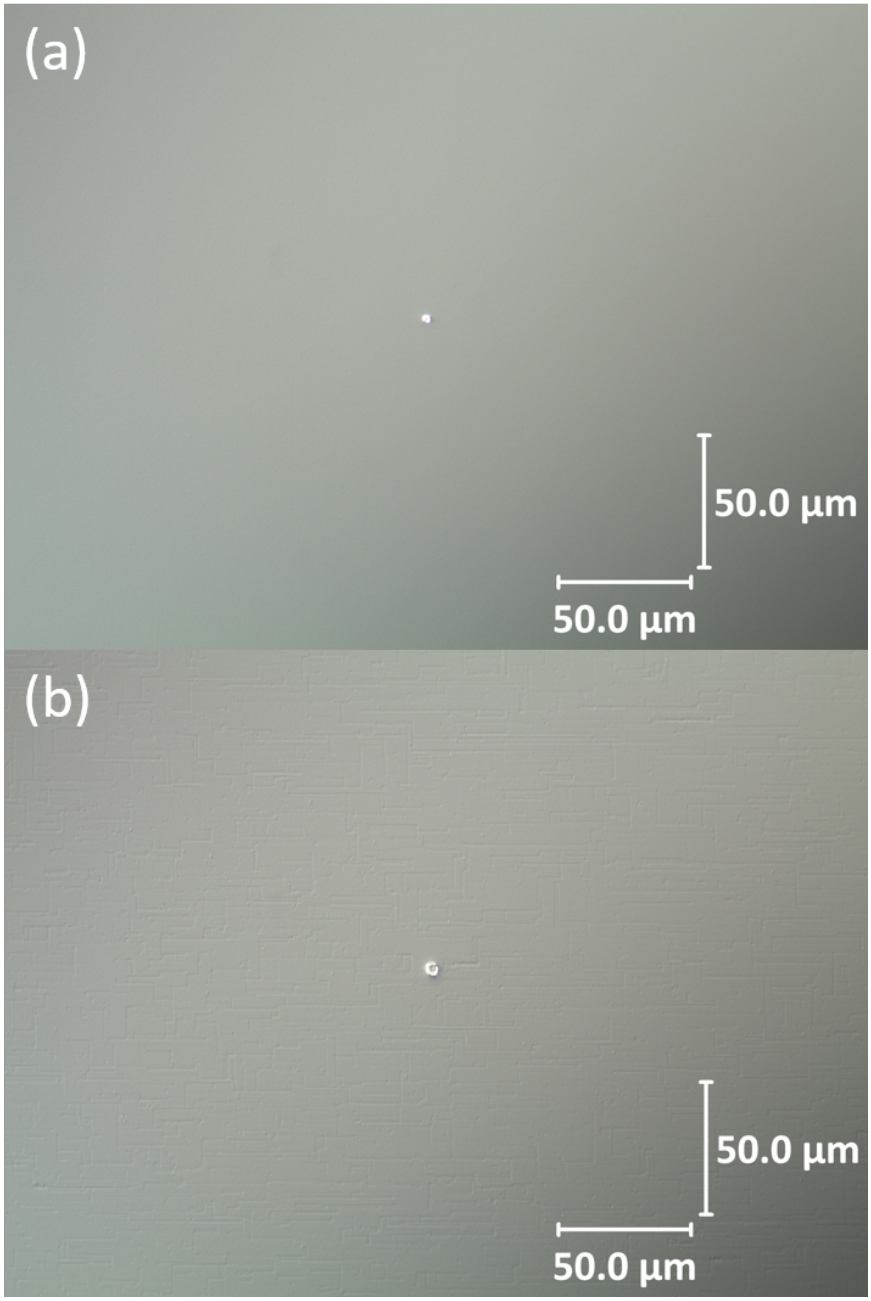

Figure 6.4: Nomarski images at 40× magnification of (a) G0588 and (b) G0589.

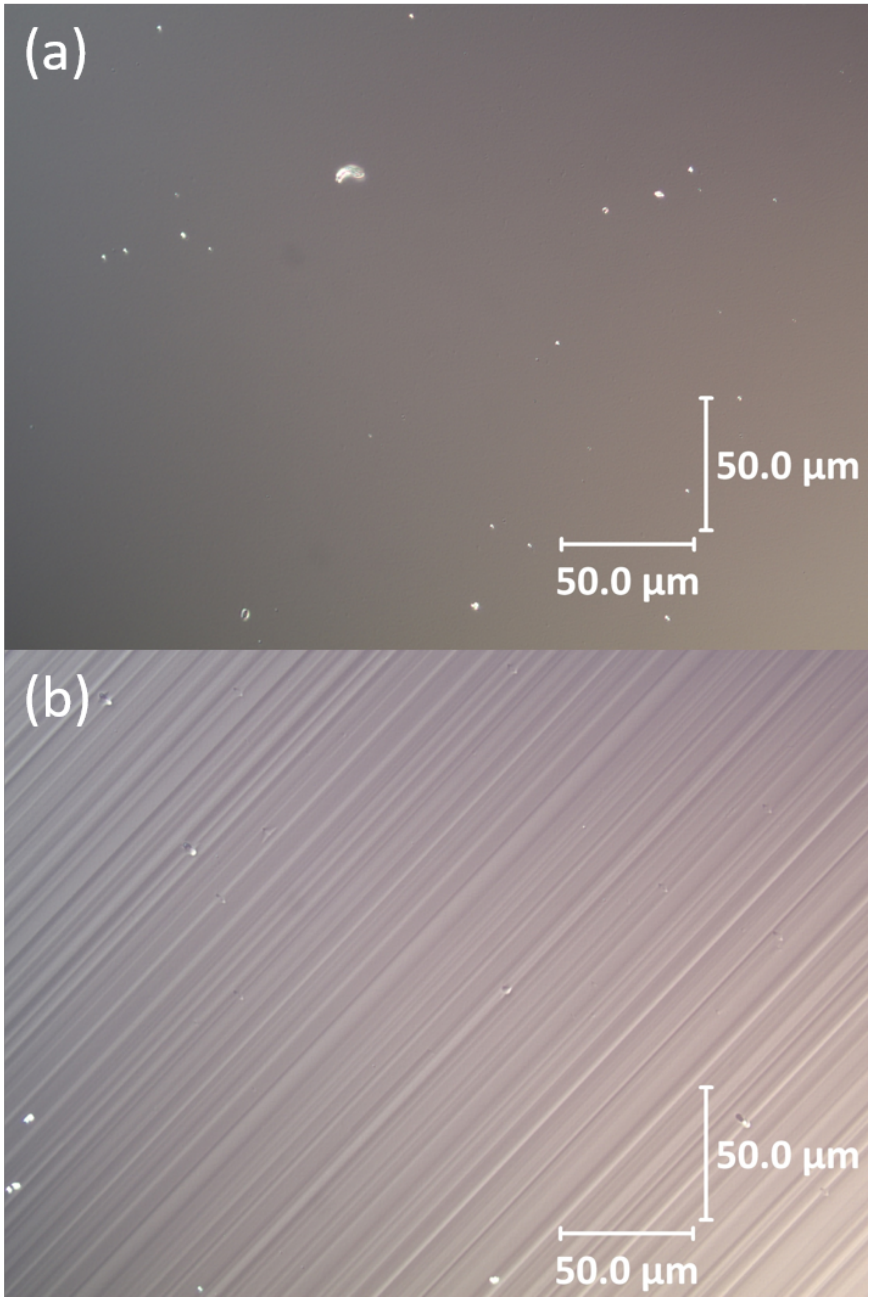

Figure 6.5: Nomarski images at 40× magnification of (a) G0675 and (b) G0690.

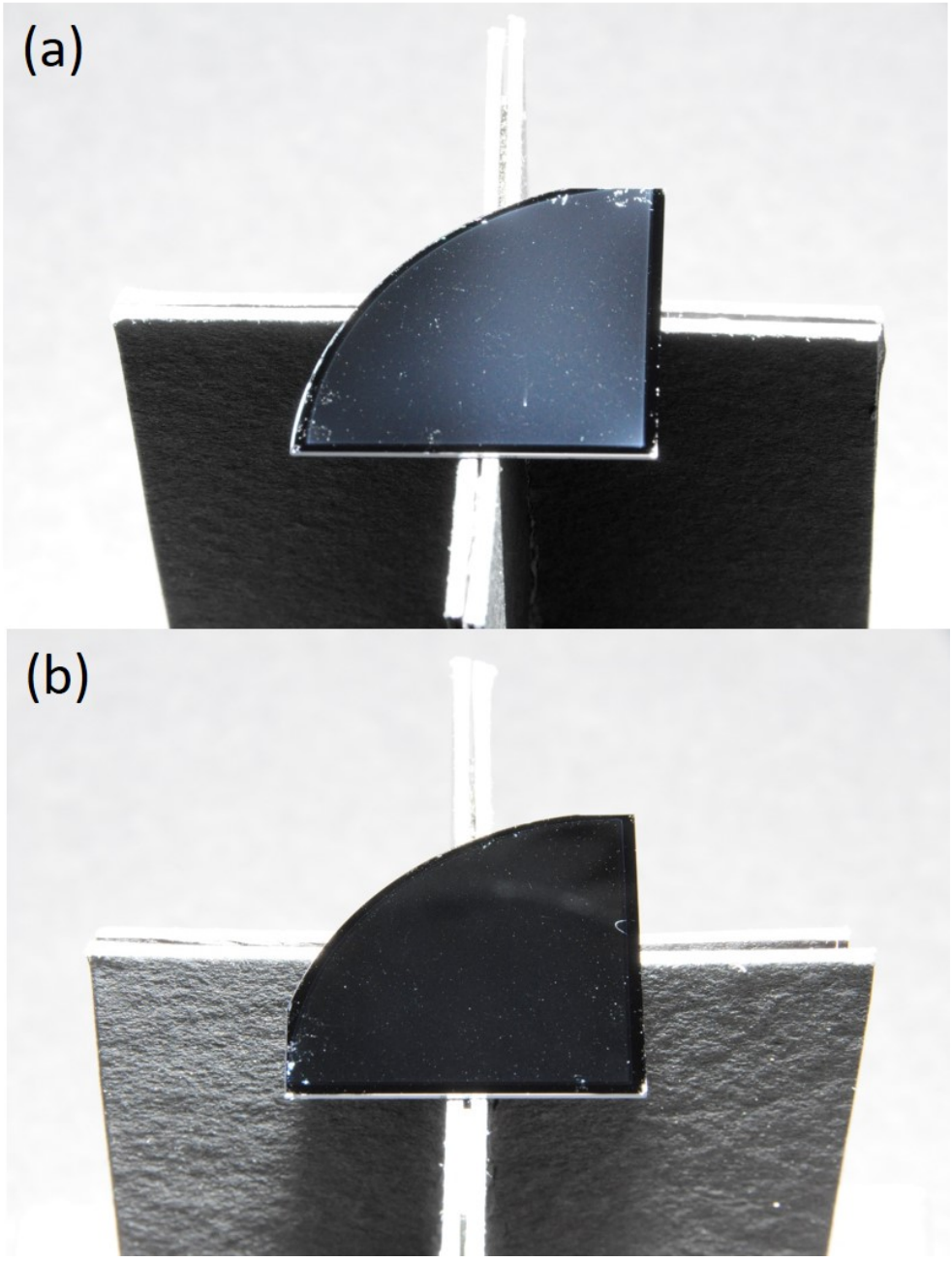

Figure 6.6: Black-box images with an exposure time of 5 ms of (a) G0623 and (b) G0625.

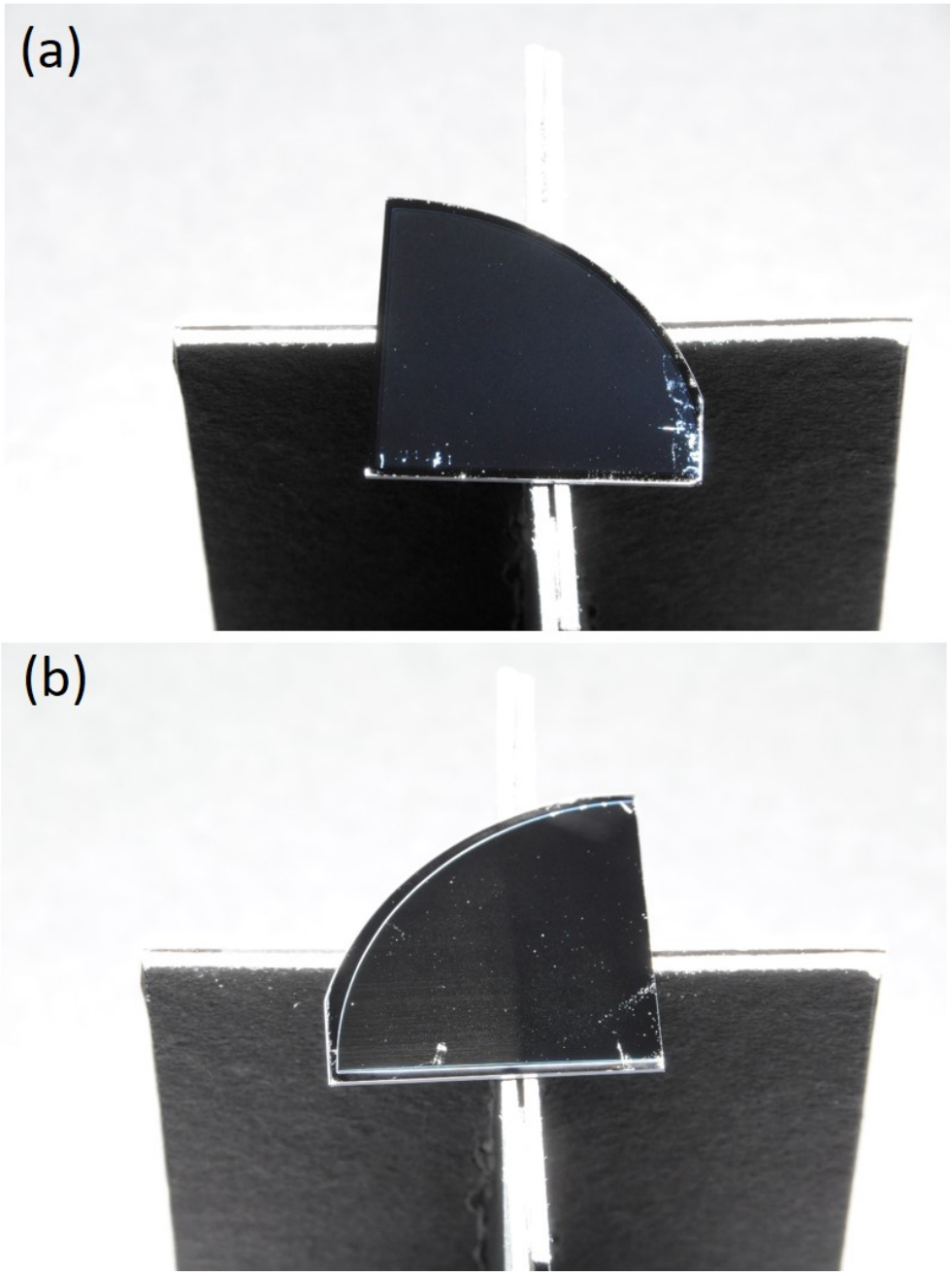

Figure 6.7: Black-box images with an exposure time of 5 ms of (a) G0675 and (b) G0690.

6.2 HRXRD Fitting of Multi-Layers vs Group III Flux Deviations

The HRXRD TA scans of selective samples in the present work are shown in Fig. 6.8. Unlike structures in previous chapters which can have their epilayer thicknesses fitted by Pendellösung fringes, separation between SL satellite peaks and oscillating optical reflectance from the substrate, the fittings of those ellipsometry calibration and PPC device growths are particularly challenging. For the structures in previous chapters that were grown with all group III cell temperatures set constant throughout the entire deposition, BFM is a reasonably reliable technique in cross-checking with the fitting results of HRXRD so that when there is a flux drift, it can be tracked easily. Unfortunately, this is not the case for quaternary p-n junctions, in which the cell temperature setpoints and hence the growth rates and group III compositions change significantly for every single layer. In particular, each p-n junction consists of 6 to 9 different ternary and quaternary compounds with various group III flux combinations. The flux stability was uncertain especially for those intermediate epilayers grown in the middle of the growth without BFM checking. Hence the number of unknown flux drifts can be over 20, much more than the case of growths with constant cell temperatures and the number of unknown flux drifts of only 2–3, one for each group III cell. In this section, a different approach is used for the HRXRD RADS fitting. To reduce the number of unknowns, the RADS model for each structure was slightly modified, in which adjacent epilayers of the same material, with the same group III compositions but different dopant or doping concentrations, were merged as one single epilayer. In addition, instead of fitting directly for thickness and composition, they were rewritten as functions of flux deviation $r = \Delta\phi/\phi = (\phi' - \phi)/\phi$ of each group III cell. Repetitive manual fittings were conducted for those structures with r_{Ga}, r_{Al} and r_{In} as variables for each epilayer. The fitting results of selective growths are shown in Tables 6.8–6.10. d and d' are the target and fitted thicknesses, u, v, w are the target and u', v', w' are the fitted group III compositions respectively.

Overall, it is discovered that an additional InAs epilayer, which is not included in any structure schematic, must be inserted between the InP(001) substrate and the 1$^{\mathrm{st}}$ epilayer, whether ternary or quaternary, in order to get a good fitting with sufficient Pendellösung fringe overlapping of the scan (blue) with the model (red). This proves that there is always a thin InAs epilayer unintentionally formed during the oxide desorption of InP substrate soaked with As. In particular, a slight change in such InAs formation thickness can strongly alter the height of the Pendellösung fringes on both sides of each model curve. An InAs epilayer of 2.5–5.0Å, roughly equals to 1–2 ML, is very common for the growths on InP under As rich condition. For the ellipsometry calibration samples, because each of them

only consists of one InAlGaAs and one InGaAs epilayer, it is easier to get a good fit for the Pendellösung fringes. From Table 6.8, G0341 has the largest error of $r_{\mathrm{Ga}} = -2.0\%$ for the InGaAs cap layer and G0501 has $r_{\mathrm{In}} = +1.9\%$ for InAlGaAs, which show that both growths were reasonably grown on target. The most complex part in this kind of HRXRD fitting is there are three flux deviations in an InAlGaAs layer, but only the InAlGaAs peak position and Pendellösung fringe period are known so this is a problem equivalent to using two equations to solve three unknowns, which can lead to infinitely many solutions. Similar to the case of InGaAs-InAlAs SL in Chapter 5, due to the similar lattice constants of GaAs and AlAs, it is nearly impossible to distinguish the flux drift between these two from the HRXRD profile alone. Therefore careful assumptions have to be made when deducing r_{Ga} and r_{Al}, e.g. assume both of them equal 2.0% for the 4000Å InAlGaAs layer in G0448, but practically there are infinitely many combinations of r_{Ga} and r_{Al} which can lead to the same or at least very similar fitting curve.

All flux deviations are shown down to 0.1% precision and roughly equivalent to the best flux stability the effusion cells can offer. It is worth noting that, however, the fitting curve is very sensitive to such flux deviation, in which a shift can be seen even with an adjustment of $< 0.1\%$. For instance, although they are already very close to each other, the red InAlGaAs peak of G0501 in Fig. 6.8(b) is not exactly aligned with the blue InAlGaAs peak at $r_{\mathrm{In}} = +1.9\%$, while the Pendellösung fringes are. By adding another 0.08% into this r_{In}, the red and blue InAlGaAs peaks can be aligned, but the Pendellösung fringes would be misaligned, which indicate that there could be possibly a flux drift of less than 0.1% during the deposition of this InAlGaAs epilayer. On the other hand, for the scans of the two SJ structures G0384 and G0448 shown in Fig. 6.8(c) and (d), the model curves are reasonably well-aligned with the scans at those ternary and quaternary peaks. For G0448, the Pendellösung fringes are well-fitted at negative ω–2θ, but the HRXRD scan intensity is too weak and noisy at ω–$2\theta > 500$" which cannot get a good fit. While for G0384, the red curve can only resemble an overall profile of the blue curve, but the small fringes cannot be fitted. In general, it is easier to get good fits for structures with thicker epilayers like G0448 thanks to their clear Pendellösung fringes with longer periods and well-defined lobes. In contrast, the epilayers in G0384 are in overall thinner which result in noisy, indistinguishable fringes and fitting those are more complex. A few other thinner structures, which do not have their HRXRD fittings shown here, have similar problems as of G0384. In general, according to the HRXRD fitting results, those PPC structures suffer from considerable flux deviations from their targets especially towards the end of growths. For G0384, all epilayers have small flux drifts except for the top InGaAs layer with $r_{\mathrm{Ga}} = +6\%$, which is consistent with the post-growth BFM measurement of Ga and this is coincidentally one of the rare cases where BFM can be used to cross-check with

the result of HRXRD fitting. Another main issue encountered with those PPC growths is the flux instability over time especially for thicker structures, which is well illustrated by G0448. It is found that the 28000Å $In_{0.532}Al_{0.097}Ga_{0.371}As$ absorber layer, consists of a 25000Å Be-doped base and 3000Å Si-doped emitter, has a significantly broadened peak and cannot be fitted if all group III fluxes were assumed to be stable. The only solution to get a good fit is to separate such epilayer into two parts, in which the first part having the In flux linearly and continuously drifted from $r_{\text{In}} = +1.9\%$ to $+3.4\%$ and the second part staying at $+3.4\%$ during deposition, with the fitted thickness being 20300Å and 8154Å respectively. To clarify, such peak broadening is unlikely due to the change of dopant cells considering both parts, with Be and Si of 2×10^{16} cm^{-3} and -1×10^{18} cm^{-3}, are lightly doped, and there was no pause of growth when switching one dopant to another.

It is clear that flux deviation and drift might cause performance issues of PPC devices, as the J-V characteristic and QE are sensitive to the InAlGaAs composition and bandgap accuracy. Measuring the BFM and adjusting the cell temperatures before deposition of every epilayer, or at least for the thicker or critical ones, is a possible solution to help alleviate the flux deviation issue. However, inserting the BFM under the wafer for measurement would block all fluxes directing towards it and the wafer surface without As supply would degrade over time, hence the substrate needs to be ramped down below 400°C for safe measurement and back to above 400°C before resuming growth. The procedures of wafer temperature ramping, BFM measurement, and cell temperature adjustment can be as long as ∼20 minutes up to an hour depending on the cell behavior. Those steps might induce further flux instability by themselves and end up consuming more material in each cell which are unfavorable, not to mention the long waiting during BFM measurement might cause substrate surface contamination over time. Therefore it requires cautious decision when attempting a BFM measurement for intermediate epilayers. The values of cell coefficients B and C might change over time too, as mentioned in Chapter 2, which can eventually affect the accuracy of compositions and bandgaps in the PPC. Therefore more frequent re-calibrations of those coefficients might become necessary. To further improve the HRXRD fittings, further research is required in understanding the actual lattice constant vs composition relation for the ternary and quaternary materials. For all the structures presented in this project, two assumptions are made: InGaAs and InAlAs obey Eq. 2.25 which includes a non-zero bowing factor as presented in previous chapters, while InAlGaAs follows Vegard's law. However, given that cell coefficient discrepancy and flux instability happened for the majority of growths presented in this work, little could be done to evaluate the validity of the lattice constant equations from those previous structures. Repetitive calibration growths with various group III composition combinations can be done to acquire more reliable bowing factors for those compounds, provided that all

Material	d (Å)	u	v	w	r_{Ga}(%)	r_{Al}(%)	r_{In}(%)	d' (Å)	u'	v'	w'
G0341											
InP(001)	inf							inf			
InAs								2.50			
$In_wAl_vGa_uAs$	10000	0.117	0.356	0.527	-0.5	-0.6	0.5	10003.60	0.116	0.354	0.530
In_wGa_uAs	100	0.474		0.526	-2.0			99.12	0.469		0.531
G0501											
InP(001)	inf							inf			
InAs								5.00			
$In_wAl_vGa_uAs$	10000	0.371	0.097	0.532			1.9	10104.87	0.367	0.096	0.537
In_wGa_uAs	100	0.474		0.526				100.00	0.474		0.526

Table 6.8: HRXRD fitting summary of calibration samples G0341 and G0501 for ellipsometry, which shows the target thickness d, target Ga, Al, In compositions u, v, w, Ga, Al, In flux deviations r_{Ga}, r_{Al}, r_{In}, fitted thickness d' and fitted Ga, Al, In compositions u', v', w'.

Material	d (Å)	u	v	w	r_{Ga}(%)	r_{Al}(%)	r_{In}(%)	d' (Å)	u'	v'	w'
InP(001)	inf							inf			
InAs								10.00			
$In_wAl_vGa_uAs$	1500	0.117	0.356	0.527				1500.00	0.117	0.356	0.527
$In_wAl_vGa_uAs$	7000	0.267	0.203	0.53			1.0	7039.68	0.266	0.202	0.532
$In_wAl_vGa_uAs$	4000	0.117	0.356	0.527			-1.5	3966.45	0.118	0.359	0.523
In_wGa_uAs	500	0.474		0.526	6.0		-3.5	503.40	0.497		0.503

Table 6.9: HRXRD fitting summary of single-junction (SJ) sample G0384, which shows the target thickness d, target Ga, Al, In compositions u, v, w, Ga, Al, In flux deviations r_{Ga}, r_{Al}, r_{In}, fitted thickness d' and fitted Ga, Al, In compositions u', v', w'.

group III cells are ensured to be sufficiently stable without any noticeable flux drift. On the other hand, the effect of possible lattice relaxation induced by the strongly strained $In_{0.3}Al_{0.7}As$ had been neglected, which is acceptable for the fitting of G0448 since it was grown on the top of the structure. Nonetheless, for those with such layer at the bottom, say, G0589, which has obvious relaxation lines in the Nomarski image in Fig. 6.4(b), such factor should be taken into account.

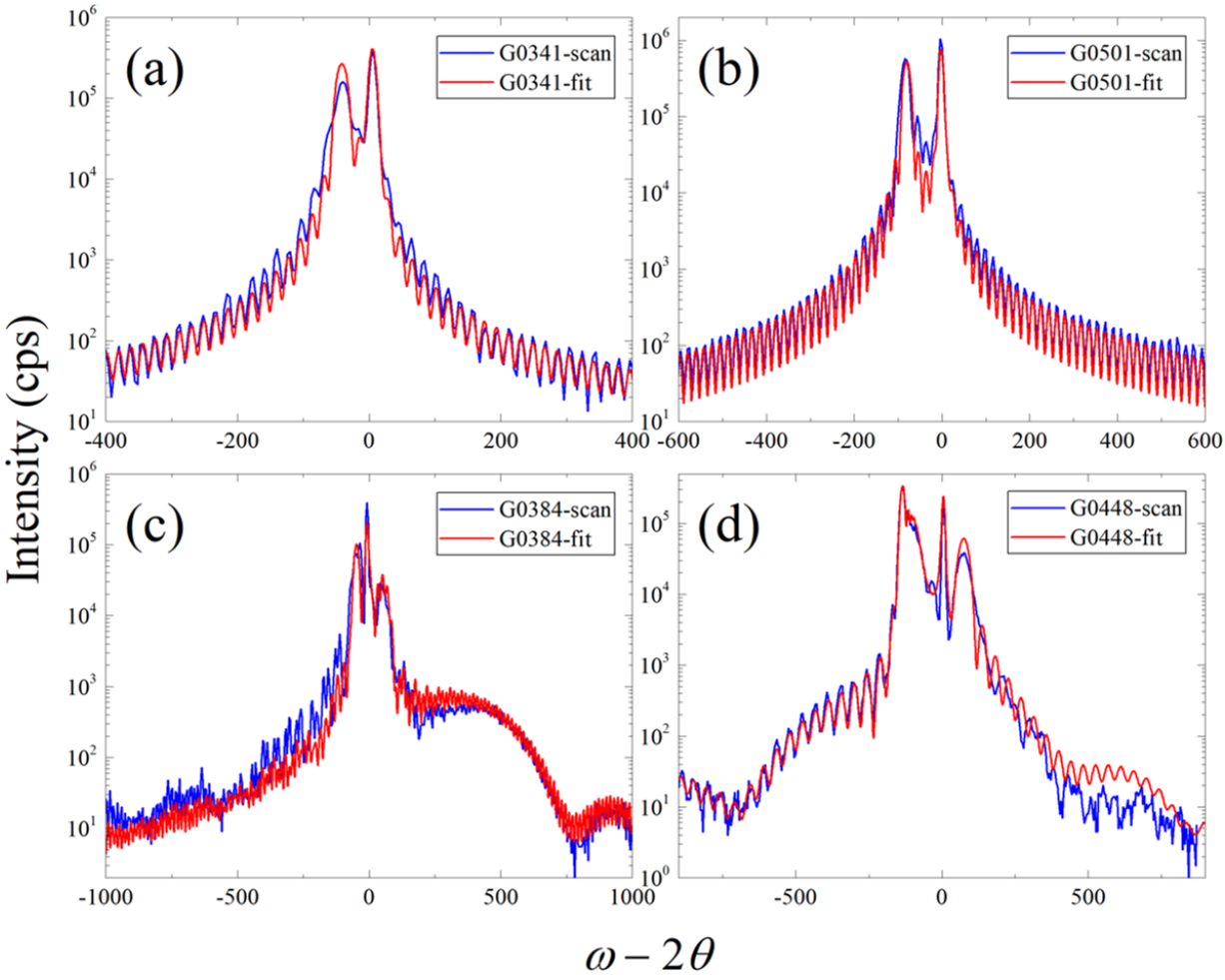

Figure 6.8: HRXRD TA coupled scans (blue) and fitting (red) of (a) G0341, (b)G0501, (c) G0384 and (d) G0448.

Material	d (Å)	u	v	w	r_{Ga}(%)	r_{Al}(%)	r_{In}(%)	d' (Å)	u'	v'	w'
InP(001)	inf							inf			
InAs								5.00			
$\mathrm{In}_w\mathrm{Al}_v\mathrm{Ga}_u\mathrm{As}$	1500	0.117	0.356	0.527			1.0	1508.47	0.116	0.354	0.529
$\mathrm{In}_w\mathrm{Al}_v\mathrm{Ga}_u\mathrm{As}$	20000	0.371	0.097	0.532			1.9 → 3.4	20300.00	0.367 → 0.364	0.096 → 0.095	0.537 → 0.540
$\mathrm{In}_w\mathrm{Al}_v\mathrm{Ga}_u\mathrm{As}$	8000	0.371	0.097	0.532			3.4	8154.12	0.364	0.095	0.540
$\mathrm{In}_w\mathrm{Al}_v\mathrm{Ga}_u\mathrm{As}$	4000	0.117	0.356	0.527	2.0	2.0	0.4	4044.21	0.118	0.359	0.523
$\mathrm{In}_w\mathrm{Al}_v\mathrm{As}$	100		0.7	0.3		3.0	-3.0	97.88		0.712	0.288
$\mathrm{In}_w\mathrm{Ga}_u\mathrm{As}$	250	0.474		0.526				250.00	0.474		0.526

Table 6.10: HRXRD fitting summary of single-junction (SJ) sample G0448, which shows the target thickness d, target Ga, Al, In compositions u, v, w, Ga, Al, In flux deviations r_{Ga}, r_{Al}, r_{In}, fitted thickness d' and fitted Ga, Al, In compositions u', v', w'.

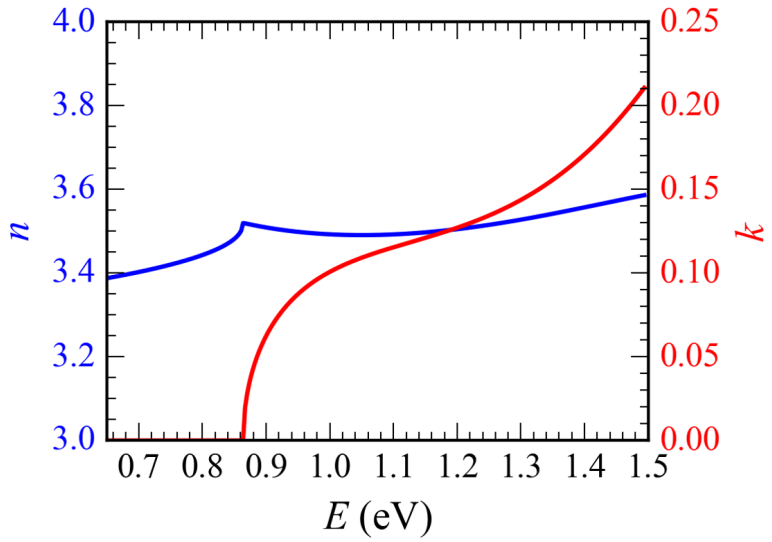

Figure 6.9: Complex refractive index of $In_{0.532}Al_{0.097}Ga_{0.371}As$ determined by spectroscopic ellipsometry of G0501. Figure adopted and reprinted from Ref. [79].

6.3 Applications in Ellipsometry Calibrations and PPC Devices

Spectroscopic ellipsometry measurements were performed on calibration samples G0341, G0343, G0345, G0389 and G0501. Illustrated for G0501 in Fig. 6.9, by applying Adachi-New Forouhi dispersion formula, the refractive index was found to be of $n \approx 3.5$, the bandgap was $E_g = 0.864$ eV and the absorption coefficient obtained from the extinction coefficient k was shown to be 8×10^3 cm^{-1}. The results are consistent with the QE measurements performed on trial SJ samples with the same InAlGaAs absorber composition.

Fig. 6.10 illustrates the SJ PPC devices built on the G0587 wafer with cells of various sizes. Device characterizations were performed on the largest cells with an active area of $\sim$12mm^2, with each sample positioned on a temperature-controlled chuck for the measurements. J-V characteristic was done using a laser with a centre wavelength of 1319 nm for different intensities and the QE was measured at the wavelength range of 1000–1500 nm. The J-V curves of the processed G0587 and G0588 SJ devices, with their structure almost identical except the InAlGaAs absorber of 4.1 and 0.84 μm respectively, are shown in Fig. 6.11. G0587 and G0588 had expected absorbances of 95% and 45% of the light respectively, with the latter one being a bit less than that of the top junction from a two-junction

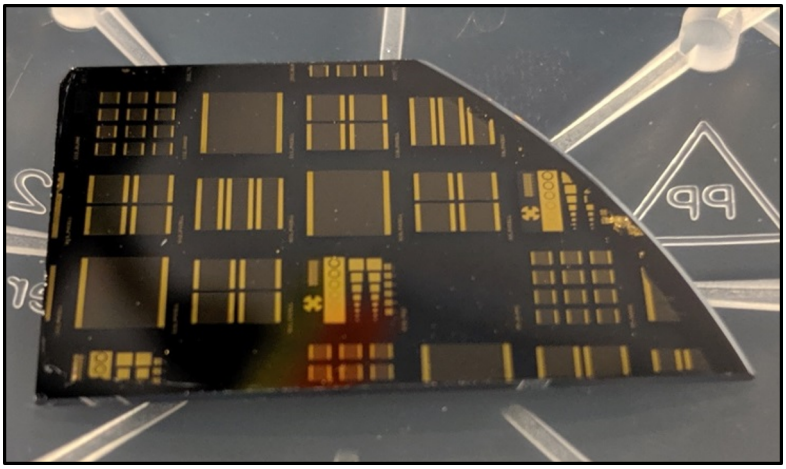

Figure 6.10: SJ PPC devices built on the G0587 wafer with cells of various sizes. Figure adopted and reprinted with permission from SUNLAB, University of Ottawa.

PPC. For the open-circuit voltage V_{OC}, both devices range from 0.3–0.4 V with G0588 of ∼30 mV larger due to its larger average carrier density. The QE curves of G0587 and G0588 are shown in Fig. 6.12. Besides external quantum efficiency (EQE), the adjusted QE which is defined as EQE/$(1-\mathcal{R})$ with $\mathcal{R}$ as the specular reflectance is also shown. It is similar to the internal QE but it does not account for transmission losses in devices. Under the ideal scenario, the adjusted QE is equivalent to the material absorbance. G0587 has the adjusted QE of 89% at the laser line, lower than the expected value of 95%, while for G0588 it is 44%, very close to the expected value of 45%. The thicker device generally suffers from limited diffusion that part of the generated carriers from the active layers recombined before they diffuse to the p-n junction. Since thinner cells have better carrier collection, an MJ device with several thin subcells is more likely to perform better than an SJ device with the same total thickness.

The J-V characteristics of trial TD structures G0624, G0625 and G0675 are shown in Fig. 6.13 with the supposed operating region for an MJ device locates at the left of the peak. A good TD should have a low resistance to minimize the voltage drop across it and in order not to limit the PPC's performance, its peak tunneling current should be larger than the total current in the PPC device. Fig. 6.13(a) shows the semi-log plot of the tunneling current vs bias voltage of G0624 and G0675. For G0675 with its growth temperature dropped to 460°C when the InAlGaAs epilayer deposition was switched from n^{++} to p^{++}, it shows a huge peak tunneling current of 1129Acm^{-2}, which is by far the best performing tunneling diode ever reported. Such current is 80 times compared to the

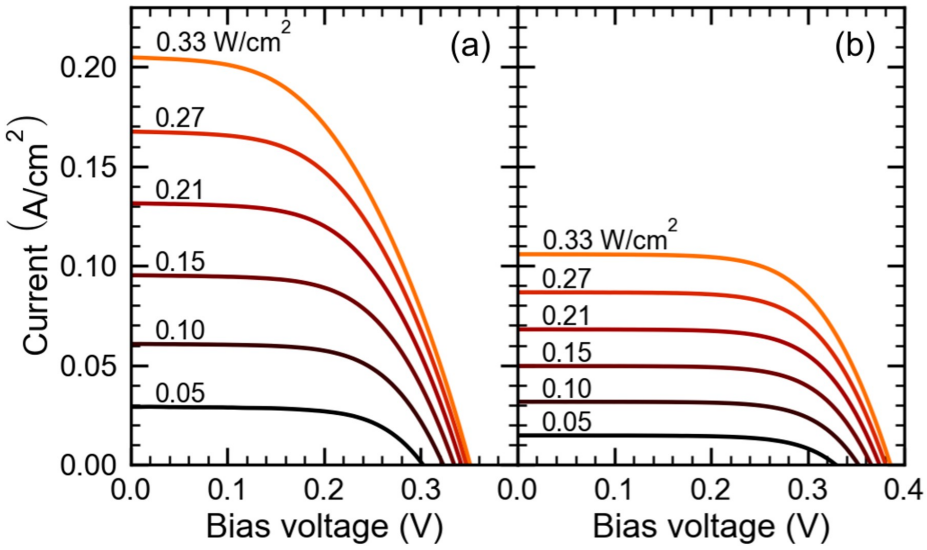

Figure 6.11: J-V characteristics for SJ PPCs under 1319 nm laser illumination at intensities between 0.05 and 0.33 Wcm^{-2} for (a) G0587 and (b) G0588. Figure adopted and reprinted with permission from SUNLAB, University of Ottawa.

case of G0624 in which the temperature was kept at 480°C. This can be explained by the fact that the drop of growth temperature by 20°C in G0675 can suppress Be diffusion [6]. The J-V characteristics of G0675 with its peak tunneling current much more than that of the 100Acm^{-2} operation range reveals that the TD should be able to operate under the illumination of $>$ 100Wcm^{-2}. For comparison, the J-V characteristics of G0625 devices with different areas are shown in Fig. 6.13(b). Unlike its Be-doped counterpart, G0625 does not show the proper J-V profile and its current is much smaller than that required for PPC operation. Similar to InGaAs-InAlAs SL in Chapter 5, this reveals that carbon is unsuitable as a p-dopant in InAlGaAs either, probably again due to carbon's amphoteric nature.

For an ideal TJ device, the laser line should align with the adjusted QE peak which is close to 50%. The two subcells should absorb the same amount of light and produce the same current. However, for G0690, the 1310 nm laser line locates at the left of the adjusted QE peak which is close to 40% as shown in Fig. 6.14(a). This means the top subcell absorbed more light than targeted, reduced the remainder of light reaching the bottom subcell and this limited the total current. Such a shift of the QE curve from the ideal position indicates that those InAlGaAs absorber layers have smaller bandgap than expected and this was due to the actual In flux was more than expected during G0690

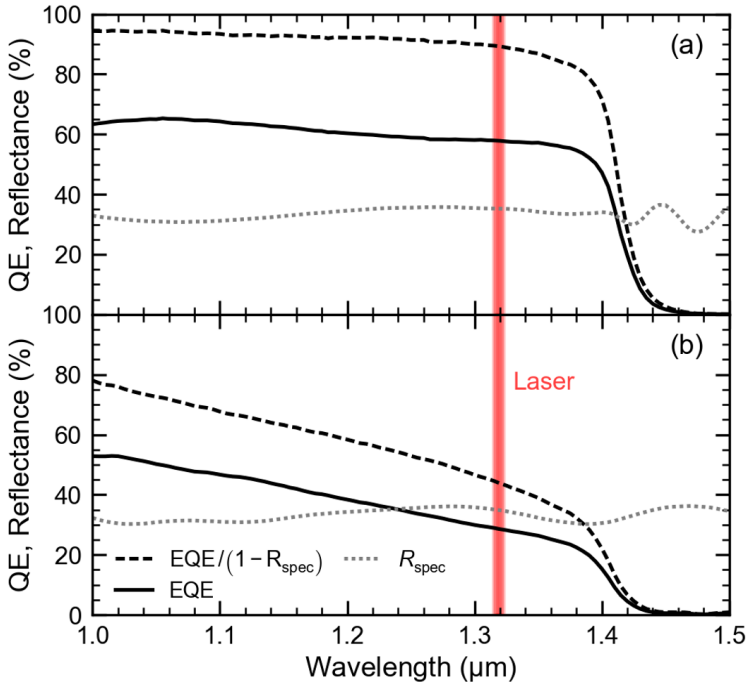

Figure 6.12: QE and specular reflectance measurements for SJ PPC devices built from (a) G0587 and (b) G0588. Figure adopted and reprinted with permission from SUNLAB, University of Ottawa.

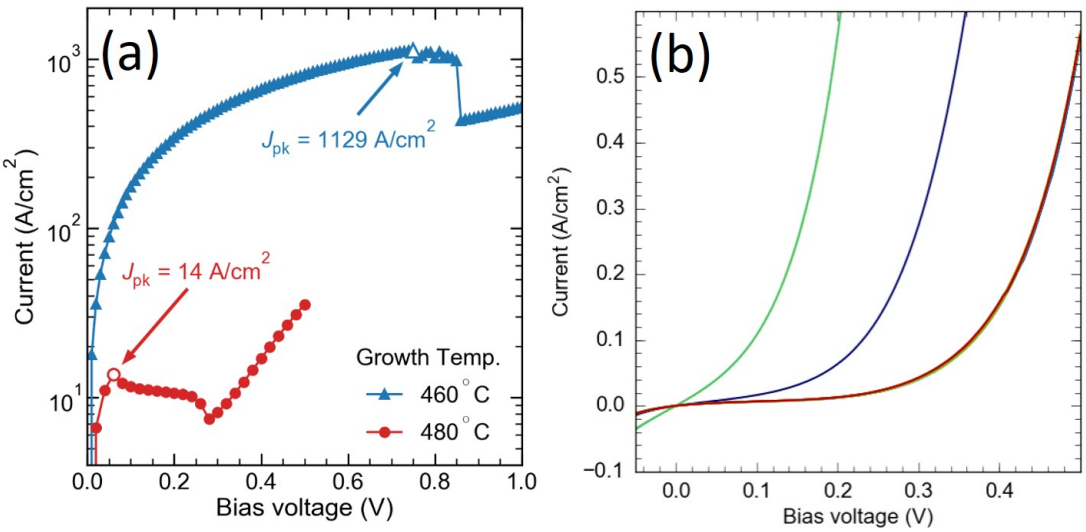

Figure 6.13: J-V characteristics for TDs (a) G0624 (red), G0675 (blue) and (b) G0625. Figure adopted and reprinted with permission from SUNLAB, University of Ottawa.

growth. From the Nomarski and black-box images in Figs. 6.5 and 6.7, besides both wafers having some point defects, G0675 is still reasonably smooth but G0690 suffered from significant lattice relaxation due to its lattice constant larger than that of InP, which created those defects and limited its minority carrier diffusion length. The J-V characteristics of G0690 with a range of intensities are shown in Fig. 6.14(b). The V_{OC} is ∼0.66 V for intensity at 0.33Wcm^{-2}, which corresponds to ∼0.33 V for each subcell, close to the V_{OC} in G0587 and G0588.

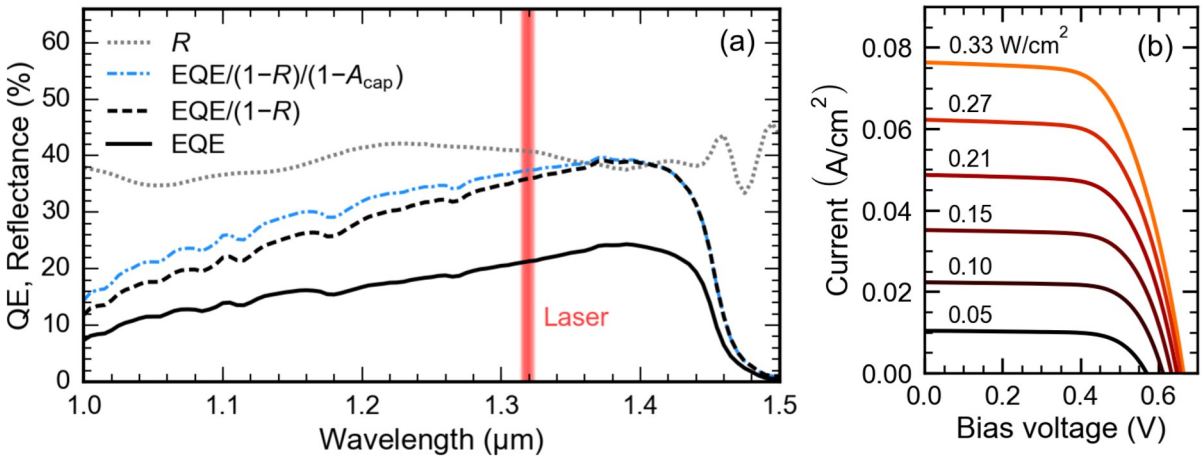

Figure 6.14: (a) EQE and specular reflectance measurements for TJ PPC device built from G0690, with adjusted QEs account for $\mathcal{R}$ and for InGaAs cap absorbance A_{cap}; (b) J-V characteristics for SJ PPCs under 1319 nm laser illumination at intensities between 0.05 and 0.33 Wcm^{-2} for G0690. Figure adopted and reprinted with permission from SUNLAB, University of Ottawa.

Chapter 7

Conclusion

MBE optimizations of several III-V compounds: LT GaAs, InGaAs-InAlAs SL and InAlGaAs, for applications in 780 and 1550 nm pumped THz TDS and 1310 nm pumped PPCs, are presented.

An effective ISP technique is demonstrated, which is the first method enabling reliable temperature monitoring of small bandgap semiconductors during MBE growth at the LT regime where pyrometer does not work. Unlike single-wavelength pyrometry, the technique relies on integrating the thermal emission from the substrate over the spectral range where the substrate is opaque to manipulator heater radiation, using a compact InGaAs array spectrometer. This approach significantly improves the signal to noise ratio at low temperature and greatly reduces the influence of light interference effects present for single-wavelength instruments. A calibration procedure that relies on the well-known temperature dependence of the band edge absorption in a SI GaAs substrate, is proposed. The approach used for subtracting the background radiation signal coming from other hot objects in the MBE reactor is also discussed. With these procedures in place, the wafer temperature can be reliably monitored down to about 200°C. In addition, the same spectrometer can be used to monitor the temperature of semiconductors with wider bandgaps, such as GaAs or InP, by using the well-established BET method. The method of acquiring temperature by fitting the blackbody radiation curve used by some groups or companies is not really applicable in the environment of MBE because there are many other hot sources in the growth chamber and we cannot really unscramble that to get the wafer temperature. Here ISP offers the ability for stray light compensation, which other temperature monitoring techniques are lacking. The application of simultaneous temperature monitoring with BET and ISP for the growth of narrow-bandgap metamorphic buffers on a GaAs substrate is demonstrated. In general, ISP works well not only for narrow bandgap materials but

also for any material that is opaque to the substrate heater, e.g. back coated substrates or In-mounted substrates on Molybdenum plate, provided that the surface emissivity is close to that of the calibration wafer, or being known by other means such that the ISP coefficients can be adjusted as appropriate.

LT GaAs based THz PCAs were developed for the 780 nm pumped THz TDS system. A series of LT GaAs samples were prepared with various growth and annealing temperatures followed by characterizations. While 470 nm reflectance and Nomarski microscopy illustrated that smooth GaAs surface morphology with high epitaxial quality can be maintained at a growth temperature as low as 230°C, RHEED revealed that the epitaxial single-crystalline quality decreased as the growth temperature decreased. From HRXRD, it was verified that As Op is not a dominant factor for altering the material properties of LT GaAs. On the other hand, changing the growth temperature by 10°C would result in a significant shift of the LT GaAs peak position in HRXRD for the as-grown wafers, which indicated that even a slight shift in growth temperature would drastically affect the amount of excess As incorporation. Multiple Tx and Rx were processed on LT GaAs materials prepared under different growth and annealing conditions. Repetitive THz TDS tests were conducted with various combinations of Tx and Rx. The study showed that the growth temperature is not a dominant factor in THz pulse width and BW; instead, the annealing temperature and PCA design play the key role. It was concluded that an Rx with a lower annealing temperature of 450–460°C for 10 minutes and 20D40P design gave the narrowest THz pulse as short as 0.33 ps in the temporal domain and generated the broadest 20 dB BW of 2.48 THz in the spectral domain. On the other hand, although an Rx with a higher annealing temperature of 600–610°C for 10 minutes and D20 design had a much wider pulse and thus narrower BW, they produced much higher photocurrent, thus gave significantly better SNR and stronger THz amplitude, which was about 10 times larger compared to its lower annealing temperature, 20D40P PCA counterparts. Due to time and resource limits, only a few combinations of antenna type, growth and annealing temperature for Tx and Rx are covered in this work and more measurements with different PCA combinations must be done to further optimize the THz TDS performance. Besides MBE growth, the processing is another dominant factor of the PCA quality and therefore consistent processing procedures have to be established to improve the reproducibility of THz TDS results.

MT and LT InGaAs-InAlAs SL samples, either undoped or with Be or C doping, were grown lattice-matched on SI (Fe) InP(001) substrates at various doping concentrations. Radiative heating on substrates and opacity developed with increasing InGaAs deposition thickness made BET eventually unreadable during growth. 4pp measurements revealed that the C-doped SL samples, either with δ or conventional 3D doping, exhibited low

dark resistance which were unsuitable to be fabricated as PCAs. ECV showed that, even with the same dopant filament current applied, the actual C doping level on InGaAs was significantly lower than that of GaAs. The results conclude that carbon is not a suitable p-dopant material for InGaAs. The Be-doped LT InGaAs-InAlAs SL sample with the heaviest doping concentration of 8×10^{18} cm^{-3} exhibited average sheet resistance of 17.69 MΩ/sq. Multiple Tx and Rx devices were processed. 1550 nm pumped THz-TDS measurements were conducted with both processed Be-doped LT InGaAs-InAlAs SL and LT GaAs used as Rx with the latter one operated via two-step midgap mediated excitation. The results indicated that the annealing temperature, rather than the Rx material type, was the dominant factor of THz pulse width and bandwidth. Overall, more optimizations have to be done to further improve the THz TDS bandwidth to be comparable to the best records reported in the literature [58, 105]. For example, in order to shorten the photoconductive transient duration of LT GaAs and LT InGaAs-InAlAs SL based Rx, time-resolved pump-probe measurements have to be done on grown wafers to determine the carrier lifetime of those materials, which help optimize the value to as short as ∼0.1 ps as reported in Ref. [61].

InAlGaAs based structures were grown lattice-matched on SI (Fe), p$^+$(Zn) and n$^+$(S) InP(001) substrates for ellipsometry calibrations and PPC fabrications. Nomarski images showed smooth morphologies (no observable bumps in 40× magnification) with most growths except for those with highly strained $In_{0.3}Al_{0.7}As$ etch stop deposited at the bottom of the structure which could result in significant lattice relaxation as thin as 100Å. HRXRD revealed that the lattice matching of those structures with multiple ternary and quaternary epilayers of various group III compositions are particularly challenging. HRXRD fittings of representative calibration and p-n junction structures are demonstrated, with the group III flux deviations treated as variables for each epilayer. Flux drift issue during growth is discussed with an example given, where the HRXRD scan can be properly fitted only when In flux drift is taken into account. Ellipsometry measurements of InAlGaAs samples with various bandgaps showed good agreements with the QE measurements of trial SJ samples. *J*-*V* characteristics of tunnel diodes revealed that Be diffusion can be suppressed by decreasing the growth temperature in the p-doped region by 20°C, which gave record-breaking peak tunnel current above 1000Acm^{-2}. 1319 nm pumped *J*-*V* and QE measurements of SJ and TJ PPC devices are illustrated, which showed open-circuit voltages up to $V_{OC} = 0.38$ and 0.66 V for SJ and TJ PPC devices respectively under 0.33 Wcm^{-2} illumination. The open-circuit voltages and QE for both SJ and TJ devices were lower than their expected values, especially for TJ, which can be attributed to bandgap narrowing due to overshooting of In flux during the growth. Those can be improved by more precise flux calibrations.

To summarize, this work establishes the MBE growth conditions of several III-V materials which help development of cutting-edge, portable and cost-effective optoelectronic devices for THz and power-over-fiber applications. Additional research is needed for further optimizations. For instance, the accuracy of temperature monitoring at the LT regime can be further improved by determining the emissivity of different III-V materials. With the spectrometer of integration time of 0.05–0.2 s, the ISP signal has a fluctuation error of about $\pm 10^{\circ}$C in the LT regime where the radiation from other sources becomes more dominant. Since the material properties of LT materials are very sensitive to growth temperature, more advancements need to done in ISP calibration and stray light compensation in order to further reduce such uncertainty. To improve the performance of the telecom fiber laser pumped THz system, PCA dark resistance can be further optimized by increasing the Be concentration beyond 1×10^{19} cm^{-3} and tuning the growth temperature. By doing time-resolved pump-probe measurements, the carrier lifetime of grown wafers can be optimized. Last but not least, more precise cell calibration and BFM measurement procedures have to be established to improve the flux stability and reliability for growing lattice-matched, ternary and quaternary compound based multi-layer p-n junctions.

Bibliography

[1] M. Henini. *Molecular Beam Epitaxy: From Research to Mass Production*. Elsevier, 2013.

[2] R. F. C. Farrow. *Molecular Beam Epitaxy: Applications to Key Materials*. Noyes Publications, 1995.

[3] J. N. Miller, D. M. Collins, and N. J. Moll. Control of Be diffusion in molecular beam epitaxy GaAs. *Applied Physics Letters*, 46(10):960–962, 1985.

[4] E. G. Scott, D. Wake, G. D. T. Spiller, and G. J. Davies. Beryllium diffusion in GaInAs grown by molecular beam epitaxy. *Journal of Applied Physics*, 66(11):5344–5348, 1989.

[5] N. Jourdan, F. Alexandre, C. Dubon-Chevallier, J. Dangla, and Y. Gao. Heavily doped GaAs(Be)/GaAlAs HBTs grown by MBE with high device performances and high thermal stability. *IEEE Transactions on Electron Devices*, 39(4):767–770, April 1992.

[6] R. A. Metzger, M. Hafizi, W. E. Stanchina, T. Liu, R. G. Wilson, and L. G. McCray. Confinement of high Be doping levels in AlInAs/GaInAs npn heterojunction bipolar transistors by low temperature molecular-beam epitaxial growth. *Applied Physics Letters*, 63(10):1360–1362, 1993.

[7] W. P. Gillin, D. J. Dunstan, K. P. Homewood, L. K. Howard, and B. J. Sealy. Interdiffusion in InGaAs/GaAs quantum well structures as a function of depth. *Journal of Applied Physics*, 73(8):3782–3786, 1993.

[8] S. V. Ghaisas and S. Das Sarma. Surface diffusion length under kinetic growth conditions. *Phys. Rev. B*, 46:7308–7311, Sep 1992.

[9] T. Suzuki and T. Nishinaga. Surface diffusion and atom incorporation kinetics in MBE of InGaAs and AlGaAs. *Journal of Crystal Growth*, 111(1):173 – 177, 1991.

[10] J. F. Nützel and G. Abstreiter. Segregation and diffusion on semiconductor surfaces. *Phys. Rev. B*, 53:13551–13558, May 1996.

[11] M. R. Melloch, J. M. Woodall, and E. S. Harmon. Low-temperature grown III-V materials. *Annual Review of Materials Science*, 25:547–600, 1995.

[12] M. R. Melloch, D. D. Nolte, J. M. Woodall, J. C. P. Chang, D. B. Janes, and E. S. Harmon. Molecular beam epitaxy of nonstoichiometric semiconductors and multiphase material systems. *Critical Reviews in Solid State and Materials Sciences*, 21(3):189–263, 1996.

[13] O. Gul, H. Zhang, Jouri D. S. Bommer, M. W. A. de Moor, D. Car, S. R. Plissard, E. P. A. M. Bakkers, A. Geresdi, K. Watanabe, T. Taniguchi, and L. P. Kouwenhoven. Ballistic majorana nanowire devices. *Nature Nanotechnology*, 13(13):192–197, 2018. Gl2018.

[14] M. T. Deng, C. L. Yu, G. Y. Huang, M. Larsson, P. Caroff, and H. Q. Xu. Anomalous zero-bias conductance peak in a Nb-InSb nanowire Nb hybrid device. *Nano Letters*, 12(12):6414–6419, 2012. PMID: 23181691.

[15] V. Mourik, K. Zuo, S. M. Frolov, S. R. Plissard, E. P. A. M. Bakkers, and L. P. Kouwenhoven. Signatures of majorana fermions in hybrid superconductor-semiconductor nanowire devices. *Science*, 336(6084):1003–1007, 2012.

[16] D. E. Mars and J. N. Miller. An indium-free mount for GaAs substrate heating during molecular beam epitaxial growth. *Journal of Vacuum Science & Technology B: Microelectronics Processing and Phenomena*, 4(2):571–573, 1986.

[17] S. L. Wright, R. F. Marks, and W. I. Wang. Reproducible temperature measurement of GaAs substrates during molecular beam epitaxial growth. *Journal of Vacuum Science & Technology B: Microelectronics Processing and Phenomena*, 4(505), 1986.

[18] A. J. SpringThorpe, T. P. Humphreys, A. Majeed, and W. T. Moore. *In situ* growth rate measurements during molecular beam epitaxy using an optical pyrometer. *Applied Physics Letters*, 55(20):2138–2140, 1989.

[19] E. S. Hellman and J. S. Harris. Infra-red transmission spectroscopy of GaAs during molecular beam epitaxy. *Journal of Crystal Growth*, 81(1):38 – 42, 1987.

[20] W. S. Lee, G. W. Yoffe, D. G. Schlom, and J. S. Harris. Accurate measurement of MBE substrate temperature. *Journal of Crystal Growth*, 111(1):131 – 135, 1991.

[21] S. R. Johnson, C. Lavoie, M. K. Nissen, and T. J. Tiedje. Optical apparatus and method for measuring temperature of a substrate material with a temperature dependent band gap. *U. S. patent*, (5,388,909), 1995.

[22] M. Nouaoura, L. Lassabatere, N. Bertru, J. Bonnet, and A. Ismail. Problems relevant to the use of optical pyrometers for substrate temperature measurements and controls in molecular beam epitaxy. *Journal of Vacuum Science & Technology B: Microelectronics and Nanometer Structures Processing, Measurement, and Phenomena*, 13(1):83–87, 1995.

[23] Y.-S. Lee. *Principles of Terahertz Science and Technology*. Springer, 2009.

[24] H. Eisele, A. Krotkus, R. E. Miles, and X. C. Zhang. *Terahertz Frequency Detection and Identification of Materials and Objects*. Springer, 2007.

[25] A. Rostami, H. Rasooli, and H. Baghban. *Terahertz Technology: Fundamentals and Applications*. Springer Berlin, 2011.

[26] M. Perenzoni and D. J. Paul. *Physics and Applications of Terahertz Radiation*. Springer, 2014.

[27] M. Abo-Bakr, J. Feikes, K. Holldack, P. Kuske, W. B. Peatman, U. Schade, G. Wüstefeld, and H.-W. Hübers. Brilliant, coherent far-infrared (THz) synchrotron radiation. *Phys. Rev. Lett.*, 90:094801, Mar 2003.

[28] U. Schade, K. Holldack, P. Kuske, G. Wstefeld, and H.-W. Hbers. THz near-field imaging employing synchrotron radiation. *Applied Physics Letters*, 84(8):1422–1424, 2004.

[29] V. L. Bratman, Yu. K. Kalynov, and V. N. Manuilov. Large-orbit gyrotron operation in the terahertz frequency range. *Phys. Rev. Lett.*, 102:245101, Jun 2009.

[30] M. Yu. Glyavin, A. G. Luchinin, and G. Yu. Golubiatnikov. Generation of 1.5-kW, 1-THz coherent radiation from a gyrotron with a pulsed magnetic field. *Phys. Rev. Lett.*, 100:015101, Jan 2008.

[31] T. Idehara, H. Tsuchiya, O. Watanabe, La Agusu, and S. Mitsudo. The first experiment of a THz gyrotron with a pulse magnet. *International Journal of Infrared and Millimeter Waves*, 27(3):319–331, Mar 2006.

[32] M. Mineo and C. Paoloni. Corrugated rectangular waveguide tunable backward wave oscillator for terahertz applications. *IEEE Transactions on Electron Devices*, 57(6):1481–1484, June 2010.

[33] A. Dobroiu, M. Yamashita, Y. N. Ohshima, Y. Morita, C. Otani, and K. Kawase. Terahertz imaging system based on a backward-wave oscillator. *Appl. Opt.*, 43(30):5637–5646, Oct 2004.

[34] B. A. Knyazev, G. N. Kulipanov, and N. A. Vinokurov. Novosibirsk terahertz free electron laser: instrumentation development and experimental achievements. *Measurement Science and Technology*, 21(5):054017, Mar 2010.

[35] G. P. Williams. Far-IR/THz radiation from the jefferson laboratory, energy recovered linac, free electron laser. *Review of Scientific Instruments*, 73(3):1461–1463, 2002.

[36] A. Maestrini, B. Thomas, H. Wang, C. Jung, J. Treuttel, Y. Jin, G. Chattopadhyay, I. Mehdi, and G. Beaudin. Schottky diode-based terahertz frequency multipliers and mixers. *Comptes Rendus Physique*, 11(7):480 – 495, 2010. Terahertz electronic and optoelectronic components and systems.

[37] J. Ward, E. Schlecht, G. Chattopadhyay, A. Maestrini, J. Gill, F. Maiwald, H. Javadi, and I. Mehdi. Capability of THz sources based on schottky diode frequency multiplier chains. In *2004 IEEE MTT-S International Microwave Symposium Digest (IEEE Cat. No.04CH37535)*, volume 3, pages 1587–1590 Vol.3, June 2004.

[38] J. V. Siles and J. Grajal. Physics-based design and optimization of schottky diode frequency multipliers for terahertz applications. *IEEE Transactions on Microwave Theory and Techniques*, 58(7):1933–1942, July 2010.

[39] F. Maiwald, F. Lewen, B. Vowinkel, W. Jabs, D. G. Paveljev, M. Winnewisser, and G. Winnewisser. Planar schottky diode frequency multiplier for molecular spectroscopy up to 1.3 THz. *IEEE Microwave and Guided Wave Letters*, 9(5):198–200, May 1999.

[40] A. Nahata, A. S. Weling, and T. F. Heinz. A wideband coherent terahertz spectroscopy system using optical rectification and electro-optic sampling. *Applied Physics Letters*, 69(16):2321–2323, 1996.

[41] K.-L. Yeh, M. C. Hoffmann, J. Hebling, and Keith A. Nelson. Generation of 10μJ ultrashort terahertz pulses by optical rectification. *Applied Physics Letters*, 90(17):171121, 2007.

[42] A. Rice, Y. Jin, X. F. Ma, X.C. Zhang, D. Bliss, J. Larkin, and M. Alexander. Terahertz optical rectification from ⟨110⟩ zincblende crystals. *Applied Physics Letters*, 64(11):1324–1326, 1994.

[43] K. Kawase, M. Mizuno, S. Sohma, H. Takahashi, T. Taniuchi, Y. Urata, S. Wada, H. Tashiro, and H. Ito. Difference-frequency terahertz-wave generation from 4-dimethylamino-n-methyl-4-stilbazolium-tosylate by use of an electronically tuned Ti:sapphire laser. *Opt. Lett.*, 24(15):1065–1067, Aug 1999.

[44] Y. Sasaki, A. Yuri, K. Kawase, and H. Ito. Terahertz-wave surface-emitted difference frequency generation in slant-stripe-type periodically poled $LiNbO_3$ crystal. *Applied Physics Letters*, 81(18):3323–3325, 2002.

[45] H. Hubers. Terahertz heterodyne receivers. *IEEE Journal of Selected Topics in Quantum Electronics*, 14(2):378–391, March 2008.

[46] K. Moon, J. Choi, J.-H. Shin, S.-P. Han, H. Ko, N. Kim, J.-W. Park, Y.-J. Yoon, K.-Y. Kang, H.-C. Ryu, and K. H. Park. Generation and detection of terahertz waves using low-temperature-grown GaAs with an annealing process. *ETRI Journal*, 36(1):159–162, 2014.

[47] S. Preu, G. H. Dhler, S. Malzer, L. J. Wang, and A. C. Gossard. Tunable, continuous-wave terahertz photomixer sources and applications. *Journal of Applied Physics*, 109(6):061301, 2011.

[48] E. Bründermann, D. R. Chamberlin, and E. E. Haller. High duty cycle and continuous terahertz emission from germanium. *Applied Physics Letters*, 76(21):2991–2993, 2000.

[49] S. Fathololoumi, E. Dupont, C.W.I. Chan, Z.R. Wasilewski, S.R. Laframboise, D. Ban, A. Mátyás, C. Jirauschek, Q. Hu, and H. C. Liu. Terahertz quantum cascade lasers operating up to ∼200 K with optimized oscillator strength and improved injection tunneling. *Opt. Express*, 20(4):3866–3876, Feb 2012.

[50] D. J. Paul. The progress towards terahertz quantum cascade lasers on silicon substrates. *Laser & Photonics Reviews*, 4(5):610–632, 2010.

[51] B. Sartorius, H. Roehle, H. Künzel, J. Böttcher, M. Schlak, D. Stanze, H. Venghaus, and M. Schell. All-fiber terahertz time-domain spectrometer operating at 1.5 μm telecom wavelengths. *Opt. Express*, 16(13):9565–9570, Jun 2008.

[52] I. Kostakis, D. Saeedkia, and M. Missous. Terahertz generation and detection using low temperature grown InGaAs-InAlAs photoconductive antennas at 1.55 μm pulse excitation. *IEEE Transactions on Terahertz Science and Technology*, 2(6):617–622, Nov 2012.

[53] R. Takahashi, Y. Kawamura, T. Kagawa, and H. Iwamura. Ultrafast 1.55 μm photoresponses in low-temperature-grown InGaAs/InAlAs quantum wells. *Applied Physics Letters*, 65(14):1790–1792, 1994.

[54] R. Takahashi, Y. Kawamura, and H. Iwamura. Ultrafast 1.55 μm all-optical switching using low-temperature-grown multiple quantum wells. *Applied Physics Letters*, 68(2):153–155, 1996.

[55] Y. Chen, S. S. Prabhu, S. E. Ralph, and D. T. McInturff. Trapping and recombination dynamics of low-temperature-grown InGaAs/InAlAs multiple quantum wells. *Applied Physics Letters*, 72(4):439–441, 1998.

[56] R. J. B. Dietz, M. Gerhard, D. Stanze, M. Koch, B. Sartorius, and M. Schell. THz generation at 1.55 μm excitation: six-fold increase in THz conversion efficiency by separated photoconductive and trapping regions. *Opt. Express*, 19(27):25911–25917, Dec 2011.

[57] R. J. B. Dietz, B. Globisch, M. Gerhard, A. Velauthapillai, D. Stanze, H. Roehle, M. Koch, T. Gbel, and M. Schell. 64 μW pulsed terahertz emission from growth optimized InGaAs/InAlAs heterostructures with separated photoconductive and trapping regions. *Applied Physics Letters*, 103(6):061103, 2013.

[58] R. J.B. Dietz, B. Globisch, H. Roehle, D. Stanze, T. Göbel, and M. Schell. Influence and adjustment of carrier lifetimes in InGaAs/InAlAs photoconductive pulsed terahertz detectors: 6 THz bandwidth and 90 dB dynamic range. *Opt. Express*, 22(16):19411–19422, Aug 2014.

[59] R. J. B. Dietz, N. Vieweg, T. Puppe, A. Zach, B. Globisch, T. Göbel, P. Leisching, and M. Schell. All fiber-coupled THz-TDS system with kHz measurement rate based on electronically controlled optical sampling. *Opt. Lett.*, 39(22):6482–6485, Nov 2014.

[60] B. Globisch, R. J. B. Dietz, D. Stanze, T. Gbel, and M. Schell. Carrier dynamics in beryllium doped low-temperature-grown InGaAs/InAlAs. *Applied Physics Letters*, 104(17):172103, 2014.

[61] B. Globisch, R. J. B. Dietz, S. Nellen, T. Gbel, and M. Schell. Terahertz detectors from Be-doped low-temperature grown InGaAs/InAlAs: Interplay of annealing and terahertz performance. *AIP Advances*, 6(12):125011, 2016.

[62] D. Xia, M. N. Beattie, M. C. Tam, M. M. Wilkins, C. E. Valdivia, Z. R. Wasilewski, K. Hinzer, and J. J. Krich. Opportunities for high efficiency monochromatic photovoltaic power conversion at 1310 nm. In *2019 IEEE 46th Photovoltaic Specialists Conference (PVSC)*, pages 2303–2306, June 2019.

[63] M. Wilkins. Multi-junction solar cells and photovoltaic power converters: High-efficiency designs and effects of luminescent coupling. *Theses Collection, University of Ottawa*, 2017.

[64] A. L. Fahrenbruch, L. Lopez-Otero, J. G. Werthern, and Ta-Chung Wu. GaAs- and InAlGaAs-based concentrator-type cells for conversion of power transmitted by optical fibers. In *Conference Record of the Twenty Fifth IEEE Photovoltaic Specialists Conference - 1996*, pages 117–120, May 1996.

[65] M. Wilkins, C. E. Valdivia, A. M. Gabr, D. Masson, S. Fafard, and K. Hinzer. Luminescent coupling in planar opto-electronic devices. *Journal of Applied Physics*, 118(14):143102, 2015.

[66] S. Fafard, M. C. A. York, F. Proulx, C. E. Valdivia, M. M. Wilkins, R. Ars, V. Aimez, K. Hinzer, and D. P. Masson. Ultrahigh efficiencies in vertical epitaxial heterostructure architectures. *Applied Physics Letters*, 108(7):071101, 2016.

[67] S. Fafard, F. Proulx, M. C. A. York, L. S. Richard, P. O. Provost, R. Ars, V. Aimez, and D. P. Masson. High-photovoltage GaAs vertical epitaxial monolithic heterostructures with 20 thin p/n junctions and a conversion efficiency of 60%. *Applied Physics Letters*, 109(13):131107, 2016.

[68] N. Singh, C. Kin Fai Ho, Y. Nelvin Leong, K. E. K. Lee, and H. Wang. InAlGaAs/InP-based laser photovoltaic converter at ∼1070 nm. *IEEE Electron Device Letters*, 37(9):1154–1157, Sep. 2016.

[69] S. Wojtczuk, T. Parados, and G Walker. P/N In(Al) GaAs multijunction laser power converters. *National Aeronautics and Space Administration / Astrophysics Data System*, 1994.

[70] M. C. Tam, Y. Shi, D. Gosselink, M. Jaikissoon, and Z. R. Wasilewski. Temperature monitoring of narrow bandgap semiconductors. *Journal of Vacuum Science & Technology B*, 35(2):02B102, 2017.

[71] H. Erlig, S. Wang, T. Azfar, A. Udupa, H.R. Fetterman, and D.C. Streit. LT-GaAs detector with 451 fs response at 1.55 μm via two-photon absorption. *Electronics Letters*, 35:173–174(1), January 1999.

[72] M. Tani, K.-S. Lee, and X.-C. Zhang. Detection of terahertz radiation with low-temperature-grown GaAs-based photoconductive antenna using 1.55 μm probe. *Applied Physics Letters*, 77(9):1396–1398, 2000.

[73] T. Kataoka, K. Kajikawa, J. Kitagawa, Y. Kadoya, and Y. Takemura. Improved sensitivity of terahertz detection by GaAs photoconductive antennas excited at 1560 nm. *Applied Physics Letters*, 97(20):201110, 2010.

[74] S. Hisatake, K. Shimahashi, G. Kitahara, Y. Morimoto, H. Song, K. Ajito, and T. Nagatsuma. Homodyne detection of microwaves using low-temperature-grown GaAs at 1.55 μm. In *2011 International Topical Meeting on Microwave Photonics jointly held with the 2011 Asia-Pacific Microwave Photonics Conference*, pages 308–311, Oct 2011.

[75] J.-M. Rämer, Frank Ospald, G. von Freymann, and R. Beigang. Generation and detection of terahertz radiation up to 4.5 THz by low-temperature grown GaAs photoconductive antennas excited at 1560 nm. *Applied Physics Letters*, 103(2):021119, 2013.

[76] K. Saito, E. Tokumitsu, T. Akatsuka, M. Miyauchi, T. Yamada, M. Konagai, and K. Takahashi. Characterization of p-type GaAs heavily doped with carbon grown by metalorganic molecular-beam epitaxy. *Journal of Applied Physics*, 64(8):3975–3979, 1988.

[77] E. Tokumitsu, M. Shirahama, K. Nagao, S. Nozaki, M. Konagai, and K. Takahashi. Carbon doping in molecular beam epitaxial (MBE) growth of GaAs using neopentane as a novel carbon source. *Journal of Crystal Growth*, 127(1):711 – 715, 1993.

[78] S. J. Pearton and C. R. Abernathy. Carbon in GaAs: Implantation and isolation characteristics. *Applied Physics Letters*, 55(7):678–680, 1989.

[79] M. N. Beattie, M. M. Wilkins, M. C. Tam, C. E. Valdivia, and Z. R. Wasilewski. Optical characterization of InAlGaAs on InP for monochromatic photonic power

conversion. In *2019 Photonics North (PN)*, volume CFP1909V-ART, pages 1–1, May 2019.

[80] D. Xia, M. N. Beattie, M. C. Tam, M. M. Wilkins, C. E. Valdivia, Z. R. Wasilewski, K. Hinzer, and J. J. Krich. Detailed balance efficiency of 1310 nm multijunction photonic power converters. In *2019 International Conference on Numerical Simulation of Optoelectronic Devices (NUSOD)*, pages 69–70, July 2019.

[81] Y. Hu, M. C. Tam, and Z. R. Wasilewski. Unintentional As incorporation into AlSb and interfacial layers within InAs/AlSb superlattices. *Journal of Vacuum Science & Technology B*, 37(3):032902, 2019.

[82] L. Samuelson, B. Junno, G. Paulson, J.O. Fornell, and L. Ledebo. CBE growth of (001) GaAs: RHEED and RD studies. *Journal of Crystal Growth*, 124(1):23 – 29, 1992.

[83] Z. R. Wasilewski, M. M. Dion, D. J. Lockwood, P. Poole, R. W. Streater, and A. J. SpringThorpe. Composition of AlGaAs. *Journal of Applied Physics*, 81(4):1683–1694, 1997.

[84] P. F. Fewster. Interface roughness and period variations in MQW structures determined by x-ray diffraction. *Journal of Applied Crystallography*, 21(5):524–529, 1988.

[85] T. Sasaki, H. Suzuki, A. Sai, J.-H. Lee, M. Takahasi, S. Fujikawa, K. Arafune, I. Kamiya, Y. Ohshita, and M. Yamaguchi. *In situ* real-time x-ray reciprocal space mapping during InGaAs/GaAs growth for understanding strain relaxation mechanisms. *Applied Physics Express*, 2:085501, Jul 2009.

[86] K. Shimomura, H. Suzuki, T. Sasaki, M. Takahasi, Y. Ohshita, and I. Kamiya. Direct observation of strain in InAs quantum dots and cap layer during molecular beam epitaxial growth using *in situ* x-ray diffraction. *Journal of Applied Physics*, 118(18):185303, 2015.

[87] M. Takahasi, T. Kaizu, and J. Mizuki. *In situ* monitoring of internal strain and height of InAs nanoislands grown on GaAs(001). *Applied Physics Letters*, 88(10):101917, 2006.

[88] F. Briones, D. Golmayo, L. Gonzlez, and A. Ruiz. Phase-locked RHEED oscillations during MBE growth of GaAs and $Al_xGa_{1-x}As$. *Journal of Crystal Growth*, 81(1):19 – 25, 1987.

[89] W. G. Breiland and K. P. Killeen. A virtual interface method for extracting growth rates and high temperature optical constants from thin semiconductor films using *in situ* normal incidence reflectance. *Journal of Applied Physics*, 78(11):6726–6736, 1995.

[90] V. K. Dixit, S. D. Singh, T. K. Sharma, T. Ganguli, R. Jangir, S. Pal, B. Q. Khattak, A. K. Srivastava, H. Srivastava, and S. M. Oak. Studies on GaAs/AlGaAs based (p and n-type) quantum well infrared photodetector structures grown using MOVPE. In *2007 International Workshop on Physics of Semiconductor Devices*, pages 355–358, Dec 2007.

[91] G Yakovlev, D Frolov, and V Zubkov. Investigation of delta-doped pHEMT InGaAs/GaAs/AlGaAs structures by the electrochemical capacitance-voltage technique. *Journal of Physics: Conference Series*, 690:012015, feb 2016.

[92] A. C. Seabaugh, W. R. Frensley, R. J. Matyi, and G. E. Cabaniss. Electrochemical C-V profiling of heterojunction device structures. *IEEE Transactions on Electron Devices*, 36(2):309–313, Feb 1989.

[93] E. Peiner, H.-H. Wehmann, H. Iber, S. Mo, G.-P. Tang, A. Bartels, A. Schlachetzki, A. Koch, K. Dettmer, and M. Hollfelder. High-quality $In_{0.53}Ga_{0.47}As$ on exactly (001)-oriented Si grown by metal-organic vapour-phase epitaxy. *Journal of Crystal Growth*, 172(1):44 – 52, 1997.

[94] M. Udhayasankar, C. Rigo, J. Kumar, and P. Ramasamy. On the development of an electrolyte for ECV profiling of AlInAs. In *Conference Proceedings. 2000 International Conference on Indium Phosphide and Related Materials (Cat. No.00CH37107)*, pages 150–153, May 2000.

[95] W. G. Breiland. Reflectance-correcting pyrometry in thin film deposition applications. *S. N. Laboratories, Albuquerque, NM*, 2003.

[96] M. Pluta. Nomarski's DIC microscopy: a review. In Maksymilian Pluta and Mariusz Szyjer, editors, *Phase Contrast and Differential Interference Contrast Imaging Techniques and Applications*, volume 1846, pages 10 – 25. International Society for Optics and Photonics, SPIE, 1994.

[97] M. Mittendorff, M. Xu, R. J B Dietz, H. Knzel, B. Sartorius, H. Schneider, M. Helm, and S. Winnerl. Large area photoconductive terahertz emitter for 1.55 μm excitation based on an InGaAs heterostructure. *Nanotechnology*, 24(21):214007, apr 2013.

[98] F. W. Smith, H. Q. Le, V. Diadiuk, M. A. Hollis, A. R. Calawa, S. Gupta, M. Frankel, D. R. Dykaar, G. A. Mourou, and T. Y. Hsiang. Picosecond GaAs-based photoconductive optoelectronic detectors. *Applied Physics Letters*, 54(10):890–892, 1989.

[99] C. Kadow, S. B. Fleischer, J. P. Ibbetson, J. E. Bowers, A. C. Gossard, J. W. Dong, and C. J. Palmstrm. Self-assembled ErAs islands in GaAs: Growth and subpicosecond carrier dynamics. *Applied Physics Letters*, 75(22):3548–3550, 1999.

[100] M. Suzuki and M. Tonouchi. Fe-implanted InGaAs terahertz emitters for 1.56 μm wavelength excitation. *Applied Physics Letters*, 86(5):051104, 2005.

[101] I. Kostakis, D. Saeedkia, and M. Missous. Characterization of low temperature InGaAs-InAlAs semiconductor photo mixers at 1.55 μm wavelength illumination for terahertz generation and detection. *Journal of Applied Physics*, 111(10):103105, 2012.

[102] R. Yano, Y. Hirayama, S. Miyashita, N. Uesugi, and S. Uehara. Arsenic pressure dependence of carrier lifetime and annealing dynamics for low-temperature grown GaAs studied by pump-probe spectroscopy. *Journal of Applied Physics*, 94(6):3966–3971, 2003.

[103] M. Martin and E. R. Brown. Photoconductive materials for THz generation at 1550 nm: ErAs:GaAs vs InGaAs based materials. *Proceedings of SPIE*, 9362, 2015.

[104] A. C. Warren, N. Katzenellenbogen, D. Grischkowsky, J. M. Woodall, M. R. Melloch, and N. Otsuka. Subpicosecond, freely propagating electromagnetic pulse generation and detection using GaAs:As epilayers. *Applied Physics Letters*, 58(14):1512–1514, 1991.

[105] S. Kono, M. Tani, P. Gu, and K. Sakai. Detection of up to 20 THz with a low-temperature-grown GaAs photoconductive antenna gated with 15 fs light pulses. *Applied Physics Letters*, 77(25):4104–4106, 2000.

[106] G. Zhao, R. N. Schouten, N. van der Valk, W. Th. Wenckebach, and P. C. M. Planken. Design and performance of a THz emission and detection setup based on a semi-insulating GaAs emitter. *Review of Scientific Instruments*, 73(4):1715–1719, 2002.

[107] S. Verghese, K. A. McIntosh, S. Calawa, W. F. Dinatale, E. K. Duerr, and K. A. Molvar. Generation and detection of coherent terahertz waves using two photomixers. *Applied Physics Letters*, 73(26):3824–3826, 1998.

[108] M. P. Lumb, M. Gonzlez, M. K. Yakes, C. A. Affouda, C. G. Bailey, and R. J. Walters. High temperature current voltage characteristics of InP-based tunnel junctions. *Progress in Photovoltaics: Research and Applications*, 23(6):773–782, 2015.

[109] M. P. Lumb, M. K. Yakes, M. Gonzalez, R. Hoheisel, C. G. Bailey, W. Yoon, and R. J. Walters. Development of tunnel junctions with high peak tunneling currents for InP-based multi-junction solar cells. In *2012 38th IEEE Photovoltaic Specialists Conference*, pages 000949–000953, June 2012.

[110] k-Space Associates Inc. *Technology Overview Note: kSA BandiT Blackbody Temperature Measurement*, 2008.

[111] C. Schietinger. *Advances in Rapid Thermal and Integrated Processing*, volume 318 of *NATO ASI Series E: Applied Sciences*. edited by F. Roozeboom, Kluwer Academic Publishers, The Netherlands, 1996.

[112] P. Thompson, Y. Li, J. J. Zhou, D. L. Sato, L. Flanders, and H. P. Lee. Diffuse reflectance spectroscopy measurement of substrate temperature and temperature transient during molecular beam epitaxy and implications for low-temperature III-V epitaxy. *Applied Physics Letters*, 70(12):1605–1607, 1997.

[113] S. Johnson, C.-H. Kuo, M. Boonzaayer, W. Braun, U. Koelle, Y.-H. Zhang, and J. Roth. *In situ* temperature control of molecular beam epitaxy growth using band-edge thermometry. *Journal of Vacuum Science & Technology B: Microelectronics and Nanometer Structures Processing, Measurement, and Phenomena*, 16(3):1502–1506, 1998.

[114] D. P. Docter, J. P. Ibbetson, Y. Gao, U. K. Mishra, T. Liu, and D. E. Grider. Analysis of V/III incorporation in nonstoichiometric GaAs and InP films using SIMS. *Journal of Electronic Materials*, 27(5):479, May 1998.

[115] H. R. Potts and G. L. Pearson. Annealing and arsenic overpressure experiments on defects in gallium arsenide. *Journal of Applied Physics*, 37(5):2098–2103, 1966.

[116] M. Lagadas, Z. Hatzopoulos, K. Tsagaraki, M. Calamiotou, C. Lioutas, and A. Christou. The effect of arsenic overpressure on the structural properties GaAs grown at low temperature. *Journal of Applied Physics*, 80(8):4377–4383, 1996.

[117] M. Lagadas, M. Androulidaki, Z. Hatzopoulos, and M. Calamiotou. Dependence of arsenic antisite defect concentration and two dimensional growth mode on LT GaAs growth conditions. *Microelectronic Engineering*, 43-44:581 – 586, 1998.

[118] R. Yano, Y. Hirayama, S. Miyashita, H. Sasabu, N. Uesugi, and S. Uehara. Pump–probe spectroscopy of low-temperature grown GaAs for carrier lifetime estimation: arsenic pressure dependence of carrier lifetime during MBE crystal growth. *Physics Letters A*, 289(1):93 – 98, 2001.

[119] I. S. Gregory, C. Baker, W. R. Tribe, M. J. Evans, H. E. Beere, E. H. Linfield, A. G. Davies, and M. Missous. High resistivity annealed low-temperature GaAs with 100 fs lifetimes. *Applied Physics Letters*, 83(20):4199–4201, 2003.

[120] A. Jooshesh, F. Fesharaki, V. Bahrami-Yekta, M. Mahtab, T. Tiedje, T. E. Darcie, and R. Gordon. Plasmon-enhanced LT-GaAs/AlAs heterostructure photoconductive antennas for sub-bandgap terahertz generation. *Opt. Express*, 25(18):22140–22148, Sep 2017.

[121] S. Gupta, M. Y. Frankel, J. A. Valdmanis, J. F. Whitaker, G. A. Mourou, F. W. Smith, and A. R. Calawa. Subpicosecond carrier lifetime in GaAs grown by molecular beam epitaxy at low temperatures. *Applied Physics Letters*, 59(25):3276–3278, 1991.

[122] B. Paquette, B. Gsib, and R. Arés. Temperature mapping using single wavelength pyrometry during epitaxial growth. *Journal of Vacuum Science & Technology B*, 29(6):060604, 2011.

[123] D. Olego, T. Y. Chang, E. Silberg, E. A. Caridi, and A. Pinczuk. Compositional dependence of band-gap energy and conduction-band effective mass of $In_{1-x-y}Ga_xAl_yAs$ lattice matched to InP. *Applied Physics Letters*, 41(5):476–478, 1982.

[124] J. P. Praseuth, M. C. Joncour, J. M. Gérard, P. Hénoc, and M. Quillec. Growth and characterization of AlGaInAs lattice matched to InP grown by molecular-beam epitaxy. *Journal of Applied Physics*, 63(2):400–403, 1988.

[125] E. H. Li. Material parameters of InGaAsP and InAlGaAs systems for use in quantum well structures at low and room temperatures. *Physica E: Low-dimensional Systems and Nanostructures*, 5(4):215 – 273, 2000.